Analysis of dynamical interactions of axon shafts and their biophysical modelling

Daniel Smít

▶ **To cite this version:**

Daniel Smít. Analysis of dynamical interactions of axon shafts and their biophysical modelling. Neurons and Cognition [q-bio.NC]. Université Pierre et Marie Curie - Paris VI; Univerzita Karlova (Prague), 2017. English. NNT : 2017PA066095 . tel-01620166

HAL Id: tel-01620166

https://theses.hal.science/tel-01620166v1

Submitted on 20 Oct 2017

HAL is a multi-disciplinary open access archive for the deposit and dissemination of scientific research documents, whether they are published or not. The documents may come from teaching and research institutions in France or abroad, or from public or private research centers.

L'archive ouverte pluridisciplinaire **HAL**, est destinée au dépôt et à la diffusion de documents scientifiques de niveau recherche, publiés ou non, émanant des établissements d'enseignement et de recherche français ou étrangers, des laboratoires publics ou privés.

Charles University in Prague
First Faculty of Medicine

Université Pierre et Marie Curie Paris VI

Study programme: Lékařská biofyzika
(Studijní obor) École Doctorale Cerveau-Cognition-Comportement



Mgr. Daniel Šmít

Analysis of dynamical interactions of axon shafts and their biophysical modelling

Analýza dynamických interakcí těl axonů a jejich biofyzikální modelování

Doctoral Thesis

Supervisors: Martin Zápotocký, PhD
(Školitelé) Alain Trembleau, PhD

Prague & Paris, 2017

Declaration

I declare that the work presented in this thesis is my original research work done under the supervision of Martin Zápotocký and Alain Trembleau and that I have duly noted and cited all used sources and literature. I also declare that the work was not used to obtain any other or the same academic degree.

I hereby give consent for cataloguing an electronic version of this thesis in the interuniversity database system Theses.cz, for the purpose of systematic similarity checks of theses.

Prohlášení

Prohlašuji, že jsem závěrečnou práci zpracoval samostatně pod vedením Martina Zápotockého a Alaina Trembleau a že jsem řádně uvedl a citoval všechny použité prameny a literaturu. Současně prohlašuji, že práce nebyla využita k získání jiného nebo stejného titulu.

Souhlasím s trvalým uložením elektronické verze mé práce v databázi systému meziuniverzitního projektu Theses.cz za účelem soustavné kontroly podobnosti kvalifikačních prací.

In Prague, 10.04.2017

Daniel Šmít

Identification record

ŠMÍT, Daniel. Analysis of dynamical interactions of axon shafts and their biophysical modelling [Analýza dynamických interakcí těl axonů a jejich biofyzikální modelování]. Prague, 2017. 256 pages, no attachments. Doctoral Thesis. Charles University in Prague, First Faculty of Medicine, Institute of Physiology, CAS, Université Pierre et Marie Curie—Paris VI, supervised by Martin Zápotocký and Alain Trembleau.

Keywords: axon, fasciculation, axon shaft, bundling, neural development, cell culture, olfactory epithelium, biomembrane force probe, cell adhesion, mechanical tension

ŠMÍT, Daniel. Analýza dynamických interakcí těl axonů a jejich biofyzikální modelování [Analysis of dynamical interactions of axon shafts and their biophysical modelling]. Praha, 2017. 256 stran, bez příloh. Disertační práce. Univerzita Karlova v Praze, 1. lékařská fakulta, Fyziologický ústav AV ČR, Université Pierre et Marie Curie, Paris VI, vedoucí práce Martin Zápotocký a Alain Trembleau.

Klíčová slova: axon, tvorba svazků axonů, tělo axonu, vývoj nervového systému, buněčná kultura, čichový epitel, biomembránová silová sonda (biomembrane force probe), buněčná adheze, mechanické napětí

Contents

Abstract in English

While axon fasciculation plays a key role in the development of neural networks, very little is known about its dynamics and the underlying biophysical mechanisms. In a model system composed of neurons grown *ex vivo* from explants of embryonic mouse olfactory epithelia, we observed that axons dynamically interact with each other through their shafts, leading to zippering and unzippering behaviour that regulates their fasciculation. Taking advantage of this new preparation suitable for studying such interactions, we carried out a detailed biophysical analysis of zippering, occurring either spontaneously or induced by micromanipulations and pharmacological treatments.

We show that zippering arises from the competition of axon-axon adhesion and mechanical tension in the axons. This is upheld on quantitative level by conforming change of network global structure in response to various pharmacological treatments, without active involvement of growth cones. The manipulations of interacting shafts provide qualitative support for the hypothesis, and also allow us to quantify the mechanical tension of axons in our system. Furthermore, we introduce a biophysical model of the zippering dynamics, which efficiently serves the purpose of estimating the magnitude of remaining involved biophysical quantities. We provide several independent and mutually consistent quantifications of the force of axon-axon adhesion, which is to our knowledge first such estimate. The framework of our model allows us to carefully examine dissipative forces related to local shaft dynamics, determine dominating dissipative mechanism for a particular type of observed process, and estimate the value of corresponding friction coefficient.

We perform image segmentation of the time lapse videomicroscopy recording of the developing axonal network from the time lapse recording, and extract statistical and shape descriptors of its graph representation. We show that the network global statistics and local geometry changes are correlated and their time course consistent with qualitative predictions of our zipper model. We then quantitatively relate the individual zipper properties to global characteristics of the developing axon network *ex vivo*, and apply the model framework to reconcile *in vivo* data of population-wide distribution of axon incidence angles with data of probability of particular axon crossing in that population, reported by Roberts and Taylor in 1982. We compare the topological evolution of our *ex vivo* system to two-dimensional froths; the unique character of axonal network evokes many analogies with liquid foams, while it demonstrates many unique features, notably more robust stability of topological configurations and reversibility of some processes which change topology.

We show that there is a consistent mechanism which governs local interactions between axon shafts, supported by broad experimental evidence. This mechanism can be reconciled with changes in global structure of axonal network developing on slower time scale, analogically to well-studied relation between local relaxations, and topological changes and coarsening in two-dimensional liquid foams. We assess our observations and analysis in light of possible *in vivo* functional significance and propose a new role of mechanical tension in neural development: the regulation of axon fasciculation and consequently

formation of neuronal topographic maps.

Abstrakt v Češtině

Ačkoli hraje tvorba svazků axonů zásadní roli při vývoji nervových sítí, velice málo je známo o její dynamice a jejích výchozích biofyzikálních mechanismech. V modelovém systému neuronů kultivovaných *ex vivo* z explantátu embryonického myšího čichového epitelu jsme pozorovali dynamické interakce mezi axony prostřednictví jejich těl, které vedly k procesům zazipování a odzipování a regulovaly tak tvorbu svazků. Tento systém se ukázal jako vhodný způsob přípravy vzorku pro studium takovýchto interakcí, využili jsme jej ke provedení podrobných biofyzikálních analýz zipovacích procesů, které nastávaly buďto spontánně, nebo byly vyvolány mechanickými nebo farmakologickými manipulacemi.

Ukážeme, že k zipování dochází na základě protichůdných tendencí adheze mezi těly axonů a mechanického napětí v axonu. Tato teze je kvantitativně podpořena odpovídajícími změnami globální struktury axonální sítě bez účasti růstových vrcholů, pokud dojde k farmakologické manipulaci kultury. Mechanické manipulace interagujících těl axonů pak poskytují kvalitativní oporu tvrzení, a umožňují změřit hodnoty mechanického napětí axonů systému. Dále také představíme biofyzikální model popisující dynamiku zipovacích procesů, který nám umožní efektivně stanovit hodnoty zbývajících biofyzikálních parametrů. Poskytneme několik metodicky nezávislých, ale souladných, kvantifikací síly adheze mezi jednotlivými axony, což je první odhad této veličiny vůbec. V rámci tohoto modelu podrobně prozkoumáme disipativní síly související s lokální dynamikou těl axonů, stanovíme nejvýznamnější disipativní mechanismy pro různé typy pozorovaných procesů, a odhadneme hodnotu odpovídajícího koeficientu tření.

Provedeme segmentaci záznamu časového vývoje axonální sítě a extrahujeme statistické a geometrické míry struktury jejího grafu. Ukážeme, že změny globální statistiky sítě a změny lokální geometrie jsou korelované, a jejich časový vývoj je v souladu s předpověďmi našeho modelu na kvalitativní úrovni. V návaznosti na to kvantifikujeme vztah mezi jednotlivými vlastnostmi zipů a globálními charakteristikami vyvíjející se axonální sítě *ex vivo*. V rámci modelu rovněž vysvětlíme vztah mezi mezi daty pořízenými *in vivo* Robertsem a Taylorem v roce 1982, která uvádějí populační rozdělení pozorovaných úhlů, po kterými se dva axony potkávají, a daty, která ve stejném systému udávají pravděpodobnost, že pro daný pár axonů při kontaktu dojde k zipovacímu procesu. Srovnáme také vývoj topologie našeho *ex vivo* systému s analogickým vývojem ve dvourozměrných pěnových strukturách. Jedinečný charakter axonální sítě má mnoho podobností s dvourozměrnou kapalnou pěnou, avšak má také mnoho jedinečných vlastností, například vyšší stabilitu některých konfigurací a vratnost některých topologických změn.

V rámci práce presentujeme důsledný mechanismus, který popisuje vzájemné lokální interakce těl axonů, podpořený nahromaděnými experimentálními důkazy. Tento mechanismus lze vztáhnout ke změnám globální struktury axonální sítě na pomalejších časových škálách, analogicky jako v případě dobře prostudovaného vztahu mezi místními relaxačními procesy, topologickými změnami a hrubnutím ve dvourozměrných kapalinových

pěnách. Nakonec tato pozorování a analýzu diskutujeme v rámci možného funkčního významu *in vivo* a přikládáme mechanickému napětí novou roli ve vývoji nervové sítě: možnost regulace tvorby svazků axonů a jejich prostřednictvím také vliv na formování neuronálních topografických map.

Résumé en Français

La fasciculation des axones joue un rôle essentiel dans le développement des réseaux neuronaux. Cependant, la dynamique de la fasciculation axonale, ainsi que les mécanismes biophysiques à l'œuvre dans ce processus, demeurent encore très mal compris. En vue d'étudier les mécanismes de fasciculation d'axones ex vivo, nous avons développé un système modèle simple, constitué par des explants d'épithélium olfactif de souris embryonnaires en culture, à partir desquels poussent les axones des neurones sensoriels olfactifs. Grâce à une étude en vidéomicroscopie, nous avons observé que ces axones interagissent de façon dynamique par leur fibre (indépendamment du cône de croissance), à la manière de fermetures éclair pouvant se fermer («zippering») ou s'ouvrir («unzippering»), ce qui conduit respectivement à la fasciculation ou à la défasciculation des axones. Mettant à profit cette nouvelle préparation expérimentale pour l'étude des interactions dynamiques entre axones, nous avons développé une analyse biophysique détaillée des processus de zippering/unzippering, qu'ils soit spontanés ou induits par des micromanipulations ou des traitements pharmacologiques.

Nous montrons que le zippering est le résultat d'une compétition entre les forces d'adhésion inter-axones et leur tension mécanique. Le zippering à l'échelle d'axones individuels (ou de petits faisceaux d'axones) s'accompagne de changements quantitatifs de la conformation globale du réseau en réponse à des traitements pharmacologiques agissant sur la tension des axones, sans que cela passe par des effets sur les cônes de croissance. L'utilisation de la technique de «Biomembrane Force Probe» nous a permis, en réalisant des micromanipulations de fibres axonales, de quantifier la tension d'axones dans notre système, et d'apporter un support qualitatif à notre hypothèse. En outre, nous avons développé un modèle biophysique de la dynamique du zippering, qui nous permet d'estimer efficacement l'évolution de l'amplitude des forces impliquées. En utilisant plusieurs méthodes indépendantes, nous avons calculé l'ordre de grandeur de la valeur les forces d'adhésion entre axones, ce qui n'avait jamais été réalisé auparavant, sur aucun système. Le cadre de notre modèle nous permet d'examiner par ailleurs de façon rigoureuse les forces dissipatives liées à la dynamique locale des fibres axonales, de déterminer les mécanismes dissipatifs dominant dans des cas particuliers de processus observés, et d'estimer la valeur des coefficients de friction correspondants.

Nous avons procédé à la segmentation du réseau axonal en développement à partir des enregistrements de vidéomicroscopie de notre système, et extrait les descripteurs statistiques et de forme de sa représentation graphique. Nous montrons que les statistiques globales du réseau et les changements de sa géométrie locale sont corrélés, et que leur évolution temporelle est cohérente avec les prédictions qualitatives de notre modèle de zippering. Nous avons également relié de façon quantitative les propriétés des zippers individuels aux caractéristiques globales du réseau d'axones en développement ex vivo, et appliqué le cadre de notre modèle aux observations faites in vivo par Roberts et Taylor en 1982, concernant la distribution des angles d'incidence des axones au sein d'un réseau périphérique et la probabilité de croisement d'axones. Nous avons comparé l'évolution

topologique de notre système ex vivo à celle de mousses à deux dimensions. Le caractère unique du réseau axonal évoque de nombreuses analogies avec des mousses liquides, tout en comportant des propriétés spécifiques, en particulier la robustesse des configurations topologiques, et la réversibilité des processus changeant sa topologie.

En conclusion, nous mettons en évidence dans notre travail l'existence d'un mécanisme biophysique cohérent de contrôle des interactions locales entre fibres axonales. Ce mécanisme local est à mettre en relation avec les changements de la structure globale du réseau axonal (degré de fasciculation) qui s'opèrent sur une échelle temporelle plus longue. Cette relation est analogue à celle, bien connue, des relaxations locales et des changements topologiques des mousses liquides en deux dimensions. Enfin, nous discutons la signification fonctionnelle de nos observations et analyses, et proposons un nouveau rôles de la tension mécanique dans le développement du système nerveux : la régulation de la fasciculation des axones et, en conséquence, de la formation des cartes topologiques au sein des réseaux neuronaux.

Chapter 1

Introduction

The present work is a cross-disciplinary undertaking; it is a combination of neurobiology, developmental biology, biophysics, and computational modelling. It encompasses a project based on *in vitro* observations, biophysical micro-manipulation experiments, theoretical and computational analyses. The first part of the chapter Introduction, sections 1.1 and 1.2, covers the biological aspects of the work. Contemporary understanding of neural development, axon guidance, fasciculation and sorting is explained, as well as the model system used in the thesis project, the olfactory system (OS). In the second half of the chapter, sections 1.3, 1.6 and 1.7, biophysical literature preceding the project is presented, covering biophysical properties of the growing axons, experimental techniques, fasciculation and guidance modelling, network kinetics and theoretical approaches in general.

1.1 Neural development

During evolution, multicellular organisms have developed nervous systems allowing them to perceive their environment and internal state, to process internal and external information, and to develop motor behaviours. The cells of the developing neural system undergo differentiation through neural induction of a neuroectoderm within the embryo. Neural progenitor cells divide to produce progenitors of glial cells and neurons. A plethora of generated cell types (neuroblasts, glioblasts) migrate towards their final location, depending on their type and nervous system area. Neurons differentiate and develop an axon and dendrites. Axons, tipped by a growth cone (GC), grow towards genetically determined areas of projection within and outside the nervous system, guided by a combination of environmental and intrinsic cues (Kolodkin and Tessier-Lavigne 2011; Tessier-Lavigne and Goodman 1996). This development finally produces complex neural networks in which neurons are interconnected with each other and with other cells (i.e. muscle cells) of the body. In most systems, networks then go through postnatal activity-dependent remodelling steps leading to their full functional maturation.

1.1.1 Neural tracts

The development of the mammalian neural system, which is highly elaborate and comprises a very high number of neurons and neural connections, requires guided growth of millions of axons over long distances, their branching and formation of appropriate

connections with their targets (see fig. 1.1a for illustration). This very complex process necessitates unique sets of strategies to efficiently establish the proper wiring without errors. To support axon navigation towards remote targets, the process is separated into a sequence of guidance decisions, employing intermediate targets comprising glial cells or intermediate guidepost cells (Chédotal and Richards 2010; Raper and Mason 2010). The brain wiring often extends over considerable lengths, and is based on a functional specificity—different regions of the brain have specific functions related to their neuronal identity, shape and synaptic connection pattern. The functional specificity is controlled by gene expression early during the development.

The early developing brain is typically pioneered by groups of axons that grow in weakly coherent bundles, which become thicker over time as later follower axons are added, see fig. 1.1b. Initially established tracts are invariant across individual embryos, which means that guidance mechanisms must be in place and the guidance information must be not only available in the developing system but also detectable and processable by the outgrowing neural cells. The pioneer axons can have distinct character from the later axons, they gradually navigate short segments between decision points and serve as guideposts for other neurons. Despite the decision-making and substratum-providing role of the pioneers, they are not always essential for the followers to reach their targets (Raper and Mason 2010).

Generally, axons heavily depend on two major strategies to navigate: forming bundles with pioneering axons by adhering to each other, mediated by cell adhesion molecules (CAMs), or following diffusible or cell-surface-bound guidance ligands produced by other cells (or specifically by other GCs) along their track. Individual axons may use both strategies successively during the complex journey towards their target, responding at each choice point to a variety of guidance cues. Axon tracts in vertebrates are built on a large scale, comprising thousands of axons with common source and target, gradually developing over an extensive period of time. These axons can, in principle, be guided by isotypic interactions between earlier and later axons (pioneer-follower) or between cotemporally growing axons (community). The process can be illustrated on a well studied example of retinal ganglion cells: (i) it has been shown, that a removal of pioneer axons completely blocks retinal exit, and (ii) introduction of mutant axons can, through the community axon-axon interactions, mislead the population at the choice points (Pittman et al. 2008).

In general, pioneers provide essential information that follower axons use for normal pathfinding. They establish a basic axonal scaffold early while the embryo is small and the guidance cues are closely packed, which is preserved until adulthood as the organism grows (see fig. 1.1b). The followers can respond to some of the cues pioneers use to navigate, but their overall navigation efficiency, over expanding distances, is highly enhanced by the cues provided by the pioneers themselves (Raper and Mason 2010). While these mechanisms were formulated in general, and thoroughly described for some parts of the nervous system, specific involved processes (e.g. specific guidance molecules, receptors, pathways) are often not established with certainty (e.g. for the olfactory system). The question of navigation strategies of axons, and fasciculation in particular, is closely related to this work, which focuses on the role of local dynamical axon interactions

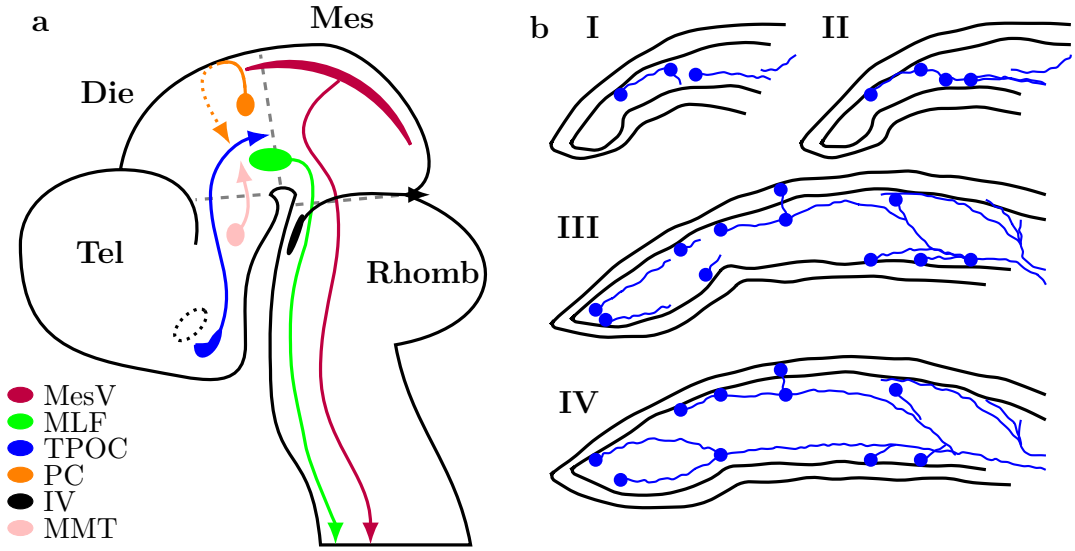

Figure 1.1: **a**: A scheme of mouse brain and early stage of developing neural tracts. Abbreviations: MesV, descending tract of the mesencephalic nucleus of the trigeminal nerve, MLF, medial longitudinal fasciculus, TPOC, tract of the postoptic commissure, PC, posterior commissure, IV, trochlear nerve, MMT, mammilothalamic tract, Tel, telencephalon, Mes, mesencephalon, Die, diencephalon, Rhomb, rhombencephalon. Adapted from (Chédotal and Richards 2010). **b** I-IV: Neuronal connections in the developing grasshopper limb. As the limb develops, progressively more distal neurons differentiate and pioneer short segments of perpheral nerve before fasciculating with more proximal pathways pioneered earlier. Once established connections are preserved with increasing size of the limb during growth. Adapted from (Raper and Mason 2010).

in global geometry and kinetics of axon population.

1.1.2 Growth cones

GC tips the growing axon. As observed in a culture dish, a GC is a flattened, fan-shaped structure, with many highly dynamic lamellipodia and filopodia (reinforced by actin) that radiate outwards, and stable central domain (supported by microtubules), as shown in fig. 1.2. GCs express adhesion molecules and receptors at their surface (see fig. 1.3), which make them responsive to locally and remotely produced guidance cues, and in turn guide the GCs along prescribed path. From guidepost to guidepost, GCs are sequentially responding to the provided cues and spatially modulating this response. GCs often change their morphology, e.g. when they extend, steer or retract. Changes in cytoskeletal dynamics constitute the GC's main response to attraction or repulsion by the cues, usually under further modulation by adhesion to the substrate. Strong attachment is required for extension, while detachment from the substrate results in axonal retraction (Kolodkin and Tessier-Lavigne 2011).

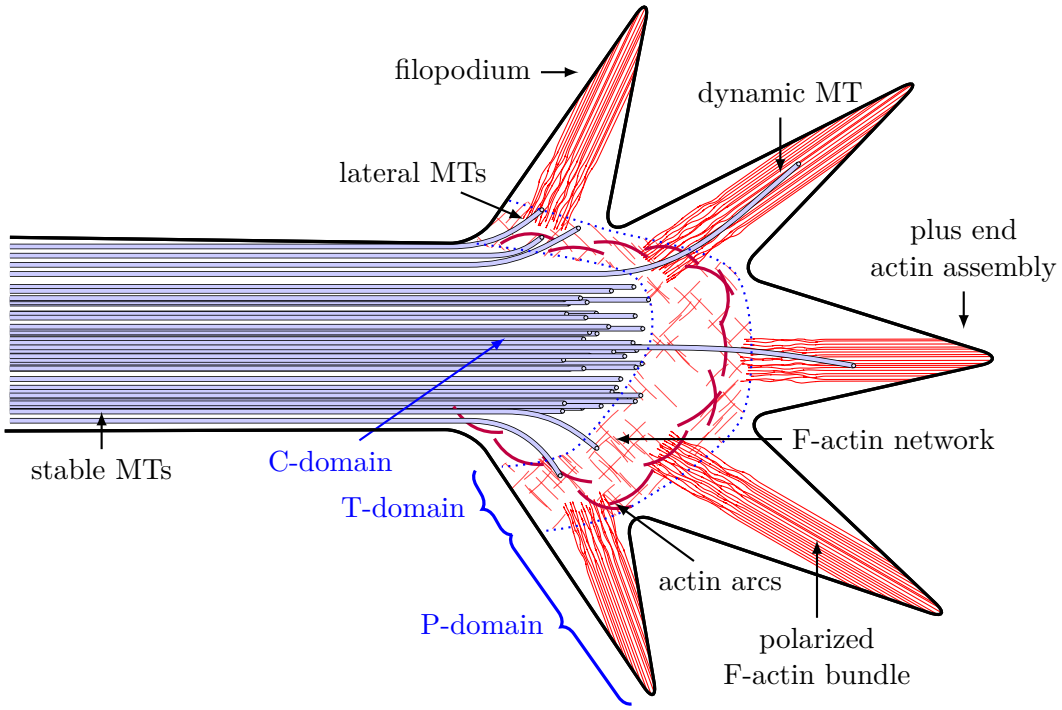

Figure 1.2: Illustration of a growth cone. The axon shaft is mainly formed by the stable MTs and its end is continued by GC's C-domain, lateral and dynamic MTs extend towards the GC and its filopodia. The outreaching filopodia of P-domain are formed by F-actin bundles, their outer plus ends are sites of F-actin assembly. Actin is depolymerised in the T-domain which contains F-actin network and reinforcing actin arcs.

Rather than passing through permissive spaces filled with yielding material, GCs prefer to grow on surface of adjoining cells, in particular glial cells, which may have growth stimulating effects (e.g. expressing trophic factors). A transitory population of neural

cells can be formed to assist GCs in tract formation, despite it plays no role in the mature nervous system. The character of the substratum determines the shape and dynamics of the GC: (i) During extension on axon bundles (ABs) in tracts in vivo, GCs are prolonged, with convex and concave lamellar wings extending from a central shaft. The lamelae wrap around the bundles. (ii) GC becomes complex when it pauses at the choice points, or at the entry of target region. The extension of the axon is interrupted, but the filopodia continue to extend and retract locally. (iii) When an aversive cue is encountered, GC condenses, becomes an appendage-free stump and often retracts. The changes in the shape therefore signal changes in the environment and present cues along the path of growth (Raper and Mason 2010).

The GCs are the cornerstone of axon guidance, they are equipped to recognize different types of signals, e.g. from their substratum (other GCs or extracellular matrix (ECM)); both diffusible and short-range (see fig. 1.3). Gradients of the diffusible guidance molecules are a notable feature of long-range axon targeting, and the GCs are axons' instrument to robustly read and mediate reaction to the gradients of guidance cue molecules (GCMs) in the developing nervous system. It is clear that both attractive and repulsive guidance mechanisms act upon the GC, despite the exact parameters have not yet been fully quantified (Tessier-Lavigne and Goodman 1996). While several decision-making strategies lead to similar predicted guidance performance, it has been demonstrated by (Mortimer et al. 2009) that a likely optimal mechanism is based on the sum of ligand-activated receptors weighted by their distance form the GC's centre—the receptor-sensing on the GC extremities carries more weight in the decision-making process. Such strategy offers high chemotactic sensitivity, with performance depending on both cue concentration and steepness of the concentration gradient. Detecting an appropriate cue gradient then facilitates steering of the axon tip, turning it towards or away from the gradient source.

Turning of a GC is a complex process largely based on the reorganization of actin and MTs. Actin filaments of a GC are organized into two distinct populations: dense and parallel filaments pointing outwards and into filopodia, and intervening networks of loosely interwoven filaments (red lines in fig. 1.2). Fast growing barbed tips (plus ends) of filopodial filaments are directed outwards, extension or retraction of the filopodium depends on the balance between the polymerization of actin at the barbed ends and the retrograde flow of the entire filaments. The filopodia extend asymmetrically before the GC turning and are supposed to steer the GC through differential adhesion, generate mechanical force and transduce distal signals. MTs form stable, cross-linked bundles in the axon shaft (Peter and Mofrad 2012), while they extend and retract as they explore the surroundings of the the GC (blue tubes in fig. 1.2). The (dynamical) MTs grow preferentially along the filopodial actin filaments in order to support stabilization and dilatation of a single filopodium during GC turning. These MTs stabilize and bundle in the general regions of GC advance, and ultimately determine where the new shaft will be formed upon the leading edge advance (Dent et al. 2011; Dickson 2002; Kolodkin and Tessier-Lavigne 2011; A. K. Lewis and Bridgman 1992; C. H. Lin, Espreafico, et al. 1996).

The polymerization of actin occurs behind the leading edge of the advancing growth

cone and actin depolymerization simultaneously occurs in the C-domain, while the retrograde flow brings F-actin from the leading edge back to the C-domain (the process is called treadmilling). When the rate of recycling of depolymerized monomers towards the leading edge balances the treadmilling towards the centre, adhesive contacts with the substrate become absent and the GC does not advance. Modulation of this balance by guidance cues then decides whether the GC undergoes advance, retraction or steering (in case of non-isotropic gradient field of GCMs). Linkage of F-actin to the substrate through the action of receptors and receptor complexes located on the cell surface, which can associate themselves with both the actin and the extracellular components of the substrate, facilitate GC advance through the cessation of net retrograde flow of F-actin along the interaction axis. All major adhesion receptor families use substrate-coupling mechanism to transduce actin flow (driven by myosin) into forward GC movement, including immunoglobulin (Ig) superfamily molecules, N-cadherin and integrins (Dent et al. 2011; Kolodkin and Tessier-Lavigne 2011; C.-H. Lin and Paul Forscher 1995; Suter and K. E. Miller 2011).

Although not required for MT exploration of P-domain, filopodial actin bundles guide the polymerization of MTs, while removing them at the same time from the P-domain by coupling to retrograde flow. In addition, during the GC steady state, F-actin flow, MT polymerisation and depolymerisation, MT retrograde and anterograde translocation and prevalence of actin-MT coupling do not exhibit significant regional variations; only significant variation exists for dynamic exploratory MTs, which are more prevalent in the distal side regions of the GC (see fig. 1.2). Lower retrograde flow of these MTs suggests lower actin-MT coupling in the region and possibly increases GC's sensitivity to guidance cues. The steering is then mediated by CAMs, causing initial signalling, followed by leading edge protrusion, C-domain advance accompanied by attenuation of retrograde F-actin flow, traction force generation and MT extension to adhesion sites. Detailed biophysical description of the process is given in the section Mechanical properties of axons (Lee and Suter 2008).

It is well established that the actin cytoskeleton is critical for GC motility, while MTs are essential for axonal elongation. Coordinated actin-MT interactions are the main regulators of MT rearrangements during the adhesion-evoked growth; actin and MT structures appear highly coupled. Actin arcs in the T-domain (magenta in fig. 1.2) and actin structures in C-domain undergo forward translocation together with MTs focusing the C-domain towards the adhesion site during the GC advance. The bulk of peripheral zone MTs along the interaction axis extend into the actin-free zone and later bundle as the elongation consolidates, regulated by Rho-, Rho kinase- and myosin II-mediated actin arc contractility (Lee and Suter 2008; A. W. Schaefer et al. 2002; Suter and K. E. Miller 2011).

All the GC's behaviour can be modulated by GCMs, regulating F-actin and MT assembly, actin translocation, MT dynamic instability and the attachment to the substrate. Some of the cues directly or indirectly modulate small GTPases, trigger signalling events, and regulate MT dynamics through inhibition or promotion of MT polymerisation, initiate nucleation of a new actin filament, promote filament elongation, or regulate the retrograde flow of actin filaments. These processes may eventually result in initiation,

extension, stabilisation or retraction of an individual filopodium (Dickson 2002; Kolodkin and Tessier-Lavigne 2011).

1.1.3 Axon guidance

Axon guidance is a very sophisticated and subtle task, outlined in the section Neural tracts. It employs signalling pathways organised around a limited number of specialised molecules (families of proteins acting as ligands and receptors), expression of which is temporally and spatially controlled, to efficiently establish a pioneer framework of nervous system. The whole process relies on reuse and accumulation. Developing axons prefer to grow along pre-existing axonal tracts. Later arriving axons tend to fasciculate with the pioneering ones, which have already established a neural tract blueprint (fig. 1.1b). It has been shown that the pioneering axons can be distinct from the follower axons in terms of growth cone morphology, behaviour and actin dynamics. The follower axons are less complex, grow at higher speed through the choice points (e.g. the midline), with higher actin dynamics (Bak and Fraser 2003; Kulkarni et al. 2007). Observations suggest that the pioneer axons recognise guidance cues distributed in a regionalised manner in the neuroepithelium. CAMs, e.g. cadherin and adhesion molecules of the Ig superfamily, may explain the selective preference of pioneer axons for (or exclusion from) particular domains (fig. 1.3)(Chédotal and Richards 2010).

The guidance of an axon is driven by four major mechanisms, while the significance of each mechanism depends on the particular context. These involve:

- (1) attractive and (2) repulsive short-range contact-mediated mechanism involving non-diffusible molecules on cell surface and ECM.
- (3) attractive and (4) repulsive interactions with distant diffusible GCMs.

These four canonical interactions outline axon's path globally and modulate it locally, as illustrated in fig. 1.3. Besides these driving mechanisms, axons require permissive and adhesive substrate to advance, while the repulsive contact mechanism helps to confine the axons to a particular neural tracks; local repulsion can likewise deflect or arrest an axon, or even cause GC's collapse and retraction (Tessier-Lavigne and Goodman 1996).

The neural tracts in the brain often span over long distances (e.g. cortico-spinal axons, see fig. 1.1a) and their formation is therefore subdivided into several shorter steps. Along such path, transient glial and neuronal populations act as 'guidepost cells' or 'corridor cells'. Such cells initially migrate, directed by GCMs, and reside along the track, where the neural path will later form (Chédotal and Richards 2010). The complex task of reaching a distant target is reduced to the simpler task of navigating each individual segment and choice point in turns. As the GCs approach an intermediate target, they tend to slow down (particularly the pioneers, (Bak and Fraser 2003)) and assume more complex morphology with more filopodia to better sample the environment. The growth is therefore composed of simple linear growth alternating with complex decision-making behaviour at the decision points (Tessier-Lavigne and Goodman 1996).

The problem of synapse formation is very broad in its complexity: some of the neurons completely lack axons (e.g. granule cells in the olfactory bulb[1]), others have to form

[1]The granule cell dendrites still navigate and form synapses with incoming axons.

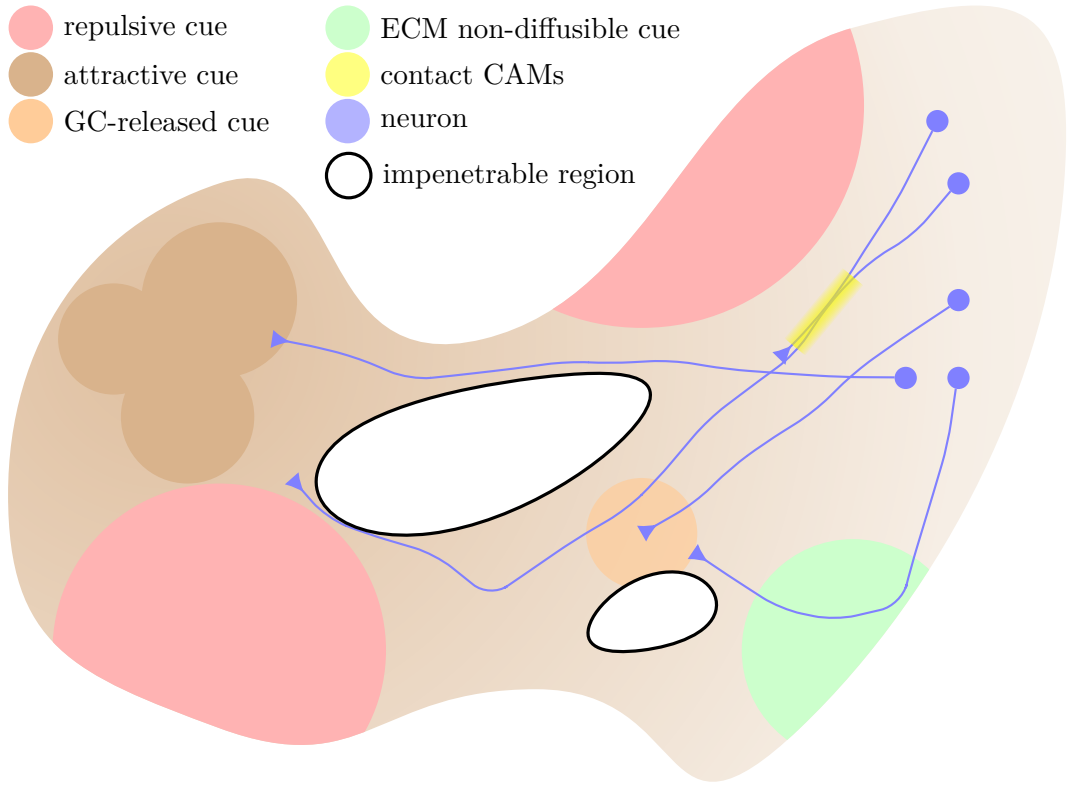

Figure 1.3: The neuron axons (blue) grow from cell bodies (on the right) towards the target area on the left (three brown dots); they might need to avoid impenetrable regions on the way (white with black border). The target area generates a gradient of diffusible attractive molecules (brown) to guide axon GCs towards itself—GCs grow stochastically, biased towards the gradient direction. Repulsive diffusible cues (red) may either repulse GCs towards other axons to induce axon bundling, or repel them in the direction of target area, away from restricted areas (bottom left). ECM non-diffusive membrane cues (green) also interact with axons and help to guide them. Axons in contact (either GCs or ASs) can interact through surface CAMs (yellow). The GC can also diffuse guidance molecules (orange) of its own to attract or repel the other GCs.

precise distant point-to-point connections with unique target cells. A distinction can be also made between projecting axons with targets in other parts of the organism (e.g. cortico-spinal axons guided by multiple GCMs; they can be centimetres long in mice and metre long in humans), and interneurons which form contacts with other neurons in their immediate vicinity, under specific patterns (e.g. CAM-guided interneurons in forebrain and hindbrain). The precise synaptic location within the target region is usually determined by a combination of concentration gradients of a few types of GCMs,

which can be detected by complementary gradients of receptors on the axons' GCs; such organisation allows GCs to determine the direction independently of their location. In addition, the distribution of axon terminals on the target cells is mostly not random, but confined to specific compartments of the target cell (body, dendrites, etc.) (Chédotal and Richards 2010; Mortimer et al. 2009; Tessier-Lavigne and Goodman 1996).

Different tracts are formed on different levels of guidance complexity. For the most complex wirings (e.g. olfactory system treated in the section 1.2), each axon must be adapted to make a series of appropriate choices. It becomes necessary for the axons to differ in their response to the same cue according to current context, in order to follow divergent pathways—a single axon must also be able to respond to the same cue differently at different points of its track and during different stages of development, it must be able to modulate its responsiveness to the set of cues presented along its trajectory. To give examples: (i) cyclic nucleotides (e.g. cAMP) may modulate the responsiveness and toggle a repulsive/attractive response of axon to a particular cue, (ii) axon migrating along or against a ligand gradient may depend on local translation of mRNAs in the GC to maintain its sensitivity, (iii) GC's responsiveness to a specific cue can be completely switched once it reaches an intermediate target (e.g. midline) (Dickson 2002; Kolodkin and Tessier-Lavigne 2011).While the early axonal tracts are highly conserved among vertebrates, on the level of individual axon, the navigation is not always error-proof and point-precise; the projections are, to lesser or greater degree, influenced by stochastic processes, and later refined by activity-dependent pruning (Chédotal and Richards 2010).

1.1.4 Guidance cues

The reproducible patterns of axonal outgrowth in developing embryos, and the preferences of particular axons for particular substrates and choices imply, that the guidance information must be reproducibly localised in the environment. The information could take multiple forms (Raper and Mason 2010):

(I) **Adhesive cues** fall into two major categories, ECM components expressed in cellular interstices or basement membranes, and CAMs expressed on non-neuronal or neuronal surfaces (fig. 1.3). These molecules are recognised by complementary axon-specific receptors expressed on GCs, through which the molecules indirectly influence the GC motility. GCs selectively grow on more compliant substrata (detailed in the section Mechanism of growth cone advance), on which they exert higher force and are more difficult to dislodge.

(II) **Trophic signalling molecules** promote neuronal survival, GC motility and outgrowth, while their steep gradients can orient the axonal outgrowth. Besides chemoattractant roles of some growth factors, the general role of trophic factors is to assure stabilisation and survival of neurons and their processes once they have made appropriate connections.

(III) **Tropic guidance cues** communicate navigation information to the GC, attracting or repelling it (fig. 1.3). This is a large category of cues, actively guiding axons to

the appropriate target locations. These can act at the distance as diffusible cues, or interact directly with the receptors on the surface of the axon. The idea was initially proposed in chemoaffinity theory by Sperry (Sperry 1963), which served as a basis for many axon guidance models.

(IV) **Modulatory guidance cues** modulate axons' response to the tropic cues, without innate tropic effects. They can for example completely switch GC's response to a particular tropic cue, between attractive and repulsive (e.g. at the midline), or mediate the strength of the response.

Clearly, an individual guidance molecule can match several of these categories, while its effect is always determined by the receptors expressed on the axon surface. Subpopulations of neurons of divergent pathways express different sets of receptors, interacting with temporally and spatially discontinuous guidance cues, and undergoing selective fasciculation. Generally, the interaction of a ligand with a receptor can trigger a transduction pathway, which induces changes within the axon, causing extension, retraction or steering of the GC. It is therefore not surprising, that multiple guidance effects do not simply add up, but interact in a non-linear manner (Raper and Mason 2010).

The pathfinding mainly depends on two large CAM families: Ig and cadherin superfamily. Some members of these families can mediate homophilic adhesion, acting as both ligand and receptor, while others serve as either heterophilic ligand or receptor for cell-surface or ECM molecules (which include laminin, collagen, tenascin and thrombospondin). The ECM molecules can act as promoters or inhibitors of neurite outgrowth and extension *in vitro*, while many of them are expected to play roles in axon guidance *in vivo* (Tessier-Lavigne and Goodman 1996). Chemoaffinity had been initially attributed to the CAMs, they had been supposed to passively guide the GCs by providing permissive substrate and promoting axon outgrowth (e.g. integrins, fasciclin or neural cell adhesion molecules). Signalling and regulating capacities of these CAMs (e.g. DCC and Robo act as receptors for GCMs), as well as other proteins directly stimulating GC turning, were identified only later (Chilton 2006; Kolodkin and Tessier-Lavigne 2011).

Besides the direct contact interaction, ligand-dependent signalling transduction pathways play a key role in pathfinding. In addition to Ig and cadherins, families of GCMs include also netrins, slits, semaphorins and ephrins (Dickson 2002; Kolodkin and Tessier-Lavigne 2011). These cues directly stimulate axon steering by regulating cytoskeletal dynamics in the GC through signalling pathways (detailed in section Mechanism of growth cone advance). Conversely, GCs also release some of the GCMs. To generate complex wiring of the CNS using only several GCMs (discovered to-day), the multi-functionality of those molecules is necessary: the extracellular guidance cue can both attract GCs or repel them, depending on the current context (see fig. 1.3); the same GCMs can act over the distance or in short-range interaction (immobilized on the producing cell), they can stimulate or suppress axon branching and elongation, or can control mapping of appropriate topographic location; e.g. ephrins are mediated by Eph receptors, acting both as attractants and repellants, with implicated roles in pruning and synaptogenesis; ephrins A and B generate two gradients in the optic tectum to establish topographical ordering (Chilton 2006; Dickson 2002; Kolodkin and Tessier-Lavigne 2011).

After the formation of pioneering axon tracks during initial pathfinding, fasciculation occurs through axon-axon interactions mediated by Ig CAMs (e.g. NrCAM, L1-CAM, or TAG-1) (Chédotal and Richards 2010), Eph ligands, transmembrane Semaphorins, or cadherins (Kolodkin and Tessier-Lavigne 2011; Tessier-Lavigne and Goodman 1996). The molecules can have both contact-mediation and distant guidance roles. Several guidance molecules can act as attractors inducing fasciculation for some axons and as repellants inducing defasciculation to another axons, depending on the receptors on the GCs. For example, netrin attractive effects are mediated by receptors of DCC family, while the repulsive effects are mediated by members of the UNC5 family (Round and Stein 2007); semaphorins are both secreted and transmembrane cues recognised by receptors of the plexin family, and serve as crucial repulsive cues initiating defasciculation, as well as attractive cues in other contexts (Kolodkin and Tessier-Lavigne 2011).

Selected cell adhesion molecules

The neural cell adhesion molecule (NCAM) is a cell surface adhesion glycoprotein of Ig family implicated in the development and stability of nervous tissue, one of the most abundant in the nervous system. Extracellular segments contains two fibronectin type III repeats and five tandem Ig domains, which are the active participants of the binding. Post-translational modification of NCAMs (with polysialic acid covalently attached to its Ig domains) allows changes in binding mechanism according to organism's stage of development. NCAMs form homophilic bonds of two distinct binding events (i.e. have two possible binding configurations), which exhibit similar bond energies and unbinding rates at lower loading rates but diverge as the loading rate increases. The study (Wieland et al. 2005) indicates, that the Ig3 domain is crucial for the stronger bond, while Ig1 and Ig2 mediate the weaker bond. It has been also shown, that a flexible hinge exists, which alters the orientation of the adhesive domains and thus accommodates differences in intercellular space.

The polysialic acid (PSA) plays a major role in progenitor cell migration and differentiation, axon pathfinding and targeting, and plasticity changes; it has large hydrated volume that serves to modulate the distance between cells—PSA is a crucial part of vertebrate mechanism for global regulation of cell interactions. PSA chain is produced by Golgi polysialyltransferases, with slightly variable length. It exerts 'permissive regulation', allowing other factors to override existing cell interactions (e.g. adhesion), or 'insulative regulation', prohibiting cell from premature actions. Up-regulation of PSA results in conditions permissive for changes in cell position and shape. For cells to form close contact, intermediate water must be removed; long PSA structure binds a lot of water, hampering the cell approach, inducing steric repulsion and attenuation of cell-cell bonds mediated by NCAMs, but also cadherins or Ig CAMs (Brusés and Rutishauser 2001; Rutishauser 2008). The properties of PSA make it convenient to use during experiments *in vitro*, to interfere with intercellular adhesion in the culture.

Cadherin family molecules are expressed in virtually all solid tissues. Their different expression patterns, binding capacities and adhesion specificity are thought to be responsible for the formation of tissue boundaries and cell sorting. They mediate homophilic

adhesion between cells in a Ca^{2+}-dependent manner (Ramsey A. Foty and Malcolm S. Steinberg 2004). The prototypical examples of the cadherin family are E-cadherin and N-cadherin, which have been shown to be adhesive specific at single molecule level (Panorchan et al. 2006). In living cells, N-cadherin and E-cadherin molecules show a qualitative and quantitative difference in their binding mechanism; particularly N-cadherins interact through single-well potential, while it is double-well for E-cadherins (switching between wells at the loading rate $\sim 500\ \frac{\mathrm{pN}}{\mathrm{s}}$), which also manifests higher mean bond rupture force. More interestingly, heterotypic interactions between type I cadherins, E-cadherins and N-cadherins, were not observed in the study (ibid.). Biophysical properties of CAMs are treated in more detail in the section Detailed cell adhesion molecules properties.

1.1.5 Fasciculation

The pioneering axons form initial tracks growing between the choice points, usually navigated by gradients of GCMs sensed by their GCs (see the section Axon guidance and fig. 1.3). They are often better equipped for such tasks than axons participating in the same connection in the later stage of development (Bak and Fraser 2003; Kulkarni et al. 2007). The later axons on the other hand take advantage of these prepared framework paths and adhere to the pioneer axon trails in the process of fasciculation, which assists their approach to the target location.

Axon bundles (fascicles) are formed when axons are in contact. Follower axons have multiple ways of approaching the bundle. The direction of growth of their GCs has a stochastic component, this movement is however biased by the (i) presence of GCM concentration gradients (attractive or repulsive) released by the target/guide post cells, (ii) attractive GCM concentration gradients released by other GCs of the same subpopulation (see fig. 1.3), (iii) properties of the underlying substrate, its permissivity, compliance and tension (Franze et al. 2009), and (iv) GC's general aversion to direction change. In effect, subpopulations of axons follow the direction of a particular GCM gradient and probe their environment due to stochastic features of GC movement, which facilitate collisions with other axons, contact interaction and potential aggregation (Hentschel and A. v. Ooyen 1999).

Convergence of random movements is further supported by repulsive GCMs (inhibitory factors) released by the encompassing environment, which 'push' axons towards each other, making the environment less attractive (Tessier-Lavigne and Goodman 1996). In some cases, axons forming a bundle can be funnelled and unsheathed by specialised cells, which assist formation and wrap the nerve (e.g. ensheathing cells in the olfactory system, see section Olfactory ensheathing cells). To initiate the contact, it is usually sufficient to approach the other axon within $\approx 10\,\mu\mathrm{m}$, which is the approximate length of GC filopodia (fig. 1.2) and of active side processes outgrowing from the AS.

Once the contact between the ASs is formed, the composition of CAMs on the participating axons determines the character of the interaction, which can be attractive or repulsive, of variable strength. An adhesive combination of CAMs has an effect of 'pulling' axons together, mediating axon fasciculation; in vertebrates, the molecules are mostly of Ig CAM and cadherin families. The CAM-dependent strength of the interac-

tion can induce segregation of subpopulations of axons (see section 1.5, exemplified in section 1.2.4), i.e. if adhesion within a particular subgroup (homotypic) is stronger than cross-adhesion between axons of different subgroups (heterotypic). The fasciculation is not necessarily a permanent event, but is under influence of spatial and temporal signals.

GCs often extend along the surface of other axons in axon fascicle and exit such fascicles to initiate the new section of their path, eventually forming a synapse. The balance of attractive and repulsive contact forces can be shifted not only by a change of CAMs composition, but also by a shift in other factors, for example, PSA was shown to interfere with Ig CAM L1/NgCAM mediating axon-axon adhesion, and driving defasciculation of motor axons in chick embryo. Similar interference and defasciculation can be observed in *Drosophila* motor axons from major motor nerve driven by secreted Beat protein (ibid.). Expression of regulating factors generally depends on the location and the stage of development (Brusés and Rutishauser 2001).

Classical understanding of fasciculation as part of axon guidance (section Axon guidance) assumed that a static AS trail is formed by (stochastic) GC advance, where the fasciculation is regulated by the GC alone (e.g. no side-processes, no dynamic shaft-shaft interaction) (Kolodkin and Tessier-Lavigne 2011; Tessier-Lavigne and Goodman 1996). The tension and relaxation within the AS (Bray 1979; Dennerll, Lamoureux, et al. 1989), traction force generated at the GC (Betz et al. 2011; Lamoureux, Buxbaum, et al. 1989; Lee and Suter 2008) and active tension generation within the whole axon (O'Toole, Lamoureux, et al. 2015) however act to straighten and relax the ASs and mechanically align the AS and the GC orientation (H. Nguyen et al. 2016), while adhesive contact forces act to reorganise ASs of the proximal fascicles (behind the GCs). This means that some rearrangements of non-distal parts of the axonal geometry and topology might take place.

1.1.6 Zippers

The interaction of ASs was first inferred by Roberts and Taylor (Roberts and J. S. H. Taylor 1982) from static electron microscope images, and its kinetics was later observed by Voyiadjis (Voyiadjis et al. 2011) in optical microscope time lapse videos.

Roberts observed the formation of the sensory neurite plexus on the basal lamina of trunk skin in *Xenopus* embryos using electron microscope, and identified interesting statistics of axon incidence (approach) angles. The neurites meeting at incidence angles close to 90° would tend to cross over one another, the neurites meeting at more shallow angles would fasciculate. Particularly, absence of angles <30° was observed, suggesting that an active rearrangement of the shafts takes place. If no modifications took place, the distribution would have been rather uniform even for shallow angles. The distribution of parting angles was similar, suggesting that the rearrangement process might be a generic feature of the AS interaction, independent of GC activity.

Roberts also noticed, that the probability of AB crossing increases roughly linearly with the incidence angle. To explain such behaviour, the authors assumed an axon prefers to adhere to another shaft, rather than to the substrate. Under shallow angles, the area of adhesion is larger and uneven on either side of the axon, the fasciculation

and alignment are favoured, while in the case of nearly normal approach angles, initial contact area is smaller and equally distributed on either side, so the axons prefer to preserve their current direction and cross over. For such mechanism of fasciculation, the GC action is not essential, the bundling can occur through contact of the two shafts later after GC crossing (Roberts and J. S. H. Taylor 1982).

In the study (Voyiadjis et al. 2011), dorsal root ganglia (DRG) axons were grown in constraining stripes, and recorded in the time lapse video. It has been shown that despite individual axon's stochastic motion, the bundles tend to align along the stripe axis, and that the individual bundles persist after crossings or encounter, their calibre may however change as axons are transfered between the bundles through competing fasciculation/defasciculation processes. If GCs are absent, the transfer can be mediated by zippering and unzipperng of the constituting axons. In such case, two two bundles in contact either increase or decrease the length of the adhering section of their shafts. To provide an idea of the process time scale, the velocity of the observed zippering was $(0.65 \pm 0.13)\ \frac{\mu m}{min}$ (ibid.).

1.1.7 Neural maps

The use of space to encode information is a fundamental organisational principle of the nervous system. Neural maps are used in all sensory modalities and motor control. In a continuous map, nearby neurons in the input field (which tend to respond to a particular stimulus together) connect with the nearby neurons in the target field, preserving spatial order (e.g. visual system, fig. 1.4a). In a discrete neural map, the spatial organisation of one field reflects discrete qualities (e.g. olfactory receptor types) of neurons in the other field (e.g. olfactory system, fig. 1.4b). These two described types form two poles of a neural map spectrum, with many falling somewhere in between. For example higher visual maps combine continuous representation of visual field, while discrete elements represent direction of motion, or somatosensory maps continuously represent the body surface but discrete units are embedded, representing whisker barrels. While the two types of mapping use distinct mechanisms, the final refinement and removal of strayed projections is usually activity-dependent. The neurons activated by the common input (i.e. nearby retinal ganglion cells or olfactory sensory neurons of the same type) fire in correlated manner, triggering action potential (AP) in the postsynaptic neuron, strengthening the synapse and physically stabilising it; the synapse of unrelated sensory neurons, firing independently, is not reinforced, progressively weakened and their presynaptic and postsynaptic structures are eventually retracted (Cline 1998; Luo and Flanagan 2007).

ACTIVITY-DEPENDENT SYNAPSE PRUNING

Continuous map formation is often driven by pairs of GCM gradients (e.g. EphA/ephrin-A, EphB/ephrin-B in the visual system) determining the two-dimensional target location, which are however not necessarily orthogonal. The gradients themselves would not be sufficient, another crucial feature is bifunctionality, i.e. the axon response to the ligand is concentration dependent (e.g. inhibition/promotion of growth, repulsion/attraction). The Eph/ephrin ligand-receptor pairs often form spatial counter-gradients, the level of expression of ephrins determines the threshold concentration for Eph (e.g. switching

from repulsion to adhesion in retina). Such gradient-driven positioning provides relative target regions for the invading axons, to ensure smooth and precise map formation (fig. 1.4a); within these regions, axon-axon short-range CAM-mediated competition takes place. The output map is topologically equivalent to the input map. Such combination of strategies remains robust in the changing environment (e.g. changing GCMs concentrations, map shape and size) during development and evolution (Luo and Flanagan 2007).

Discrete units of the **discrete map** represent individual input channels of the peripheral filed (e.g. odorant receptors (ORs) in the OS, barrel whiskers)—a neuron has an intrinsic identity (e.g. of protein expression or functional), which determines the pathfinding process independently of its spatial location. The mechanisms of pathfinding are seemingly more complex and less explored than in the case of continuous map; unlike its continuous counterpart, discrete mapping changes the topology from peripheral to target field. The mapping is determined by the environmental cues (e.g. Slit1 and Robo2 in the OS) and the corresponding intrinsic identities regulating receptor expression or relevant signalling pathways (e.g. G-protein signalling in the OS). This means that the system of GCM–receptor gradient correspondence (as in the continuous mapping) is still viable, however the graded levels of receptors are not determined spatially but by the neuronal identity, which corresponds to the desired target spatial organisation (see fig. 1.4b). Such mechanism allows initially disparate spatial organisation to map into structured target pattern.

The present work is focused on the OS, which is a typical example of a discrete mapping (see section Olfactory system). To provide slightly broader context, other sensory systems will be shortly discussed and compared to the OS.

Visual system

The visual system (VS) is a typical example of a continuous neural mapping—it preserves the positional organisation between the input image and its representative topographical map (fig. 1.4a)—but is combined with feature-specific laminar (i.e. discrete) organisation (fig. 1.4b). Processing of the visual information begins already in the retina, which is a layered structure, comprising about 100 types of cells. Photoreceptive cones and rods in the posterior retina absorb incoming light and generate AP travelling anteriorly through the layered structure to bipolar and horizontal cells, to amacrine cells and finally to the retinal ganglion cells (RGCs), which are the retina's only output neurons. In the layers (S1-S5), the raw point signal from the cones and rods is processed and separated into parallel channels (covering identical input field area) encoding features such as motion, edges and simple shapes. The RGCs project dendrites into a specific lamina in the inner plexiform layer (representing particular feature) forming connection with bipolar and amacrine cells, and analogically project their axons into a particular layer of the superior colliculus (SC). This way, individual features are extracted and transmitted (in the form of layers), while their mutual spatial organisation is preserved (in the form of topographic map) (Missaire and Hindges 2015).

The CAMs play crucial role in multistep development of the VS, they are involved

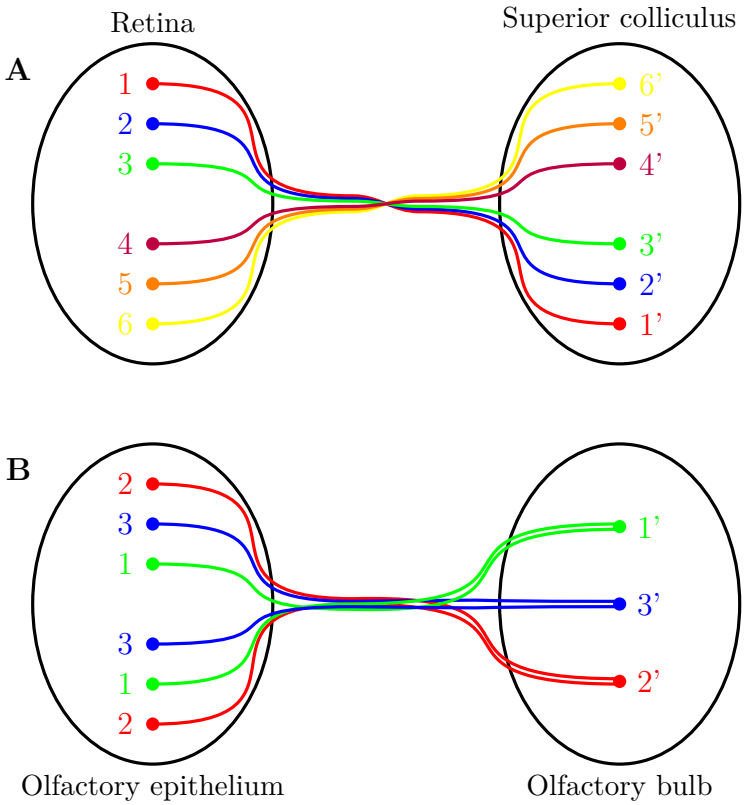

Figure 1.4: **a**: Continuous neural mapping (e.g. visual system), **b**: discrete neural mapping (e.g. olfactory bulb)

in neuritogenesis, pathfinding and type-specific connectivity of circuits processing distinct visual features (i.e. the layers). Upon RGC differentiation, CAMs (N-cadherin, NCAM, L1) induce neuritogenesis and activate axon CAM-mediated outgrowth pathways towards the SC. The layer specificity of a RGC, both in the inner plexiform layer (dendrites) and in the laminae of the SC (axons) is determined by intrinsic CAM composition, providing RGC's identity. Topographic map formation is controlled by activity-dependent mechanisms and multiple pairs of axon-guidance molecules forming gradients in the retina and SC (EphA/ephrin-A, EphB/ephrin-B) with additional modulation by L1 and NrCAMs. The spatial organisation in retina, the nearest-neighbour relationship, is maintained during the projection to the SC through strict homophilic adhesion mediated by CAMs. Conversely, in olfactory map formation in the OS, the projecting axons of the same neuronal identity are spatially dispersed but converge onto single globular location of the olfactory bulb (OB). The process of sorting begins with GCM-mediated formation of coarse map, while precise local sorting occurs autonomously by axon-axon interactions, without target-derived cues. There is no nearest-neighbour conservation. The information coded in the olfactory map on the OB is processed in the local neuronal circuits and conveyed by tufted and mitral cells to the olfactory cortex (OC) (Luo and Flanagan 2007; Missaire and Hindges 2015; Mori and Sakano 2011).

Auditory system

The functions embedded in the auditory system (AuS) impose special demands on organisational features and precision of its assembly. The cochlear sensory epithelium creates frequency map, rather than a space map (as is case of visual or somatic systems), while information about interaural time and intensity difference is crucial for sound localisation. Neural processing of auditory stimuli in mammals begins in the cochlea, where the sensory hair cells (HCs) in organ of Corti encode changes in sound pressure—deflections in their stereocilia responding to basilar membrane movements result in transmitter release onto distal processes of spiral ganglion neurons (SGNs). A strong correlation between stereocilia displacement (frequency dependent) and HC position forms an ordered representation of frequencies; the frequency map is conveyed onto SGNs, from where it propagates into the central auditory system (fig. 1.4a) (Cramer and Gabriele 2014).

The Eph/ephrin signalling plays several important roles in the auditory pathway; the signalling can be bidirectional (ligand-receptor pair can switch roles; signalling can be triggered through binding of ligand) and bifurcational (attractive or repulsive). The GCMs provide guiding gradients as well as contact discrete cues. Initial innervation of inner and outer HCs by processes of SGNs is likely segregated by EphA4 (expressed in type I inner HC-specific SGNs) and ephrinA5 (expressed in HCs), long-range and short-range cues. General projection from Cochlea towards the brainstem travels through cranial nerve VIII; while EphA4 seems to be graded in a manner consistent with the frequency axes, it is also expressed in auditory region of the nerve, while EphB2 is expressed in vestibular region. Together, the organ of Corti, SGNs and their developing connections exhibit complex complementary and overlapping Eph/ephrin expression patterns, which preserve low frequency to high frequency continuous ordering. The tonotopic map

is recreated in auditory brainstem nuclei based on ephrinB2 and EphA4 gradients. On contrary, the epithelium map in the OS is not continuously ordered, but rather stochastic, so the ordering is not merely preserved as in the ascending pathways of the AuS, but rather emerges to form a discrete map of the OB, in contrast to the tonotopy in the AuS's brainstem nuclei (Cramer and Gabriele 2014; Webber and Raz 2006).

1.2 Olfactory system

In sense of the topographic projections, the OS is on the other end of neural maps spectrum than the VS. The map on the OB is discrete (fig. 1.4b), its formation was already touched upon in the section Neural maps. In the adult mammalian OS, there is an intriguing topographic projection pattern of axons between the olfactory epithelium (OE) and the OB (fig. 1.5). Olfactory sensory neuron (OSN) axons exit the OE and extend towards the OB, where they coalesce into glomeruli. In mice, each OSN expresses 1 of ∼1200 ORs and is spatially bound by this intrinsic OR to a particular zone of the OE, numbered I to IV from dorsal to ventral (Ressler et al. 1993). Within those zones, however, OSNs of particular OR are not distributed contiguously but stochastically, intermingled with OSNs of other OR types. Due to the scattered distribution and a high number of OR-types of the OSNs, the proximal ABs are highly heterogeneous in terms of the OR identity (Nedelec et al. 2005), however upon reaching the OB, the OSNs expressing the same OR coalesce to form one or two glomeruli per hemibulb (typically single medial and single lateral glomerulus in each bulb). The hierarchical fasciculation process is mediated by OR-specific levels of GCM receptors expressed by the axons for navigation in the mesenchyme, and by homotypic CAM adhesive interaction for coalescence within the inner olfactory nerve layer (ONL) of the OB (A. M. Miller, Maurer, et al. 2010). Neural activity may have a significant role in determining the position and purity of a glomerulus; this could be not only AP correlation pruning (i.e. 'fire together, wire together', introduced in the section Neural maps), but also non-electrical spontaneous receptor baseline activity signalling pathways (Zou et al. 2009). As shown by (M. L. Schaefer et al. 2001; Strotmann et al. 2000), the final glomerular layout (neighbour relationship) can be locally slightly variable within a defined domain (of ∼30 glomeruli) of the OB, even between genetically identical animals. The organisation of the OS is illustrated in the fig. 1.5 and described in detail in the section Anatomical and structural features (Lodovichi and Belluscio 2012; Mombaerts 2006; Schwarting and Henion 2011).

Layout

Specifically in the OS, continuous remodelling of the axonal tracks occurs throughout the life due to the renewal of the OSNs, glomeruli continue to form and mature postnatally into adulthood. During the adulthood olfactory neurogenesis, the nascent OSN axons grow from the OE and navigate towards the corresponding OR-defined glomeruli along the established paths, while older axons degenerate and are removed by glial cells. A lifetime of an OSN is around 3 month, while (1–3) % of OSNs are renewed each day (Mombaerts 2006; Nedelec et al. 2005; Zou et al. 2009).

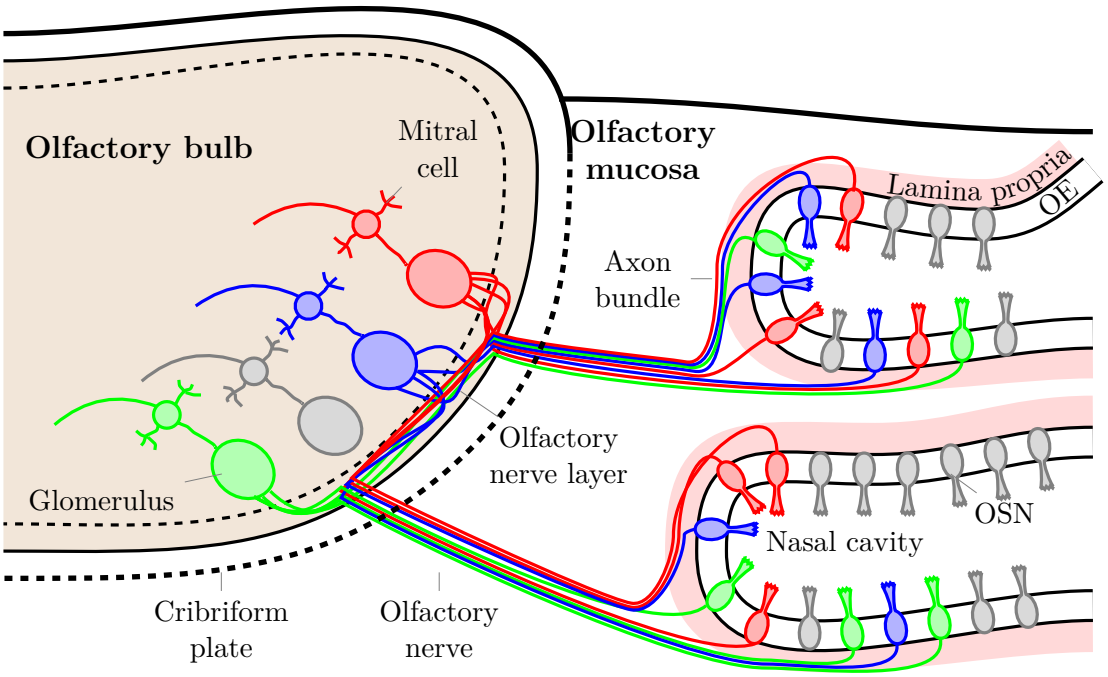

Figure 1.5: Organisation of the mouse main olfactory system. The OSNs located in the olfactory mucosa project into glomeruli of the OB, in which they contact bulbar neurons such as mitral cells. Each OSN expresses one OR gene (indicated by the colour code in the figure) and all the axons of the OSNs expressing the same OR converge into a few OR-specific glomeruli (see colour code correspondence). On the way from the OE to the OB, OSN axons assemble to form ABs in the lamina propria, before they coalesce into branches of the ON that cross the cribriform plate. OSN axon bundles remain heterotypic until they reach the ONL of the OB. In this layer, the OSN axons rearrange in a homotypic way and converge onto their target glomeruli.

Olfactory transduction

Odourant[2] is initially detected in the nasal epithelium, its perception depends on its physical and chemical features, i.e. molecular size and shape, and the presence of chemical functional groups. The fig. 1.6 illustrates two OR-initiated signalling pathways. The major components of canonical olfactory signalling (fig. 1.6b) are concentrated in specialized sensory cilia that protrude into the nasal cavity from the single apical dendrite of OSNs (see fig. 1.5). ORs are 7-transmembrane receptors that couple downstream

[2] A ligand molecule inducing particular odour response.

signalling through heterotrimeric G-protein[3] (composed of α, β and γ subunits). In mature olfactory sensory neurons, the complex includes G_{olf} subunit, highly expressed in the OSNs. Odourant-OR binding stimulates G_{olf}, which activates adenylyl cyclase type III (ACIII) increasing intracellular cAMP concentration, which opens cyclic nucleotide gated (CNG) channel complex, influx of Ca^{2+} through this channel opens Ca^{2+}-dependent Cl^- channels, which results in a depolarising Cl^- efflux leading to an AP, illustrated in the fig. 1.6b. The signalling pathway is important not only for transduction, but it seems it plays a crucial role in the OSN axon guidance process through the action of G_s homologue of G_{olf} in immature OSNs (fig. 1.6a, detailed in the section Anterior-posterior axis) (Mombaerts 2006; Schwarting and Henion 2011; Zou et al. 2009).

[3]or in short, G-protein-coupled receptors (GPCRs)

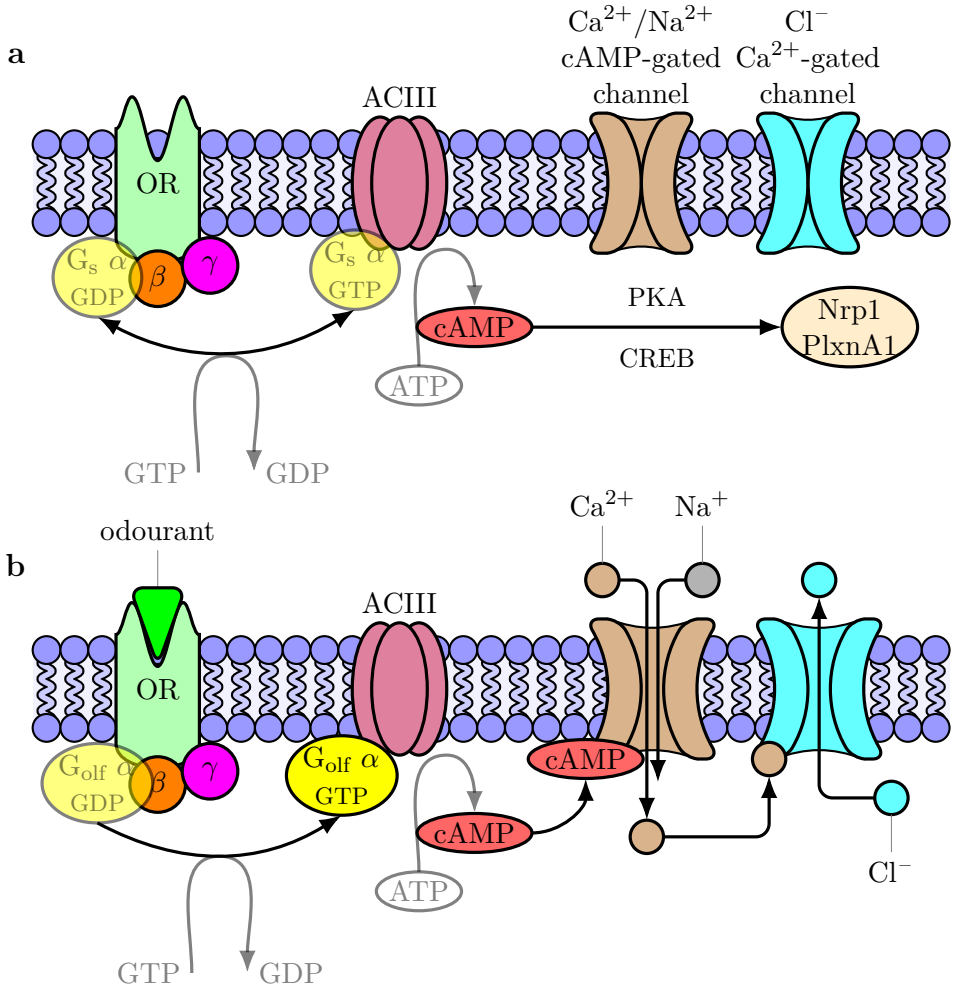

Figure 1.6: **a**: State of the immature OSN membrane without presence of ligands. The G_s homologue is coupled to the OR, CNG and Cl^--gated channels are closed. Odorants are absent, the OR switches between active and inactive conformations, generating spontaneous baseline activity, releasing and binding G_s in the process. Each OR has unique baseline activity, producing unique level of G_s-initiated cAMP through ACIII, which controls production levels of GCMs (e.g. Nrp1 and PlxnA1) implicated in A-P OSN axons projection. **b**: Canonical olfactory signalisation pathway is activated by the binding odourant. α subunit of G_{olf} is phosphorylated and activates ACIII, which produces cAMP from ATP. The cAMP opens CNG channel to Ca^{2+} and Na^+ ions, triggering influx into the cell. The incoming Ca^{2+} ions open Ca^{2+}-gated channel allowing efflux of Cl^- ions from the cell, leading to depolarisation and generation of an AP. Adapted from (Nishizumi and Sakano 2015).

1.2.1 Anatomical and structural features

As shown in the fig. 1.5, the OSN cell bodies are found in the olfactory mucosa, an odours-detecting sensory organ located in the nasal cavity. It is composed of two tissue layers, (i) the OE, containing several cell types, the sustentacular cells, glandular cells, neuronal progenitor stem cells (horizontal basal cells) and numerous OSN bipolar cell bodies (more than 2 million in mice), and (ii) lamina propria underneath the OE, containing blood vessels, special glial cell called olfactory ensheathing cells (OECs) and small early bundles of OSN axons. These ABs gradually coalesce and exit the lamina propria. Assemblies of the large bundles form the branches of the ON, that cross the cribriform plate (plate of the perforated ethmoid bone) at multiple points before connecting the OB. The ABs then defasciculate within the most peripheral part of the bulb, the ONL, before entering a glomerulus in which OSNs branch and connect to apical dendrites of bulbar principal cells (mitral and tufted cells) as well as periglomerular cells. These initial projections undergo postnatal activity-dependent sensory-input-based refinement (see section Neural maps) (A. M. Miller, Maurer, et al. 2010; Nedelec et al. 2005).

OSN axons are unmyelinated fibres of a very small rather uniform diameter ($\approx$200 nm in mice). Their structural organisation throughout the olfactory tract depends on the mutual contact interactions as well as interactions with the OECs and ECM, while the positioning of the tract and the final target OB subdomains are determined by the GCMs and CAMs. The OSN axons form initial small ABs in the lamina propria ($\sim$150 axons, $\sim$5 µm in diameter), engulfed by OEC processes. As they get further from the origin, they become packed at very high density within larger ABs, with diameters up to 20 µm containing 2000–3000 of OSN axons (Y. Li, Field, et al. 2005). OEC's thin peripheral processes wrap the ABs, while some processes penetrate the bundles (detailed in the section Olfactory ensheathing cells). The branches of the ON are formed by several large ABs, but each bundle is surrounded by its own basal lamina and thus physically separated from neighbouring bundles. At the level of the ON, assemblies of the large bundles are wrapped by surrounding olfactory nerve fibroblasts (ONFs). Upon the arrival to the OB, the tight bundles bring OR-heterogenous population of axons originating from a particular area of the OE, with limited rearrangement along the path. The heterotypical ON branches therefore have to defasciculate and rearrange into homotypic bundles forming the glomeruli (Y. Li, Field, et al. 2005; A. M. Miller, Maurer, et al. 2010; Nedelec et al. 2005).

1.2.2 Expression of a single odourant receptor type

In (Clowney et al. 2011), it was reported that 1431 OR genes and pseudogenes in mice are known (study performed on C57/Bl6 mice), 1075 of those encode functional receptor proteins (Monahan and Lomvardas 2015). Of those, about 160 are of Class I found in fish and other vertebrates, while 1271 are mammal-specific Class II ORs. Class I ORs are encoded by a single large gene cluster on a single chromosome, the Class II OR genes are distributed in clusters across most of the chromosomes (the role of classes is further discussed in the section Regional sorting) (ibid.). The OR genes do not have identical onset and kinetics of expression and the number of OSNs expressing a particular gene

can vary by as many as 2 orders of magnitude (Mombaerts 2006).

In mammalian OS, each OSN expresses only one functional OR gene. To guarantee expression of only single gene per OSN, a simple mechanism of locus control region (LCR) was initially proposed. LCR is a *cis*-acting regulatory region that controls multiple genes clustered at a specific genetic locus. Two examples of an LCR in the mouse OS were identified, named *H* and *P*. It is assumed that transcription factors (Lhx2, Emx2, O/E family proteins) bind to the *H* region and form a complex that remodels the chromatin structure near the cluster activating one OR promoter site at the time. The *H* region activity is *cis*, *trans* activity was ruled out in (Nishizumi, Kumasaka, et al. 2007). In the human visual system, LCR facilitates an exclusive stochastic choice of either red or green photopigment gene. This would not fully work in the OS, because LCR-promoter interaction would not preclude the activation of a second OR gene in the other allele or in other OR gene cluster. This is likely resolved by coupling slow chromatin-mediated activation process to a fast negative-feedback signal of functional, robustly expressed, OR protein, preventing activation of other OR genes, so-called allelic exclusion. In rare cases of expression of two functional OR species simultaneously, activity-dependent elimination takes place (Monahan and Lomvardas 2015; Mori and Sakano 2011; Nishizumi and Sakano 2015; S. Serizawa 2003).

Allelic exclusion enforces singular, monoallelic OR expression. The OR is selected randomly during the early differentiation from the repertoire of OSN's OE zone (I–IV). To be transcribed and translated to a sufficient level, the first OR induces the unfolded protein response (UPR), which coordinates a multipart response, expressing chaperones and slowing the rate of protein translation except for transcripts with short open reading frames in the 5' untranslated region, one of which (very abundant in the OE's immature OSNs) is activating transcription factor 5 (ATF5), which is required for OR negative feedback (blocking expression of other ORs) and OSN maturation. The other OR genes are silenced by heterochromatin, a compact structure inaccessible to many transcription factors. This silencing, surprisingly, precedes OR expression—heterochromatin marks (H4K20m3 and H3K9me3) are present in cells differentiating into OSNs before they express OR and remain in mature, OR-expressing OSNs, except for the chosen allele. OR expression therefore requires derepression of a previously silenced OR gene, which is performed by a histone demethylase LSD1 (demethylates gene silencing and gene expression marks). After the derepression, LSD1 is a target of OR-dependent negative feedback—translation of ATF5 induces expression of ACIII which leads to downregulation of LSD1 preventing further OR gene activation. Beside the demethylation, LSD1 is also involved in promotion of inactivation of ORs that fail to activate the OR feedback pathway, therefore switching off dysfunctional OR genes. In such case, the OSN can switch to another OR gene, which shows that the expression of OSN's OR is not irreversibly programmed (Dalton et al. 2013; Lewcock and Reed 2004; Y. R. Li and Matsunami 2013; Lyons et al. 2014; Monahan and Lomvardas 2015; Nishizumi and Sakano 2015; Rodriguez 2013).

Singularity of OR choice by chromatin-based regulation depends on the time scale of involved processes. For the mechanism to be successful, the feedback inhibition must shut off derepression before another OR activation occurs, otherwise a rare coexpression

takes place. From an observed rate of coexpression (about 2 %) and the inhibition delay (1–2) h, it was theoretically estimated that the OR activation rate is 1 every (5–10) d (Tan et al. 2013), which roughly agrees with the timing of OSN differentiation. The model also predicts, that failed feedback or sustained LSD1 expression would result in persistent OR switching rather than coexpression, which was experimentally supported. It also predicts, that the initial desilencing is the slow, rate-limiting step gating OR choice (Monahan and Lomvardas 2015; Tan et al. 2013).

1.2.3 Olfactory sensory neuron axon projection and coarse pretarget sorting

The initial development of the primary olfactory pathway from the OE to the OB begins on embryonic day 9 (E9) with the differentiation of neurons within the olfactory placode (OP), while the first OSN axons cross the basal lamina of the developing OE on E10 to E10.5, illustrated in the fig. 1.5. The OSN axons follow a scaffold of migrating neuronal cells that emerge from the OP at E10, about a day before the OSN axons, thus playing the role of 'guidepost cells' located along the growing axons' path, within filopodial reach from one another. By E11, the OSN axons start to intermingle with the heterogeneous population of the migrating cells, including gonadotropin-releasing hormone (GnRH) neurons and OECs, to form so-called migratory mass (MM) and extend towards the future OB. The OECs likely migrate from the main OP and join the nascent ON as early as E10.5, wrapping the MM by E12. A few axons penetrate the telencephalon around E11.5 (brain scheme shown in fig. 1.1), but most OSN axons remain restricted to the presumptive ONL until E15, when the glomerulogenesis begins—this waiting period may contribute to the segregation of OSN axons subpopulations, which becomes evident by E12 (A. M. Miller, Maurer, et al. 2010; A. M. Miller, Treloar, et al. 2010).

Migratory mass

Besides GnRH-expressing cells, the MM contains cells expressing olfactory marker protein (OMP), mirroring OSN axons trajectory, and also cells expressing ORs; these likely provide guidance cues to the OSN axons extending towards the telencephalon. OSNs are highly heterogeneous in terms of expressed OR-specific marker molecules (e.g. NQO1/OCAM, Nrp1, Robo2). Sorting according to the molecular phenotype occurs through interactions within the MM as the OSN axons traverse the lamina propria into the mesenchyme by the E10.5, and becomes more clear in the ON pathway (fig. 1.5); despite, final coalescence of OR-specific subpopulations does not occur until the OSN axons cross into the inner ONL of the bulb. The OSN axon coalescence and targeting is likely a hierarchical process, in which multiple mechanisms determine regional positioning in the OB, while the OR expression underlies the final convergence of the axons within the inner ONL and the formation of glomeruli. While the sequential migration of diverse cells from the OP followed by the emergence of OSN axons forming fascicles supports the hypothesis that placode-derived migratory cells contribute to a scaffold for extending OSN axons and early ON formation, it also seems that the molecular diversity of migratory cells within the framework likely contributes to axon sorting and formation of initial topography between the OE and the OB (A. M. Miller, Maurer, et al. 2010; A. M. Miller, Treloar, et al. 2010; Treloar et al. 2002).

Olfactory ensheathing cells

The OECs play role in OS development from the early stages (E10.5), they participate in formation of the MM, facilitate axon clustering and wrap them to form nascent ON, gradually tightly bundling the advancing OSN axons (A. M. Miller, Treloar, et al. 2010). The OECs are crucial not only for proper OS development, but particularly for its renewal and regeneration capacities[4]. The OECs form a continuous channel enclosing the OSN axons from the olfactory mucosa to the OB (see fig. 1.5), and send sheet-like interlocular processes inside the AB. On their outer surface, they have a basal lamina and an outer encirclement of the ONFs. On the side of olfactory mucosa, the bodies of OECs lie in the lamina propria and receive the OSN axons from early differentiating OSNs and assist in initial bundle formation. At the OB end, the basal lamina and the ONF leave the ON joining the leptomeninges fibroblasts, while the OECs interdigitate with OB astrocytic processes to form capsule of the glomeruli (Ekberg et al. 2012; Y. Li, Field, et al. 2005).

Unlike other glia, the OECs can migrate from the periphery into the central nervous system (CNS). And unlike Schwann cells, they do not myelinate individual OSN axons, but wrap the whole AB (Ekberg et al. 2012). They are actively phagocytic, removing degenerating axons, and provide continuous stable channels along which newborn OSN axons can regenerate; the OECs do not migrate nor proliferate, in case of axonal injury. This feature was studied by (Y. Li, Field, et al. 2005), where rapid OSN death was induced by intracranial axontomy, and the degenerating OSNs were replaced from mucosal stem cells. The degenerating axons left empty space within the ON encased by thin processes of OECs, which were internalising the degrading material. By the day 10 after the axotomy, the axon debris was phogocytosed and the OEC processes became hypertrophic, filling the empty space, but preserving ON's tubular structure. Over the following weeks, new axons advanced through the ON and OEC recovered their original thin anatomy. During the whole regeneration process, however, the adaptations of the OECs (and possibly ONFs) assured stable geometry of the ON.

The OECs are intimately associated with the axons during the stages of guidance, sorting and precise targeting. OECs are thought to promote axonal growth by providing substrate containing CAMs and trophic agents. In addition, OECs are themselves subjected to axonal guidance factors and ECM proteins regulating their migration. These features (providing and responding to cues) complement the observation that OECs migrate ahead of the extending OSN axons in the MM and extensively interact with the axons (through lamellipodial waves), supporting the idea that the migration of OECs is directly related to the rate of OSN axons growth. Within the ONL, the OECs are thought to contribute to the defasciculation of the mixed ABs and later to assist the sorting and refasciculation (which is mainly regulated by CAM-specific contact interactions, presented in section 1.2.4) of axons according to their OR identities. The population of

[4] Their capacities were demonstrated also outside the field of neural development, as promising regenerative agents of spinal cord injuries, demonstrated in animals (Keyvan-Fouladi et al. 2003; Y. Li, Decherchi, et al. 2003) and also clinically (Tabakow et al. 2013). A successful reparative outcome involves the formation of a highly organised tissue bridge consisting of an aligned array of nerve fibres ensheated by OECs, with an outer perineurial-like wrapping of ONFs.

OECs is heterogeneous, with distinct anatomical localisation, behaviour and expression pattern of certain molecules. Some of the molecules are classical GCMs and may repel or attract particular subpopulations of OSN axons. The differences are also between peripheral and central OECs; peripheral cells adhere to each other and migrate together whereas central cells demonstrate a combination of adhesion, repulsion and indifference, and are associated only loosely (Ekberg et al. 2012).

Regional sorting

Initial coarse sorting of OSN axons occurs already in the lamina propria prior reaching the OB (see fig. 1.5). According to Sakano and colleagues (Kobayakawa et al. 2007; Tsuboi, Miyazaki, et al. 2006) this sorting pattern gives rise to two distinct projection domains on the bulb, and the OSNs can be classified along these target domains into two subpopulations: (i) D_I OSN axons project into the dorsal region of the bulb (red in fig. 1.7a), and (ii) D_{II} OSN axons project into the central and ventral region of the bulb (blue in fig. 1.7a). According to (Bozza et al. 2009), these OSN types naturally determine specific selection of OR gene from two phylogenetically distinct gene groups: type D_I leads to selection of OR with Class I promoter, while D_{II} of Class II promoter (see also section 1.2.2). Besides distinct target domains, the two OR groups exhibit also differential dependence on Lhx2 for maturation, Class I ORs represent only 10 % of the OR genes in mouse and are expressed in the dorsal OE, whereas Class II ORs are expressed in the dorsal and ventral OE. The OSNs in the ventral regions of the OE, which project to the central and ventral OB domain, are also distinguished by the expression of olfactory cell adhesion molecules (OCAMs) (homophilic CAMs related to NCAMs, also transiently expressed in dendrites of dorsal mitral and tufted cells), which are not involved in axonal wiring, however play role in proper segregation of axon-dendritic vs dendro-dendritic synaptic circuits within glomeruli (Mombaerts 2006; Walz et al. 2006).

Classes of OR promoters

The OSN type naturally implicates that the (otherwise randomly) selected OR must belong to a particular promoter class, i.e. $D_I \rightarrow$Class I OR and $D_{II} \rightarrow$Class II OR. It also turns out, that the OSN type directly controls the OSN axon projection target domain independently of the identity of selected OR gene. This has been demonstrated by an experiment in (Bozza et al. 2009): if an OR gene is deleted in a particular OSN, such neurons would still project to appropriate domains according to their original D_I or D_{II} OSN type, however the glomerular structure (which is OR-dependent) would be lost and axons would project diffusely across the dorsal area (e.g. axons of deleted Class I OR S50) or ventral area (e.g. axons of deleted Class II OR M72). In addition, swapping neuron's coding sequence from Class I promoter OR to Class II promoter OR and vice versa does not effect the target regions in either case, confirming that the projection does not depend on the OR itself but rather on the type of OSN (i.e. D_I or D_{II}). It has been also shown, that the projection domain correlates with functional odour response (ibid.).

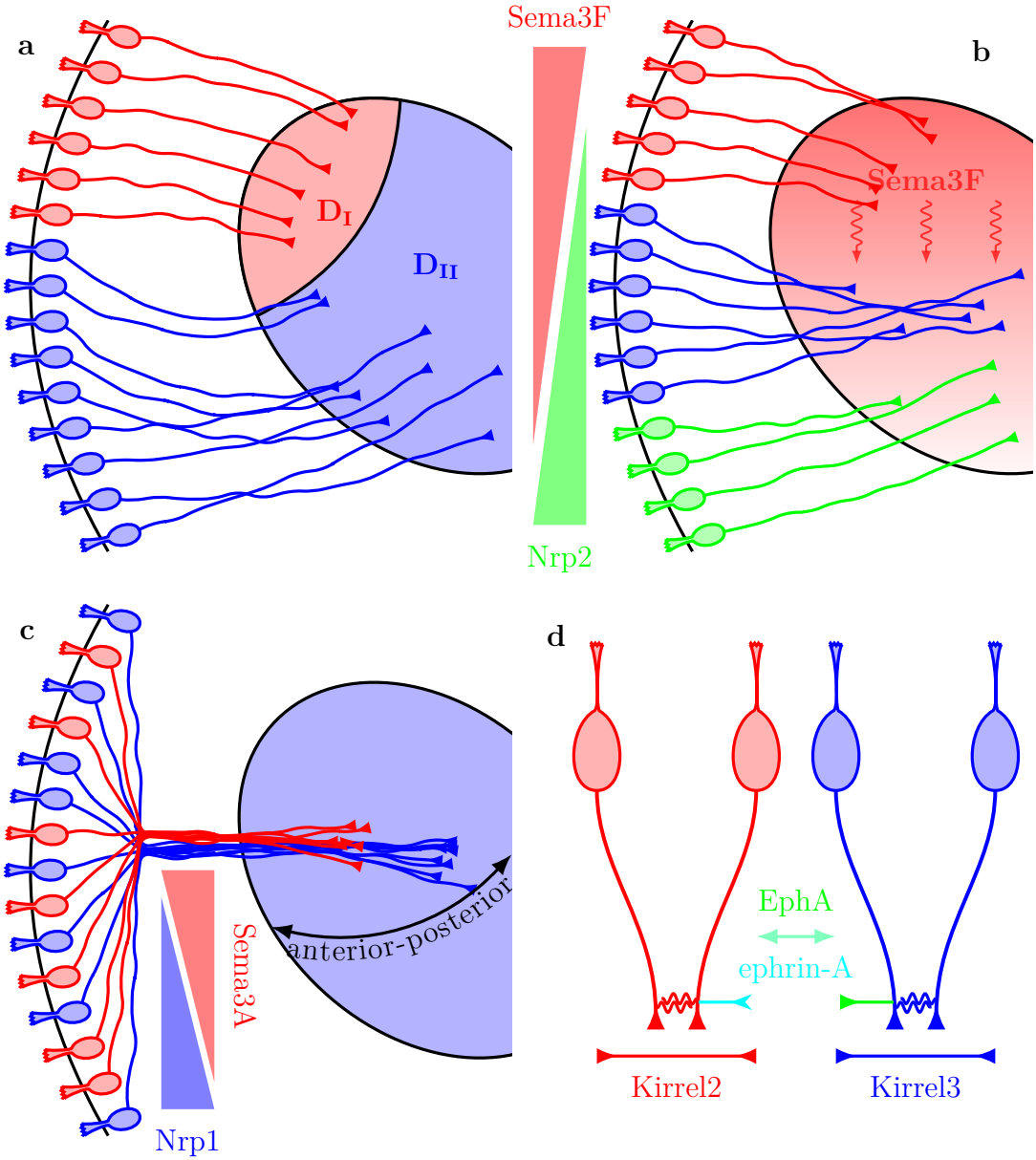

Figure 1.7: Various projections mechanisms in the OS. In the panels **a**, **b**, **c** the OSN axons grow from the OE on the left towards appropriate areas of the OB on the right. Note the images illustrate the projection, but may ignore other features, e.g. the ON. **a**: Initial projection of D_I and D_{II} types of OSNs (red/blue) into their corresponding domains on the OB. **b**: D-V projection of the OSN axons. According to their position on the OE, the OSN axons project to the corresponding area of the OB. The dorsal (red, Sema3F^{high}) OSN axons arrive to the dorsal part of the OB before other axons, repulsed by ventral gradient of Slit1. Upon, arrival, their GCs release Sema3F and repulse Nrp2^{+} axons (medium in blue, high in green axons) into the ventral part of the OB. **c**: A-P projection of the OSN axons. Axon-axon repulsive interaction mediated through Sema3A-Nrp1 counter gradients segregates axons within the bundle (expression of the CAMs is given by OR spontaneous baseline activity) and consequently along the A-P axis. **d**: Local axon sorting on the glomeruli. Expression of Kirrel2/Kirrel3 and EphA/ephrin-A CAMs depends on the intrinsic neural activity (CNG channel). Kirrels drive homotypic coalescence into a single gromerulus, while EphA/ephrin-A drives heterotypic segregation of individual glomeruli. Adapted from (Nishizumi and Sakano 2015).

Anterior-posterior axis

As a rule, axons of a single OR type coalesce onto a single glomerulus (in roughly each of four OB hemi-maps). Unlike in the VS, there is no correlation between the A-P position of the OSN on the OE and its axon target on the A-P axis of the OB, i.e. the nearest neighbour relation does not hold. It has been well established in the 90's that ORs play a critical role in controlling the projections of OSN axons. More recent work showed that cAMP, downstream of the OR in the transduction pathway, was involved in this process (reviewed in (Nishizumi and Sakano 2015; Zou et al. 2009)), which regulates transcription level of axon-guidance and axon-sorting molecules through OR-derived cAMP signals (see fig. 1.6a). It turns out, that both the identity of the OR and the amount of the OR protein have influence on the cAMP levels (Mori and Sakano 2011). It is likely, that cAMP controls the guidance through non-AP (i.e. non-electric) signalling, as mice with functional ACIII but lacking CNG channels (thus electrically inactive; compare panels of the fig. 1.6) showed normal coalescence into glomeruli (D. M. Lin et al. 2000).

According to the view of Sakano and colleagues, in immature OSNs, Nrp1 and its complementary repulsive ligand Sema3A are expressed at axon termini in opposite graded manner (fig. 1.7c) along the A-P axis and regulate A-P positioning of the glomeruli. Each OR generates unique level of cAMP molecules through G_s protein (expressed in immature OSNs, fig. 1.6a), which activates ACIII to produce cAMP from ATP, influencing relative expression of the Nrp1 and Sema3A cues. Note that such regulation is driven by ligand-independent spontaneous baseline activity of the ORs. OSNs producing high levels of the cAMP ($Nrp1^{high}/Sema3A^{low}$) project their axons to the posterior OB and are presorted to the outer-lateral compartment of the AB, whereas those producing low levels of cAMP ($Nrp1^{low}/Sema3A^{high}$) project to the anterior OB and are presorted to the central compartment of the AB, as illustrated in the fig. 1.7c (Nishizumi and Sakano 2015). This olfactory map formation along the A-P axis is therefore facilitated by proper axon pretarget sorting within the AB. Although the OSN axons may be sorted autonomously within the bundles, they still require an extrinsic cue, probably Sema3A, for orientation along the correct axis before projecting onto the OB (Mori and Sakano 2011; Nishizumi and Sakano 2015).

Dorsal-ventral axis

The OSN axon mapping onto the 2D OB surface requires two target coordinates, one is defined along the A-P axis and determined as described in the previous section, the other along the D-V axis, presented in this section. It has been shown that anatomical locations of OSNs in the OE correspond to the D-V positioning (see fig. 1.7b) of their glomeruli in the OB, possibly as a result of micropatterning. Similarly as Nrp1/Sema3A receptor-ligand expression regulates A-P positioning, Nrp2/Sema3F receptor-ligand repulsive pair forms two counter-gradients in the OB along the D-V axis and regulate the axonal projections along this axis. Unlike the A-P axis, Nrp2 and Sema3F expression is not downstream of OR in signalling pathway (i.e. it is independent on OR signalling). It appears that both the OR gene choice and Nrp2/Sema3F expression levels are commonly

regulated by positional information within the OE.

The D-V glomerular structures do not appear simultaneously, but first emerge in the anterodorsal domain of the OB and expand ventrally. Initial arriving axons, expressing Robo2 receptor (red in fig. 1.7b), are repulsed by its ligand Slit1 (expressed in the ventral OB) into anterodorsal region (Nguyen-Ba-Charvet et al. 2008); Sema3F is then secreted by these early arriving axons (not by the OB itself) to repel later arriving axons, that express Nrp2 (blue and green in the fig. 1.7b), into the ventral zone (Mori and Sakano 2011; Nishizumi and Sakano 2015; Takeuchi et al. 2010).

1.2.4 Local sorting on the olfactory bulb

For the final sorting, axon-axon contact interactions are critical, organising axons into smaller bundles to facilitate proper targeting later in the process. Homotypic axon-axon interactions keep the like axons together, while the heterotypic axon-axon interactions have anti-fasciculation effect and ensure proper segregation and guidance to divergent targets (fig. 1.7d) (Raper and Mason 2010).

Regional coarse sorting in the mesenchyme and in the olfactory nerve is based on molecular phenotype of participating cells, influenced by molecules like OCAMs, Nrp1, Robo2, lectins etc. This suggests that the regional topographic organisation of the OB is established pretarget, before reaching the ONL, as described in the section 1.2.3, particularly in the paragraph concerning the migratory mass. Conversely, the OR-specific populations remain heterotypically fasciculated through the mesenchyme. Stable homotypic fasciculation of OSN axons does not necessarily occur prior to axons crossing into the inner ONL, at the area of the target glomerulus on the OB (see fig. 1.5). As the axons enter the inner ONL, they form large homotypic fascicles immediately prior to coalescing into a glomerulus. This suggests that the OR-dependent self-sorting through differential affinity of OR-homotypic and OR-heterotypic axons (see section 1.5 and section Extended active walker model)—a process called homotypic fasciculation—is most probably initiated as axons cross the outer-inner ONL boundary. It is however possible, that the OR-mediated contact interaction between axons is switched on at a specific place (i.e. in the inner ONL) or time (A. M. Miller, Maurer, et al. 2010). Interestingly, it has benn shown (in the early postnatal OS), that the OR gene expression begins about 4 days after the birth of OSNs, a time point at which their axons navigate in the ONL, and so the OR-type-dependent homotypic fasciculation cannot start prior this point (Rodriguez-Gil et al. 2015).

Through mechanisms suggested in the section 1.2.3, pretarget coarse continuous olfactory map is generated by D-V patterning based on the OE location and A-P patterning based on spontaneous OR-derived cAMP signals. Some of the glomeruli are intermingled before birth; refinement takes place during neonatal period through fasciculation and segregation of axon termini. According to the Sakano Laboratory, the final sorting process also depends on the cAMP signalling, but the mechanism is slightly different from A-P organisation and involves ligand-dependent neuronal activity (Shou Serizawa et al. 2006) (reviewed in (Nishizumi and Sakano 2015)).

When odourants bind to an OR, the olfactory-specific G-protein G_{olf} activates ACIII

generating cAMP which leads to AP by opening CNG and Cl^--gated channels (see figs. 1.6b and 1.7d). Different, OR-specific levels of neuronal activity determine different, OR-specific and complementary (high/low) expression levels of axon-sorting molecules necessary for glomerular segregation—high CNG channel activity → Kirrel2^{high}/Kirrel3^{low}, EphA^{high}/ephrin-A^{low} and vice versa. The Kirrels homotypically bind identical partners (e.g. Kirrel2-Kirrel2), while the EphA/ephrin-A have heterotypically repulsive effect, as shown in the fig. 1.7d; this leads to sorting and glomeruli coalescence, which is demonstrated by a differential (mosaic) patterns of these CAMs from one glomerulus to another. A slight (experimental) increase in level of some of these CAMs (e.g. Kirrel2) in a part of population expressing particular OR leads to coalescence of affected axons into a separate glomeruli. This suggests that glomerulogenesis and segregation are very sensitive to the expression levels of cell-recognition molecules (Nishizumi and Sakano 2015).

To conclude, differential OR-specific expression of Nrp1/Sema3A, Nrp2/Sema3F and Kirrel2/3, ephrin-A/EphA molecules in immature and mature OSNs, respectively (figs. 1.7b to 1.7d), allows stepwise formation and refinement of the olfactory map. The final part of the process converts the coarse continuous olfactory map to the discrete one, the segregation performs also map refinement and removal of satellite glomeruli (Mombaerts 2006; Mori and Sakano 2011; Nishizumi and Sakano 2015; Zou et al. 2009).

Alternatively, Mombaerts (Mombaerts 2006) proposes that the OSN axons sorting is driven by the process of differential adhesion (general theory presented in the section 1.5) mediated by homophilic interaction between complexes that contain ORs or OR fragments (similar to Kirrel2/Kirrel3, EphA/ephrin-A mechanism offered by (Nishizumi and Sakano 2015)), analogically to the association of antigen-derived peptides with major histocompatibility complex molecules. Different affinities among axonal populations then produce particular arrangement of glomeruli. The sorting therefore depends on the expressed repertoire of the ORs and not on a predetermined spatial map in the OB. This has been supported by (St. John et al. 2003), who showed that even if secondary neurons are removed (mitral and tufted cells), the OB is genetically malformed or even surgically removed, the OSN axons still form (or attempt to) glomeruli in the presumptive location of the OB.

1.2.5 Differential usages of G_{olf} and G_s in olfactory sensory neurons

As aforementioned in the section Local sorting on the olfactory bulb and illustrated in the fig. 1.6, there are two types of G-protein in the OSNs, G_s and G_{olf}, coupled to the ORs. Although G_s and G_{olf} are biochemically similar (sharing 88 % of aminoacid identity), the latter is expressed in the cilia of mature OSNs and its activity depends on ligand-OR interaction, while the former is expressed in immature OSNs. GPCRs, including ORs, are known to possess active and inactive conformation. Agonist stabilizes the receptor in the active form, inverse agonist in the inactive form. If neither is present, GPCR spontaneously switches between the two conformations and activates signalling pathway, stimulating ACIII to produce cAMP, as shown in the fig. 1.6a. Various ORs have various but specific baseline activity levels resulting in specific level of produced cAMP (Nishizumi and Sakano 2015).

Agonist-dependent activity producing AP through pathway utilising CNG channel (fig. 1.6b) was studied in (Shou Serizawa et al. 2006). As discussed in the section 1.2.4, high CNG channel activity $\rightarrow$ Kirrel2^{high}/Kirrel3^{low}, EphA^{high}/ephrin-A^{low} and visa versa. Such tendency was demonstrated by a simple naris occlusion (suppressing odourant-dependent signalling) and also by CNG channel inactivation in mice. The CNG activation leads to an AP and Ca^{2+} influx, which generally regulate expression of particular genes, potentially cell-recognition molecules. At the same time, naris occlusion does not seem to impair A-P targeting, which might be therefore regulated by OR's intrinsic spontaneous baseline activity (as described in the section Anterior-posterior axis).

Agonist-independent activity (fig. 1.6a) was studied in (Nakashima et al. 2013) using β2-adrenergic receptor (β2-AR), a GPCR with high sequence homology to ORs, to replace OR coding sequence. β2-AR in transfected cells maintains one-OR rule and couples to α-subunit of both G_{olf} and G_s and substitutes ORs for receptor-instructed axonal projection and glomerulus formation. Studies of 3D structure (Rasmussen et al. 2011) of the β2-AR also hinted on modus operandi of the GPCRs in the OS: the extracellular cavity determines ligand specificity and firing rates, whereas the intracelular cavity determines the G-protein functional selectivity for transduction pathway and levels of baseline activity. In the OS, the G_s takes advantage of intracellular diversity of ORs for axonal wiring specificity in development, whereas G_{olf} reflects the extracellular diversity of OR protein to detect various odourants and regulate olfactory map refinement (fig. 1.6)(Nishizumi and Sakano 2015).

In the experiment (Nakashima et al. 2013), in case of high baseline activity β2-AR mutant OSNs, the glomeruli were shifted posteriorly as compared to WT while Npr1 expression levels increased and PlxnA1 levels decreased, low baseline activity β2-AR mutant OSNs acted in the opposite manner, glomeruli shifted anteriorly, Npr1 expression decreased and PlxnA1 levels increased (cf. fig. 1.6a). Notably, the expression levels of agonist-dependent activity controlled glomerular segregation molecules (e.g. Kirrel2/Kirrel3) were not affected (cf. fig. 1.6b) (ibid.). Note that while the behaviour observed for β2-AR mutant OSNs fits into larger picture, there is no strong evidence that the OR-expressing OSNs would behave exactly the same way.

It seems likely that A-P targeting and glomerular segregation are regulated by two distinct OR-derived cAMP signals. Considering the temporal aspect, at E13.5, A-P targeting molecules (e.g. Nrp1, Sema3A) were present, but not the glomerulus segregation molecules (e.g. Kirrels), which became prominent at the late embryonic stage. Similarly, G_s was present at E13.5, but not G_{olf}, which was detected at E17.5, indicating G_{olf} is not necessary for expression of A-P targeting molecules. In addition, cAMP agonist-independent signals are higher for G_s than G_{olf}, while they are comparable for agonist-dependent signals. To conclude, G_s plays a major role for the A-P targeting in immature OSNs, while G_{olf} for glomerular segregation in mature OSNs (ibid.).

1.2.6 Olfactory map and further processing

Each glomerulus in the OB receives information generated by the activation of a single OR type, as all OSN axons converging to a given glomerulus express the same

OR. OSN axons generate excitatory synaptic connections on primary dendrites of mitral/tufted projection neurons, and on periglomerular interneurons. Periglomerular cells are mostly inhibitory, they extend their neurites into multiple glomeruli in the local neighbourhood. Mitral cells lie mainly (400–500) µm deep in the OB, whereas tufted cells lie in the external plexiform layer, between the mitral cells and the glomeruli. Since each mitral/tufted cell extends a single primary dendrite into a glomerular structure, each glomerulus therefore constitutes a single-OR channel at the level of the OB (cf. parallel channel structure in the section Visual system). Mitral/tufted cells also have lateral dendrites extending over long distance across the OB forming synapses with granule cells (interneurons) (Mori and Sakano 2011; Zou et al. 2009).

Each of the left and right OBs has each two nearly mirror-symmetric maps, lateral map (rostro-dorso-lateral) and medial map (caudo-ventro-medial), each receiving inputs from analogical area of the OE. Both maps are linked by collaterals of tufted cells, suggesting functional interactions between glomuruli of the same OR type. Each mitral cell projects axon collaterals to nearly all areas of the OC, while a single tufted cell projects its axon only to restricted parts of the anterior areas of the OC. While tufted and mitral cells project paralelly to the OC, they convey different aspects of the odour, as tufted cells respond with lower concentration threshold, wider dynamic range regarding odour concentrations and higher temporal resolution (reviewed in (Mori and Sakano 2011)).

Glomeruli are grouped into dorsal and ventral domain, first forming in the dorsal domains (fig. 1.7b) and extending ventrally. As discussed in the section 1.2.3, the dorsal domain is divided into two areas, D_{I} of Class I ORs (fish-type, around 160) and D_{II} of Class II ORs (terrestrial-type, around 1300), while ventral OB zone is mostly Class II ORs and can be understood as an extension of the D_{II} (fig. 1.7a). Each bulb comprises two mirror-symmetric maps (medial and lateral), each having D_{I}, D_{II} and ventral domains. The dorsal domains are associated with innate behavioural response, like fear or aggression, the ventral domain is rather associated with learned behavioural response. Besides being organised into these domains, individual glomeruli have a molecular receptive range (MRR), they respond to a range of odourants sharing common molecular features (e.g. a functional chemical group). Glomeruli with similar MRR form a molecular feature cluster at a stereotyped location (Mori and Sakano 2011; M. L. Schaefer et al. 2001; Schwarting and Henion 2011).

The glomerulus likely acts as a functional unit in which sensory input signals converge and activate circuitry that shapes the signal before transmitting it to the higher centres. It is still unclear how the information is encoded by the glomeruli, but one of the clues is topographical mapping of odour spaces onto glomeruli (e.g. a particular location for esters or aldehyde-containing odours) stimulating concentration-dependent activation. A glomerulus (and its constitutive neurons) can be identified by its odour response profile[5] (to hundreds of odours). While the glomerular layout, the mutual position of glomeruli of particular OR, is preserved between individual animals to a precision of ∼1 glomerular spacing (see an introductory comment on the layout and (Strotmann et al.

[5]Note the response profile, or 'odour tuning' is not the same thing as the MRR, the MRR determines the domain of the possible response, but not its strength (tuning).

2000)), mapping of odour tuning to glomerulus position (i.e. similarity of tuning curves of neighbouring glomeruli) is only very coarse (precision ∼5 glomerular spacings), no chemotopic order is apparent on the fine scale—no correlation between response to an odorant and proximity of any two glomeruli; a similar thing can be said about tuning curves of the neighbouring mitral cells (Soucy et al. 2009). On the other hand, ORs with similar sequence are clustered in the genome and are often expressed in overlapping patterns in the OE and form neighbouring glomeruli (Tsuboi, Yoshihara, et al. 1999). This is consistent with the presumed role of OR in OSN axon guidance, according to which OSN axons expressing similar OR would respond similarly to the guidance cues. This suggests that glomerular organisation may be primarily a developmental solution; the new ORs formed by a mutation eventually form a novel glomerulus nearby to the original unmutated site (which is consistent with the emergence of new glomeruli in some of the OR-replacement transgene experiments) (Mombaerts 2006; Zou et al. 2009).

1.3 Mechanical properties of cells

In cellular development, physiology and regeneration, mechanical force plays a fundamental role. It takes part in cytoskeletal dynamics, transport, guidance, and molecular motor activity. The mechanical interactions between a cell and its environment depend on the forces acting on and exerted by the cell, mechanical properties of the cell and the environment, and their mutual coupling; these are described by mechanical parameters of cells and tissue, such as stress, strain, stiffness, viscosity or contractility (Athamneh and Suter 2015; Franze 2013).

The mechanical information is detected through **mechanosensation** processes, which respond to both internal and environmental mechanical stimuli and initiate signalling pathways (electrical or chemical); the complete process of conversion of mechanical stimuli to a signal is called **mechanotransduction**. The information is integrated by the biological system, and used when the decisions are made during differentiation, growth, proliferation, migration and general function. The mechanical cues also influence the directed movement of cell motility (Lo et al. 2000), in the process known as **mechanotaxis**. Besides implication in cellular functions and motility, the mechanical forces and their detection by specialised cells provide a basis for sensory systems (e.g. tactile or auditory) (Franze 2013).

Biological tissues and cells are generally viscoelastic, their response to an external force depends on the time scale over which the force is applied. Initial elastic response on a short time scale generates normal and shearing stresses (e.g. spring-like behaviour), and is temporally followed by a period of viscous relaxation (e.g. piston-like behaviour), if the acting force is prolonged. The cells mechanically interact with their environment and ECM, they form adhesion through CAMs, and are subjected to friction on the interface. The cell motility (and its probing functions) depends on its ability to transmit force to the environment through adhesion complexes, coupling traction-generating cytoskeleton to the ECM (ibid.).

1.3.1 Basic viscoelastic concepts

A basic terminology will be shortly reviewed at this point (more detailed review in (Baumgart 2000; Jonathon Howard 2001)), see fig. 1.8 for illustration. If force $\vec{F}$ is applied on a material (e.g. cell or tissue), it responds by deformation and build-up of tension. For simplicity, we will consider homogeneous and isotropic material (i.e. relation between the deformation and external force has the same form at each point of the material and in each direction of applied external force). As can be seen in fig. 1.8a, material stretches from the unloaded length l_0 to a stretched length l, and the **tension** T (normal stress) builds within the material. For the force of magnitude F applied across a cross-section A, the tension would be given as $T = {}^{F}/_{A}$. The extension of the material along the axis of applied force is $\Delta l = l - l_0$, the **strain** of the material in the given direction is $\epsilon = {}^{\Delta l}/_{l_0}$. For elastic material, which obeys Hooke's law (they resume original shape once external force is discontinued), the stress-strain relation is linear, given by Young modulus (E), that is $T = E\epsilon$. If the applied external force acts in a parallel direction to the body surface, as shown in fig. 1.8d, the deformation ensues and a shear stress T_γ builds up in the material. In a simple case of small deformations, the shear stress-strain relation is linear, $T_\gamma = G\gamma$, where G is the shear modulus and γ is the shear strain, the change of angle as a result of deformation (see fig. 1.8d).

An ideal spring is a one-dimensional illustration of Hooke's law (see fig. 1.8b). The relation between acting force F and extension Δx is given by $F = k \cdot \Delta x$, where k is the **stiffness** of the spring[6] (sometimes also called **rigidity**, inverse of the stiffness, ${}^{1}/_{k}$, is called **compliance**). If the tension cannot be instantly distributed within the material along the axis of applied force (see fig. 1.8c), for example as a result of friction (represented by dashpots in the fig. 1.8c), a spatial **gradient of tension** is formed within the material, which gradually vanishes as the material relaxes.

The ideal dashpot (piston, dampener) is, analogically to the ideal spring, uniaxial representation of Newtonian fluid—material model characterised by local linear relation between the stress T and **strain rate** $\dot{\epsilon}$, $T = \eta\frac{d\epsilon}{dt}$, where η is material viscosity. The dashpot external force response can be described as $F = H \cdot v$, where F is the external force balanced by the stress within the material, H is dashpot's viscosity coefficient and v is the velocity of dashpot opening[7] (see fig. 1.8e). If a dahspot and a spring are arranged in parallel, in so called Voigt element, a dampened elastic material model is obtained (see figs. 1.10a and 1.11a).

The viscoelastic materials can be roughly classified into viscoelastic solids, modelled by a spring in series with a Voigt element (fig. 1.10a), and viscoelastic fluids, described by Maxwell fluid (fig. 1.10b). If step strain ϵ is induced in **viscoelastic solids** and then kept constant, the stress T in the material gradually relaxes, but retains finite non-zero value, and the flux of material j stops in finite time. If the strain fixation is released, the material slowly resumes its original shape. Conversely, if **viscoelastic fluid** is fixed

[6] Note that while Hooke's law equation was given in terms of local length changes, while the spring equation represents a system of finite size; $[k]$= N/m but $[E]$= Pa.

[7] Also the dashpot is finite size representation of the local stress-strain rate relation; $[\eta]$= Pas but $[H]$= Ns/m.

under constant strain, it undergoes internal creep, until the tension vanishes. The flux slows but continues until $t \to \infty$. Release of completely relaxed viscoelastic fluid produces no restitution. There is an ongoing debate, whether neurites have characteristics of rather solids (Ahmadzadeh et al. 2014; Bernal et al. 2007; Dennerll, Lamoureux, et al. 1989) or fluids (O'Toole, Lamoureux, et al. 2008; O'Toole, Lamoureux, et al. 2015), on what time scale (Dennerll, Lamoureux, et al. 1989; O'Toole, Lamoureux, et al. 2008), and whether they are sufficiently described as passive materials (Bernal et al. 2007; O'Toole, Lamoureux, et al. 2015).

Note that in this work, studied objects (i.e. axons) are well approximated as one-dimensional, and therefore, the axial tension T will be usually used to refer to the total tensile force across the presumed cross-section A, typically expressed in pN or nN.

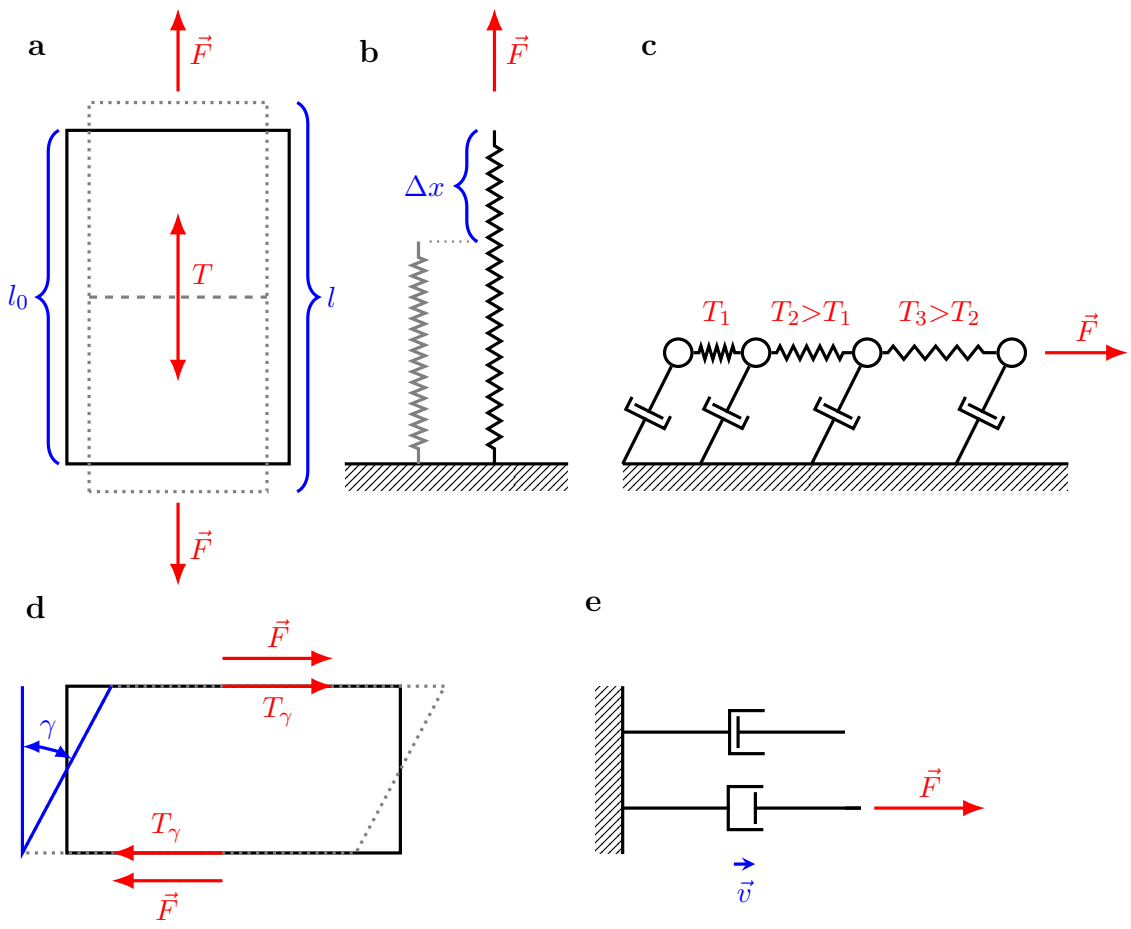

Figure 1.8: Illustration of biophysical concepts. **a**: A homogeneous material is stretched by an external force $\vec{F}$, causing extension $l_0 \rightarrow l$ and a build-up of tension T within the material. **b**: Uniaxial illustration of Hooke's law as an ideal spring. The spring gets stretched from unloaded state (left), length increases by Δx, related to acting force by the spring's stiffness k, $F = k \cdot \Delta x$. **c**: Illustration of tension gradient. As the applied force $\vec{F}$ cannot be distributed instantly across the whole length of the material (e.g. due to friction, represented by dashpots), a gradient of tension T develops within the material. **d**: Illustration of shear stress. External force $\vec{F}$ acts parallelly to the surface, inducing shear strain—the deformation angle γ. **e**: Uniaxial illustration of viscous element, dashpot. Force acting on the dashpot $\vec{F}$ is opposed by tensile force, it is proportional to the dashpot opening velocity $\vec{v}$, $F = H \cdot v$.

1.3.2 Friction forces

As cellular bodies (of size $L \sim 5\,\mu m$) move through the viscous fluid (at velocity $v \sim 1\,\frac{\mu m}{s}$), they experience a **drag force** acting against their motion. The character of movement in such environment can be described by the Reynolds number, given as

$$Re = \frac{\rho L v}{\eta} \approx 10^{-6},$$

where ρ is the environment density ($1029\,\frac{kg}{m^3}$ for water) and η is the viscosity coefficient of the fluid ($10^{-6}\,\frac{nN\,s}{\mu m^2}$ for water). If (i) $Re \gg 1$, the acceleration of the body is mainly opposed by inertia of its mass, turbulent flow occurs, producing instabilities, while in case (ii) $Re \ll 1$, the main role is played by the drag force, the flow is laminar, characterised by constant smooth motion. As the Reynolds number scales with the object size and velocity, it is much smaller than 1 for the cellular bodies; the biological system on cellular level is strongly overdamped and inertial forces are negligible. At such conditions of low Reynolds number, the drag force is proportional to body's velocity, given by Stokes law, $\vec{F}_d = -\eta_S \vec{v}$, where η_S is proportionality coefficient dependent on the viscosity and body geometry (e.g. $\eta_S = 6\pi\eta r$, for a sphere of radius r) (Jonathon Howard 2001).

Similar result can be obtained for the **substrate friction**. Molecules on both, mutually moving (at velocity v), adjacent surfaces form transitory bonds, while the rate of formation and dissolution of the bonds $1/\tau_+$ (τ_+ is average attachment duration) is much faster than the change in mutual position (see fig. 1.10c). A bond is therefore on average stretched by the distance $v\tau_+$. Considering there is on average N_+ attached molecules per unit area at a time, and k_m is a stiffness of presumably elastic bond, then the average substrate friction force per unit area is given as

$$\frac{\vec{F}_\eta}{A} = -k_m N_+ \tau_+ \vec{v} = -\eta_f \vec{v},$$

in a form analogical to Stokes drag, with proportionality constant $\eta_f = k_m N_+ \tau_+$, where A is the area of contact (ibid.).

1.3.3 Adhesion and interfaces

The work of **adhesion** is a (positive) energy necessary to separate two unit areas, of phases denoted *1* and *2*, from contact to infinity in vacuum, $W_{12} > 0$ (fig. 1.9a). In case the two media are identical, i.e. a single medium *1* is separated creating two free surfaces of unit area, the energy is called a work of **cohesion**, $W_{11} > 0$. Closely related quantity is **surface energy**, which represents the free energy change when free surface (i.e. in contact with vacuum) of a unit area is created, $\gamma_1 = 1/2 W_{11} > 0$ (fig. 1.9b-(i)). Note that the surface energy γ_1 is equivalent to the quantity **surface tension** σ_1 of the phase *1*[8].

[8] The units $[\gamma] = \frac{J}{m^2} = \frac{N}{m} = [\sigma]$ of the quantities are equivalent. The term surface tension is usually not applied to solids.

In the following paragraphs, we will mostly concentrate on surfaces of liquids. If two immiscible liquids, phases *1* and *2*, are brought in contact in a surrounding vacuum, the **interfacial energy** γ_{12} represents the change in the free energy incurred by expanding their contact surface by a unit area (fig. 1.9b). The interfacial energy can be understood as a sequence of (i) expansion of each phase's free surface by a unit area ($^1\!/_2 W_{11}, ^1\!/_2 W_{22}$), and (ii) bringing those free surfaces into mutual contact ($-W_{12}$,cf. fig. 1.9a), that is, $\gamma_{12} = {}^1\!/_2 W_{11} + {}^1\!/_2 W_{22} - W_{12} = \gamma_1 + \gamma_2 - W_{12}$, also know as Dupré equation. The equation is formally the same, as if phase *1* enveloped by another phase *2*, was divided creating 2 unit surfaces of phase *1*.

If the interface *1/2* is energetically preferable to two separate surfaces *1* and *2*, i.e. $\gamma_{12} < 0$, then the area between the unlike phases *1* and *2* will tend to expand, and one phase would eventually dissolve in the other (contradicting the immiscibility). On the other hand, if an inverse process occurs, in which two originally separate surfaces of phase *1* form a contact within an environment *2* (i.e. $2W_{12} \rightarrow W_{11} + W_{22}$, for instance two droplets *1* merging within an environment *2*), it will produce a change in free energy $(-\gamma_{12}) < 0$ and the total energy of the system will decrease (Israelachvili 1985, Chapter 17).

The concept of **surface tension** can be alternatively introduced on the microscopic (particle) level (more relevant to section Differential adhesion hypothesis). The surface tension arises at the interface between the liquid and the external phase[9]. At the interface, there exists an imbalance between the forces exerted on the surface particles by the interior particles of the liquid and the forces originating in the external phase. While the internal particles are exposed to the attractive forces from their neighbouring particles and experience a zero net force on average, the interface particles are subjected to lower forces from the external phase (i.e. $\gamma_{12} \equiv \sigma_{12} > \sigma_1$). Consequently, the energy of the surface particles is higher as compared to the bulk particles, and they experience constant net force directed towards the interior, minimising the liquid surface area S (and the total interface energy, $S \cdot \gamma_{12}$)(Glazer 1999; Schoetz 2007).

The **surface tension** σ has thus implications on liquid geometry. An immiscible droplet will naturally assume a minimal surface area determined by the Laplace equation,

$$\Delta p = \frac{2\sigma}{r}, \tag{1.1}$$

where Δp is the pressure excess of the interior liquid, and r is the droplet radius (cf. Young-Laplace law) (Isenberg 1978; Schoetz 2007). If the droplet comes in contact with a solid phase in a gas environment, the three phases form three interfaces (with different **interfacial tensions**). At the meeting point of these three interfaces, the interfacial tensions are in force equilibrium and determine the droplet contact angle ϕ, given by the Young equation,

$$\sigma_{sl} + \sigma_{lg} \cos\phi - \sigma_{sg} = 0, \tag{1.2}$$

where the interfacial tensions belong respectively to solid-liquid, liquid-gas and solid-gas (Isenberg 1978). Since the surface tension and free surface energy are equivalent, the

[9] In case of identical phases, i.e. liquid-liquid, the term **interfacial tension** is used.

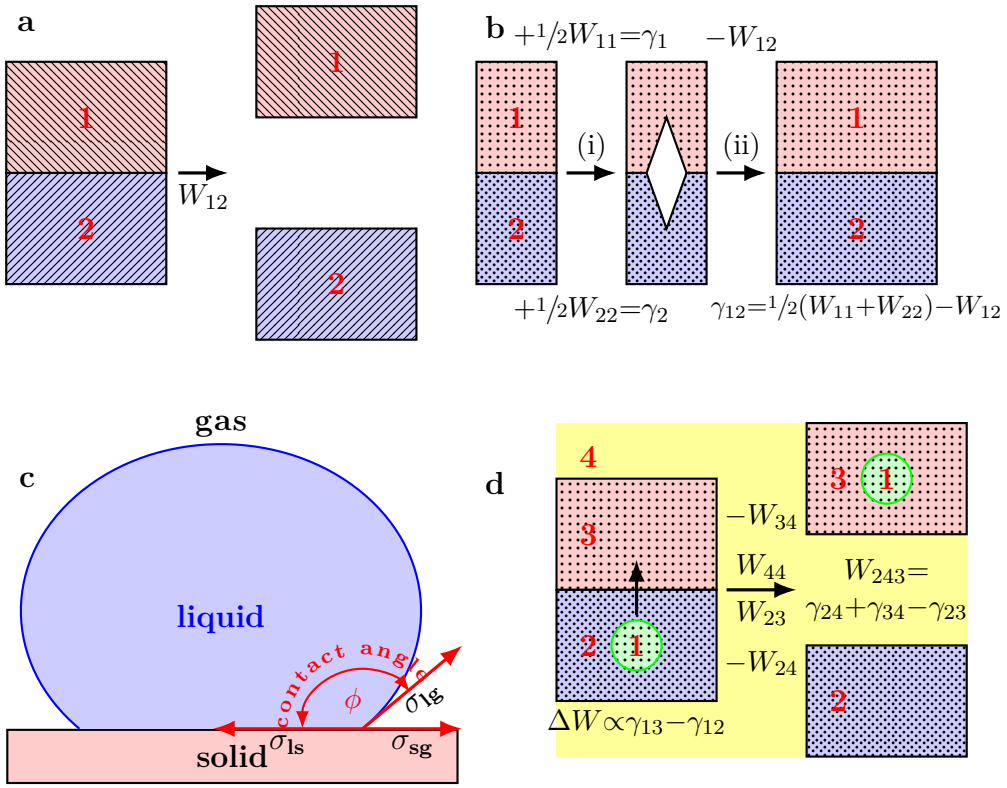

Figure 1.9: Illustration of interface concepts. **a**: Energy of adhesion W_{12} is work necessary to separate two unit surfaces of phases *1* and *2* from contact to infinite distance in vacuum. If *1*=*2*, i.e. two unit surfaces are being created from a single phase *1*, the work $W_{11} = 2\gamma_1$, where γ_1 is defined as surface energy per unit surface area of the phase *1*. **b**: Interface energy per unit area of contact of two liquid phases *1* and *2*, γ_{12}, can be understood as stepwise creation of a free surface (i.e. interface with vacuum) on the interface of 2 ½ unit areas per each phase (requiring work of ${}^1\!/_2W_{11}{=}\gamma_2$ and ${}^1\!/_2W_{22}{=}\gamma_2$) and bringing the free surfaces into contact (yielding work $-W_{12}$), $\gamma_{12} = {}^1\!/_2(W_{11} + W_{22}) - W_{12}$. **c**: Dupré equation, a liquid droplet on a solid phase in a gas phase. The contact angle ϕ is determined by the mutual ratio of interface energies, which are equivalent to interface tensions, $\sigma_{lg}, \sigma_{ls}, \sigma_{sg}$. **d**: In the process marked by '↑' on the left, there occurs a transfer of a particle of phase *1*, of unit surface area, through an interface from the liquid *2* to the liquid *3*; the energy balance is determined by mutual interface energies of the particle and environments. In the process marked by '→', a separation of the phases *2* and *3* within environment *4* takes place. Based on the sign of W_{243}, if $W_{243} < 0$, the liquid *4* will separate phases *2* and *3*, while if $W_{243} > 0$, either *2* envelops *3* (or vice-versa), or the *2*/*3* interface remains partially spread, and all three liquids remain in contact. In case environment *4* was a vacuum, $W_{44} = W_{24} = W_{34} = 0$, and we obtain the situation in the panel **a**.

energy required to separate a unit area surface of such droplet from the solid is given as $W_{sl} = \sigma_{sg} + \sigma_{lg} - \sigma_{sl}$, combined with the eq. (1.2) yields an alternative form of the Dupré equation, $W_{sl} = \sigma_{lg}(1 + \cos\phi)$ (see fig. 1.9c). Two extremal solutions exist for this equation

$$\begin{aligned} &\sigma_{sg} > \sigma_{sl} + \sigma_{lg} \Rightarrow \phi = 0; && W_{sl} = 2\sigma_{lg} && \text{complete wetting,} \\ &\sigma_{sl} > \sigma_{sg} + \sigma_{lg} \Rightarrow \phi = \pi; && W_{sl} = 0 && \text{no wetting,} \end{aligned}$$

where the droplet either completely wets the solid phase, or forms a closed sphere and does not wet the solid phase at all (Isenberg 1978; Schoetz 2007).

In biological systems, interfaces are not formed in vacuum, as illustrated in fig. 1.9d, where enveloping environment *4* is present. A macroscopic particle (of a unit surface area) of phase *1* (i.e. a cell; see fig. 1.9d'↑') may transfer between phases *2*→*3*. This involves separation of the interface *1*/*2* (W_{12}) and self-merger of the free surface *2*, ($-\frac{1}{2}W_{22}$), and the reverse process in the phase *3*, thus $\Delta W = (W_{12} - \frac{1}{2}W_{22}) - (W_{13} - \frac{1}{2}W_{33}) = \gamma_{13} - \gamma_{12}$ (Israelachvili 1985, Chapter 17).

Similarly, a separation of the two immiscible phases *2* and *3* may occur in an environment *4* (see fig. 1.9d'→'), the change in energy for such process, using the same reasoning as above, is $W_{243} = W_{23} + W_{44} - W_{24} - W_{34} = \gamma_{24} + \gamma_{34} - \gamma_{23}$. If $W_{243} < 0$ (*2* repulse *3* in *4*, so-called 'spreading pressure'), liquid *4* will displace liquid *3* and totally wet the surface of *2*, implying that $\gamma_{24} + \gamma_{34} < \gamma_{23}$. In the opposite case, $W_{243} > 0$, then $\gamma_{24} + \gamma_{34} > \gamma_{23}$ and the interface *2*/*3* remains intact, either *2* completely wets *3* (or vice-versa) or partial spreading ($\phi \in (0, \pi)$) occurs. In the latter case, all three media remain in contact (ibid., Chapter 17).

The adhesion, surface energy and interface energy concepts are based on the microscopic theory of matter, reviewed in detail in (ibid.). They will serve as a basis for the later section Differential adhesion hypothesis, introducing the phenomenon of cell and tissue sorting. Since interactions between molecules are the underlying mechanism of cellular adhesion, we will shortly introduce geometric and physical properties of common cell adhesion biomolecules.

Detailed cell adhesion molecules properties

The topic of CAMs was introduced in the section Selected cell adhesion molecules. In this section, particular biophysical parameters as size or bond strength and energy landscape of specific CAMs (NCAMs, cadherins) will be presented. The CAMs can be studied on a single molecule basis using surface force apparatus (SFA), a force measurement technique quantifying the interaction potentials between two surfaces as a function of the separation distance with precision of ±1 Å, with force measurement sensitivity in the range of inter-membrane van der Waals attraction (C. P. Johnson et al. 2004).

For the full NCAM ectodomains, the initial steric repulsion could be observed at the inter-surface distance ≈48 nm (for ectodomain stretching normally, the expected length would be 2·27=54 nm) while the steep repulsive barrier appears at 22 nm (as compared to expected 27 nm). This can be explained by a flexible hinge tilting the external domains relative to the surface at the angle ≈145°. The distinct binding events, two adhesive

configurations, were observed at (31.0 ± 0.5) nm and (39.0 ± 0.5) nm, both corresponding to a tilt of $(135 \pm 3)°$ (ibid.).

In case of Cadherins, as reported in (Prakasam et al. 2006; Sivasankar et al. 1999), the initial steric repulsion was observed at the distance 57 nm, while the onset of steep steric repulsion was estimated at <25 nm, with actual length of the ectodomain of 22.5 nm. Unlike the NCAM, no flexible hinge was reported, however a linker protein links an ectodomain to the membrane. Three distinct homophilic binding configurations were reported for most of Cadherins (middle configuration is missing for E-cadherin). The binding distance estimates for the N/N-cadherin binding events are (39.1 ± 1.0) nm, (46.8 ± 1.2) nm and (54.3 ± 0.9) nm; the difference of corresponding bond lengths for E/E-cadherin and C/C-cadherin is <2 nm. The applied technique is very precise in terms of spatial organisation of the CAM, but does not provide detailed information about the bond energy landscape.

To study the bond energy landscape in detail (introduction to the bond theory can be found in (Evans and Ritchie 1997; Husson et al. 2009)), individual protein-protein bond can be probed using atomic force microscope (AFM) technique, which allows to scan a range of bond loading rates. Proteins are covalently attached to both the AFM tip and a test surface; the tip repeatedly brings proteins in contact and pulls them apart at a given speed (determining the loading rate). The bond rupture is indicated by a step in the time course of AFM tip deflection. In the work (Wieland et al. 2005), the technique was used to demonstrate the presence of two distinct binding events for homotypic adhesion of NCAMs, testing the most probable rupture force for a range of loading rates (200–10 000) $\frac{\mathrm{pN}}{\mathrm{s}}$. The probability distribution of rupture force exhibited two peaks, (41 ± 6) pN and (55 ± 11) pN at low loading rates (781 $\frac{\mathrm{pN}}{\mathrm{s}}$), which moved to higher values and became more distinct for higher loading rate (7423 $\frac{\mathrm{pN}}{\mathrm{s}}$) at values (70 ± 6) pN and (106 ± 15) pN. The energy barrier height of both binding events was estimated as $(19.6 \pm 0.5)\,\mathrm{k_B T} \approx 8 \times 10^{-11}$ nJ (ibid.).

Similar study was performed on cadherins (E-cadherin and N-cadherin) in (Panorchan et al. 2006), using molecular force probe (MFP) and two individual cells. The E-cadherin had double-well potential (like NCAM), with mean bond rupture forces 73 pN and 157 pN for loading rates 1000 $\frac{\mathrm{pN}}{\mathrm{s}}$ and 10 000 $\frac{\mathrm{pN}}{\mathrm{s}}$ respectively, whereas the N-cadherin exhibited only single broad potential well[10] with mean rupture force of (30–40) pN for the same loading rates. While three distinct binding events were observed for the N-cadherin in (Prakasam et al. 2006), their energies are relatively low and more clustered, which could have made their individual potential wells indistinguishable in the MFP experiment. The bond lifetime of the N-cadherin and the weaker E-cadherin was at the order of 1 s, the stronger E-cadherin bond lifetime was 0.25 s. It seems that the weaker E-cadherin bond dominates for loading rates <500 $\frac{\mathrm{pN}}{\mathrm{s}}$, then the stronger bond takes over. The innermost and outermost homophilic bond energy barrier height was estimated as $(6.2 \pm 1.5)\,\mathrm{k_B T} \approx 2.5 \times 10^{-11}$ nJ and $(2.5 \pm 0.5)\,\mathrm{k_B T} \approx 1 \times 10^{-11}$ nJ for E-cadherin, and $(2.2 \pm 0.3)\,\mathrm{k_B T} \approx 0.9 \times 10^{-11}$ nJ and $(1.0 \pm 0.2)\,\mathrm{k_B T} \approx 4 \times 10^{-12}$ nJ for N-cadherin (ibid.).

[10] wider than both E-cadherin wells combined

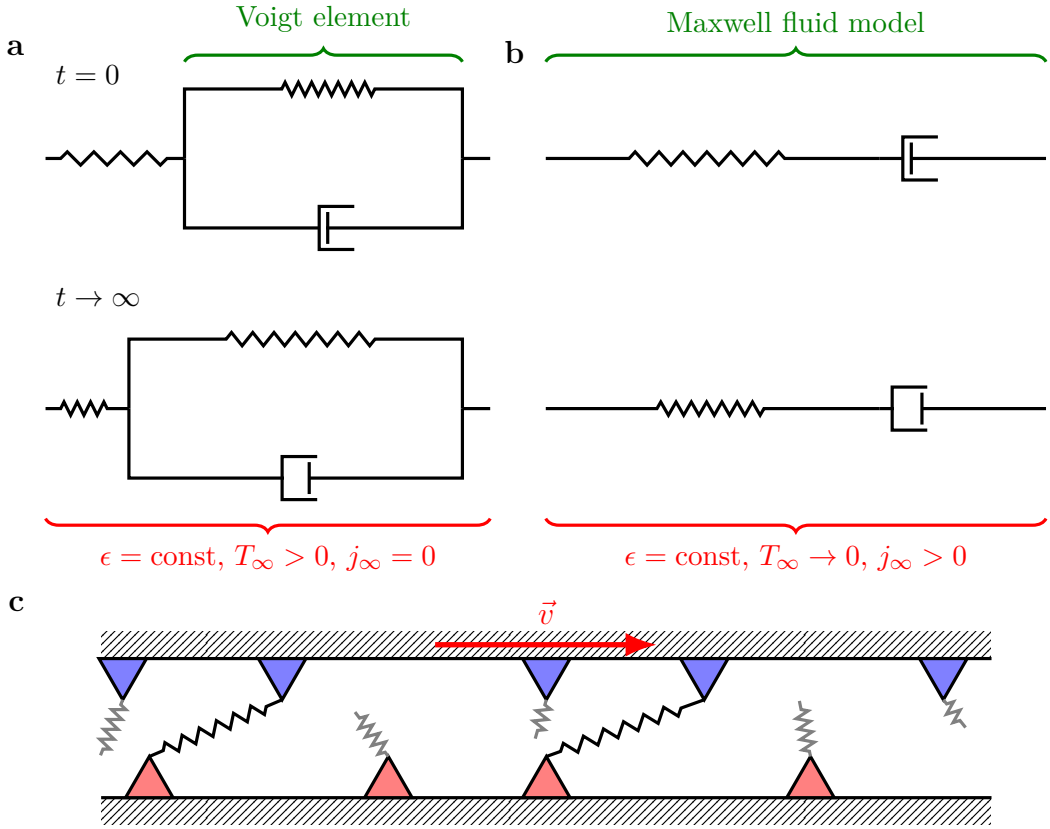

Figure 1.10: Illustration of viscoelastic behaviour and friction. **a**: Illustration of viscoelastic solid. If the material is step-stretched at the time $t = 0$ and the strain is held constant, $\epsilon = \text{const}$, it partially relaxes, the stress decreases to a non-zero value, $T(0) > T(t_1{>}0) > T_\infty > 0$, and the flux of material stops, $j_\infty = 0$. If fixation is released, the body returns to its original shape. **b**: Illustration of viscoelastic fluid. Step-stretched material is held on constant strain. The material gradually completely relaxes, while the material flux gradually slows down no small but non-zero values, $T_\infty \to 0$, $j_\infty > 0$. Material retains its deformed shape, if fixation is released after complete relaxation. **c**: Illustration of substrate friction. The bonds between molecules (triangles) on mutually moving surfaces form elastic bonds (springs), which spend time τ_+ in the bound state. Stretching of these bonds generates the friction force.

1.4 Mechanical properties of neurons

1.4.1 Roles of mechanical forces in neurogenesis and arborisation

Significance of mechanical forces becomes evident already during the early neurogenesis, when the stiffness of the substrate regulates cellular differentiation (Engler et al. 2006). Mesenchymal stem cells differentiate into neuronal phenotype, while stiffer substrates promote differentiation into glial cells (Georges et al. 2006). This is consistent with brain

tissue, initially soft but gradually stiffening, switching from neurogenesis to gliogenesis. Later in the development, the neurons prefer to grow on softer substrates—they are stiffer than neighbouring glial cells, which in contrast prefer stiffer substrates. This complementary preferences likely attract the two populations to each other, which may play a role during myelin sheath formation (Franze 2013).

During the neurodevelopment and pathfinding, neurons and GCs are likely to encounter gradients of stiffness in the environment and take advantage of mechanotaxis (Lo et al. 2000). It has been shown *in vitro* that neurites preferentially align along the direction of stretching of the substrate (Chang et al. 2013), and that the tension along the neurites may contribute to the migration directionality (Hanein et al. 2011). It has been further shown that forces influence axogenesis (Bray 1984) and that the stiffness of the substrate determines neuronal morphology, and number, length and branching pattern of neurites (Anava et al. 2009). The same is true for tension along neurites, it influences the geometry of the neurite branches as well as of the neuronal soma (Bray 1979; Hanein et al. 2011).

The regulation of neurite arbour morphology determines connectivity diagram of neuronal system; arborisation allows a single neuron's axon to form synapses with multiple target dendrites and establish a more complex circuit. While the fine elimination of excessive synapses is activity-dependent, the early network is likely pre-pruned by activity-independent mechanisms (e.g. tension, adhesion). This was supported by Anava using carbon nanotube (CNT) islands (Anava et al. 2009): upon contact of a neurite with a CNT island, tension increased (straightening the neurite) and collateral branches, less firmly attached to the substrate, detached and retracted, preserving only single taut branch in place. The results are consistent with experiments in culture without CNT elements (Shefi, Ben-Jacob, et al. 2002), where the conserved branch simply interacts with another neurite. Initial neurite contact can therefore take advantage of activity-independent mechanism, and optimise the arbour before a synapse is formed.

1.4.2 Role of mechanical forces in the growth cone dynamics

In addition to the regulation of cell motility, axon pathfinding and neurite arbour morphology, the mechanical forces play an essential part in the underlying processes of GC dynamics and steering. The mechanical and topographical guidance cues acting through the GCs are complementary to the biochemical mechanisms presented in the section Axon guidance. The GCs read the deformation and stiffness of the ECM through actin dynamic turnover (see the section Growth cones), and mediate the mechanotransduction (Kerstein et al. 2015). GC's mechanotransduction integrates inputs from cell adhesion receptors, GC-ECM coupling proteins and mechanosensitive ionic channels, as well as reversible cytoskeletal reorganisation on micron-scale (Athamneh and Suter 2015). However, the ultimate mechanical feature vested in the GC is its ability to generate the **traction force**—this force drives the GC's movement and determines its direction, while at the same time it produces a (gradient of) tension within the AS.

The traction force is essentially generated by coupling of highly dynamic F-actin flow to the ECM through adhesion receptors (Ig CAMs, N-cadherin and integrins) at the

P-domain (actin assembly location) adhesion sites (Athamneh and Suter 2015). The coupling depends on the environment stiffness—the substrate must be sufficiently compliant to allow adhesion maturation and to support the gradual build-up of tension. The traction force magnitude is highly variable, as (i) various neuronal types respond differently to a given level of substrate stiffness, and (ii) individual GCs exhibit a biphasic profile of force, which initially increases with substrate stiffness, but plateaus after a threshold stiffness is reached (Kerstein et al. 2015; Suter and K. E. Miller 2011).

The scanning force microscopy (SFM) technique was used to study these mechanoregulative processes. Short-time external stress was imposed on a leading edge of a GC (Franze et al. 2009), demonstrating, that a neurite responds by shortening and retraction if the external stress exceeds particular threshold (274 Pa for PC-12 neurons). The retraction is likely controlled by signalling of mechanosensitive ion channels in the GC membrane, rather than being just a passive mechanical effect. The observed retraction threshold is linked to (PC-12) GC's ability to deform only environments with Young modulus up to $E \sim 300$ Pa, which roughly corresponds to the estimated stiffness value of the GC itself (Betz et al. 2011; Franze et al. 2009). The GCs are thus stimulated to advance on a softer substrate, while a stiffer one induces negative mechanotransductive feedback, in agreement with observed GC's preference to grow on softer glias *in vivo* (Lu et al. 2006).

Mechanism of growth cone advance

The traction force built up by a GC is typically around 0.5 nN for PC-12 neurons (Dennerll, Joshi, et al. 1988) (measured as the rest tension of the AS), but can reach up to 100 nN for *Aplysia* neuron GC as reported in (Athamneh, Cartagena-Rivera, et al. 2015). The GC advance and steering, mediated through F-actin and MT dynamics, is powered by molecular motors: myosin II is essential for generation of retrograde F-actin flow and actin-filament recycling in the T-domain, while dynein and kinesin play a major role in MT anterograde movement (Athamneh and Suter 2015).

The mechanism of GC advance was studied using fluorescent speckle microscopy (FSM) (Salmon and M. Waterman 2011) combined with restrained bead interaction (RBI) assay. In the study (Lee and Suter 2008), a bead coated with *Aplysia* cell adhesion molecule (apCAM) is used to mimic adhesive substrate and induce adhesion mediated GC steering. The bead is restrained by a microneedle (MN) (i.e. it is not carried away by GC's retrograde flow), inducing a GC biphasic response towards the bead: (i) the **latency** phase beginning with bead placement and involving adhesion formation and signalling but little morphological changes, (ii) followed by a **traction** phase, characterised by a major structural, biophysical and cytoskeletal changes.

The technique was used to show, that the P-domain MTs extend preferentially along the C-domain–bead adhesion site (BAS) axis[11] (and not in the off axis areas) during the latency phase, while the C-domain remains static. These MTs strengthen the actin-CAM coupling. On the other hand (see fig. 1.2 for illustration), the FSM showed, that the F-actin flow along the C-domain–BAS axis (i) did not change during the latency phase

[11] The adhesion site is usually localised in the P-domain.

after the bead had been added—the flow was $(5.1 \pm 0.3)\,\frac{\mu m}{min}$, a typical value for both on-axis and off-axis flow— (ii) during the traction phase, the on-axis flow underwent about 80 % (down to $1.6\,\frac{\mu m}{min}$) attenuation and the T-domain moved forward, finally (iii) after the bead had been released, the on-axis flow increased to $12.7\,\frac{\mu m}{min}$, suggesting the bead was under strong tension (ibid.).

The technique also showed, that during the latency period, (i) the rates of polymerisation and depolymerisation, retrograde and anterograde translocation of the **exploratory** MTs (localised distally, in the P-domain), did not change appreciably, neither on C-domain–BAS axis, nor off this axis, (ii) despite the rates did not change, the on-axis exploratory MTs spent less time in depolymerisation and retrograde translocation (due to partial F-actin flow decoupling), while time in translocation and polymerisation pauses increased[12], (iii) MTs in T-domain and C-domain coupled with actin arcs in T-domain and actin bundles in C-domain respectively and reoriented towards the bead. During the traction period, the reduction of P-domain actin structures behind the bead resulted in reorientation of actin arcs (in the T-domain and C-domain) towards the bead and their immobilisation. The arcs narrowed the C-domain and focused the MTs towards the bead. Bulk MTs and actin bundles in the C-domain translocated anterogradely towards the bead at $(2.69 \pm 0.05)\,\frac{\mu m}{min}$, at the same speed as the C-domain boundary and the leading edge (Lee and Suter 2008; A. W. Schaefer et al. 2002).

The current models (reviewed in (Suter and K. E. Miller 2011)) imply, that dynamic exploratory MTs are important for the axonal guidance and adhesion site stabilisation, while the MT assembly in the GC (slowly transported through the axon) is critical for axonal extension. Therefore, a sustained GC advance is clearly dependent on the component transport; and while this regulative intra-axonal transport is a complex process, it has been shown that it is to a large extent modulated by axonal tension (Ahmed and Saif 2014), which can induce axonal growth (Bray 1984; O'Toole, Lamoureux, et al. 2015).

1.4.3 Mechanical properties of axons

A wide range of biophysical experimental techniques for micro-manipulations and microscopy appeared in recent years and allowed to perform experiment on axons. Each manipulation tool has a distinct force-range of operation and particular advantages and disadvantages. Some of the techniques were already mentioned in the previous paragraphs. These experimental techniques played a crucial role in our understanding of axonal mechanical properties.

One of the first techniques used was force-calibrated MNs, a direct and approachable method with resolution 1 pN, used in the 1970's and 1980's by Bray (Bray 1979) to demonstrate that GCs generate traction force, that the direction of GC advance is determined by the direction of tension between the GC and the rest of the cell, and to provide evidence that axon tension and its diameter (calibre) are correlated, which was further supported in (Anava et al. 2009). Bray used the same technique again later (Bray 1984) to show that the neurites grow in response to an external mechanical force

[12] MT dynamics reviewed in (Joe Howard and Hyman 2003)

and that a new axon can be initiated by applying sufficient tension to the neuron. The papers developed a methodology of vector analysis to calculate the total force exerted by neurites on neuron's soma, and to determine force equilibrium at a branching point, proposing a relation between the branching angle the ratio of neurites' tensions. The existence of force equilibria was further demonstrated by Joshi (Joshi et al. 1985).

Joshi's work was expanded by Dennerll (Dennerll, Joshi, et al. 1988), using MN to quantitatively analyse elastic properties of (PC-12) axons. A straight axon was deflected laterally using a force-calibrated MN, establishing an equilibrium between the calibrated MN flexure force and axon's normal tension projection, and released after (2–3) s (avoiding viscous effects). The model assumed elastic axon stretching (i.e. Hooke's law) and linear force-deflection relation for the MN, other possible forces were neglected—each equilibrium thus fully defined by the axon distension and MN deflection. The data were fitted by the model yielding the values of axonal rest tension, clustered around (200–400) pN (but spanning $(10–10^3)$ pN), and axon stiffness, clustered around (100–200) $\frac{\mathrm{pN}}{\mu\mathrm{m}}$.

The model was extended in (Dennerll, Lamoureux, et al. 1989) to account for the viscous effects: the spring representing axon elasticity was put in series with a Voigt element without substrate friction (viscoelastic solid model illustrated in fig. 1.10a). The axon was laterally deflected and then let to relax over time, the evolution of distension of the axon (∼axon strain) and of MN deflection (∼axon tension) were recorded. The observed axon dynamics was consistent with the passive viscoelastic solid model—fitting the data, the authors were able to estimate elastic and viscous parameters of the model (detailed in the section 1.4.4). When the external pulling force exceeded the threshold of ≳1 nN, the axon exhibited continued towed growth (see fig. 1.11a). Conversely, a low threshold was observed—if an axon tension decreased below this threshold, the axon shortened in order to regenerate it.

This tensile regulation of axonal outgrowth was further studied in (Zheng et al. 1991), where the exerted force was gradually increased over several hours by (250–500) pN every (30–60) min. The authors observed linear relationship between the growth rate and tension ($0.15\,\frac{\mu\mathrm{m}}{\mathrm{h\,pN}}$) for tensions above the thresholds clustered around (0.5–1.5) nN. Such mechanism allows growing animals to maintain moderate rest tension in their axons. The observations *in vitro* were confirmed on *Drosophila* embryos *in vivo* in (Rajagopalan et al. 2010).

If the axonal growth is stimulated by low force levels over long time, there is no obvious thinning or disruption of the cytoskeleton and normal electrophysiology is preserved. On the other hand, an acute stretching, resulting in high tension, impairs axonal regeneration. Crucial addition of new cytoskeletal mass involves the transport of both individual MT polymers and soluble tubulin subunits. The axonal elongation rate of $\sim 1\,\frac{\mathrm{mm}}{\mathrm{d}}$ (Suter and K. E. Miller 2011) is therefore likely limited by the average velocity of the low velocity transport (LVT) of neurofilaments and MTs, estimated at $\sim 0.5\,\frac{\mathrm{mm}}{\mathrm{d}}$ (Brown et al. 2005) (smaller proteins can be transported at much higher rate of $(2–8)\,\frac{\mathrm{mm}}{\mathrm{d}}$ (Brown 2000)). The LVT is a complex phenomenon, where the MT-based motors (e.g. kinesin) transport soluble cytoskeletal elements and polymers, and all the proteins spread by diffusion within the framework of the stretching AS (K. E. Miller and Heidemann 2008). Despite the LVT limitation, the axon elongation rates can in some cases exceed the

tubulin transport rate—local protein synthesis is then presumably taking place, while mechanostransduction pathway activated by axon stretching promotes protein synthesis in other parts of the cell and increases the rate of the LVT (Suter and K. E. Miller 2011).

1.4.4 Modelling of axon shaft mechanics

As mentioned in the section Mechanical properties of axons, a passive axon behaves as a viscoelastic material (Janmey et al. 2007). It has elastic, spring-like response to a short term external force (seconds to minutes), and undergoes viscous relaxation—well modelled by a Voigt element—if the external force persists over intermediate time interval (tens of minutes to hours) (O'Toole, Lamoureux, et al. 2008); these are features of a viscoelastic solid (fig. 1.10a). In case of towed growth over a long time scale, the axon elongation rate is proportional to the external force and can be represented by a dashpot (Zheng et al. 1991), closer to the features of viscoelastic solid (fig. 1.10b). Combining these characteristics, a segment of an axon (see fig. 1.11a) can thus be modelled by a spring (of stiffness k_1) in series with a Voigt element (stiffness $k_2 < k_1$, viscosity coefficient H_1), with another dashpot in series (H_2) representing the towed growth; the combination is called Burgers model (Dennerll, Lamoureux, et al. 1989). The parameter which determines if the time scale of observation is short, intermediate or long, is the viscoelastic relaxation time constant given as a ratio of viscosity coefficient and Young's modulus, $\tau = \eta/E$, for cells, a typical value is $\tau \sim 10\,\mathrm{s}$ (O'Toole, Lamoureux, et al. 2015).

To explore consequences of viscoelastic behaviour of the AS, a biophysical model was developed by O'Toole in (O'Toole, Lamoureux, et al. 2008), considering the following: (i) experiments have shown, that while proximal sections of axonal cytoskeletal framework are stationary, the distal segments (particularly near the GC) do stretch, and accompanying slow axonal anterograde transport of cytoskeleton (i.e. the LVT) is observed, (ii) this behaviour persists (the more distal the more prominent) even if GC advance stops, likely propelled by the built up tension—suggesting fluid, rather than solid behaviour of the AS, (iii) the model treats axonal behaviour on longer timescales, during which viscous term dominates. In such long time scale model, the immediate (k_1 in fig. 1.11a) and intermediate (k_2, H_1 in fig. 1.11a) temporal terms are excluded, only the towed-growth dashpot (H_2 in fig. 1.11a) is included. To combine the fluid-like behaviour with substrate friction (see also (Aeschlimann and Tettoni 2000)), axon is represented by a series of infinitesimal elementary towed-growth dashpots with local elongation viscosity coefficient $\eta^{\Updownarrow}$ (infinitesimal analogue of the H_2), while each element experiences substrate friction force proportional to its velocity (fig. 1.10c), with axial substrate friction coefficient $\eta^{\parallel}$; the model is illustrated in fig. 1.11b. In the model, both coefficients, $\eta^{\Updownarrow}$ and $\eta^{\parallel}$ are taken constant; i.e. substrate friction dissipation factor remains uniform along the axon and elongational dissipation factor is generally unaffected by axon thinning.

Each element of length dx at axon position x (for axon of current length $L(t)$, $x = 0$ at soma) experiences strain rate $\dot{\epsilon}(x, L(t)) = \frac{f(x,L(t))}{\eta^{\Updownarrow}}$, where $f(x, L(t))$ is the net force acting at the position x at the time t; each element dx is also subjected to the length-proportional substrate friction $df_\eta(x, L(t)) = -\eta^{\parallel} v(x, L(t))dx$, where $v(x, L(t))$

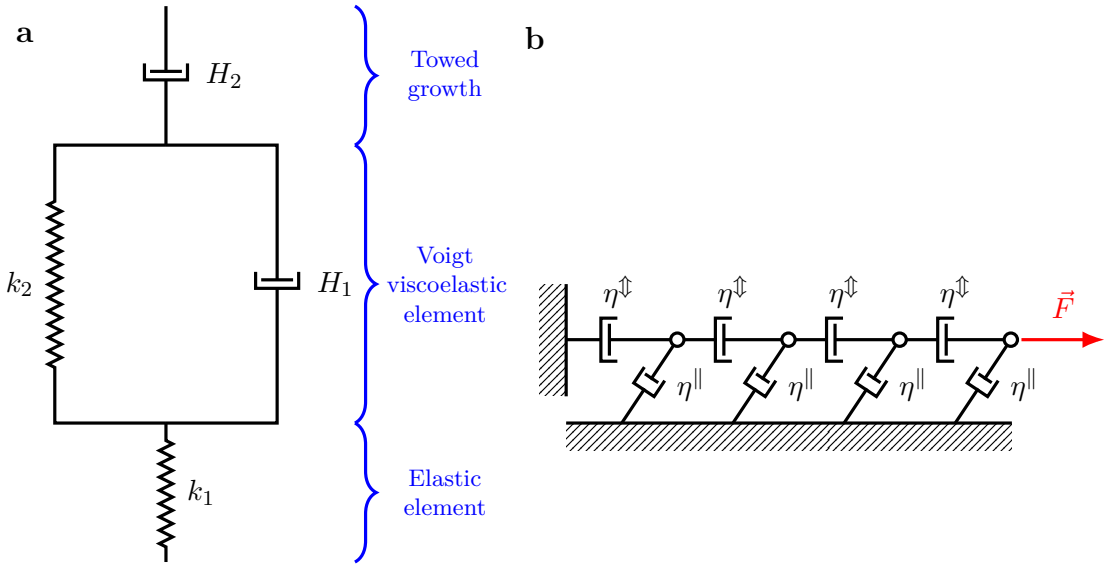

Figure 1.11: **a**: Burgers element representing stress-strain relation of an element of axon. In response to external force, the axon initially stretches elastically (k_1), viscoelastic relaxation occurs (Voigt element, H_1, k_2<k_1) on the time scale of ∼10 min, and finally, on the time scale ∼1 h, towed growth is induced (H_2). **b**: O'Toole's axons model for towed growth. Unlike in the panel **a** and the model proposed by Dennerll, where axon is treated as a single segment, O'Toole represents the axon as a series of infinitesimal viscous elements. The wide dashpots with viscosity coefficient $\eta^{\Updownarrow}$ represents internal dissipation, when prolonged axial external force $\vec{F}$ is applied, while more narrow dashpots with coefficient $\eta^{\parallel}$ represent axial substrate friction (see fig. 1.10c). In analogy with the fig. 1.8c, such model leads to a gradient of tension along the axon.

is the absolute velocity of the element (i.e. velocity with respect to the substrate), see figs. 1.11b and 1.12a for illustration. The absolute velocity is given by the sum of deformation rates ($\dot{\epsilon}dx$) of all elements in the interval $(0, x)$, i.e.

$$v(x, L(t)) = \int_0^x \dot{\epsilon}(x', L(t))dx' = \int_0^x \frac{f(x', L(t))}{\eta^{\Updownarrow}}dx'.$$

The net force acting at each element is given by the GC traction force F_0 reduced by the sum of axial substrate dissipation $\int df_\eta$ in the interval $(x, L(t))$, i.e.

$$f(x, L(t)) = F_0 - \int_x^{L(t)} \eta^{\parallel} v(x', L(t))dx' = F_0 - \frac{\eta^{\parallel}}{\eta^{\Updownarrow}} \int_x^{L(t)} \int_0^{x'} f(x'', L(t))dx''dx'.$$

Combining the two equations, closed form solution can be obtained (O'Toole, Lam-

oureux, et al. 2008).

$$f(x, L(t)) = \frac{F_0 \cosh(x\sqrt{\eta^{\parallel}/\eta^{\updownarrow}})}{\cosh(L(t)\sqrt{\eta^{\parallel}/\eta^{\updownarrow}})} \tag{1.3}$$

$$v(x, L(t)) = \frac{F_0 \sinh(x\sqrt{\eta^{\parallel}/\eta^{\updownarrow}})}{\sqrt{\eta^{\parallel}\eta^{\updownarrow}}\cosh(L(t)\sqrt{\eta^{\parallel}/\eta^{\updownarrow}})}. \tag{1.4}$$

Towing experiments confirmed, that section of an axon lifted from the substrate has linear velocity profile ($\eta^{\parallel} \to 0, v(x) \to {}^{F_0 x}/_{\eta^{\updownarrow}}$), while the section before the point of separation from the substrate experiences dissipation and the velocity profile corresponds to the eq. (1.4). The axons in contact with the substrate ($\eta^{\parallel} \neq 0$) and with low elongational friction $\eta^{\updownarrow}$ will tend to stretch very easily, so the force will be quickly dissipated by the substrate friction near the GC and only limited LVT would occur along the AS; if the towing force F_0 is too high, the axon will begin to thin (which is usually not observed in natural growth), more prominently at the distal region.

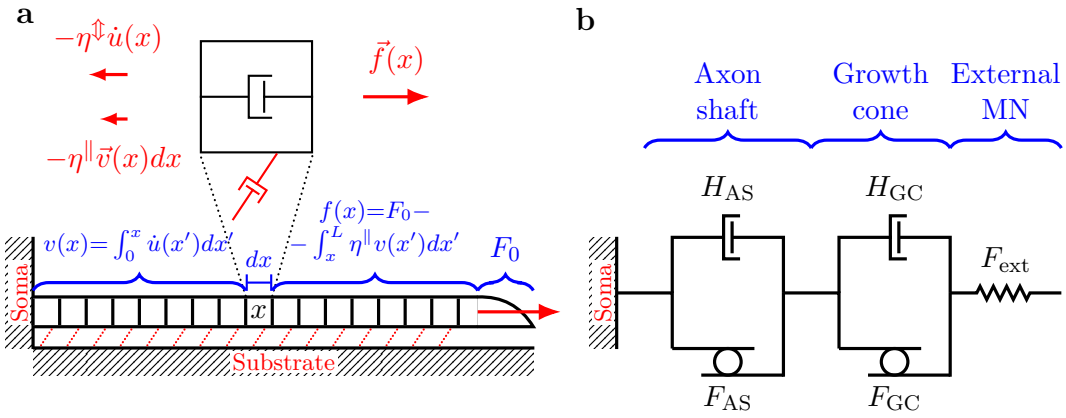

Figure 1.12: Illustration of O'Toole's models. **a**: Discretisation of an axon. The GC exerts force F_0 at the tip (position L), while the AS is modelled as a viscous fluid subjected to friction with the substrate. At an infinitesimal element of the axon dx at position x, acts force $\vec{f}(x)$ generated by the GC but diminished by the substrate friction contributions $\eta^{\parallel} v(x')dx'$ of all elements dx' in the interval (x, L); friction at any point x' depends on element's velocity $v(x')$ with respect to the substrate, given as total deformation (extension) in the interval $(0, x')$. Based on such assumptions, closed equations for velocity and force profiles along the axon can be obtained, see eqs. (1.3) and (1.4). **b**: Model of axon, where AS and GC generate internal tension using molecular motors, illustrated by the circle between parallel lines, generating forces F_{AS} and F_{GC} for the axon shaft and the growth cone respectively. Viscosity of the axon is represented by the dashpots labelled η_{AS} and η_{GC}. F_{ext} is an external force induced by a MN or another tool, see details in the main text. Note that no substrate friction is considered in the model of panel **b**.

In a further study related to O'Toole's model, Lamoureux et al (Lamoureux, Heidemann, et al. 2010) tracked the position of branching points, mitochondria, and mi-

crobeads attached to axon surface, and confirmed that the axon shaft framework is not stationary, but advances with the whole stretching neurite structure. The observations also confirmed, that the more proximal parts of the neurite move at slower rate than the more distal ones. When stretched, axon would becomes thinner and density of mitochondria decreases, but eventually, over the course of several hours, axon with stationary GCs recovers its pre-towing width and mitochondria density—new material is added along the whole axon, not exclusively behind the GC. The results are closely matching the model developed in (O'Toole, Lamoureux, et al. 2008).

In (O'Toole and K. E. Miller 2011), this biophysical model was modified to calculate flux of material in growing/towed axons, to study the LVT. The total flux was considered to linearly decrease away from the neuronal soma; the contribution of stretching flux was separated from the total flux, showing that the stretching-generated flux can account for $\sim$50 % of the LVT for axons lengthening at rapid rates in absence of substrate friction. The work shows, that in distal axon region, the total flux is dominated by the stretching flux (exact interval depends on parameters).

The LVT and axonal viscoelastic properties were examined further in (O'Toole, Lamoureux, et al. 2015). Material in axons was experimentally tracked: (i) if the material remained static over time under constant neurite strain (static GC) and stable rest tension, the behaviour would correspond to viscoelastic solid (fig. 1.10a), (ii) on contrary, if a continuous flow of the material was observed under the constant strain, it would exhibit characteristics of a viscoelastic fluid (fig. 1.10b). Distal section of an axon was detached from the substrate and let to relax (compare with the section 1.4.3), observing steady state tension of (1.3 ± 0.3) nN (chick sensory neurons); this means that contractile and steady net force is generated in neurites. To study LVT, mitochondria were tracked producing kynographs; fast moving mitochondria ($>100\,\frac{\mu m}{h}$) were excluded, as they were transferred either by kinesin or dynein. Remaining mitochondria, bulk-moved by the LVT, advanced in anterograde direction at average velocity $(17.0 \pm 1.5)\,\frac{\mu m}{h}$, exhibiting velocity gradient increasing along the axon, suddenly dropping at the GC's C-domain. The result is consistent with the values presented in section Mechanical properties of axons, $\approx 40\,\frac{\mu m}{h}$ (Brown et al. 2005). Such continuous anterograde transfer of mitochondria and presumably also other material suggests, that on the time scale of the LVT, the axons behave as a viscoelastic fluid.

In case of passive viscoelastic fluid, the internal tension would gradually relax with the material flow (fig. 1.10b). O'Toole's experiments in (O'Toole, Lamoureux, et al. 2015) however indicate otherwise, suggesting the steady state axonal tension is actively generated. The biophysical model presented in the work implements molecular-motor-generated contractile forces within the sub-cellular compartments AS and GC (denoted F_{AS} and F_{GC} respectively). Each of the two serial compartments also has intrinsic viscous characteristics, represented in the model by a dashpot (coefficient H_{AS} for AS and H_{GC} for GC) arranged in parallel with the corresponding motors element. The whole model setting is attached to the immobile soma on one end, and serialised with a pulling needle, represented by a spring (exerting external force F_{ext}), on the other end; the full illustration is shown in fig. 1.12b. Considering the total length of the axon is a

sum of AS and GC lengths, we can write

$$\frac{dL}{dt} = \frac{dL_{\mathrm{AS}}}{dt} + \frac{dL_{\mathrm{GC}}}{dt} = \frac{F_{\mathrm{ext}} - F_{\mathrm{AS}}}{H_{\mathrm{AS}}} + \frac{F_{\mathrm{ext}} - F_{\mathrm{GC}}}{H_{\mathrm{GC}}}.$$

As the length of the neurite becomes steady over time, $\dot{L} = 0$, the external measured force is equal to the neurite rest (steady state) tension $F_{\mathrm{ext}} = F_{\mathrm{ss}}$, which can be written as

$$F_{\mathrm{ss}} = F_{\mathrm{AS}} \frac{H_{\mathrm{GC}}}{H_{\mathrm{AS}} + H_{\mathrm{GC}}} + F_{\mathrm{GC}} \frac{H_{\mathrm{AS}}}{H_{\mathrm{AS}} + H_{\mathrm{GC}}}.$$

The last expression decomposes the measured steady state force F_{ss} into internally generated force components, modulated by the ratio of compartment viscosities ${}^{H_{\mathrm{AS}}}/_{H_{\mathrm{GC}}}$. Note that the F_{ss} approaches the force of the softer region, e.g. ${}^{H_{\mathrm{AS}}}/_{H_{\mathrm{GC}}} \to 0, F_{\mathrm{ss}} \to F_{\mathrm{AS}}$.

It is possible to estimate F_{AS} and F_{GC} by systematically varying the applied F_{ext} and monitoring the strain of sub-cellular compartments. When the strain of particular compartment does not change, it means the force generated in the compartment by molecular motors equals the applied force. Being able to directly measure the three forces, the ratio of viscous parameters can be calculated as $\frac{H_{\mathrm{AS}}}{H_{\mathrm{GC}}} = \frac{F_{\mathrm{AS}} - F_{\mathrm{ss}}}{F_{\mathrm{ss}} - F_{\mathrm{GC}}}$, providing insight into mechanical properties of elementary functional components of axons (ibid.).

O'Toole's works are particularly important, as they in detail describe axons from mechanical point of view, phenomenologically incorporating actively-generated forces (i.e. GC-generated traction force F_0 or molecular-motor-generated contractile forces F_{AS}, F_{GC}) and dissipative forces (both friction $\eta^{\parallel}$, and viscous $\eta^{\Updownarrow}$, H_{GC}, H_{AS}). Their works often emphasise the fluid characteristics of the axons and focus on passive axonal transport (particularly in relation to the LVT) and growth. Despite the models are only one-dimensional and usually focused on the long time scale dynamics, they were adapted to justify simplifications of axon viscoelasticity in our model of dynamics of axon-axon contact interactions.

1.5 Differential adhesion hypothesis

Tissue segregation during embryonic development is a phenomenon brought forward by differences in strength of adhesion between mobile cells. During the differentiation, the variability of cell adhesion generates interfacial tension at cell population boundaries. Different types of intercellular adhesion are mediated by cadherins, integrin-fibronectin bonds and cell-ECM adhesions (Ramsey A. Foty and Malcolm S. Steinberg 2004). Spontaneous sorting and cell population interfaces emerge only in systems, where heterotypic adhesion (adhesion between cells of different types, cross-adhesion) is weaker than the mean value of homotypic adhesions (adhesion between the cells of the same type, self-adhesion; see fig. 1.13d, cf. fig. 1.9d). These phenomenons resemble the segregability properties of liquids (see section Adhesion and interfaces); analogies between the underlying mechanisms can be found: (i) passive mobility and active motility of cells are analogous to the Brownian motion of particles (Glazer 1999, p. 45), and (ii) short-range CAM-mediated adhesive forces are analogous to the intermolecular van der Waals forces

(Glazer 1999, p. 67). As proposed by the Differential adhesion hypothesis (DAH), the combination of random cellular movement and the local contact interactions determine the optimal local binding partners of a cell, and drive the biological system towards the state of minimal binding energy (Ramsey A. Foty and Malcolm S. Steinberg 2004; Malcolm S. Steinberg 1970). The DAH offers explanations for (a) fragment shape-smoothing toward a spherical shape (fig. 1.13a, cf. eq. (1.1)), (b) transitivity of complete wetting, or 'enveloping', (fig. 1.13b, cf. Dupré equation), and (c) unique final organisation of two populations, independent of initial configuration (fig. 1.13c, cf. fig. 1.9d). The hypothesis was recently reviewed in (Malcolm S Steinberg 2007).

The central quantity of the DAH is tissue surface tension, σ, which is an apparent surface (interface) tension of an aggregate of particular cells (analogous to liquid surface tension presented in section 1.3.3). The σ arises from differences in mechanical energy of surface cell[13] (W_s) and interior cell (W_i) per unit area—the energy of the interior cell is relatively lower ($W_i < W_s$), due to negative energy of saturated intermolecular attraction (Ramsey A. Foty and Malcolm S. Steinberg 2005; Harris 1976).

$$\sigma = \frac{W_s - W_i}{A} \mid A \text{ is area of a surface cell} \tag{1.5}$$

The σ should not be confused with the cortical tension β of individual cells. The existence of the tissue surface tension, σ, and its numerical values were established experimentally (R. A. Foty et al. 1996; Ramsey A. Foty, Forgacs, et al. 1994; Norotte et al. 2008) supporting the DAH. It has been also shown in (Duguay et al. 2003) that under the experimental conditions, the σ is predominantly generated by interactions of the adhesion molecules (dependent on their expression levels, (Ramsey A. Foty and Malcolm S. Steinberg 2005)) expressed on cellular surfaces and to much lower extend by differences in the cortical contractility (β) of individual cellular surfaces.

The surface and interfacial tensions of binary liquid systems specify not only miscibility or immiscibility, but also the precise final state configuration the system will approach (fig. 1.13d). The mutual spreading preferences are determined by the relative surface tensions σ, where the phase of lower σ tends to envelope the other, independently of CAM types expressed (note that the types of CAMs still influence the values of σ)(R. A. Foty et al. 1996; Ramsey A. Foty and Malcolm S. Steinberg 2005). For instance, homotypic and heterotypic adhesive interactions between great majority of cadherin subtypes are very similar in strength, but one phase is usually enveloped by another (less cohesive) in binary systems (see also (R. A. Foty et al. 1996)). This indicates that cohesion very strongly depends on expression levels—by increasing or decreasing expression of cadherin subtype in a heterotypic binary system, internalised and externalised phases can switch positions, due to the change of the relative cohesion. This suggests that segregation of cells is not necessarily driven by difference of types of expressed CAMs but supposedly also by the level of their expression (Ramsey A. Foty and Malcolm S. Steinberg 2004, 2005; Malcolm S Steinberg 2007).

[13] Surface cells may still form contacts with external environment, however as long as the tissues remain segregated, the heterotypic adhesiveness is weaker than the homotypic.

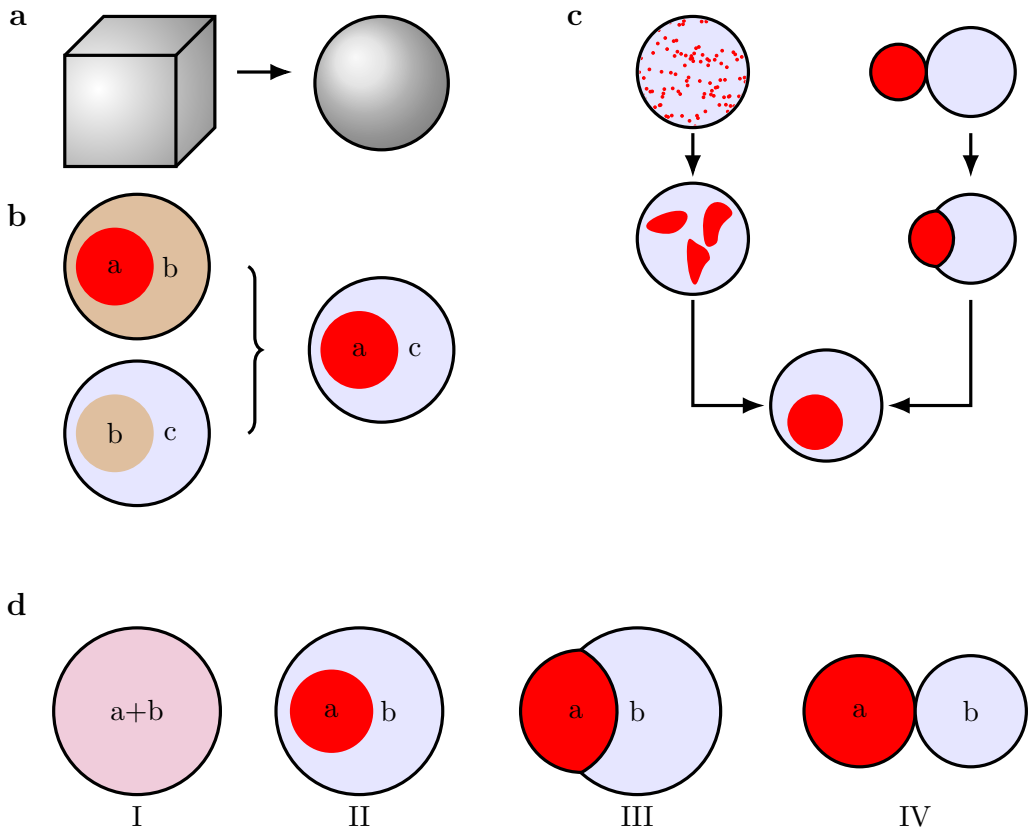

Figure 1.13: Illustrations for differential adhesion hypothesis (DAH) concepts. **a**: Rounding; the cells tend to form spherical shape to maximise binding energy. **b**: In a set of mutually immiscible phases, the tendencies of one phase to spread over another are transitive: if b spreads over a (i.e. b has lower surface tension, lower cohesivity) and c spreads over b, then c will tend to spread over a. **c**: Intermixed phases sort out by a process of coalescence, forming continuous externalising phase which envelops (to some degree) a discontinuous internalising phase. When the same phases touch together as separate masses, one spreads over another to approach the same configuration approached by sorting out of intermixed phases. **d**: Possible states of binary system depending on the homophilic (w_a,w_b) and heterophilic (w_ab) adhesion strength (i.e. cohesion and cross-adhesion). **I** $w_\mathrm{ab} > {}^{(w_\mathrm{a}+w_\mathrm{b})}/_2$, mixing of the two phases occurs, preferential cross-adhesion. **II** $w_\mathrm{b} < w_\mathrm{ab} < w_\mathrm{a}$, less cohesive phase envelops the more cohesive one, intermediate cross-adhesion. **III** $w_\mathrm{ab} < w_\mathrm{a} < w_\mathrm{b}$, less cohesive phase is partially engulfed by the more cohesive one, weak cross-adhesion. **IV** $w_\mathrm{ab} = 0$, complete sorting, no cross-adhesion.

Experiments in (Ramsey A. Foty and Malcolm S. Steinberg 2005) showed the surface tension for cadherins on L cell aggregates in the range (0.7–6) $\frac{\mathrm{nJ}}{\mathrm{nm}^2}$ for (25 000–225 000) cadherins per cell. The tissue surface tension dependence on the number of cadherins per

cell was roughly linear, with the rate of $0.023\,\frac{\mathrm{nJ}}{\mathrm{nm}^2\,\mathrm{k}\mathcal{M}}$[14]. With surface tensions roughly the same for each cadherin subtype and also for their aggregate. This supports the claim, that the segregation of cell populations expressing different cadherins cannot be ascribed to differences in cadherins' mutual affinities unless differences in the cadherins' expression levels, sufficient to cause such behaviour, are rigorously excluded (Ramsey A. Foty and Malcolm S. Steinberg 2005). The DAH was further supported by experiments covering rhombomere-boundary formation in zebrafish using loss-of-function experiments in (J. E. Cooke et al. 2005), suggesting that DAH acts in parallel with original Eph-ephrin repulsion model—Eph4A-expressing cells and ephrinB2-expressing cells repulse each other, and EphA4-expressing cells promote mutual (homotypic) adhesion within their rhombomere. The DAH was adapted as a continuous biological physics model in (Armstrong et al. 2006), where the population of discrete cells was generalised as cell density. The model computationally recreated the experimental observations and theoretical predictions, and for the first time replicated patterns shown in fig. 1.13d (in one and two dimensions). Lastly, (James A. Glazier and Graner 1993; Graner and James A. Glazier 1992) points out an analogy between cell tissue and soap bubbles and their dynamics; their extended Potts model confirms the predictions of the DAH, rounding, sorting and annealing. Relationships between adhesion modelling, biological cell-sorting, and geometrical models are reviewed in (Graner 1993; Graner and Sawada 1993).

Modifications of the DAH

The DAH has been shown, experimentally and computationally, to accurately model cellular aggregates and the interface effects (Ramsey A. Foty and Malcolm S. Steinberg 2005; Malcolm S Steinberg 2007). It is however important to keep in mind the differences between a cellular cluster and a liquid droplet; many of such differences were discussed in (Harris 1976), mainly (i) cells do not form a thermodynamically closed system, they produce energy, (ii) adhesive and attractive forces are not equivalent in cells, some of the adhesions are formed only after the surfaces have been brought together, (iii) following from the previous point, the work of de-adhesion is not a reversible work of adhesion, and (iv) intercellular contacts are not distributed homogeneously on the cell surface, but rather form focal points, so minimisation of total adhesive energy does not necessarily mean maximisation of total mutual contact area. In addition, a role of differential interfacial tensions in sorting was proposed in a local force equilibrium model (G. W. Brodland 2002; W. G. Brodland and H. H. Chen 2000) and computationally tested; the resulting predictions for cell population mixing, engulfing, partial spreading and segregation were reconciled with earlier experimental results. This approach extends the notion of cell from a point object and incorporates its mechanical energy, which depends on shape and cortical tension (contractility)(Manning et al. 2010).

The interplay of adhesion and contractility was treated by a minimal mechanical model (ibid.); energy for each cell was given by

$$W_{\mathrm{cell}} = \left(\beta - \frac{\gamma}{2}\right) P_C + \alpha P_C^2 + \beta P_{NC} \mid V = 1,\ \alpha > 0 \Leftrightarrow \gamma/\beta > 2$$

[14] $\frac{1}{\mathrm{k}\mathcal{M}}$ means per 1000 molecules

where P_C is the surface area of contact with other cell, P_{NC} the surface area without contact, α is a coefficient of restoring (phenomenological) force, β is the interfacial tension of cell-medium interface (dominated by myosin-generated cortical tension), and γ is the effective adhesion, incorporating all energetic contributions of adhesion (cadherins+associated actin network). The $V = 1$ is individual cell constant volume constraint (incompressibility, shear resistance). Effects of passive cortical elasticity (of actin network) and cadherin molecule recruitment to the site of adhesion (adhesion maturation) were neglected. Under the assumptions, the tissue surface tension σ is obtained from eq. (1.5). In numerical solution of the model for $\gamma/\beta < 2$, σ/β depends roughly linearly on γ/β, as compared to exactly linear relationship predicted by the DAH; individual cells tend to remain compact and the behaviour is dominated by the value of adhesion parameter (DAH). A crossover exists at $\gamma/\beta = 2$, when the adhesion starts to stretch the surface cells (optimally spread over 3 interior cells), and the system becomes regulated by a cortical restoring force (αP_C^2) (ibid.).

Some aspects of OS development (see sections 1.2.3 and 1.2.4) can be interpreted in the presented framework of DAH, even though such interpretation is only speculative. Axon fasciculation and sorting in the OS is, among many other factors, dependent on axon-axon adhesion (Schwarting and Henion 2011; Whitesides and LaMantia 1996). A cross-section of axon bundle can be understood as a two-dimensional aggregate of several cell types, for which the DAH predicts segregation and emergence of boundaries between heterotypical subpopulations (such effects are already emerging in the MM(A. M. Miller, Treloar, et al. 2010)). It has been observed (Imai et al. 2009) that during the A-P presorting, axons form a hierarchical central-lateral structure within axon bundle correlated with their A-P placement and presumably axon type (Nishizumi and Sakano 2015), which is consistent with σ-dependent enveloping predicted by the DAH. σ increases linearly with CAM expression levels(Ramsey A. Foty and Malcolm S. Steinberg 2005), simple type-dependent CAM surface density would therefore be sufficient to guarantee sorting of heterotypic axons into segregated bundles—specific composition of the CAMs is not necessary according to DAH. Lastly, DAH predicts specific final state for multitude of initial conditions. While this is easy to see for 2-type system, it might be less valid for the 1000-types OS. In spite, it is very likely that the differential adhesion plays a role in transition from stochastic OSN distribution of the OE to the highly conserved organisation of the OB (A. M. Miller, Maurer, et al. 2010).

1.6 Fasciculation modelling approaches

Various approaches can be taken to model axon fasciculation, focusing on the characteristics of fasciculating population (Chaudhuri, Borowski, Mohanty, et al. 2009; Chaudhuri, Borowski, and Zapotocky 2011) or GC dynamics under influence of chemical gradients (Hentschel and A. v. Ooyen 1999) for example. The aim of the models is usually to use well defined local (microscopic) biophysical equations to study global (macroscopic) features of the system. There are several drawbacks for axon fasciculation modelling, (i) the major one is considerable difficulty to model physics of filaments, particularly

in three-dimensional geometry (examples can be found in (Bergou et al. 2008; Camalet and Jülicher 2000; Lagomarsino et al. 2003; Lowe 2003; Wiggins and Goldstein 1998), or as a part of the thesis (Gauger 2005)), which becomes even more challenging, when (ii) interaction between filaments takes place (reviewed in (Barthel 2008), another examples in (Liu 2006; Zubler et al. 2009)), or (iii) substrate friction is involved (O'Toole, Lamoureux, et al. 2008). The following section will be therefore limited on the models focused on the most biophysically relevant aspects, simplifying the continuum and contact mechanics involved, but investigating the guidance and segregation processes.

1.6.1 Concepts of axon guidance modelling

As discussed in section 1.1.7, information in brain is often represented in the form of topographic maps. These maps usually connect two-dimensional input structure representing the outside world to a two-dimensional structure, where processing begins. Understanding the formation process of these maps during development helps to understand the computational functions of the brain structures in the adulthood. Mathematical models allow us to gain such insight: (i) they are more explicit than traditional biological models, (ii) allow for biophysical parameter range estimation, and (iii) often result in non-intuitive predictions. Historically, the models often helped to clarify crucial ideas. While the initial models (1970's) were more detailed and sophisticated, they were usually only one-dimensional, due to limited computational power. Over time, the models became more simple and specialised, attempting to explain isolated subsets of data.

While narrowing down the scope of the model can provide better understanding for particular mechanisms, it relaxes more general constraints on the system at the same time. Loosened limits on parameters and simplifications of underlying mechanisms then allow several modelling approaches to account for the same experimental data (Geoffrey J. Goodhill and Richards 1999; Simpson and Geoffrey J. Goodhill 2011). Such simplifications may include

1. reduced geometry (no complex *in vivo* geometry),
2. probabilistic rules for axon-axon interaction (no biophysics),
3. chemotaxis and growth as directed random walk (no mechanism for chemoaffinity, turning or GC advance),
4. ignoring branching or physical constraints (no competition for space).

A model addressing all the listed points in a simple way was proposed in (Simpson and Geoffrey J. Goodhill 2011). This model incorporates corrections to basic geometry, biophysical model for receptor-based axon-axon interaction and space competition, chemoaffinity and branching. Model's ability to replicate experimental data across a variety of circumstances (i.e. experimentally manipulated development) depended heavily on graded interaction of multiple constraints posed by the listed items. Several illustrative models will be presented in detail in the following sections; a detailed historical review of axon guidance modelling can be found in (Geoffrey J. Goodhill and Xu 2005).

1.6.2 Models of single axon growth

Explicit treatment of axon-axon interactions can be neglected in some models of nervous systems, particularly in systems dominated by guidance cues or physical constraints. The following works model development of populations of axons in such systems and are a suitable illustration of single axon growth modelling. In (Borisyuk, T. Cooke, et al. 2008), a simple model of axon growth was proposed. The authors formulated a mathematical model to simulate the growth of axons in the spinal cord of *Xenopus* tadpole. The model aimed simplicity, using only minimal number of parameters (e.g. implicit fasciculation, phenomenological chemoaffinity). Particular care for choice of parameters is crucial in modelling in general, as it helps to separate the studied problem into major components and quantify their respective contributions. This work also illustrates some generic, often recurring, ideas of axon modelling. It imposes only a small number of basic biological rules (no explicit guidance cue gradient, no cell-cell recognition) and combines deterministic and stochastic terms to describe axon dynamics (common for models in this section).

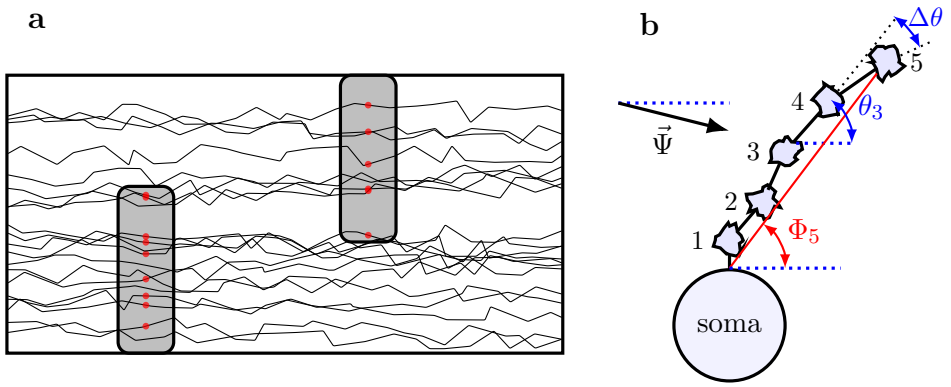

Figure 1.14: **a**: The axons are initiated at a random location on the left and grow towards the right side, according to eq. (1.6) (this picture is only illustration). With probability obtained from experimentally obtained PDF, each neuron may form a synapse, marked by a red circle, with dendrites on particular locations (marked by the grey boxes). **b**: The GC grows in steps from the soma, at each time step, it follows angle $\theta(t)$, which is influenced by the general GC direction $\Phi(t)$, the outer gradient $\vec{\Psi}$ and a stochastic component ξ, according to the eq. (1.8).

In the implementation, axons are initiated on one side of a rectangular area (representing *Xenopus* spinal area), grow with small stochastic changes to their orientation (ξ), and form synapses with dendrites (dendrites are static) with a probability given by an experimentally obtained PDF, see fig. 1.14a. Horizontal (longitudinal, rostro-caudal) axis is labelled x, the vertical (D-V) axis is labelled y, the angle of GC orientation θ is

measured from the x axis. The system of the governing difference equations is

$$\begin{aligned} x_{n+1} &= x_n + \Delta\cos(\theta_n) \\ y_{n+1} &= y_n + \Delta\sin(\theta_n) \\ \theta_{n+1} &= (1-\gamma)\theta_n + \mu(\bar{y} - y_n) + \xi_n, \end{aligned} \tag{1.6}$$

where Δ is the length of iterative step, γ represents tendency of the GC to align with the longitudinal x axis (implicit guidance cue effect), $\bar{y}$ is the attractor location steering GCs away from the system boundaries (effectively representing D-V gradients of repellent signals, fasciculation or attractive guidance cues) and μ is the strength of this attraction, finally ξ is the stochastic component.

This minimalistic model captures the basic features of axon growth in the system, even though some are accounted for only implicitly (e.g. gradients, fasciculation). The parameters were optimised so that the model-generated population had D-V distribution of axons very close to the experimentally measured histogram. This growth model was applied to reconstruct a connectome of the *Xenopus* tadpole spinal cord involving several types of neurons (Borisyuk et al. 2011); biological experimental data were used to assign initial distributions of cells bodies, dendrite and axon lengths. A large connectome of >100 000 synapses was generated with statistical properties closely matching the experimental data of individual neuron types, while neural network connectivity graph properties were similar to those of experimental neural network of *Xenopus* as well as different animals.

Major oversimplification in the original model (Borisyuk, T. Cooke, et al. 2008; Borisyuk et al. 2011) was no explicit treatment of chemotaxis. The modelled axons of *Xenopus* tadpole spinal cord do not appear to grow towards a particular target, but rather form synapses along their shafts—this makes their whole growth pathway a crucial aspect of any connectome model (Borisyuk et al. 2014; Roberts, Conte, et al. 2014). The authors therefore modified the eq. (1.6) for GC deviation angle θ to explicitly depend on guidance cue gradients:

$$\begin{aligned} \theta_{n+1} =& \theta_n \pm g_R(x_n, y_n)\sin\theta_n - \\ &- \left[g_D(x_n, y_n)e^{\beta_D(y_n - y_D)} - g_V(x_n, y_n)e^{-\beta_V(y_n - y_V)}\right]\cos\theta_n + \xi_n, \end{aligned} \tag{1.7}$$

where $g_R(x,y)$, $g_D(x,y)$ and $g_V(x,y)$ are GC sensitivities to rostral, dorsal and ventral cue gradients respectively, they are spatially dependent and neuron type specific. The gradients themselves are described by a decaying exponential function with rates β_D and β_V ($\beta > 0$), and sources at system dorsal and ventral borders y_D and y_V ($y_V \le y_n \le y_D$). The rostro-caudal gradients are replaced by a simple polarity in this model, '+' or '−' sign determines ascending or descending direction of axon growth (neuron-specific sensitivity). The functions representing the GC cue sensitivities $g(x,y)$ can be easily formulated to switch between attractive and repulsive response, depending on a particular GC location (x,y), or to adapt to different developmental stages. The 3 sensitivity parameters $g(x,y)$ and the stochastic parameter ξ were estimated by optimisation procedure, during which the statistics of model generated connectome were compared to the statistics obtained from experimental data (Borisyuk et al. 2014).

The neural signalling in the model-generated connectome (ibid.) was analysed in (Roberts, Conte, et al. 2014). It has been shown that a proper stimulation generates a regular motor activity (swimming), as observed in experimental conditions. The model therefore demonstrates, that a set of simple rules and initial conditions (i.e. soma position, initial turning angle θ, final length) which generates the connectome without neuron identity recognition or synapse refinement, is sufficient to produce a functional model of *Xenopus* spinal cord (ibid.). In all the models, the effect of guidance cues is implemented on high level, there is no model of detection at the GC site and no quantification of guidance molecules propagation.

Conceptually similar model was formulated in (H. Nguyen et al. 2016). It treats turning of a GC in constant external gradient $\vec{\Psi}$, growing from the soma—slope of the line between the anchor point on the soma and the GC is labelled Φ, illustration is shown on the fig. 1.14b. The dynamics of the GC is then determined by

$$\Delta\theta(t) = \underbrace{a\angle\left(\Phi(t), \theta(t)\right)}_{\text{direction persistence}} + \underbrace{b\angle\left(\vec{\Psi}, \theta(t)\right)}_{\text{gradient steering}} + \underbrace{\xi}_{\substack{\text{stochastic} \\ \text{term}}} \tag{1.8}$$

which is closely similar to the eq. (1.6). The angle symbol $\angle$ determines a signed angle between the two arguments, in the range $(-\pi, \pi)$, i.e. $\angle(\Phi, \theta) = \Phi - \theta$, if $\theta < \Phi$, then $\Delta\theta > 0$ and θ increases, and vice versa. In the first term of eq. (1.8), coefficient a scales the strength of axons persistence, acting to align current GC direction θ with general axons direction Φ, similar to the eq. (1.6) term with γ. In the second term, coefficient b scale the strength of the response to the constant gradient $\vec{\Psi}$, similar to the eq. (1.6) term containing $\bar{y}$. Finally, both eqs. (1.8) and (1.6) contain practically identical stochastic term ξ.

The model represented by the eq. (1.8) was used in combination with experiments in (ibid.) to demonstrate the persistence of axon bearing in the environment of gradient follows a power law, $\Phi(t) \propto t^{\alpha-1} = t^{-b/(a+b)}$, corresponding to the observed GC turning saturation over time. The work further showed that the AS very efficiently straightens between the GC and the anchor point (impaired with increasing stochastic component) which is an important assumption in the modelling presented in the results section of this thesis.

Simple, phenomenological models as presented in this section were used to study network architecture, distribution of synaptic inputs (Borisyuk, T. Cooke, et al. 2008), characteristics of connectome (Borisyuk et al. 2014), electrical activity pathways (Roberts, Conte, et al. 2014), GC turning saturation (H. Nguyen et al. 2016), or stochastic and deterministic behaviour of a GC (Maskery et al. 2004). On the down side, however, they do not attempt to address features of axons with respect to the biophysical details (e.g. no diffusion equation, no viscoelasticity of the AS, no GC chemoaffinity, implicit modelling of bundling). The following models expanded the premises of these formulations to answer questions regarding the mechanism of action.

1.6.3 Modelling growth cone gradient detection

Shortcoming of phenomenological treatment of GC chemotaxis were addressed in a classical paper (Berg and Purcell 1977), the paper proposed a biophysical model of chemotaxis mechanisms, which were further analysed in (G. J. Goodhill and Urbach 1999). The model assumes a spherical GC of diameter a uniformly covered by N receptors which interact with diffusible ligand of local concentration ρ, the concentration fluctuates in the GC vicinity with standard deviation $\Delta\rho_{\text{noise}}$. The functional dependent of fractional noise on number of ligand molecules m in the GC vicinity can be estimated as $\Delta\rho_{\text{noise}}/\rho \sim 1/\sqrt{m}$ at any given instance, and can be reduced by averaging over M measurements by a factor $\sim 1/\sqrt{M}$. In (Xu et al. 2005), optimal time averaging period in real axons was estimated as T=3 min. While longer time averaging decreases noise level monotonously, too long averaging could perpetuate an accidental bias formed on the GC. Similarly, a spatial averaging across the GC decreases the input noise, while too large averaging distance would impair detector's directional sensitivity; optimal averaging length was estimated as $1/3\,a$ (ibid.).

The analysis shows (G. J. Goodhill and Urbach 1999) that GC sensitivity is less influenced by the number of receptors (for $N \gtrsim 10\,000$) or variability of GC size a, but increases significantly with the averaging time of measurement T. It also indicates that spatial concentration gradient detection (i.e. $\propto \rho(x_1(t_0)) - \rho(x_2(t_0))$) is typically preferred *in vivo* over temporal mechanism (i.e. $\propto \rho(x(t_1)) - \rho(x(t_2))$)—temporal mechanism would result in less smooth GC path than indicated in experiments. For typical biological values, the analysis (ibid.) predicts minimum detectable gradient in range 0.5–10 %, while the maximum guidance distance from the source at the order $x_{\max} \sim 1$ cm. It also shows that optimally shaped concentration dependence on distance from the source, $\rho(x)$, is a convex function; detection is not possible above certain concentration threshold $\rho_{\max} \approx 10\text{–}100\,\rho_{\frac{1}{2}}$ (at $C = C_{\frac{1}{2}}$, 1/2 of GC receptors are occupied), and a steeper gradient is necessary if concentration becomes low (ibid.). Finally, it has been proposed, that filopodia actively assist gradient sensing, averaging stochastic response to the gradient, their distribution becomes asymmetric shortly after gradient emerges and the GC apparently attempts to extend new filopodia in the direction of the maximum concentration of the chemotropic factor (which facilitates turning). More detailed analysis of the role of filopodia can be found in (G. J. Goodhill, Gu, et al. 2004).

1.6.4 Guidance and bundling

Concise introduction to biophysically more complete models of axon guidance and bundling can be found in (Hentschel and A. v. Ooyen 1999). The authors formulated and computationally implemented a detailed biophysical model of axon chemotaxis and GC-AS contact interaction. The work provided an insight into viability of particular dynamics being driven by contact and diffusible agents; initially scattered axon GCs first form fascicles, extend bundled towards the target location, and finally de-bundle prior the final innervation. The model considers

1. an exclusively diffusible version—only chemoattractant and chemorepellant gradi-

ents are dispersed from the environment and the GCs, and

2. a contact version—single target secrets attractive guidance gradient, complemented by GC-AS contact interaction.

Diffusible GCMs are released from the source location and spread according to diffusion equation of substance with limited lifetime (i.e. the GCMs are degraded). The full time-dependent diffusion equation has the form

$$\frac{\partial \rho_\mu}{\partial t} = \underbrace{D_\mu \triangle \rho_\mu}_{\text{diffusion}} - \underbrace{\delta_\mu \rho_\mu}_{\text{decay}} + \underbrace{S_\mu(\vec{r},t)}_{\text{sources}}, \tag{1.9}$$

where $\rho_\mu = \rho_\mu(\vec{r},t)$ is concentration of chemical μ, D_μ is its diffusion constant, δ_μ is its decay rate constant and S_μ is the source term. For simplicity, source is assumed to be a set of point sources, i.e. $S_\mu(\vec{r},t) = \sum_i \sigma_\mu(\{\rho(\vec{r}_i,t)\})\delta(\vec{r}-\vec{r}_i)$, where δ now is Dirac delta function, σ_μ is release rate and $\vec{r}_i$ is release point (i.e. target location or a GC). In the quasi-steady state ($\dot{\rho}_\mu = 0$), the eq. (1.9) takes form

$$[\triangle - \kappa_\mu^2]\rho_\mu = -\frac{S_\mu(\vec{r},t)}{D_\mu}, \tag{1.10}$$

where $\kappa_\mu = \sqrt{\delta_\mu / D_\mu}$ is inverse diffusive length for chemical μ. Finally the equation of motion of a GC α is simply a sum of influences of all relevant cue gradients μ multiplied by appropriate (attractive $\oplus$ or repulsive $\ominus$) rates of growth λ_μ (cf. sensitivities $g(x,y)$ in section 1.6.2, and eqs. (1.7) and (1.6)), that is

$$\dot{\vec{r}}_\alpha = \sum_\mu \lambda_\mu^{\oplus} \nabla \rho_\mu(\vec{r}_\alpha,t) - \sum_\mu \lambda_\mu^{\ominus} \nabla \rho_\mu(\vec{r}_\alpha,t). \tag{1.11}$$

The functional form of ρ_μ and $\nabla\rho_\mu$ (cf. section 1.6.3) can be obtained using Green functions; explicit results can be found in the Appendix A of (ibid.).

Strictly diffusible model

The first version of the model considers three types of diffusible signals of particular release rates σ_μ, diffusion constant D_μ and spatio-temporal concentration $\rho_\mu(\vec{r},t)$, (i) a chemoattractant released by the target guiding the GCs (ρ_{target}); (ii) a chemoattractant released by other GCs facilitating bundle formation (ρ_{GC}), or filopodia extending from the GC (with GCMs on the surface); and (iii) chemorepellant released by the GCs facilitating de-bundling (ρ_{rep}); its release is however triggered only in a proximity of the target (i.e. $\sigma_{\text{rep}} = \sigma_{\text{rep}}(\rho_{\text{target}})$). In the (ibid.), the functional dependence of chemorepellant was determined by Michaelis-Menten relationship (Michaelis and Menten 1913),

$$\sigma_{\text{rep}}(\rho_{\text{target}}) = \sigma_{\text{rep,max}} \frac{\rho_{\text{target}}^m}{\rho_{\text{a}}^m + \rho_{\text{target}}^m} \mid \rho_a : \sigma_{\text{rep}}(\rho_a) = \frac{\sigma_{\text{rep,max}}}{2}, \tag{1.12}$$

where $\sigma_{\text{rep,max}}$ is the maximal rate of release, and m is Hill coefficient (mostly $m = 2$ in the work). The dynamics of the axons is given by the eq. (1.11).

Contact model with guidance

The second version combines the target-released GCMs (ρ_{target}) and contact (short-range) interactions between the axons mediated by CAMs (treated probabilistically). In this model, the GCs do not secrete any diffusible molecules themselves ($\sigma_{\text{GC}} \equiv 0$), the initial contact between the axons is facilitated by random component of axon GC movement (term $\vec{\xi}$ in eq. (1.13)) or possibly 'pushed together' by external repelling gradients (see section Fasciculation). The eq. (1.11) takes the form (involving only attractive response to gradient $\lambda^{\oplus}$)

$$\dot{\vec{r}}_\alpha = \lambda^{\oplus} \nabla \rho(\vec{r}_\alpha, t) + \vec{\xi}_\alpha(t), \tag{1.13}$$

where $\vec{\xi}_\alpha$ is the stochastic component of GC α. The probability of bundling of axons in contact, P_b, is given by equation (similar to eq. (1.12) but decreasing with ρ_{target})

$$P_b = P_{b,\max} \left[1 - \frac{\rho_{\text{target}}^k}{\rho_b^k + \rho_{\text{target}}^k} \right] \mid \rho_b : P_b(\rho_b) = \frac{P_{b,\max}}{2}.$$

De-bundling probability P_d of axons in contact is given by the Michaelis-Menten relationship, eq. (1.12), which increases with target guidance cue concentration ρ_{target}. As a bundle aggregates more axons, its random movements decrease: assuming individual GC random movements (i.e. GC traction force variations) are normally distributed (e.g. caused by substrate variations), then average effective random force on the bundle will scale as $1/\sqrt{n}$, where n is the number of axons in the bundle (Hentschel and A. v. Ooyen 1999).

Model versions comparison

The first version of the model (section Strictly diffusible model) shows more robust bundling. The gradients brought axons naturally together and formed a bundle (initial distribution of GCs was dense as compared to the chemoattractant length scale), which also smoothly defasciculated after getting to the proximity of the target and activation of repellant, ρ_{rep}. Note, that attractive gradients originating from individual targets, $\nabla\rho_{\text{target}}$, are small compared to a bundle width w (i.e. $\nabla\rho_{\text{target}} \cdot w \ll 1$), their effect is nearly the same on all the GCs in the bundle, and cannot (for reasonable range of parameters) facilitate de-bundling—this points to the crucial role of the repulsive GCMs, ρ_{rep}, because simple deactivation of attraction between axons ($\lambda^{\oplus}_{\text{GC}} \to 0$) would be insufficient. This version of the model is also robust, if a small stochastic component $\vec{\xi}$ is added. On the other hand, the pure gradient driven model is sensitive to deviations from optimal sensitivity/gradient combination $[\lambda\nabla\rho]_{\text{opt}}$. If $\lambda_{\text{target}}\nabla\rho_{\text{target}} \ll [\lambda\nabla\rho]_{\text{opt}}$, axons have tendency to form random clusters, conversely, if $\lambda_{\text{target}}\nabla\rho_{\text{target}} \gg [\lambda\nabla\rho]_{\text{opt}}$, axons grow orderly towards targets, without tendency to fasciculate; cf. biophysical limitations of gradient detection discussed in section 1.6.3 (G. J. Goodhill and Urbach 1999; Hentschel and A. v. Ooyen 1999).

The second version of the model (section Contact model with guidance) shows poor initial bundle formation; some improvement might be possible with repulsive gradients from

ECM pushing the axons together or larger stochastic movement $\vec{\xi}$ (which however disrupt local topographic ordering). An interesting feature is spontaneous emergence of pathfinding axons—unbundled axons have larger stochastic component (bundle's $\vec{\xi}_{\text{bundle}} \sim {}^{1}/\sqrt{n}$, see above), which brings them with higher probability to the steeper target guidance gradient ($\nabla\rho_{\text{target}}$). Other axons become attached to the pioneer axons by the contact interaction (with probability $P_b \sim {}^{1}/\rho_{\text{target}}$) and follow them to the target location. Similarly to the previous version, individual attractive target gradients ($\nabla\rho_{\text{target}}$) at the target location are not able to sufficiently separate the bundle, even if contact attraction is deactivated ($P_d = 1, P_b = 0$). Obviously, repulsive contact interaction would not drive defasciculation over the wide area of necessary innervation. And because higher stochastic component would disrupt topographical ordering, it seems unavoidable that pre-target de-bundling depends on diffusible agents (ρ_{rep}) (Hentschel and A. v. Ooyen 1999).

Arjen van Ooyen and Johannes Krottje later greatly generalised the mathematical framework covered in this section in a beautiful and extensive review (Krottje and A. v. Ooyen 2006), covering the general framework, mathematical modelling and numerical methods with examples. To provide a very short comment, they extended the model by GC state other than just position $\vec{r}$.

$$\begin{pmatrix} \vec{r} \\ \vec{s} \end{pmatrix} = \begin{pmatrix} G^r(t) \\ G^s(t, \rho_1(\vec{r},t), \nabla\rho_1(\vec{r},t), \ldots, \rho_m(\vec{r},t), \nabla\rho_m(\vec{r},t)) \end{pmatrix}, \tag{1.14}$$

where $\vec{s}$ can represent GC sensitivity, geometry, internal state or production rates. ρ are concentration fields as before, governed by eqs. (1.9) and (1.10). The review provides tools to treat non-steady-state fields and non-point field sources or environment with forbidden areas (i.e. holes).

The models of this section treat carefully biophysical concepts of diffusion or GC-AS interaction of the deterministic growth factors and preserve the stochastic component ($\vec{\xi}$), while attempting to simulate more realistic environment geometry. Neither of these works ((Hentschel and A. v. Ooyen 1999; Krottje and A. v. Ooyen 2006)) however explores in detail the global axon population's statistics emerging from the well-defined local biophysical rules. The approach outlined in the following section addresses these points.

1.6.5 Path aggregation

Axon targeting and bundle formation can be likened to the process of path aggregation, common in basin formation, insect pheromone trail formation, formation of pedestrian trails or aggregation of liquid droplets on the window pane. There are two approaches to the problem, (i) active walker model, where the walker introduces local changes to the system, as she passes through; other (later) walkers are then influenced by these changes, (ii) models dealing with non-interacting random walkers moving through a fluctuating environment (e.g. the river formation model). A common feature in path aggregation phenomenon is path decay. Over a period of time, the established path may be removed from the system, gradually or abruptly (Chaudhuri, Borowski, Mohanty, et al. 2009).

Onwards, only active walker models will be of our interest, well covered in (Helbing, Keltsch, et al. 1997; Helbing, Schweitzer, et al. 1997). These models allow, through the

$$\text{walker} \Rightarrow \text{environment} \Rightarrow \text{other walker}$$

influence scheme, emergence of nonlinear feedback and spatial self-organisation. The trail formation can be described within a stochastic framework. The walkers are continuously changing their environment by leaving markings while moving. These markings can be described by a potential $G(\vec{r},t)$, which has local durability lifetime $T(\vec{r})$, a ground state to which it relaxes $G_0(\vec{r})$, and the source components (walkers). The motion of a walker α at her current position $\vec{r}_\alpha$, is given by the Langevin equation

$$\frac{d^2\vec{r}_\alpha(t)}{dt^2} = \frac{d\vec{v}_\alpha}{dt} = \underbrace{-\gamma_\alpha \vec{v}_\alpha(t)}_{\text{friction force}} + \underbrace{\vec{f}_\alpha(t)}_{\substack{\text{deterministic} \\ \text{force}}} + \underbrace{\sqrt{2\epsilon_\alpha\gamma_\alpha}\vec{\xi}_\alpha(t)}_{\text{stochastic force}}, \tag{1.15}$$

where $\vec{v}_\alpha$ is the actual velocity of the walker, $\gamma_\alpha = {}^1/_{\tau_\alpha}$ represents friction coefficient determined by relaxation time τ_α. The last term represents stochastic force, ϵ_α is the intensity of the force and $\vec{\xi}_\alpha$ the direction, which is often assumed to be Normally distributed. $\vec{f}_\alpha$ is deterministic influence given by the intentions of the walker and interactions with other walkers.

We can consider several simplifications:

1. Only walker-trail interaction, walkers do not interact with each other, then $\vec{f}_\alpha = \frac{v_\alpha^0}{\tau_\alpha}\vec{e}_\alpha(\vec{r}_\alpha,\vec{v}_\alpha,t)$, v_α^0 is desired speed and $\vec{e}_\alpha = \vec{e}_\alpha(G(\vec{r},t),\vec{r}_\alpha,\vec{v}_\alpha)$ is the desired direction expressed as a function of the potential.
2. Homogeneous ground potential (e.g. $G_0 \equiv 0$), initial marking trails are formed arbitrarily, either randomly (e.g. ants searching for food) or towards a particular destination (e.g. axon attracted towards the OB), then marking potential $G(\vec{r},t)$ can be decomposed into target attraction potential $U_\mu(\vec{r})$ and attraction potential of trails $V(\vec{r},t)$ (cf. $\nabla\rho_{\text{target}}$ and $\nabla\rho_{\text{GC}}$ in section 1.6.4). The direction vector becomes $\vec{e}_\alpha(\vec{r}_\alpha,\vec{v}_\alpha,t) \propto \nabla[U+V]$.
3. Relaxation time scale τ_α is much shorter than the time scale of marking potential change $\tau_\alpha \ll T$.

The equation of motion eq. (1.15) can be simplified into

$$\begin{aligned}\dot{\vec{r}}_\alpha = \vec{v}_\alpha(\vec{r}_\alpha,t) &\approx v_\alpha^0\vec{e}_\alpha(G(\vec{r},t),\vec{r}_\alpha,\vec{v}_\alpha) + \sqrt{2\epsilon_\alpha\tau_\alpha}\vec{\xi}_\alpha(t) \\ &\approx v_\alpha^0\frac{\nabla[U+V]}{|\nabla[U+V]|} + \sqrt{2\epsilon_\alpha\tau_\alpha}\vec{\xi}_\alpha(t)\end{aligned} \tag{1.16}$$

Particular forms of the $\vec{e}_\alpha$ and macroscopic formulation of the path formation problem can be found in (Helbing, Schweitzer, et al. 1997).

Basic active walker model

A model of GC-mediated axon fasciculation was developed in (Chaudhuri, Borowski, Mohanty, et al. 2009), where paths (trails) represent axons or axon bundles and the

GCs advance by directed random walk on a discrete grid, i.e. walker coordinates (x, y) have integer values. It belongs to the category of active walker models with attractive interaction and abrupt decay (probabilistic instant trail removal). The interaction does not happen directly between the walkers (GCs), but each walker interacts with a trail of another walker (AS), see fig. 1.15a. The walkers are initiated randomly at the base ($y = 0$, x is uniform random) with a given birthrate α, and advance towards larger y, making left or right steps on the tilted lattice (fig. 1.15a), i.e. $(x-1, y+1)$ or $(x+1, y+1)$ respectively. The decision to turn left or right depends on the occupancy at the prospect sites and their nearest neighbouring sites, labelled *1*, *2*, *3* and *4* in fig. 1.15a. The walkers move left or right with equal probabilities if both sites are equal (i.e. occupied or not), but always prefer occupied site over unoccupied. If two distinct walker trails (AS) are not separated by an unoccupied lattice site, they are considered to be part of a single fascicle (at the given y coordinate).

The work of (ibid.) can be explained in the general active walker framework presented in the section Path aggregation (Helbing, Schweitzer, et al. 1997). The model satisfies the conditions of simplified eq. (1.16), the equation needs to be rewritten into model's discrete formulation illustrated in fig. 1.15a. Trail marking distribution $\rho(x, y, t)$ is discrete binary function,

$$\rho(x, y, t) = \begin{cases} 0 \mid \text{if no trail is present,} \\ 1 \mid \text{if trail is present, no matter how many axons.} \end{cases}$$

The desired velocity magnitude for each walker μ is constant and uniform $v_\mu^0 \equiv v$, $\forall\mu$. The direction parameter $\vec{e}_\mu(\rho(x, y, t), (x, y)_\mu) \propto \nabla[U + V^{(\mu)}]$ depends on the target potential $U(x, y)$, and trail marking potential $V(x, y, t; y_\mu(t))$. Using the coordinate system as illustrated in fig. 1.15a, the y component of direction parameter $[\vec{e}_\mu]_y = \frac{1}{\sqrt{2}} \binom{0}{1}$ corresponds to target potential $U(x, y) = y$. The x component $[\vec{e}_\mu]_x = \frac{1}{\sqrt{2}} \binom{\pm 1}{0}$ depends on the trail potential on the discrete lattice (see fig. 1.15a) given as

$$V(x, y, t; y_\mu(t)) = \sum_{\substack{\Delta x = \\ \{-2,0,2\}}} \sum_{x,y} \delta_{x,x+\Delta x}\, \delta_{y,y_\mu+1}\, \rho(x, y, t),$$

where δ is Kronecker delta, and parameter $y_\mu(t)$ is the current y position of walker μ, to forbid backtracking. For example, the potential value at point *2* in fig. 1.15a is determined by marking distribution values at points *1*, *2* and *3*. Because the walkers advance in y direction independently of $V^{(\mu)}$, we can replace $\nabla V^{(\mu)} \to \frac{\partial}{\partial x} V^{(\mu)}$, which can be in turn discretised into a difference, i.e.

$$\begin{aligned} \frac{\partial}{\partial x} V(x, y, t; y_\mu(t))|_{(x_\mu, y_\mu)} &\approx V(x_\mu + 1, y_\mu + 1) - V(x_\mu - 1, y_\mu + 1) \\ &= \rho(x_\mu + 3, y_\mu + 1) - \rho(x_\mu - 3, y_\mu + 1), \end{aligned}$$

which yields either -1, 1 or 0. If $\nabla V|_{(x_\mu, y_\mu)} = 0$, the advance in x direction is determined by a stochastic term, $\frac{1}{\sqrt{2}}(1 - |\nabla V^{(\mu)}|)\vec{\xi}$, where the stochastic component $\vec{\xi} = \binom{\pm 1}{0}$ has

either of the two values (± 1) with equal probability (cf. eq. (1.16)). Combining the results

$$\vec{v}_\mu(x_\mu, y_\mu, t) = \frac{v}{\sqrt{2}} \begin{pmatrix} \rho(x_\mu + 3, y_\mu + 1) - \rho(x_\mu - 3, y_\mu + 1) \pm (1 - |\nabla V^{(\mu)}|) \\ 1 \end{pmatrix}. \quad (1.17)$$

Which is the equation corresponding to the choice process described in the first paragraph of the section Basic active walker model (Chaudhuri, Borowski, Mohanty, et al. 2009).

The local selection rule given by the eq. (1.17) gives rise to global features of the trail network and emerging global dynamics. In this model (ibid.), the trails are removed from the system instantly (i.e. within one iteration) at decay rate β, which is related to average axon lifetime as $T = 1/\beta$. No other type of reorganisation takes place in the network, besides the decay (at rate β) and birth (at rate α); the trails of living axons are immutable. The axon turnover is therefore the mechanism allowing emergence of the population steady state dynamics on larger timescales, which is presented in detail in the rest of this section. The turnover-driven steady state is reminiscent of the changes occurring in the mammalian OS, where OSN axons are extensively removed and new axons grown during the animal adult life (Farbman 1994; P. P. C. Graziadei and G. A. M. Graziadei 1979; Nedelec et al. 2005).

The birthrate α and the decay rate β determine the steady-state number of axons in the system, $N(y) = N_0 \exp(-\beta y)$, where $N_0 = \alpha/\beta$ is occupancy at the base ($y = 0$) at the steady state, so that $\alpha = \beta N_0$. The presence of turnover means the y-coordinate cannot be viewed as equivalent to time and the dynamics at fixed y has no analogy in one dimensional models of aggregation or coalescence. With increasing y, axons aggregate into a decreasing number of fascicles $m(y)$, containing on average $\bar{n}$ axons. In the mean-field approximation, each of the m fascicles collects axons from the base section $D \sim L/m \simeq L\bar{n}/N$, where L is the length of the base, see fig. 1.15b. Two random walkers from the opposite sides of the interval D will meet at $y \simeq (D/2)^2$. Then the power law can be obtained supposing $y \ll (L/2)^2$ (i.e. system is far from complete fasciculation) and $\beta y \ll 1$ (most of the axons survived to this level) in a form $\bar{n} = D\rho \exp(-\beta y) \simeq 2y^{1/2}\rho$, where $\rho \sim N_0/L$ is axon density at the base. This approximative prediction was supported by the results of numerical simulations (Chaudhuri, Borowski, Mohanty, et al. 2009).

Over the long time scale, the model predicts very durable autocorrelation of the $\bar{n}(t)$, $c(t) = \langle \bar{n}(t), \bar{n}(0) \rangle$. The correlation time τ_c increases with y and significantly exceeds individual axon lifetime T. Consequently, the fascicles at the given y are very stable and lose axons only by their death (decay) at rate $u_- = \beta n$, conversely they gain nascent axons originating in their basin (D, see fig. 1.15b) and some from interbasin gap (E in fig. 1.15b) at the $u_+ = \alpha D/L + (\alpha E/L)[1 - \Pi(E, y)]$, where $\Pi(E, y)$ is the probability that an axon born within the gap of size E survives as a single axons at the level y. The dynamics of a fascicle is fully characterised by the number of axons $n(t)$ and the basin size $D(t)$. It can be shown that the two are correlated and that the basin size grows linearly with the number of axons $D = S(n - 1)$ where S is time-independent average inter-axon separation. Under this assumption, it turns out that the gain rate can be approximated by a polynomial expansion $u_+(n) = a_+ + b_+ n - c_+ n^2$, where the quadratic term represents a saturation effect of the limited size of D (ibid.).

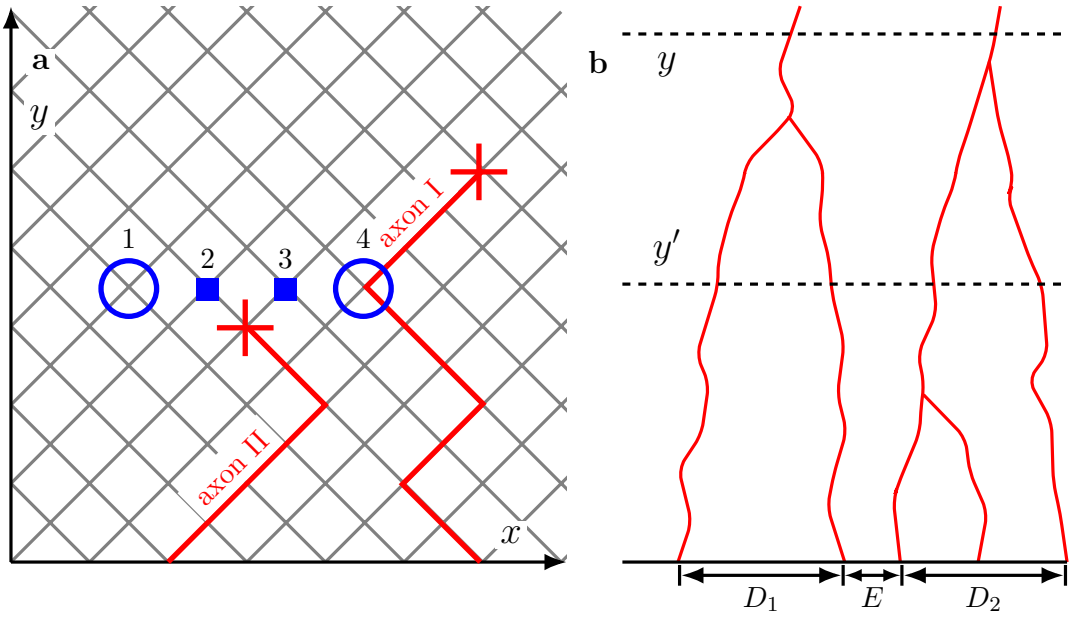

Figure 1.15: **a**: Illustration for active walker model. Axon I pioneers the way and its shaft lays the preferred trail. Axon II is later preferably attracted to the site closer to the existing trail (i.e. right). **b**: Illustration of basin formation. The two fascicles at the level y originate from two basins, D_1 and D_2. Any axon born in the basin is bound to join the fascicle. On contrary, axons born in the interbasin gap E may eventually join either of the fascicles. To give an example, for the level y the average number of axons in a fascicle is $\bar{n}(y) = 2.5$, while $\bar{n}(y') = 1.25$.

For the dynamics of a single fascicle as proposed, three different timescales emerge. Near the macroscopic stationary point $n_\mathrm{s}[u_+(n_\mathrm{s}) = u_-(u_\mathrm{s})]$, the fascicle size n correlation time $\tau = {}^1\!/\!_{(u'_-(n_\mathrm{s}) - u'_+(n_\mathrm{s}))} = {}^1\!/\!_{(\beta - b_+ + 2c_+ n_\mathrm{s})}$ (involving the quadratic saturation term), arising from the competition of neighbouring fascicles for the basin space. The linearised time scale (i.e. without the saturation effect) of approach to the steady state $\tau_\mathrm{ap} = {}^1\!/\!_{(\beta - b_+)}$. And the third time scale reflects the turnover of fascicles in the full system τ_f (ibid.).

Extended active walker model

Model of (ibid.) was further generalised and extended in (Chaudhuri, Borowski, and Zapotocky 2011). The population of axons (paths) was divided into subpopulations of particular type and the attractive interaction between the path and the GC was taken as finite in strength. In the lattice models, the range of interaction can be understood as the GC filopodia range of extension (roughly 10 µm). In this model, the interaction are additive and type-specific; a weaker nearest neighbour heterotypic interaction with negative binding energy $E_o < 0$ and stronger homotypic interaction $E_h < E_o$. Axon attempts an advance left or right with equal probabilities ½. The left move (and analogically for

the right) is accepted with the probability $p_L = \min(1, e^{-\delta E_l})$ where

$$\delta E_l = [n_h(x-3, y+1) - n_h(x+3, y+1)]E_h + [n_o(x-3, y+1) - n_o(x+3, y+1)]E_o = -\delta E_r,$$

where n_o and n_h denote the occupancy of the site by axons of different or the same type (as the walker) respectively; compare with eq. (1.17). Note that if the axon moves left, its energy is determined by the sites $E_L = E_1 + E_2 + E_3$ in the fig. 1.15a, while moving right, it is $E_R = E_2 + E_3 + E_4$—calculating the difference (i.e. δE_l) eliminates the contributions from the shared sites *2* and *3*. Also note that as compared to the previous model, (Chaudhuri, Borowski, Mohanty, et al. 2009), this model's GC decision process depends on the number of axons in the neighbouring bundles (i.e. site occupancies n_o and n_h).

Under the extended model, axon is not irreversibly fascicle-bound, the leaving step (Monte-Carlo attempted with probability ½) might be accepted even if the proposed energy change is $\delta E > 0$, with probability $p = e^{-\delta E}$. For a homogeneous population, a growing detachment rate (decreasing $|E_h|$) leads to decreasing time scale of approach to the steady state τ_{ap}, the axons born within a basin can escape the fascicle, and at the same time, the share of small-size fascicles in the distribution of fascicle sizes grows. This facilitates interactions (axon exchange) between individual fascicles on the much shorter time scale than in case of slow turnover-generated exchange of axons between basins described in the section Basic active walker model(Chaudhuri, Borowski, and Zapotocky 2011).

The purity of environment for an axon i of type *1* of a heterogeneous fascicle can be quantified as $s_i = {}^{(n_1 - n_2)}/_{(n_1 + n_2)}$, conversely for axon type 2, $s_i = {}^{(n_2 - n_1)}/_{(n_1 + n_2)}$, where n_1 and n_2 are number of type *1* and type *2* axons in this one particular fascicle. The mean purity of the environment at the level y is defined as

$$S = \frac{\sum_{i=1}^{N(y)} s_i}{N(y)} = \frac{1}{N(y)} \sum_{\text{fascicles}} \underbrace{n_1 \frac{n_1 - n_2}{n_1 + n_2}}_{\equiv \sum_{\text{type 1}} \frac{n_1 - n_2}{n_1 + n_2}} + \underbrace{n_2 \frac{n_2 - n_1}{n_1 + n_2}}_{\equiv \sum_{\text{type 2}} \frac{n_2 - n_1}{n_1 + n_2}} = \frac{1}{N(y)} \sum_{\text{fascicles}} \frac{(n_1 - n_2)^2}{n_1 + n_2}.$$

$S = 1$ then corresponds to perfectly sorted system, while $S = 0$ describes fascicles containing equal number of the two axon types. The steady state purity S_∞ is reached over time by single-exponential decay with time scale τ_s. The S_∞ is not monotonic in y, but the system reaches maximal purity at a particular distance from the starting point (for $|E_h| > |E_o|$). The axons are at first sorted by the stronger homotypic interaction, but later, the heterotypic interaction will tend to merge fascicles into larger mixed ones. If the heterotypic interaction was repulsive ($E_o > 0$), it would drive faster sorting, but would decrease the mean fascicle size $\bar{n}_o$, $\bar{n}_h$ across all the y levels (ibid.).

1.6.6 Local dynamics in absence of growth cones

The presented models attempt to treat the local phenomenological behaviour of the GC in section 1.6.2, or emulate the path formation in more biophysical perspective in

section 1.6.4. The latest presented direction in section 1.6.5 tries to find relationship between the local and the global characteristics of the pathfinding system. While various guidance strategies were implemented (from nearly stochastic to GCM field-determined), and various bundling rules used (implicit, contact or cue-guided, absolute, probabilistic), what is missing from these models is a study of the local dynamics of AS and their contact interactions within the system, independently of the presence of GCs. All of the approaches presented so far assumed geometrically immutable trails, drawn by the GC (walker) into the environment for later GCs (walkers) to read and follow (or avoid). However, local geometric and viscoelstic changes of the once laid trails may play an important role in both development and regeneration. The possibility to control the structure of rear/proximal parts of the network can have profound influence on network pruning and synaptogenesis. Although some of the approaches proposed gradual or abrupt degradation of the trail to induce network plasticity, none proposed its geometrical change and restructuring as a result of viscoelastic properties of the axons, neither was considered coarsening of the network through AS-AS contact interactions in places with minimal GC activity and motility. In the present work, we focus on this aspect and its effect on the system as a whole.

1.7 Coarsening and two-dimensional foams

The foams are formed by *voids* or *bubbles* (empty areas or bubble interiors filled with gas) and *walls* or *films* (boundaries separating voids, often fluids), creating distinct multiscale topology. Narrowing the field to liquid foams (soap foams), they can be roughly classified based on their liquid fraction ϕ into wet ($\phi \approx (0.1\text{–}0.2)$, rather spherical shape of bubbles) and dry ($\phi < 0.1$, rather polyhedral shape). In the latter case, the walls are thin films of liquid forming two interfaces with gas (Almgren and J. E. Taylor 1976). Borderlines of these walls are called *Plateau borders*, which in turn meet in vertices called *Plateau nodes*. The foams exhibit multiple spatial and temporal scales. The length scales can be separated into (i) scale of the film thickness, where physico-chemical properties of surfactants influence the forces and foam dynamics (Satomi et al. 2013), (ii) scale of the individual bubbles, driven by mechanics of the films (i.e. Young-Laplace law), and (iii) scale of the foam system, where collective behaviour plays role (i.e. coarsening, continuum-like behaviour). (Weaire, Langlois, et al. 2007).

The temporal scales are determined by the composite dynamics of the foams—they are locally mechanically equilibrated spontaneously evolving systems, where various processes evolve on different time scales:

(i) local structural relaxations ($<1\,\mathrm{s}$),

(ii) coalescence, when unstable film breaks and two bubbles merge (which can possibly induce avalanche of ruptures),

(iii) draining in presence of gravity, which removes the liquid from the system and thus drives slower processes ($\gtrsim 1\,\mathrm{min}$ (ibid.)),

(iv) coarsening, as gas flows along pressure gradient from small bubbles (removed in the process) into larger bubbles ((0.1–10) h[15]).

The evolution of foams involves dissipation originating from the shear flow of viscous liquid of the films (particularly in the wet foams), surface friction, and external confining wall drag (in two-dimensional foams). The stability of foam films can be increased by a *surfactant*, surface-active agent, which increases film robustness towards rupture and decreases tension within the films (Mancini 2005; Weaire, Langlois, et al. 2007).

1.7.1 Physics of foams

The physics of foams is to a large extent dictated by instabilities, and becomes more complicated with increasing liquid fraction, gravitational loading or gas compressibility. Despite such general complexity, many topological features in foams can be described by simple rules and stereotypical configurations (*Plateau laws*). The energy (E) of the foam system is given by $E = E_{\text{vol}} + E_{\text{surf}}$, volume and surface components respectively, where $E_{\text{surf}} = \sigma S$ is given by σ surface energy per unit area (or surface tension, refer to section 1.3.3) and the area S. Note that a film contains two surfaces (two interfaces) and its energy per unit area is then 2σ.

The structure of a metastable system spontaneously relaxes on the short time scale (item (i)) into configuration (geometry) of locally minimal energy. On the short time scale and assumption of (i) constraint bubble size (incompressible, no diffusion), (ii) negligible external force, $E_{\text{vol}} = \text{const}$, the system geometry is given by the surface term E_{surf} minimisation (under the constraint of constant bubble volumes). Particularly for foam of constant surface tension, $\sigma = \text{const}$, the problem is reduced to finding minimal surface S (under constant volume constraint and boundary conditions). Note, that the system is intrinsically unstable on longer time scales, it continues to coarsen and decrease the total surface until disappearance $S \to 0$, unless stopped by process on boundaries or short-range repulsion (J. A. Glazier and Weaire 1992; Weaire, Vaz, et al. 2006).

An ideal foam (where amount of liquid tends to zero) of $\sigma = \text{const}$ at mechanical equilibrium is characterised by *Plateau laws* (Plateau 1873):

(i) Three films (of constant σ) at a time can intersect on a Plateau border under angle $2/3\ \pi$ (see fig. 1.16a); equivalently, for 3 unit vectors $\vec{e}_i$ normal to the border and tangent to the film, $\sum_{i=1,2,3} \vec{e}_i = 0$.

(ii) At most four borders can meet at a tetrahedral node (in 3D), which is symmetric, with approach under angle $\theta_M = \text{acos}(-1/3)$.

(iii) The pressure difference across the bubble wall is proportional to the wall mean curvature, as given by the Young-Laplace law (see below).

[15] The coarsening of foams is slower on micro-scale level, due to order of magnitude smaller diffusion coefficient κ, see (Gañán-Calvo et al. 2004; Marchalot et al. 2008) and section 1.7.4.

The *Young-Laplace law* states, that the difference of pressures Δp between neighbouring bubbles is proportional to the mean curvature $H = {}^{2}/_{r}$ (related to two principal curvatures ${}^{2}/_{r} = {}^{1}/_{r_1} + {}^{1}/_{r_2}$; compare to eq. (1.1)),

$$\Delta p = 2\sigma H = \underbrace{2\sigma}_{\substack{\text{two}\\ \text{interfaces}}} \left(\frac{1}{r_1} + \frac{1}{r_2}\right) = 2\sigma\frac{2}{r}, \tag{1.18}$$

The item (i) is illustrated in fig. 1.16a. The fig. 1.16b is an orthogonal section of a three-dimensional foam; Plateau border **(I)** formed by four films (quadruple border) within the same frame has larger section length, $l_1 > l_2$, and therefore also surface energy, than the configuration formed by two triple borders **(II)**, and is prone to relaxation (I)→(II) (Mancini 2005). The transition between equilibria of ideal foams happen instantly, no viscous effects are assumed.

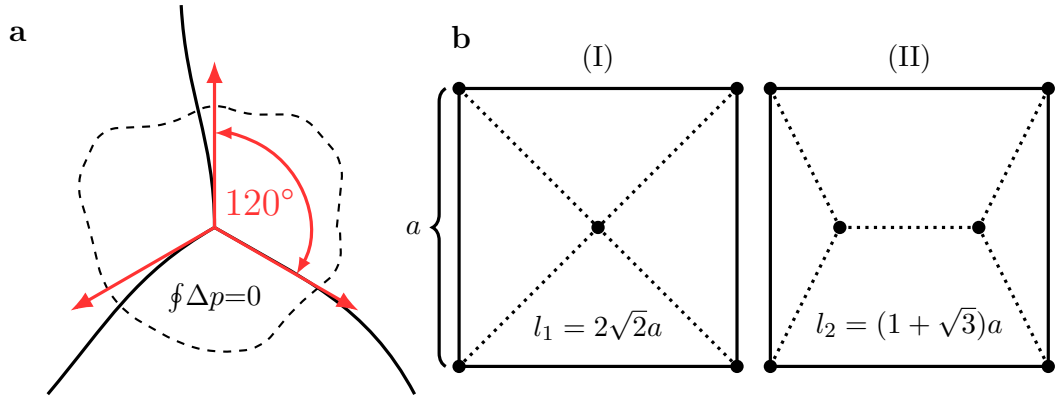

Figure 1.16: **a**: Illustration of stable Plateau border junction formed by three walls (films) under the angle ${}^{2}/_{3}\,\pi$. **b**: The configuration **I** has larger orthogonal section length and is therefore unstable to transition to the configuration **II**, which has smaller length, $l_1 > l_2$.

1.7.2 Two-dimensional foams

Ideal two-dimensional liquid foam is an analogue of ideal three-dimensional liquid foam. It partitions the plane into bubbles (of gas) and films (of liquid under tension). The vertices and edges of the 2D foams correspond to orthogonal section of three-dimensional Plateau borders and films. The 2D foams allow to study some properties of 3D foams under simpler conditions, while at the same time, they have some unique intrinsic attributes without three-dimensional counterparts (ibid.).

The topology of two-dimensional foam and its gradual coarsening is reminiscent of similar features in network of axon trails described by models in sections 1.6.3 and 1.6.5. In the Results, particularly section 3.10, we will elaborate on such two-dimensional analogy; we will therefore restrict the foam introduction to two dimensions for the rest of this section.

Experimentally, a 2D foam can be obtained by enclosing 3D soap foam between two parallel plates brought into close proximity (so called Hele-Shaw cell). Such foam may be considered quasi two-dimensional. If the plane of the plates is oriented normally to gravitational field, then the gravity effects and hydrostatic pressure variation are negligible (Mancini 2005). Illustration of such foam is shown in fig. 1.17, adapted from (Graham 2011).

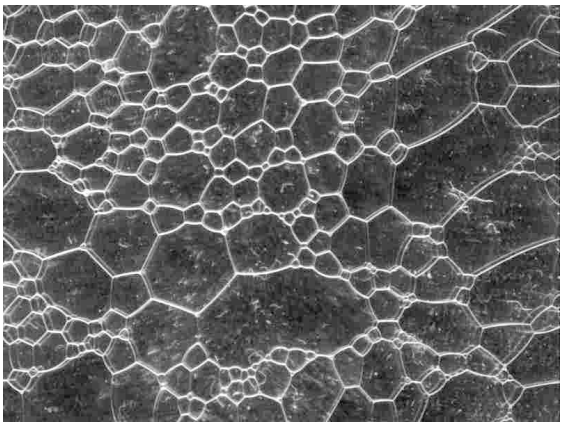

Figure 1.17: Illustration of experimental realisation of two-dimensional foam. Courtesy (Graham 2011).

While two-dimensional foams have various physical realisations, we will further focus on idealised (dry) foams, where the films can be understood as simple, one-dimensional lines, which intersect in the zero-dimensional *vertices*—the vertices contain all the liquid. In the ideal two-dimensional foams, every foam segment has 2 interfaces—no single-interface object is considered—we can therefore redefine σ as linear density of energy of a film (or linear tension), i.e. $2\sigma \to \sigma$[16].

We consider analogical assumptions as used in section 1.7.1, justified by separation of time scales (see beginning of section 1.7), that is (i) conserved bubble area (incompressibility, no diffusion), and (ii) no external (boundary) force, we therefore exclude work of pressure (i.e. E_{vol}=const) and viscous energy dissipation. Under such quasi-static conditions, the only force acting on the system is the line tension σ (with area and boundary constraints); for constant σ, system energy is given as

$$E = \sigma \sum_{i=1}^{N} l_i, \tag{1.19}$$

summed over length l_i of all the film segments $i \in (1, \ldots, N)$. The foam is equilibrated, if its structure is local minimum of the energy function E, in case of eq. (1.19), it means minimal length, analogical to minimal surface of 3D foams (section 1.7.1). Equilibrated foam is only metastable, longer time scale processes perturb the configuration and generate coarsening dynamics (Mancini 2005).

The equilibrium Plateau laws remain valid for the two-dimensional foams. If the sum of forces acting on any film or vertex is zero, pressure inside each bubble is constant, bubbles are incompressible and no diffusion occurs, then the analogical Plateau laws are:

(i) Three films of equal σ meet at a vertex, the force equilibrium is guaranteed by $\sum_{i=1,2,3} \vec{e}_i = 0$, where $\vec{e}_i$ is tangent vector of each film.

(ii) Angles between films at a vertex are $^2/_3\,\pi$, see fig. 1.16a. Tetrahedral node analogy does not exist in 2D.

[16] This means the energy of unit length $|\vec{e}|$ of a film is given as $|\vec{e} \cdot \sigma|$.

(iii) The Young-Laplace law is given by single curvature h in 2D, i.e. $\Delta p = \sigma h$, which implies the films are circular arcs with radius proportional to pressure difference.

The Young-Laplace law also implies, that the sum of drops of pressure along a closed curve is zero (see fig. 1.16a)

$$0 = \oint \Delta p(t) dt = \sum_{i=1,2,3} \Delta p_i = \sum_{i=1,2,3} \sigma h_i = 0.$$

It follows from the Plateau laws in 2D that only stable organisation of two-dimensional foam is hexagonal tessellation (i.e. honeycomb), where angles at the vertices are $2/3\ \pi$. If the number of vertices in a bubble is lower, the bubble walls become curved, leading to gas diffusion. Once regular hexagonal tessellation is perturbed by a defect, the whole system becomes unstable and eventually collapses (coarsens to the size of container). We will discuss the process in detail in section 1.7.3.

The major analogy between the axonal networks and the two-dimensional foams is in the topology. Topological changes of one can be observed (to some approximation) in the other. In the foams, these changes are driven by diffusion through films, film bursts and gradual drying or draining of the liquid. The speed of these topological processes is much higher than gradual changes of bubble area (caused by diffusion), and are usually assumed to be instantaneous—a rapid local relaxation after perturbation. During the evolution, when the foam passes from one metastable state (equilibrium) to another, we can observe two elementary topological changes:

(i) ***T1***: is a transition between two orientations of two neighbouring triple-junctions (vertices) of films. It does not change the number of bubbles, but the neighbourhoods (see fig. 1.18a). In the process, an unstable four-vertex is formed (cf. fig. 1.16b).

(ii) ***T2(3)***: represents a disappearance of a triangular bubble (void). A loop representing edges around the bubble (void) gradually collapses into a film junction (see fig. 1.18b), the energy of the foam changes continuously during the process. Note that processes of contraction of other polygonal loops exist, i.e. ***T2(4)*** or ***T2(5)***, but on a time scale of coarsening, these processes can be considered as a composition of *T1* and *T2(3)*(J. A. Glazier and Weaire 1992).

T1 processes often compound in avalanches and are crucial for two-dimensional foam relaxation. For example, in ordered honeycomb structure, they provide a migration mechanism for simple defects (e.g. neighbouring 5-sided and 7-sided cells) (J. A. Glazier and Weaire 1992; Mancini 2005; Weaire, Vaz, et al. 2006).

Equilibrated ideal two-dimensional foam embedded in an outer pressure is well defined by the Young-Laplace law and Plateau laws, void areas are constant, films are circular arcs of known curvature. In such situation, the number of edges per bubble is given. The item (i) of Plateau laws implies that $V = 2/3 E$, where V is number of vertices and E number of edges in the foam. Number of bubbles (F), edges and vertices are related by Euler's theorem of topology of cellular structure

$$F - E + V = \chi(g) = 2 - g.$$

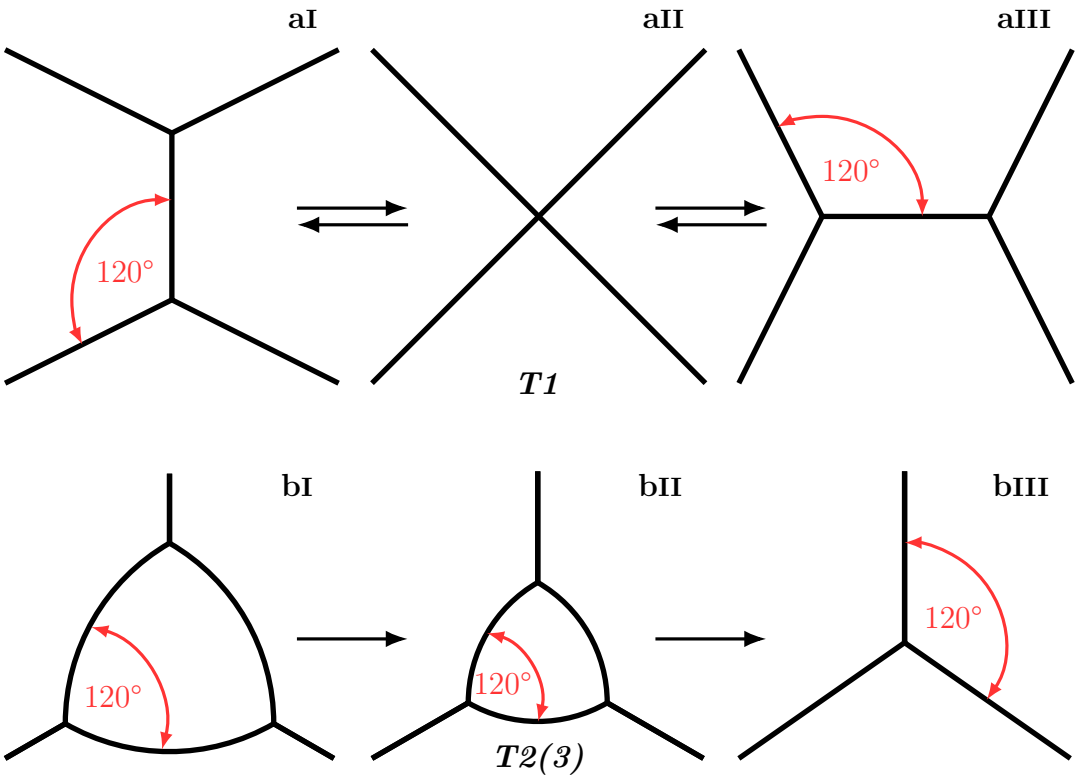

Figure 1.18: **a**: *T1* topological process. The joining edge decreases its size to zero until unstable four-vertex is formed, which soon dissociates into two triple-vertices. Note that the angle at a triple-vertex is conserved according to Plateau laws item (i). **b**: *T2(3)* topological process. Note that the loop is equilateral triangle and that its geometry is conserved during the collapse, and that the final triple-vertex forms with three angles of 120°.

In case of the two-dimensional foam, $\chi = 1$ and so

$$E = 3(F-1), \text{ and } V = 2(F-1). \tag{1.20}$$

Euler's theorem and the three-connectivity then imply that average number of edges per bubble $\langle n \rangle$ is

$$\langle n \rangle = \frac{2E}{F+1} = 6\frac{F-1}{F+1} \overset{F\to\infty}{\longrightarrow} 6. \tag{1.21}$$

If pressure inside the bubbles is uniform $p_1 = p_2 = \ldots = p_F$, then the edges are straight lines (curvature $h_{ij} = 0$), and honeycomb structure is formed (Mancini 2005).

1.7.3 von Neumann's law

The transfer of area a between two bubbles $i \to j$ is analogical to concentration gradient driven diffusion of Fick's law $J \propto -\nabla c$, where J is flux and c is concentration. For the

gas in 2D bubbles, the rate of area transfer per unit length similarly depends on the difference of pressure between the two bubbles,

$$\frac{\dot{a}_{i\to j}}{l_{ij}} \propto p_i - p_j$$
$$\dot{a}_{i\to j} = \kappa(p_i - p_j)l_{ij}, \tag{1.22}$$

where l_{ij} is the length of boundary between the bubbles, κ is diffusion constant. Note that the boundary has uniform curvature and the difference of pressures is also uniform along the boundary. Local balance of force on the slowly relaxing film (fig. 1.19a) is then given as

$$p_i - p_j = \underbrace{\sigma h}_{\substack{\text{tensile}\\ \text{term}}} + \underbrace{\eta v_\perp}_{\substack{\text{viscous}\\ \text{term}}}, \tag{1.23}$$

where η is coefficient of viscous drag and $v_\perp$ is outward pointing (i.e. $i \to j$) velocity component normal to the boundary l_{ij} of bubble i, see fig. 1.19a. The overall rate of area change for the bubble i is given by contributive changes of its boundary Γ_i with F_i neighbouring bubbles, so

$$\dot{a}_i = \oint_{\Gamma_i} v_\perp dl$$

using eqs. (1.22) and (1.23) and noting that $\oint_{\Gamma_i} \frac{\dot{a}_{i\to j(l)}}{l_{ij}} dl = \sum_{j=1}^{F_i} \dot{a}_{i\to j} = -\dot{a}_i$

$$\dot{a}_i = \oint_{\Gamma_i} \left[-\frac{\sigma}{\eta}h + \frac{(p_i - p(l))}{\eta}\right] dl = \oint_{\Gamma_i} -\frac{\sigma}{\eta}h\, dl - \frac{\dot{a}_i}{\eta\kappa}$$
$$(1+\eta\kappa)\,\dot{a} = -\kappa\sigma \oint_{\Gamma_i} h\, dl$$
$$\dot{a} = -\frac{\kappa\sigma}{1+\eta\kappa} \oint_{\Gamma_i} h\, dl \tag{1.24}$$
$$\boxed{h(l)\, dl = \frac{1}{r(l)} dl = d\phi}$$
$$\dot{a} = -\frac{\kappa\sigma}{1+\eta\kappa}\phi, \tag{1.25}$$

where $p(l)$ is pressure in the neighbouring cell at the position l, ϕ is angle integrated along the whole border, excluding the discontinuous changes of $\pi/3$ in each vertex (fig. 1.19a). The total change is then

$$\phi = 2\pi - n\pi/3 = (6-n)\pi/3 \tag{1.26}$$

substituting eq. (1.26) into eq. (1.25) yields the *von Neumann's law*:

$$\dot{a}_i = \kappa'(n-6), \tag{1.27}$$

where $\kappa' = \frac{\pi\kappa\sigma}{3(1+\eta\kappa)}$. This result shows that the rate of change of bubble area depends only on its number of sides n (J. A. Glazier and Weaire 1992; Mancini 2005). Note that

the only stable configuration is six-sided bubble foam (i.e. honeycomb); any bubble of more than 6 edges will expand (infinitely within the system boundaries), while bubbles of less than 6 edges will collapse, see fig. 1.19b. Also, compare with the Euler's theorem, which states the average number of edges to be $\langle n \rangle = 6$ in equilibrated two-dimensional foam (J. A. Glazier and Weaire 1992). In (James A. Glazier and Stavans 1989), the equation was generalized to typical internal vertex angle dependent on the number of bubble edges $\theta(n)$ yielding

$$\dot{a}_i = \kappa' \left[3n \frac{\pi - \theta(n)}{\pi} - 6 \right], \tag{1.28}$$

which reduces to eq. (1.27) for $n = 6$ and $\theta(6) = {}^{2\pi}/_{3}$.

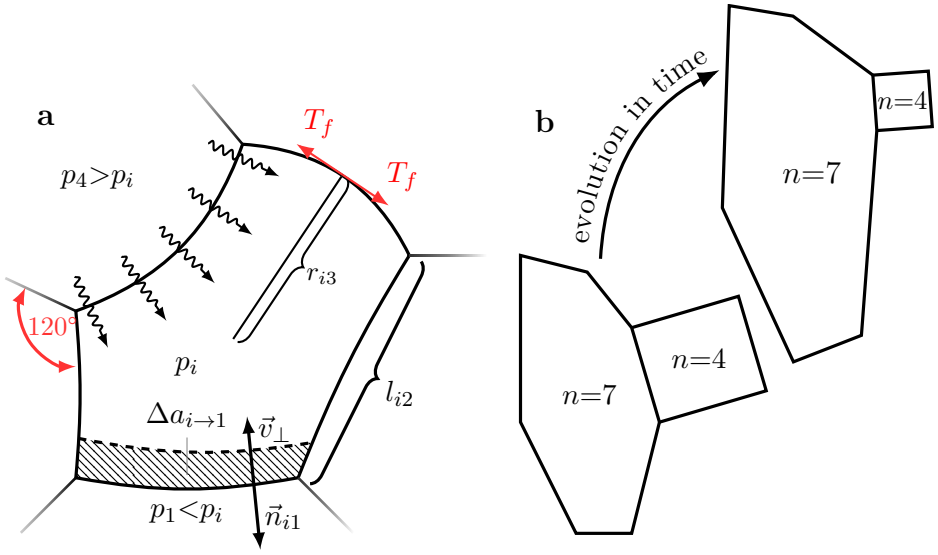

Figure 1.19: **a**: Illustration for derivation of von Neumann's law and processes involved. The vertices are formed under angles of ${}^{2}/_{3}\pi$, according to Plateau laws, pressure difference Δp_{ij} deforms inter-bubble boundaries l_{ij} into circular arcs of radii of curvature $r_{ij} = {}^{1}/_{h_{ij}}$ under film-tension T_f. Gas diffuses between adjacent bubbles (illustrated by curly arrows) with diffusion constant κ' along the pressure gradient, and transfers area, shaded in the figure (change in finite time), from bubble of larger pressure to bubble of lower pressure ($\Delta a_{i\to j} > 0$, if $p_i > p_j$ and so a partial change of bubble i area is $\Delta a_i|_{l_{ij}} < 0$). During the area transfer process, dissipative viscous drag acts on the moving boundary l_{ij}, and $v_\perp = \vec{v}_\perp \cdot \vec{n}_{ij}$, where $\vec{n}_{ij}$ is outward (i.e. along the pressure gradient) boundary unit normal vector. **b**: According to the von Neumann's law, bubbles of more than 6 edges are unstable and expand, while bubble of less than 6 edges gradually collapse and vanish.

While the von Neumann's law describes the dynamics of bubbles, it applies only to those of fixed n. As the network evolves, the topographical instabilities (see fig. 1.18) change the number of sides and additional assumptions about redistribution are necessary.

The generalisation provided by the eq. (1.28) applies beyond the dry foam limit. As more liquid accumulates in the Plateau borders, the angles at the vertices begin to deviate form $^2/_3\,\pi$, the bubbles become more isolated, more round, and background pressure starts to influence the diffusion of gas. Plateau borders effectively shorten the inter-bubble interfaces (l_{ij} in eq. (1.22)) and so reduce diffusion rates; moreover, although changes of diffusion coefficient κ' can be small (below experimental precision), their effect on the whole network can have observable impact. Under such conditions, the von Neumann's law can be modified into

$$\dot{a}(r) = \kappa' \left(\left\langle \frac{1}{r} \right\rangle - \frac{1}{r} \right) \tag{1.29}$$

where r is radius of a bubble. We can see that general predictions are the same, smaller bubbles ($r < \langle r \rangle$) will collapse and large will grow, however the two models have differing scaling states, and simulations and experiments confirm different kinetics of evolution (J. A. Glazier and Weaire 1992).

1.7.4 Scaling of two-dimensional foams

A pattern is in the *scaling state*, if the distribution and correlation functions of its dimensionless quantities remain constant in time. The only property that varies is the mean length scale. In the case of von Neumann's law, the average area of a bubble scales linearly with time, $\langle a \rangle \propto t$, as the right-side of the eq. (1.27) is otherwise constant (as long as no topological changes take place). The average cell radius scales as a square root of area and therefore

$$\langle r \rangle \propto \sqrt{\langle a \rangle} \propto (\kappa')^{1/2} t^{1/2}. \tag{1.30}$$

While in the eq. (1.29), the area scales also linearly with time, but also inversely with radius, therefore

$$\begin{aligned} \langle r \rangle &\propto \sqrt{\langle a \rangle} \propto (\kappa')^{1/2} \frac{\sqrt{\langle t \rangle}}{\sqrt{\langle r \rangle}} \\ \langle r \rangle &\propto (\kappa')^{1/3} t^{1/3}, \end{aligned} \tag{1.31}$$

so the scaling is different for the idealised dry foam described by the von Neumann's law and the wet foam with higher liquid fraction described by the eq. (1.29). The paragraph preceding the eq. (1.29) provides arguments for such disparity (ibid.).

During the presentation of foam time scales, we noted that network spatial scaling in some cases depends also on the spatial scale itself. This effect is due to diffusion coefficient κ dependence on foam spatial scale. In microfoams, at the typical bubble size of order $\sim$1 µm, κ can be an order of magnitude lower than in macrofoams ($\sim$1 cm) (Marchalot et al. 2008). Another observation showed that small, 50 µm and 80 µm, monodisperse (i.e. uniform initial bubble size) foams exhibit 10 min and 20 min delayed coarsening respectively (Gañán-Calvo et al. 2004). These two observations indicate, that at the small spatial scales, foam dynamics starts to depart from the simple scaling rules of eqs. (1.30) and (1.31).

1.8 Goals and hypothesis

1.8.1 Motivation

The wiring pattern presented in the section Olfactory system is a good illustration of intriguing complexity of neuronal guidance and targeting. In the system of many types of axons and gradual axonal turnover continuing into adulthood, precise axonal connectivity is assured by multiple diffusible guidance cue molecules and fasciculation processes. The system fasciculation is regulated by adhesive contact interactions between axons mediated by odorant receptor-specific cell adhesion molecules; axon subpopulation sorting depends on the cell-recognition through specific configurations of adhesion molecules. In previous literature, the recognition was mainly studied on the basis of growth cone detection—the receptors on the growth cone would detect molecules on another shaft and either induce approach and fasciculation, or trigger divergence and detachment. Conversely, dynamics of interaction of axon shafts, without participation of growth cones, has received very little attention.

The shaft-shaft dynamics is very difficult to observe *in vivo* and more so to separate from other influences, particularly for a changeable system like the olfactory system. An alternative possibility is to work with a culture *ex vivo*, culturing an explant of embryonic mice olfactory sensory neurons taken from the olfactory epithelium, and observe their axons outgrowing on the dish to interact with each other through the cell adhesion molecules, form fascicles and defasciculate. Under such conditions, if viable, the control over extra-neuronal influences (i.e. guidance cue molecules, substrate geometry etc.) would be robust, and time lapse optical microscopy easily achievable.

1.8.2 Hypothesis

Experiment devised in such way would allow to observe the character of shaft-shaft interactions and possibly fasciculation at the time the growth cones have mostly left the proximal area. If fasciculation could be observed under such simplified conditions as compared to the intricacy *in vivo*, it would suggest, that the axon bundling is rather natural property of axons, which is regulated through only limited number of biophysical parameters. It should be possible to describe such process by a local biophysical model, based on the experimentally measured properties of individual axons.

1.8.3 Goals

The *ex vivo* configuration can remove the complexity of the environment and reduce the problem to two dimensions. Parameters of local kinetics of the axon-axon interaction would be easily measured in the captured recordings and assessed. A simple model of the local contact interaction of two axonal shafts will be proposed, ideally reducing the biophysical complexity to two parameters: axial tension within an axon and adhesive force between the two axons. Such simplified model could be studied analytically and efficiently numerically; numerical simulations would allow to explore, how the model dynamics is modulated by various dissipative processes. Micromanipulation experiments

using biomembrane force probe technique will be designed and the biophysical parameters measured. The local model predictions for the evolution of global statistics of the network will be compared to the *ex vivo* observations.

Chapter 2

Methodology

The project relies on several experimental techniques and computational analyses. Observations *ex vivo* and their analysis are covered in section Time-lapse ex vivo videomicroscopy, electron microscopy in section Scanning Electron Microscopy. The manipulation experiments, their preparation, procedure and analysis are described in section Force measurements with Biomembrane Force Probe. Implementation of publicly released software dedicated to processing of biomembrane force probe experiments in introduced in section BFPtool implementation. Some descriptive measures and methods used on distributions are defined in section Mathematical tools for data analysis.

2.1 Time-lapse ex vivo videomicroscopy

Motivated by unexplored field of axon-axon contact interactions and its dynamics, we set up a real-time observation experiment of an OE neuronal culture *ex vivo*. Time-lapse of developing axonal network growing effectively in planar environment allowed us to study short-range events as well as global changes in statistics and topology of the whole network. All the experiments described in this section were performed at the laboratory of prof. Alain Trembleau (Development and Plasticity of Neural Networks, NPS, UPMC Paris 6). Experimental procedures involving animals, particularly preparation of OE explant and culture treatment with chemical agents, were performed by Coralie Fouquet, or in some cases by Alain Trembleau.

2.1.1 Olfactory epithelium explant cultures

All animal procedures were approved by the Île de France Ethics Committee. Pregnant female wild type (WT) Swiss mice were sacrificed by cervical elongation at E13.5, embryos were extracted from the uterus, and olfactory epithelium explants were prepared from the posterio-dorsal quarter of the septum and turbinates as follows: **first**| posterior and dorsal parts of septa and turbinates were cut into pieces in L15 medium (Gibco 21083) maintained on ice at 4 °C; **second**| they were incubated for 30 min at 25 °C in a 1:1 solution of Trypsin 0.25 % (Gibco 25050) and Pancreatin 4X USP (Gibco 02-0036DG) to separate the OE from the lamina propria; **third**| enzymatic reactions were stopped by adding 10 % foetal bovine serum (FBS) (Gibco 10270), and the biological material was rinsed in ice-cold L15 medium containing 5 % FBS; **fourth**| pieces of tissue were transferred into a glass Petri dish in which the OE sheets were cut, using a micro-scalpel, into small pieces of about (100–200) µm diameter each; **fifth**| explants were carefully

transferred into 50 mm diameter IBIDI video dishes (Biovalley) that included a 35 mm glass coverslip (Biovalley; for Biomembrane Force Probe experiments), or into IBIDI µ-slide 8 well #1.5 polymer coverslip (Biovalley 80826; for time lapse acquisition), previously coated with poly-L-lysine (0.2 $\frac{\text{mg}}{\text{ml}}$, Sigma P1524) and Laminin (0.02 $\frac{\text{mg}}{\text{ml}}$, Sigma L2020), and maintained in culture (37 °C, 5 % CO_2) until the day of experiment, in a culture medium of DMEM/F12 (Gibco 31331) containing 1 % N_2 (Gibco 17502), 0.1 $\frac{\text{mg}}{\text{ml}}$ Gentamycin (Sigma G1272), 1.5 % D-Glucose (Sigma G8769), 1 % BSA (Sigma A4161) and 7 $\frac{\text{µg}}{\text{ml}}$ ascorbic acid (Sigma A4403). 40 to 60 explants per set of experiments were prepared, originating from 10 to 12 embryos from a single mother animal.

2.1.2 Videomicroscopy recording

1 h before the start of time lapse recording, 10 mM Hepes was added to the explant cultures. Depending on the type of experiment, cultures were left without further treatment, or treated with either FBS (5 % final concentration, Gibco 10270), blebbistatin (10 µM in culture medium containing final concentration of 0.1 % dimethyl sulfoxide ($(CH_3)_2SO$) (DMSO), Sigma B0560) or cytochalasin B (2 µM in culture medium containing final concentration of 0.1 % DMSO, Sigma C6762). The frame acquisition was performed on a Leica DMI 6000B inverted microscope in a thermostated chamber (37 °C, 7 % CO_2 at the rate 10 $\frac{1}{\text{h}}$, (87–95) % humidity) using a DIC 63 × NA 1.40 IMM objective, or a dry phase contrast objective 40 × NA 0.75 Leica HCX PL APO. The microscope was mounted with a CoolSNAP HQ2 CCD camera (Photometrics, AZ, USA); the whole setup was driven by Metamorph 7.1 (Molecular Devices, CA, USA) in a multiple acquisition mode. At the acquisition interval of one minute, 9 axial planes were typically captured with an inter-planar distance of 0.5 µm or 1 µm at each of 8 to 10 positions selected around the explant. Recording of each experiment lasted (2–19) h, depending on culture survival (Šmít, Fouquet, Pincet, Zapotocky, et al. 2017).

The obtained hyperstacks (horizontal×vertical×axial×temporal) were reduced, single axial plane of best contrast was selected for each time frame. The frames were in TIFF format, 16-bit greyscale images, with pixel resolution 1392×1040 px, and uniform pixel width 0.1024 $\frac{\text{µm}}{\text{px}}$ (for the 63 × DIC objective) or 0.161 25 $\frac{\text{µm}}{\text{px}}$ (for the 40 × dry phase contrast objective). Prior to analysis, the grey level intensity histograms of the frames were normalised (ibid.).

2.1.3 Pharmacological manipulation experiments

As noted in the section 2.1.2, some cultures were treated with FBS or with pharmacological agents targeting the cytoskeleton. The pharmacological agents used with observable and reproducible effect were blebbistatin, and cytochalasin B. The experiments are summarised in the table 2.1.

In some cases, only single drug was added, typically after 1 hour of recording of untreated culture. In other experiments, the culture was pretreated with stabilising drug, blebbistatin, and a second drug was added later, typically 1 hour after the beginning of recording. The second added drug was either cytochalasin B or FBS (ibid.).

treatment	number of experiments	# of analysed experiments	observation & presumed effect
none	13	8	gradual coarsening
blebbistatin	16	2	stabilisation of the network
cytochalasin B	4	4	coarsening decrease in tension
FBS	4	2	explant contraction increase in tension
blebbistatin⇒ cytochalasin B	11	8	coarsening decrease in tension
blebbistatin ⇒ FBS	5	1	explant contraction increase in tension

Table 2.1: Table of *ex vivo* videomicroscopy time-lapse experiments. Pretreatment with blebbistatin and consecutive addition of a second drug is indicated by the arrow (⇒) symbol. The number of analysed experiments was limited by video length, quality or culture viability.

2.2 Analysis of ex vivo videomicroscopy

The obtained recordings were inspected, examining both (i) local processes in the network (section 2.2.1), and (ii) global properties of recorded network (section 2.2.4). The segmentation data manually or semi-manually extracted from recordings were further processed and mathematically analysed.

2.2.1 Analysis of local dynamics

Zippers are processes, during which two partially adhering axons dynamically adjust the length of mutual contact. The may extend or reduce the length of the adhesion segment by dynamical transition of the separation point, so-called vertex. In a straightforward type of analysis, we tracked individual zippers during dynamics. The vertex is geometrically well defined, it changes its coordinates in the field during the transition, and the coordinates can be easily measured.

A time interval was selected, covering 5 min of the vertex in equilibrium before the zipper dynamics started, and 5 min after the dynamics ended; zippers without this preceding and successive static period were discarded. To minimise disturbance from the areas adjacent to the zipper, the events were selected from sparse axonal networks. For each frame n of the time interval (at the rate of 1 $\frac{\text{frm}}{\text{min}}$), the position of the zipper vertex was manually selected and recorded as a coordinate point (x_n, y_n), and the zipper angle β_n was measured. The data were then exported to Matlab, where the distance to final

equilibrium (convergence) and velocity (of convergence) were calculated, and a fit was performed, to test, if the zipper convergence is rather exponential or linear in time—the data points were plotted against the fit line in semi-log plot (fig. 3.30). 17 measurements were performed in experiments originating from 4 mother animals, WT mice.

2.2.2 Distribution of equilibrium zipper angles

Tracking of the 17 individual suitable zippers as presented in section 2.2.1 produced a set of 34 static equilibrium angles, before and after the dynamics. This method of measurement guaranteed that angles were results of force equilibrium and not entanglement or other obstruction of zippering dynamics. To estimate the distribution of static equilibrium zipper angles in the population of OSN axons, we applied Matlab's Normal kernel smoothing method on the measured data. Note, however, that this distribution is in essence different from the angle distribution obtained in network analysis (i.e. measuring all presumed zipper angles in a single time frame, see section 2.2.4), where entangled and obstructed zippers cannot be easily excluded.

2.2.3 Segmentation of recordings

Another performed analysis covered the recorded network area as a whole. For this type of analysis, segmentation of the recording was necessary. Major criteria of frame selection for this type of analysis were good contrast, culture survival, and sufficient area and density of the network; particularly, only experiments in which axonal network showed clear evolution lasting over 1 h were accepted.

Initial time stacks (horizontal×vertical×temporal) were obtained as described in section 2.1.2. Initial preprocessing was performed using distribution Fiji (Schindelin et al. 2012) of the project ImageJ (Schneider et al. 2012). A subfield and time interval of interest were selected and extracted as a substack from each analysed stack.

In the quantitative analysis of the network, 6–12 time frames were sampled at convenient time points from the substack and extracted into individual TIFF files. In each frame, the network of axons was manually segmented into a list of edges by drawing individual straight selection lines over the image and saving the selections into a list using 'ROI manager' (*Analyze > Tools > ROI manager*), see fig. 2.1. In some cases, successive frames were consulted to decide whether a line is an axon to include or a transient side-process. The list of selections of each frame was saved into a portable ZIP file, which can be imported into ImageJ software on any machine. For each selection segment of the list, 5 parameters were extracted: minimum (x, y) coordinates of line's bounding box, width and height of the bounding box, and the angle between the segment and the abscissa (x axis). A CSV file with the measurements, one segment per line, was exported. This procedure was repeated for all frames selected for the analysis.

2.2.4 Analysis of segmented data

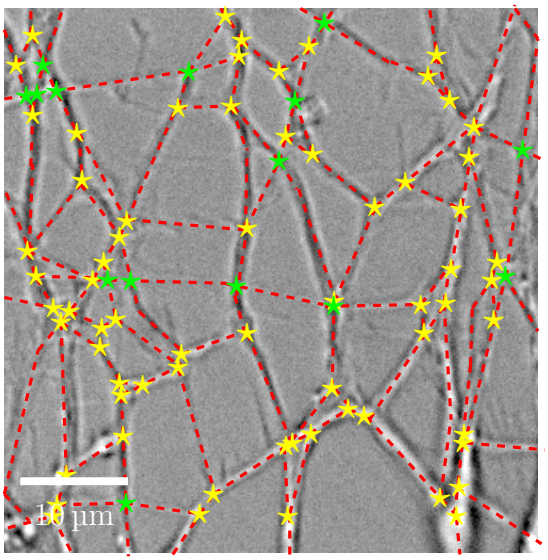

Figure 2.1: Example of manual segmentation tagging marks. Red dashed lines represent the selected segments, yellow stars mark junction points, green stars mark crossings.

A naming convention was used to import the CSV files and the linked TIFF frames into the Matlab (The Mathworks, Inc. 2015) as an organised data-structure. A script was executed to transform the 5 measured parameters of each selection segment k into a pair of coordinate endpoints A and B, $(x_{k,A}, y_{k,A})$, $(x_{k,B}, y_{k,B})$. In order to generate graph data structure (i.e. turn the network into vertices and edges with defined connectivity), the coordinates of endpoints of adjoined segments must be separated by less than 1 px, e.g. if endpoints A of segments p and q form a vertex, then the self-made algorithm requires $|(x_{p,A}, y_{p,A}) - (x_{q,A}, y_{q,A})| < 1\,\text{px}$. To satisfy such tagging precision, the selection list of each frame was iteratively treated to remove small gaps: a relaxation procedure implemented a linear relationship between each endpoint pair attractive movement $(\Delta x, \Delta y)$ and their current distance,

$$(\Delta x_{p,A}, \Delta y_{p,A}) = -(\Delta x_{q,A}, \Delta y_{q,A}) \propto |(x_{p,A}, y_{p,A}) - (x_{q,A}, y_{q,A})|$$

with a cut-off distance of (6–10) px (depending on the magnification). The procedure was considered converged, when the sum of all endpoint movements i was $\sum_i |(\Delta x_i, \Delta y_i)| < 5\,\text{px}$ (for hundreds of endpoints per frame). Other corrective steps resolved segment crossings or situations, in which an endpoint forms a junction with an interior of another segment. The final corrected selection closely corresponded to the intended initial manual selection.

A set of custom-made functions was then used with the refined segmentation list to

1. generate the graph data structure of the network,
2. detect cordless closed loops within the graph (see section 3.8.3 for details),
3. semi-automatically measure angles at the junction points; the user was prompted to choose angles to measure for each junction point, where choice was ambiguous, they could also mark the junction point as a crossing point, or exclude it from the analysis,
4. calculate the graph statistics (notably the zipper angle distribution, total network length and number of vertices, and average area of cordless loops; see section 2.6.1 for details), and
5. calculate correlations between these statics.

2.3 Scanning Electron Microscopy

Explants were fixed overnight at 4 °C in 2.5 % glutaraldehyde and 1 % paraformaldehyde in 0.1 M sodium cacodylate ($(CH_3)_2AsO_2H$) buffer, then rinsed in cacodylate buffer and fixed for 45 min in 2 % OsO_4. They were then dehydrated in a series of graded ethanol baths and transferred into hexamethyldisilazane ($[(CH_3)_3Si]_2NH$) before being airdried. The explants were finally mounted on a carbon stub and sputter-coated. Observations were made using a Cambridge Instruments Stereoscan 260 scanning electron microscope (Cambridge Instruments, MA, USA) equipped with a digital camera. Typical magnification of the acquired images was 350–1500 ×; the frames were in TIFF format, 8-bit greyscale, with pixel resolution 2992×2290 px, and pixel width 37 $\frac{\text{nm}}{\text{px}}$ (for 1000 × magnification).

Selected frames of magnification 1000 × were examined, and vertices (incidences, intersections) of the network were manually classified into 3 categories: crossings, simple laminar vertices and entangled vertices. Statistics of summary analysis of 3 frames was used to estimate the share of each category of vertex in the network.

2.4 Force measurements with Biomembrane Force Probe

2.4.1 Biomembrane Force Probe technique

The Biomembrane force probe (BFP) is a well-established technique for gentle calibrated force application and manipulation of biological specimen. It was initially presented in (Evans, Ritchie, and Merkel 1995), as a suitable tool for single-molecule force spectroscopy (W. Chen, Lou, et al. 2012; Clausen-Schaumann et al. 2000; Husson et al. 2009; Pincet and Husson 2005) and experiments on biological interfaces (W. Chen, Evans, et al. 2008; Maître and Heisenberg 2011), which focus on surface adhesion energy and membrane rigidity (see section 1.3.3). The technique is suitable for use in culture medium, it interacts softly with cells and spans over several orders of magnitude of applicable forces, (0.1–1000) pN.

The probe is composed of a micro-pipette connected to a controller acting as a manipulative apparatus, and a red blood cell (RBC) aspirated into the pipette, acting as a force transducer. The RBC is typically biotinylated and connected to a streptavidin-coated micro-bead (SB), positioned on the RBC's apex. The streptavidin-biotin attachment is a well studied bond with high (single molecule) rupture force of (50–250) pN, rising with loading rates in the range (1×10^2–1×10^6) $\frac{\text{pN}}{\text{s}}$(De Odrowaz Piramowicz et al. 2006; Grubmüller et al. 1996; Izrailev et al. 1997; Pincet and Husson 2005; Wong et al. 1999); several bound molecules should be sufficient to withstand the load on the RBC-SB interface during manipulation, for the applied probe forces of $\lesssim$1 nN. The SB is brought into contact with the studied object (sample), single molecule (e.g. protein, DNA) or interface (e.g. vesicle, cell), and allowed to form another adhesive contact. The pipette is then manipulated as necessary and controlled force is transduced by the probe onto this formed bond or interface; the whole experiment is recorded by a high throughput camera for later quantitative analysis.

2.4.2 Probe preparation

The probe was assembled as described in (Gourier et al. 2008), specifics of the procedure are presented below.

Preparation of the micropipette

The micropipettes were produced by elongation of borosilicate glass capillaries (inner/outer diameter 0.58/1 mm; Harvard Apparatus, USA) using micropipette puller (P-2000, Sutter Instruments Co., USA). The puller pulls the ends of the capillary in opposite directions, while the central part is heated by laser, the glass creeps and finally breaks, forming two micropipettes with obstructed termini. The micropipette tip is finalised in two steps:

1. under a microscope, the closed terminus is inserted several micrometres within a drop of glass melted by a heated platinum wire; once the heating is turned off, the pipette extremity is broken off by the stresses of cooling process, producing a rough-edged aperture;
2. the jagged tip is then re-inserted into the molten glass and the glass elevates within the capillary, after the heating is switched off, a clear-cut smooth edge is produced at the pipette tip.

The radius of the pipette opening can be adjusted through settings of the pipette puller and to some extend by the depth of immersion into the molten glass. Finalised micropipette was incubated in 10 % solution of bovine serum albumin (BSA) to avoid bead and cell attachment to its surface, and then filled with culture medium.

Preparation of the RBC, SB and the sample

The RBCs were obtained from a fresh human blood sample, drawn with a medical lancing device with all the necessary precaution to prevent infection risk. The protocol was approved by the ENS Safety and Ethics Committee, with an informed and written consent from a healthy volunteer donor. The RBCs were washed and biotinylated by covalently linking an amine-reactive PEG-biotin polymer (NHS-PEG3400-biotin, Interchim, Montluçon, France) to their surface, according to protocol provided by Evans (Merkel et al. 1999), and stored in PBS at 4 °C. The RBCs used in the experiments were prepared in lab of Frédéric Pincet (Surfaces Moléculaires Organisées, Laboratoire de Physique Statistique, UMR 8550, École Normale Supérieure, Paris, France).

The SBs were obtained from uniform silica microspheres (radius R_{SB}=1.5 µm, Bangs Laboratories Inc., IN, USA), cleaned in a boiling mixture of ammonium hydroxide (NH_4OH), hydrogen peroxide (H_2O_2) and water, and washed in ultrapure water. The beads were then bound with amino silane groups (N-(2-Aminoethyl)-3-aminopropylmethyl-dimethoxysilane ($C_8H_{22}N_2O_3Si$), ABCR GmbH, Germany). The silanised glass beads then underwent a reaction with a mixture of amine-reactive polyethylene oxide ($C_{2n}H_{4n+2}O_{n+1}$) with biotin (NHS-LC-LC-biotin, Interchim, Montluçon, France) and Sulfo-MBS (Pierce, c/o Touzard et Matignon, France). Finally, the biotinylated microbeads were saturated with streptavidin by incubation in

a 2 $\frac{\text{mg}}{\text{ml}}$ streptavidin solution (Jackson Immunoresearch Laboratories, Inc., USA), then washed and stored in PBS at 4 °C. The SBs were prepared at the lab of Frédéric Pincet.

Samples for the experiments were biotinylated OSNs from WT mice OE, extracted as described in the section 2.1.1. 2 days *in vitro* (DIV) OE explants cultured in 50 mm IBIDI dishes were biotinylated using EZ-Link$^{\text{TM}}$ Sulfo-NHS-SS-Biotin (Thermo Fisher scientific, MA, USA) according to manufacturer instructions. The treated explant was kept in an incubator (37 °C, 5 % CO_2). The explants were prepared and biotinylated by Coralie Fouquet or Alain Trembleau.

Experimental chamber

The experimental chamber used for BFP manipulations was equipped with a thermostat (37 °C) and a stable level of CO_2 (5 %). The whole table was furnished with pressurised shock absorbers to shield from external vibrations, and three pipette holders with linear piezoelectric translators (Physik Instrumente, Germany), each containing a liquid column to regulate the pressure in the micropipette. The sample table was mounted with Leica DMIRB inverted microscope with 40 × or 63 × NA 1.5 phase contrast objective connected to high throughput CCD digital camera (JAI, Yokohama, Japan) controlled by a computer. The camera captured the experiment at the rate 65 fps, the frames were obtained in AVI format, 8-bit greyscale with resolution 752×480 px (with uniform pixel width 0.1024 $\frac{\mu\text{m}}{\text{px}}$ at 63 × and 0.161 25 $\frac{\mu\text{m}}{\text{px}}$ at 40 ×).

Probe assembly

The final probe was assembled in the following steps:

1. Dish containing the explants was transferred into the thermostated air-cushioned chamber onto the sample table.
2. SBs were added to the culture; they randomly attached along the biotinylated OSN axons.
3. Micropipettes filled with medium were attached to the manipulators; pipette internal pressure was adjusted to match the medium pressure in the dish (i.e. no flow through the aperture).
4. Biotinylated RBCs were added to the culture; a healthy looking RBC was aspirated into one of the pipettes (at aspirating pressure ∼200 Pa) and brought into contact with an SB (for ∼2 min) to allow formation of biotin-streptavidin mediated link.

2.4.3 Manipulation experiment

Calibration

Important advantage of using the BFP to probe a biological interface is an intrinsic simplicity of reading the applied force magnitude. The force is applied onto the studied interface (i.e. SB-OSN axon) by controlled movement of the RBC-mounted pipette (RMP). As long as the pipette, RBC, SB and the attached sample are aligned along

a single axis (i.e. paraxial approximation holds), the load F exerted by the probe—mediated by the SB and transduced by the RBC—is proportional to the axial extension (deformation) of the RBC, $F \propto \Delta x$. This RBC deformation is equivalent to the change in mutual distance of the centre of the SB and a specific point of reference (anchor) on the pipette tip (fig. 2.2); it is therefore sufficient to track the position of the SB and the RMP tip throughout the recording of the experiment.

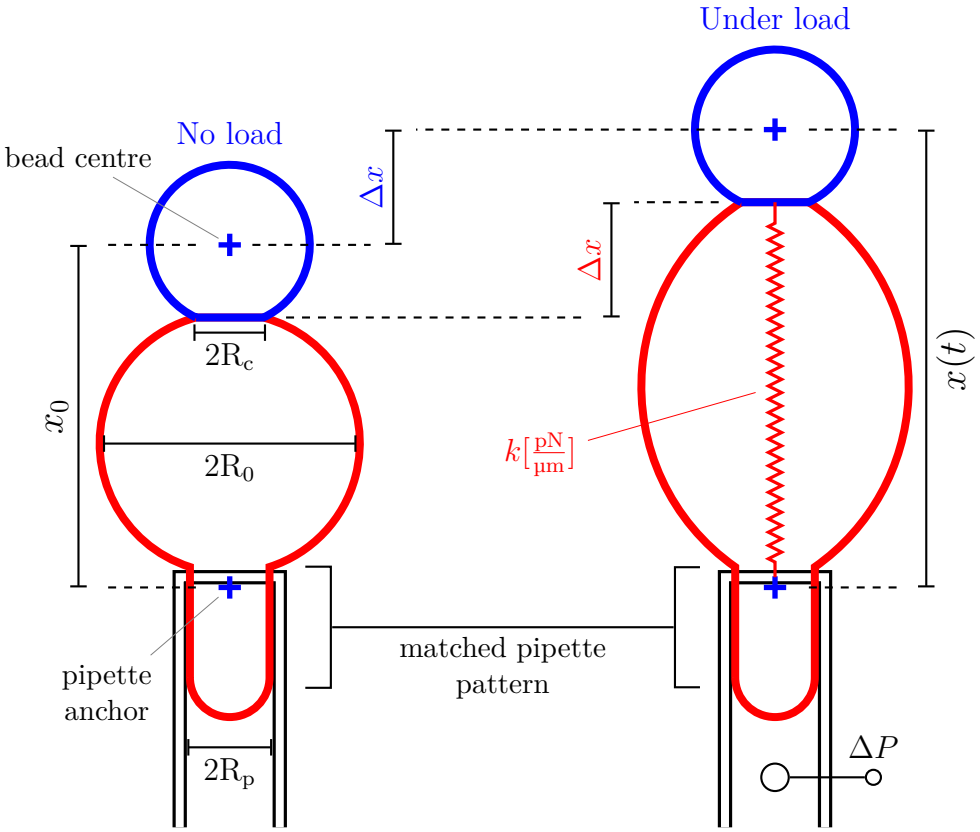

Figure 2.2: Illustration of the BFP principle. On the left, probe under *no load*, the RBC is unstrained with initial length x_0. The bead centre and pipette anchor are marked by blue cross, those are tracked points of interest used to extract the RBC extension Δx. Radii R_p, R_0 and R_c are designated. On the right, the probe is *under load*, the strained RBC has length $x(t)$ and extension $\Delta x = x(t) - x_0$, which corresponds to the change in distance between the two tracked points of interest, the bead centre and the pipette anchor. With extension $\Delta x \lesssim 0.5\,\mu m$, the linear approximation of relationship between the exerted force and extension ($F \propto \Delta x$) is satisfied, and the RBC behaves like a spring of stiffness k.

The coefficient of proportionality k corresponds to the axial stiffness of the probe, i.e. $F = k \cdot \Delta x$. This linear force-extension regime, i.e. the Hookean relationship, is known to hold well for RBC deformations smaller than $\Delta x \lesssim 0.5\,\mu m$ (Freund 2009); when this threshold is exceeded, the linear relationship overestimates the force. Beyond the linear

regime, the exact stiffness has to be calculated iteratively, using more general set of equations (Boye 2007; Simson et al. 1998).

In the linear regime, the stiffness k can be calculated using the linear approximation formula

$$k = R_p \Delta P \frac{\pi}{\left(1 - \hat{R}_p\right)} \frac{1}{\log\left(\frac{4}{\hat{R}_c \hat{R}_p}\right) - \left(1 - \frac{1}{4}\hat{R}_p - \frac{3}{8}\hat{R}_p^2 + \hat{R}_c^2\right)}, \tag{2.1}$$

where $R_p \in (0.5\text{–}1.5)\,\mu\text{m}$ is internal radius of the micropipette and $R_c \in (0.75\text{–}1)\,\mu\text{m}$ is radius of contact area of SB-RBC, $R_0 \in (2\text{–}3)\,\mu\text{m}$ is the radius of aspirated RBC without any load (see fig. 2.2), the hat designates a radius normalised by R_0, e.g. $\hat{R}_p = \frac{R_p}{R_0}$. $\Delta P \in (200\text{–}250)\,\text{Pa}$ is the aspiration pressure of the RMP. The stiffness was usually in the range $k \in (100\text{–}400)\,\frac{\text{pN}}{\mu\text{m}}$ in our experiments.

Measurement uncertainty of each diameter was given by the resolution limit of the optical microscope, $2\Delta R \leq 0.2\,\mu\text{m}$, the uncertainty of aspiration pressure was 5 Pa. For the typical values of parameters, stiffness relative error is $\delta k \approx 20\,\%$, which si comparable to the value 14 % reported in (Simson et al. 1998). Upper bound for error caused by departure from the linear regime in our experiments is $\leq 20\,\%$.

The RBC extension Δx is a difference between axial length of the unstrained RBC at the moment it first touches the SB and its axial length at any given time. Practically, the $\Delta x(t) = x(t) - x_0$ is calculated as a change in distance between the centre of the SB and a reference point on the pipette tip. To measure the unstrained distance x_0, the RBC is slowly moved toward the SB, and x_0 is measured in the frame, when the SB first recoils due to formed contact; $x(t)$ is then measured in any other time frame, see fig. 2.2. The uncertainty of Δx measurement is determined by the uncertainty of tracking procedure, see section 2.4.4, but typically $\delta(\Delta x) \approx 10\,\%$.

Procedure

We used the BFP to measure axial mechanical tension of OSN axons. Because we were not able to control the SBs attachment sites on the axons, our possibilities to manipulate particular, more convenient, configurations of axons were very limited. We therefore performed measurements on straight sections of axons, inducing axon deformation by controlled force, in the following steps:

1. The aspirated RBC was slowly brought in contact with an SB attached to an axon; the unstrained reference length x_0 was measured in the first time frame of contact (fig. 2.2).
2. The RBC was then softly pushed against the SB for several minutes, streptavidin-biotin link was formed and matured (like in fig. 2.3a).
3. The position of RMP was adjusted to impose load (F) on the SB-OSN axon interface, transduced through the RBC extension (Δx), fig. 2.3b.
4. The system was left to equilibrate over a period of more than a second[1] (called plateau, marked by black boxes in fig. 2.3c); the RBC (under load) stabilised at

[1] Note that at this point, we ignored possible viscoelastic processes of axons, which occur on larger time scales. Some analysis of axon relaxation is provided in section 3.5.7.

particular axial length $x(t) \neq x_0$.

5. The load caused deflection of the axon δ ($|\delta| \lesssim 5°$), which was later measured from the recording (fig. 2.3).
6. The position of RMP was re-adjusted several times, to create distinct plateaux, imposing 'pulling' ($\Delta x > 0, \delta > 0$; fig. 2.3b) and 'pushing' ($\Delta x < 0, \delta < 0$; fig. 2.3a); a measurement was considered reliable when $\geq$3 stable configurations (plateaux) were achieved.

The information about the applied force and corresponding induced axon deformation during the plateaux allowed us to extract the value of axon tension T, see section 2.4.4. Note that achieving $\geq$3 stable plateaux was the major drawback, as the SB-RBC link often degraded more rapidly.

Apart from the errors introduced by the BFP calibration, another uncertainty is involved through the measurement of the axon deformation angle δ. The angle is relatively small, $|\delta| \lesssim 5°$, and the axons are at the edge of optical microscope resolution ($\sim$200 µm in diameter), making the measurements difficult. The angle is usually measured 5 times per each plateau with the standard deviation of $\sigma(\delta) \approx 0.5°$, which can be quite large fraction for small deflections (i.e. high tension), $\delta(\delta) \approx 25\,\%$. The influence of individual uncertainties on the final result tension T will be discussed in the section Calculation of tension.

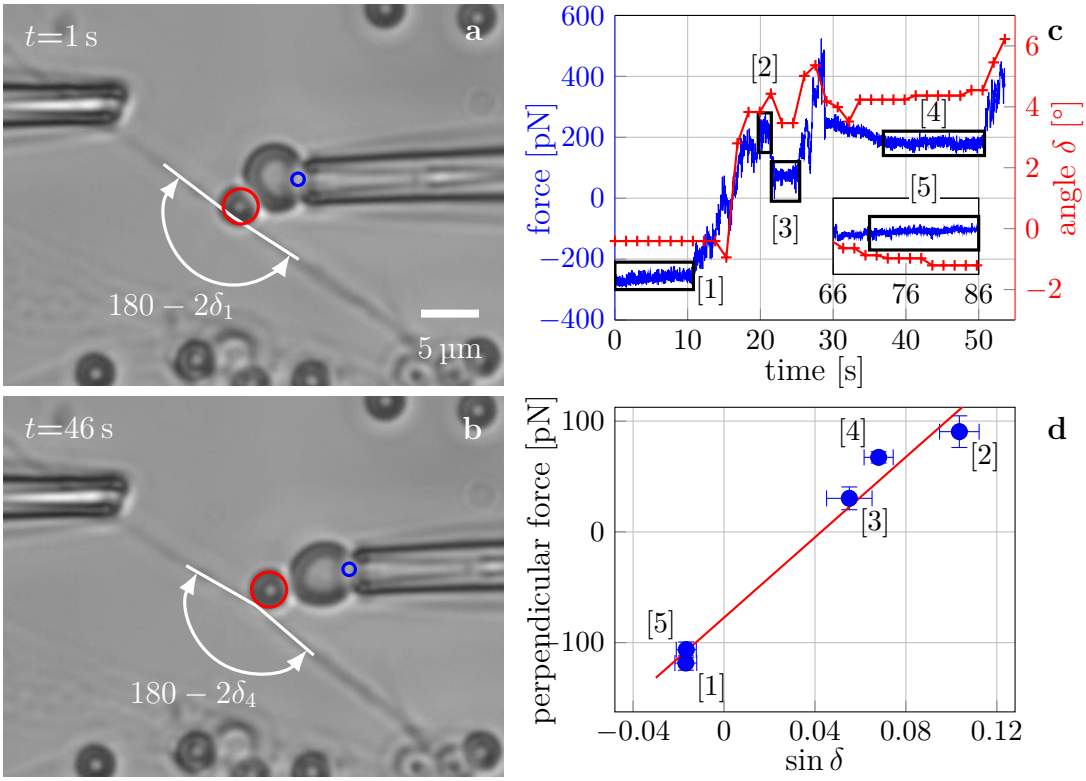

Figure 2.3: Illustration of BFP experiment. **a**: RMP adjusted to slightly 'push' the axon and deform it (corresponds to label *[1]* in the graphs). Tracked bead is indicated by the red outline, the pipette anchor by the blue ring. **b**: RMP adjusted to 'pull' the axon (corresponds to the label *[4]* in the graphs). **c**: Time course of the force measured on the probe F in blue, and time course of the angle δ in red, measured every 10 frames. Black boxes designate stable plateaux configurations. **d**: The points correspond to averaged quantities of the like-labelled plateaux in the panel **c**, the red line represents linear interpolation, its slope corresponds to the double of axon tension $2T$, and intercept to the offset of probe calibration. Error bars indicate standard deviation of the time-averaged quantity during the particular plateau.

2.4.4 Experiment processing

The quantitative results of the experiment outlined in the section Procedure are obtained by processing the videorecording. While the probe stiffness k is readily known from single a suitable frame, time course of extension $\Delta x(t)$ has to be extracted by tracking the pipette tip anchor and the centre of the SB throughout the video. $\Delta x(t)$ directly determines the time course of the applied load $F(t)$, and in combination with deformation angle $\delta(t)$ allows to calculate axial mechanical tension T of the manipulated axon.

BFP tracking

Despite the BFP technique is more than 20 years old, no freely-available dedicated processing software was available to analyse BFP recordings. In previous works, the pipette tip was not tracked, but its position was inferred from the piezoelectric controller feedback; the SB was tracked by fitting a Gaussian blob onto its intensity profile (Husson et al. 2009; Pincet and Husson 2005), or the edge of the SB was detected (W. Chen, Evans, et al. 2008; Y. Chen et al. 2015). This form of SB tracking offers high precision and speed, it however requires high contrast and stable focus, clear field and optimal axial alignment of the probe and the sample (cf. fig. 2.4a); these conditions were not always met in our experiments (fig. 2.4).

We decided to implement a custom-made tracking tool in Matlab, tailored for more general (and suboptimal) conditions of our experiments. As particularly important difference with respect to older approaches, our method processes the experimental recording post-experiment, not on-the-fly. Details of the implementation are presented in the section 2.5; a short summary is provided in this section.

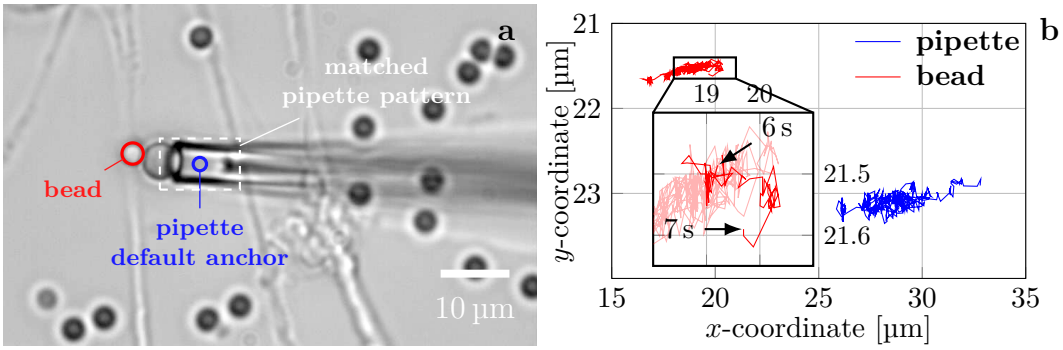

Figure 2.4: Illustration of BFP experiment tracking. **a**: A pipette with an aspirated RBC and an SB attached to an axon can be seen in the video frame. Tracked objects are delineated in colours: the SB in red, for which the coordinates of centre are recorded; the RMP tip in white, for which the coordinates of reference point (usually centre, in blue) are recorded. Note, that the probe and the sample are not aligned exactly axially (cf. figs. 2.3a and 2.3b). **b**: The recorded positions of SB centre (red) and RMP anchor (blue) during 7 s of recording. In the magnified inset, particularly the last second of SB trajectory is highlighted. Note that while the SB moves along the direction of moving pipette $\Delta x \sim 1\,\mu m$, it moves much less in the perpendicular direction $\Delta y \sim 0.1\,\mu m$.

As delineated in fig. 2.4a, two objects are being tracked in the video: the SB and the RMP. The tracking of the SB has been implemented as a circular object detection. While precision of this approach might be inferior to Gaussian blob fitting (W. Chen, Evans, et al. 2008; Evans, Ritchie, and Merkel 1995; Simson et al. 1998), it is more robust in conditions of shifting focus, which disrupts the intensity profile of the bead. The upper bound of typical uncertainty of SB tracking is $\lesssim 50\,nm$.

The tracking of the RMP is based on two-dimensional cross-correlation with a user-selected pattern; typical extend and positioning of the pattern is delineated in fig. 2.4a.

The uncertainty of the pattern detection is typically ($\lesssim$10 nm) negligible as compared to the SB detection.

Calculation of tension

The coordinates of points in fig. 2.3c denoted $(\sin\delta, F_\perp)$ corresponding to individual plateaux, were obtained as time averages over the corresponding plateau timespan. For example, for the time interval (t_0, t_1) corresponding to the plateau labelled *[1]*,

$$\begin{aligned}\tau_1 &= t_1 - t_0\\ F_\perp|_{[1]} &= \sin\theta_1 \,\frac{1}{\tau_1}\int_{t_0}^{t_1} F(t)dt \mid \theta_1 = \angle(\text{straight axon axis, pipette axis})\\ \sin\delta|_{[1]} &= \sin\left(\frac{1}{\tau_1}\int_{t_0}^{t_1}\delta(t)dt\right)\end{aligned}$$

And the error bars are standard deviations of these time averages.

The mechanical tension T in the measured axon is determined from the force balance at the point of axon deformation, perpendicular projection of the force incurred by the probe, $F_\perp$, is countered by the normal projection of axon intrinsic mechanical tension T,

$$\begin{aligned}F_\perp &= 2T\sin\delta\\ T &= \frac{F_\perp}{2\sin\delta}.\end{aligned} \tag{2.2}$$

The tension is extracted by linear regression of the measured data (fig. 2.3d), where T is given by the slope (i.e. the slope is $2T$), and non-zero intercept indicates calibration error. At this technique, it can be difficult to determine unstrained state of the RBC and therefore proper distance x_0, however measuring $\geq$3 plateau configurations allows us to circumvent the assumption of zero intercept.

The error of T is readily estimated from the quality of each fit, which is returned as its standard deviation $\sigma(T)$, and reported with each result, so that $T = (\bar{T} \pm \sigma(T))$. The values used for calculation of T are obtained by averaging over a static configuration of force plateaux, which reduces the measurement error, ideally as $\sim 1/\sqrt{f}$, where f is the number of averaged frames. Each plateau lasts more than 1 s at the rate 65 fps.

The uncertainty of the experimental procedure (i.e. the uncertainty from partial measurements) is given by the error of force measurement $F_\perp \sim k \cdot \Delta x$, $\delta k \approx 20\,\%$, $\delta\Delta x \approx 10\,\%$ (typically $\sim$50 nm for $\sim$0.5 µm). For the angle $\delta \approx 2°$, and $\Delta\delta \approx 0.5°$, $\delta(\delta) \lesssim 25\,\%$, so $\delta\left(\frac{1}{2\sin\delta}\right) \approx 30\,\%$. The total measurement uncertainty is thus approximately $\delta T \approx \sqrt{0.1^2 + 0.2^2 + 0.3^2} \approx 40\,\%$. Which is likely improved by the time averaging of the measured values. The largest uncertainty is obviously given by the system geometry, while the tracking is the most accurate.

2.4.5 Distribution of tension in population of OSN axons

The presented way of BFP application is novel, we therefore faced many obstacles. The most common drawback was failing streptavidin-biotin link between the RBC and SB, this limited number of plateaux we were able to achieve in a single measurement. Out of several dozen experiments, we obtained 7 with ≥3 stable plateaux (from 6 unique explants from 4 mother animals). For each of those measurements, we quantified the mean value and standard deviation of axon mechanical tension, $T_i = (\bar{T}_i \pm \sigma(T_i))$. Each result was then represented by a Gaussian distribution of the given parameters $\mathcal{N}(\bar{T}_i, \sigma^2(T_i))$, see fig. 3.21. And finally, the distribution of tension in axonal population $p(T)$ was estimated as a normalised sum of the individual distributions

$$p(T) = \frac{1}{N} \sum_{i=1}^{N} \mathcal{N}(\bar{T}_i, \sigma^2(T_i)).$$

The population distribution $p(T)$ was used to calculated mean tension, as well as interquartile range, see section 3.4.2 in Results.

2.5 BFPtool implementation

With the increasing amount of BFP experimental data to analyse, we decided to systematically develop a software addressing this task. We gradually built a program with core functions capable of robust processing of general BFP experimental recordings[2] and extracting the time course of applied force, $F(t)$. At the same time, particular features of our study lead us to implement precise pipette tracking, a novel feature, not included in scant earlier analytical BFP tools. We understood such software might be for a benefit of wider community using BFP, for experienced groups to broaden the scope of their analyses, and for newly interested groups, to facilitate extraction of general results. We therefore elaborated on the code, largely extended and debugged it, and released it to the community as an open-source program with an intuitive graphical user interface (GUI) to assist user with the tasks.

The tool has been implemented as a Matlab application package, bundled into an application installation file **BFPTool.mlappinstall**. The application was tested in Matlab version 2015b and 2016a with Image Processing Toolbox, under Linux (Ubuntu 16.04), Windows 10, and Mac OS 10.9 and later. It is accompanied with a user guide, tutorial and essential documentation, while the code is extensively commented. The software was published as (Šmít, Fouquet, Doulazmi, et al. 2017), and is freely available at (Šmít and Doulazmi 2017).

Workflow of the software is shown in the fig. 2.5. The red nodes indicate core functions of the software, while the blue nodes are optional features at the convenience of the user. The software was implemented for general BFP use, and is not adapted to calculate axon tension as presented in the section Calculation of tension.

[2] The methods are not limited to our experimental setting.

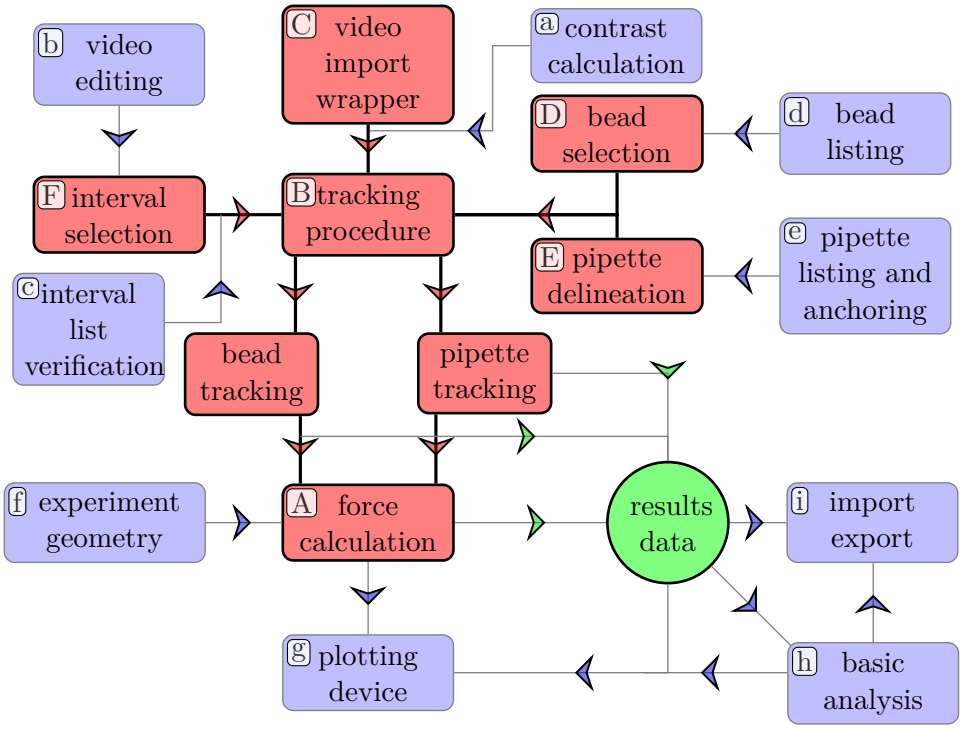

Figure 2.5: Illustration of the program workflow. The red nodes represent core program methods, which perform actual calculations, tracking and data processing. They are referred to in the text by capital letters. The blue node represent mostly supportive and convenience methods, which allow the user to customise and adjust the analysis. They are referred to in the text by lower-case letters.

2.5.1 Computational features

The methods used to calculate the force time course (*A* in fig. 2.5) and all the related data are incorporated into the Matlab class *BFPClass*. The instances of this class are constructed with initial information about the experiment (e.g. geometry, tracking settings, processing time interval), they store results (e.g. bead/pipette coordinates, force time course) and perform some of the complementary tasks (e.g. plotting, probe stiffness calculation). The class sequentially calls two external functions (*B* in fig. 2.5) to track the bead (*TrackBead*) and the pipette tip (*TrackPipette*) in the provided time interval (*F* in fig. 2.5), and calculates the force based on the returned coordinates.

Bead tracking

The bead tracking algorithm, function *TrackBead*, is based on Matlab's circle detection function *imfindcircles* from the Image Processing Toolbox, which implements a circular Hough transform (Atherton and Kerbyson 1999; Ballard 1981; Duda and Hart 1972; Yuen et al. 1990), either two-stage or phase coding variant (see reference at (The Math-

works, Inc. 2017a)). Initial bead coordinate is preselected by user (D in fig. 2.5) to track the correct bead, in case there are several beads in the field. Both algorithm variants are applied on each frame, on the area around the last confirmed coordinate of the tracked bead. A list of potential candidates is assembled from thresholded detection scores based on the *imfindcircles* detection metric $M_{b,i}$ (index i numbers the candidates) and distances d_i of each candidate centre from the centre of the last known position of the bead. The radius of the candidates must belong to the user-defined range $(R_<, R_>)$.

The bead metric is value of the Hough accumulator array for the given pixel, returned by the *imfindcircles* method, typically in the range $M_{b,i} \in (0, 3)$. A distance factor $f_i = \frac{\max(d_i, R_<)}{R_<}$ is used to decreases the weight of more remote candidates; the final sorting score of each candidate i is $\frac{M_{b,i}}{f_i} = \frac{M_{b,i} R_<}{\max(d_i, R_<)}$. The highest score, $M_b = \max\left(\frac{M_{b,i}}{f_i}\right)$, is selected as the match, the coordinate of the corresponding centre is logged and used to calculate distance d_i in the following time frame. The centre of the bead is detected with sub-pixel precision, based on the accumulator array results. The method robustly detects also partially obscured objects, however the precision decreases as more edge pixels are covered. The detection accuracy depends on the bead size and image quality, and is typically in the range (30–50) nm for intermediate conditions.

Pipette tracking

The pipette tracking algorithm, function *TrackPipette*, uses pattern matching, based on two-dimensional normalised cross correlation (J. P. Lewis 1995), implemented as Matlab function *normxcorr2* (see reference (The Mathworks, Inc. 2017c)), of a user-delineated template of the pipette tip (E in fig. 2.5) with the current video frame. After the template is repeatedly matched, being moved pixel by pixel across a prospect area in the frame, the correlation coefficients (for each template position ij), are saved in a 2D array, $M_{p,ij}$. The best match, $M_p = \max(M_{p,ij})$, is determined at single-pixel precision, and the value $M_p \in (0, 1)$ represents the pipette tracking metric value for the given time frame, with the corresponding pixel coordinate (i_0, j_0).

The array $M_{p,ij}$ is then interpolated in the vicinity of (i_0, j_0) by an elliptical paraboloid to determine the coordinate of maximal correlation with sub-pixel precision, typically $\lesssim$10 nm. The pipette detection is generally very robust and stable during the recorded time course; more precise than the detection of the bead.

Note that the both tracking methods contain quality-control metrics (in addition to M_p and M_b) and adaptive sensitivity. In case of poor image quality and underperforming detection metrics, the detection thresholds are automatically relaxed, resulting in less precise but more robust detection; conversely the thresholds are increased, if the image quality is satisfactory and metrics strong. The tracking methods can also employ auxiliary functions, like adaptive pipette pattern size, or adaptive bead radius; these are used only in case of low fidelity metric, due to extra computational cost.

Calculation of the force

The bead and pipette tracking procedures results determine the RBC deformation at any given time, $\Delta x(t) = x(t) - x_0$. The force calculation is performed in linear regime of force-extension relation of the eq. (2.1), i.e. $F(t) = k \cdot \Delta x(t)$, where k is the stiffness of the probe. The tool contains a GUI feature to measure probe geometry (i.e. R_p, R_c and R_0) directly in the video (f in fig. 2.5).

2.5.2 Interface features

The software interface is designed to import experiment recording of wide range of formats (C in fig. 2.5). Standard Matlab-supported formats include AVI, MP4, MOV, WMV, complete list can be found at (The Mathworks, Inc. 2017d). A standard format used in biophysics, TIFF, is supported through LibTIFF library (see (The Mathworks, Inc. 2017b)). For convenience, both types of data access were wrapped into a class *vidWrap*, which provides unified programmatic interface to work with the video data.

As indicated by blue nodes in the fig. 2.5, the GUI offers many supporting functions. Upon the video upload, user can perform video quality analysis (a in fig. 2.5; the contrast and contrast variability metric), and remove sub-optimal frames from the processed interval (b in fig. 2.5), while internal series of verifications checks the consistency of user inputs (c in fig. 2.5).

User can create a list of searched objects (d and e in fig. 2.5) to optimise the processing results. Once the results are generated, it is possible to perform basic fitting and analysis of the data (h in fig. 2.5) and visualise them (g in fig. 2.5) in a graph embedded in the GUI. All the data, graphs, and settings of the current session, can be exported (i in fig. 2.5) as a MAT file compatible with any Matlab-running machine, or as CSV data file for further analysis.

2.6 Mathematical tools for data analysis

In this section, we will shortly introduce mathematical methods and measures we use in the Results.

2.6.1 Axonal network statistical descriptors

During the analysis of network graph (as described in section 2.2.4), all closed cordless loops within the subfield (not closed by the edge of the field) were detected. Total length of the network in the field and the number of vertices were extracted. Some of the less obvious statistical descriptors used are:

circularity measures how circular the loops are; given as $c = \frac{4\pi A}{P^2}$, where A is loop area and P is its perimeter, thus $c = 1$ means perfect circularity and $c = 0$ means a linear object.

eccentricity measures eccentricity of the ellipse best fit to the loop; $e = \frac{\sqrt{a^2-b^2}}{a}$, where a is semi-major axis and b is semi-minor axis. The code for ellipse fit was adapted from (Chernov 2009), based on (Fitzgibbon et al. 1999).

ordering *nematic parameter*, measures the anisotropy of the network; obtained as the largest eigenvalue Q of orientational tensor

$$Q_{ab} = \frac{3}{2}\frac{1}{L}\sum_i \left[u_a^{(i)} u_b^{(i)} v^{(i)} - \frac{1}{3}\overleftrightarrow{1}_{ab}\right],$$

where i numbers all segments constituting the network, $u_a^{(i)}$ is a-component of unit vector of segment i, $v^{(i)}$ is length of segment i, $L = \sum_i v^{(i)}$ is total length of all network segments, and $\overleftrightarrow{1}_{ab}$ is unit operator. Note that the ordering tensor is weighted by lengths of individual segments $v^{(i)}$ in our implementation. The eigenvector of the largest eigenvalue is called *director* and determines the direction of largest alignment. $Q = -1/2$ means isotropic two-dimensional planar system, $Q = 1$ means perfectly aligned system (Tasinkevych and Andrienko 2010).

angle mean or median vertex angle; calculated based on distribution estimated by Matlab kernel method from a set of vertex angles manually selected by the user (if ambiguous), see section 2.2.4.

2.6.2 Transformation of probability distribution

We first introduce notation. An experimentally obtained distribution of a random variable X (e.g. by smoothing a measured histogram) is denoted as $\mathrm{PDF}_{\mathrm{exp}}(X)$, in contrast, an ideal distribution of the same variable X is denoted as $\mathrm{PDF}(X)$. In case a specific model distribution is used to approximate an ideal distribution, e.g. a lognormal, the symbol would be $\mathrm{PDF}_{\log}(X)$.

Based on the equation for static equilibrium of zipper vertex, eq. (3.9) (see section Analysis of zippers in the Results),

$$S = 2T\left(1 - \cos\frac{\beta}{2}\right)$$

we transformed the measured distribution of tensions, $\mathrm{PDF}_{\mathrm{exp}}(T) \equiv p(T)$ into a theoretically predicted corresponding distribution of angles $q(\beta) \approx \mathrm{PDF}(\beta)$, for a constant value of adhesion parameter S. After such change of coordinates, $p(T) \mapsto q(\beta)$, the distribution conserves the probability, i.e.

$$\begin{aligned} p(T)dT &= q(\beta)d\beta \\ p(T)dT = p(T(\beta))\frac{1}{\left|\frac{d\beta}{dT}\right|}d\beta &= q(\beta)d\beta \\ \frac{p(T(\beta))}{\left|\frac{d\beta}{dT}\right|} &= q(\beta), \end{aligned} \tag{2.3}$$

where the Jacobian for transformation (inverse of eq. (3.9))

$$\beta = 2\,\mathrm{acos}\left(1 - \frac{S}{2T}\right) \tag{2.4}$$

is given (rewritten in terms of β) by

$$\left|\frac{d\beta}{dT}\right| = 2\frac{-1}{\sqrt{1-\left(1-\frac{S}{2T}\right)^2}}\frac{S}{2T^2}$$

$$\frac{1}{\left|\frac{d\beta}{dT}\right|}(\beta) = \frac{S}{4}\frac{\sqrt{2\left(1-\cos\beta/2\right)-\left(1-\cos\beta/2\right)^2}}{\left(1-\cos\beta/2\right)^2}. \tag{2.5}$$

Expressing experimental distribution of tension $p(T)$ in terms of coordinates β, $p(T(\beta))$, and inserting eq. (2.5) into eq. (2.3), we obtain

$$q(\beta) = p\Bigg(\underbrace{\frac{S}{2\Psi(\beta)}}_{\equiv T(\beta)}\Bigg)\frac{S}{4}\frac{\sqrt{2-\Psi}}{\Psi^{3/2}}, \text{ where } \Psi(\beta) \equiv \left(1-\cos\beta/2\right). \tag{2.6}$$

This relation is used in several sections, notably in section 3.5.3, to estimate parameters relating random variables by comparing their experimental distributions, to relate geometric and biophysical features of the system, or to compare model-predicted effects to the experimental observations.

Chapter 3

Results

3.1 Observation of olfactory sensory neurons

We extensively covered the development of mammalian nervous system in the Introduction, particularly axon tract formation (section 1.1.1), guidance (section 1.1.3) and axon-axon interaction (section 1.1.5), and in detail explained the current understanding of the processes in context of the OS, in the section Olfactory system. It the previous studies (Honig et al. 1998; Kalil 1996; C. H. Lin and P. Forscher 1993; Tang et al. 1994; Van Vactor 1998), focus was mostly placed on the GC navigation mechanism, driven by chemotaxis or machanotaxis; the role of the GC was understood as a guarantor of axon proper targeting. In line with such assumption, a role of axon's shaft was largely reduce to a passive element of the system, a trail which does not undergo changes, but serves as an immutable guidance line for the incoming GCs of other axons (section 1.1.5).

There are however also other aspects of the process of axon fasciculation, which have not received their fair share of attention. The tight bundle formation and robust conservation of the fascicles strongly implicates role of adhesion between axon shafts, yet very little is known about the interactions between shafts, its dynamics, the underlying biophysical mechanisms and their potential regulative and functional role in axon fasciculation. In the present study, we chose to analyse these overlooked interactions and the resulting fasciculation/defasciculation processes in a convenient setting of mouse OE. We chose this model system for the features it exhibits during normal development *in vivo*, the precise projection, massive fasciculation, sorting, and defasciculation, as detailed in section 1.2; large and tight bundles are formed, coalescing into the ON, which provides an opportunity for extensive interactions between shafts.

To directly image fasciculation and defasciculation dynamics of mouse OSN axons and perform manipulation experiments on individual axons in order to study their biophysical properties, we chose to carry out the study on embryonic OE cultured explants grown on a permissive planar substrate; such experiments are not viable *in vivo*. These experiments permit direct observation of the processes on local scale, both spatially ($\sim$1 µm) and temporally ($\sim$1 min). We recorded a time lapse of OSN axons outgrowing from the explant and observed extensive interactions between their ASs, leading to zippering and unzippering processes, which triggered fasciculation or defasciculation, respectively. From the observed dynamics, we inferred that AS experience (i) viscoelastic changes, (ii) active forces generated by cellular motility and contractility, and (iii) adhesive interaction through CAMs. Such rich dynamics implies a huge functional potential

of dynamical interaction of ASs. We characterised the observed dynamics, assessed the biophysical parameters of these processes, and formulated a descriptive biophysical model.

3.1.1 Time-lapse observations ex vivo

The phenomena of our interest are short-lived local and easily distorted by external influence. The *ex vivo* time lapse videorecording experiments (see section 2.1) offered the necessary reductions to the complexity of *in vivo* system:

(i) the development of the axons and their dynamical interactions is observed directly and in real-time,
(ii) two-dimensional organisation offers complete, unmasked view of the observed field,
(iii) the experimental environment is under control and free of external influences,
(iv) culture can be directly manipulated either pharmacologically or using experimental devices (e.g. BFP).

The used embryonic OSNs (see section 2.1.1) are suitable for their morphological uniformity and absence of branching. Their attunement for fasciculation *in vivo* (section 1.2) provides predispositions for mutual dynamic contact interactions and formation of developing network in planar conditions *ex vivo*.

In the time lapse videomicroscopy experiments (section 2.1.2), we observed development of axonal network outgrowing from explants; large scale images are shown in figure fig. 3.2. The network exhibited frequent dynamic interactions between the ASs, local relatively rapid mechanistic processes leading to restructuring of the network, driving fasciculation and defasciculation.

From the basic qualitative observations of the developing cultures, where t=0 h indicates transfer of the prepared culture into the incubator, we observed three main stages of culture development:

0–48 h the GCs advance from the explant and initial structure of the network is formed;
48–72 h the GCs pause their growth at some distance from the explant and remain still during the period;
3–5 d the GCs start to detach from the substrate and retract, the network collapses during this stage.

The intermediate period (48–72 h) provided suitable conditions for analysis of network interior dynamics. The initial network conditions were set by the GC outgrowth (0–48 h) and culture front formation, subsequent hiatus of GC activity and motility provided stable boundary conditions; such stasis implies the system, particularly length and tension of axons, remained stable without observable fluctuations, over several hours. At the intermediate network area with minimal GC presence, mutual interaction between ASs took place, and larger bundles were gradually formed over the time course of several hours—the network coarsened (see fig. 3.1 and also fig. 2.1). The time scale of coarsening exceeded the simple viscoelastic relaxation timescale ($\lesssim$1 h) by an order of magnitude, pointing to a more complex dynamics taking place.

The observed coarsening—reduction of total network length—was approximately linear in time, however the time range was too short for any conclusions. In recorded time lapse sequences of network evolution in 13 explants, we typically observed that the axon network coarsened in a manner similar to fig. 3.2, or in some cases remained stable when the recording was performed over shorter time intervals. In 5 out of 6 quantitatively analysed experiments from different cultures, we observed an average reduction in length of the network of $(20 \pm 16)\,\%$, for time intervals in the range (178–295) min. The observed changes to the network topology (i.e. number of loops and vertices) exhibit similarity to topological changes observed during coarsening of two-dimensional foams (introduced in section 1.7, discussed in section 3.10), despite the character of driving forces is very different.

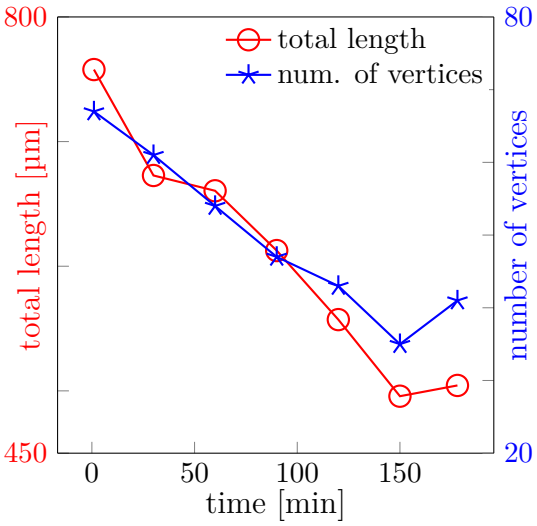

Figure 3.1: Change in network total length and number of junction points (vertices) in an interior area of the culture shown in fig. 3.2 during the first 3 h of recording. The data show gradual coarsening.

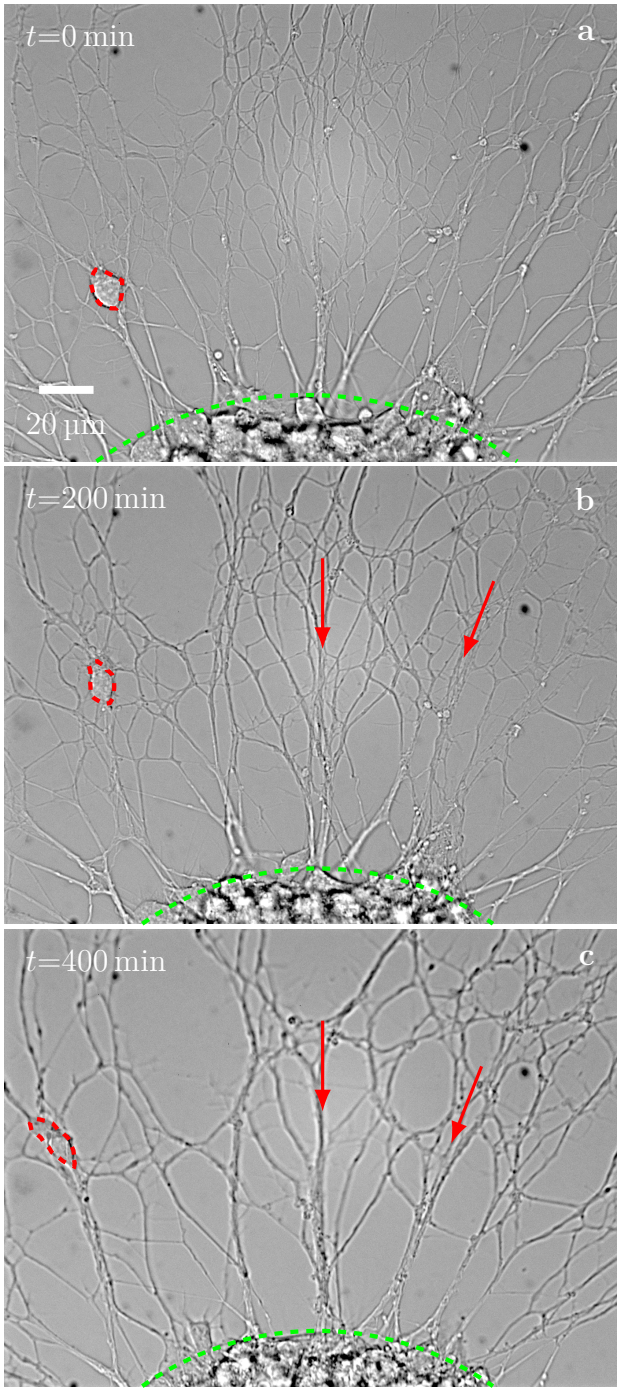

Figure 3.2: Coarsening of OSN culture over the course of 400 min. The explant edge can be seen at the bottom, marked by the green dashed line. The majority of the GCs is on the network periphery, beyond the upper edge of the field. The axonal network obviously coarsens between the frames **a**-**c**. An OEC is outlined by a red dashed line; these cells introduce perturbations into the network and influence local dynamics. Red arrows indicate gradually developing fascicles.

3.1.2 Zippers as dynamics of local contact interactions

The interior coarsening of the network, which we observed in the time lapse recording of the explant cultures, could not be driven directly by the GC motility, nearly no GCs were present in the area and no GC-mediated fasciculation activity was occurring. We therefore inspected the recording on the local spatial scale (∼1 µm) and shorter time scale (∼1 min). We observed processes much more rapid than the network coarsening, which were, however, locally altering the network, changing its length and the number of junction points (vertices). These processes were taking place through contact interaction of shafts of axons and small axon bundles.

Two examples of the observed local AS interactions, which we call 'zippers', are shown in fig. 3.3. In those processes, it is clearly visible that two axons or small fascicles with initial contact progressively extend segment of adhesion of their shafts; we call this process *advancing zippering*. The advancing zippering leads to formation of a larger fascicle. In fig. 3.3b, we can see two such processes advancing simultaneously. Inverse process is also possible (and observed), a *receding zipper*; in such case, conditions cause the two adhering axons to reduce the length of their mutual contact and facilitate defasciculation. The zippering/unzippering processes stop once they reach new equilibrium configuration determined by mechanical forces. The transition usually lasts (≈5–10) min and covers (≈5–10) µm (see fig. 3.3), so occurs on average at velocity of $\sim 1\ \frac{\mu m}{min}$, in conditions of cultured explants.

As shown in fig. 3.4a, the zippering is abundant in the culture at this stage and

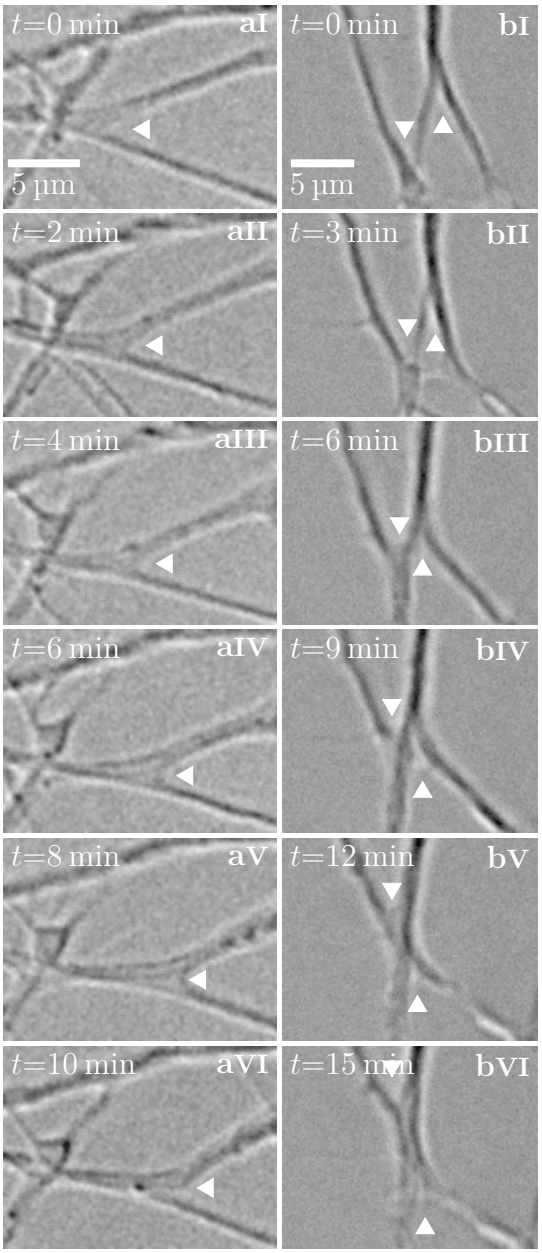

Figure 3.3: Illustration of local zippering processes. The vertex points are indicated by the white triangular arrowheads. The process timespan is at the order of (∼1–10) min and the advance covers only several micrometres. The decrease of local network length in the images is obvious.

drives coarsening and bundle formation.
The blue arrows in the figure indicate
where a new zippering process will initiate, and the red dashed lines delineate extended area of contact between participating bundles (i.e. thicker fascicle). These processes are not only responsible for decrease in network length, as shown in fig. 3.3, but may introduce a topological change by eliminating vertices from the system, as shown in fig. 3.4b. The three vertices marked by the yellow stars (fig. 3.4bI-III) gradually converge and merge into a single vertex (fig. 3.4bIV).

While the optical time lapse microscopy on the living culture provides a good picture of the local zippering processes, the dynamics itself depends on the contacts and structural features, which are below the resolution of an optical microscope. We therefore performed several scanning electron microscopy (SEM) studies of the outgrown culture, to assess the underlying configuration of filaments.

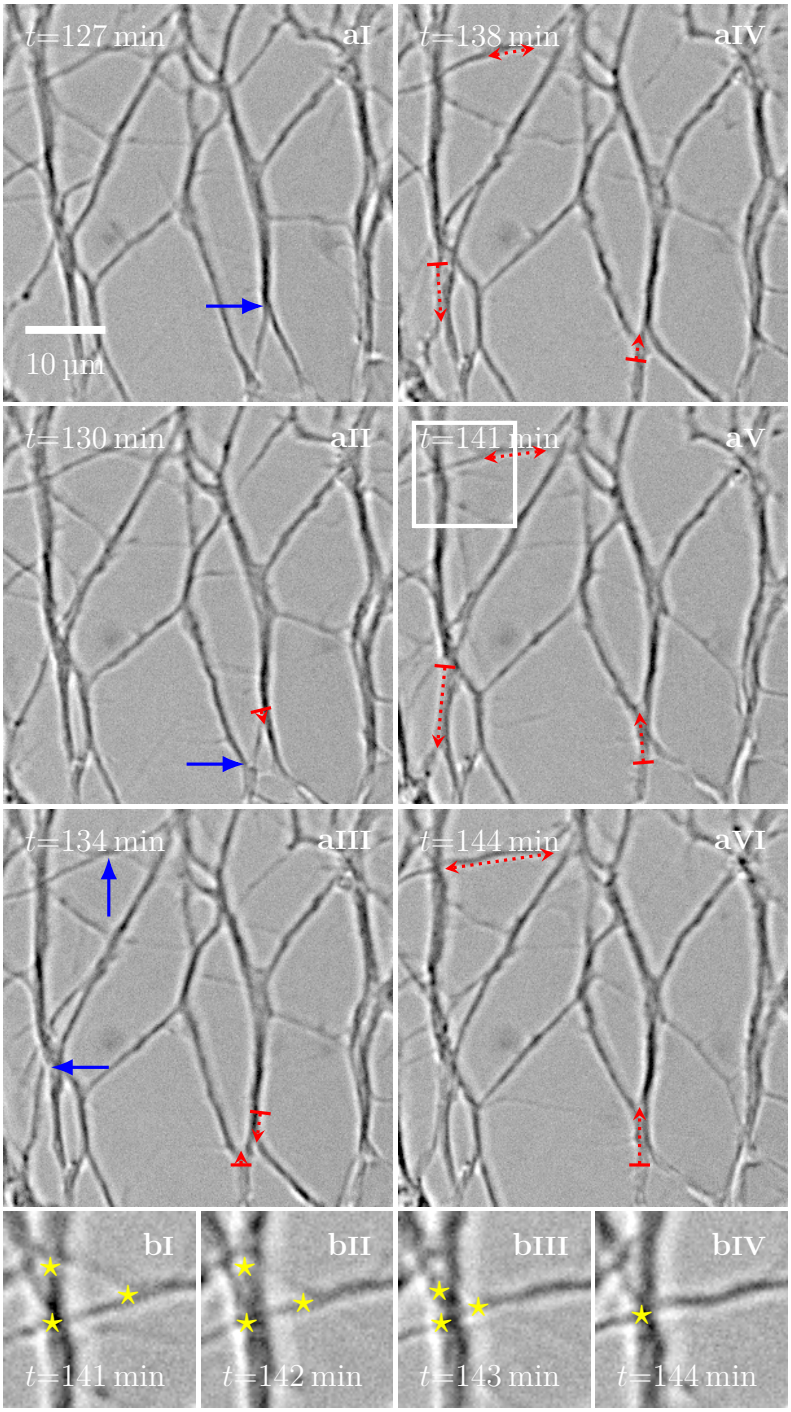

Figure 3.4: **a**: Illustration of prevalence of zippering in culture. Blue arrows indicate point where zippering will start in the following frame, red dashed arrows indicate the direction and increase in length of the advancing zipper. **b**: Magnification of area marked by the white box in frame **aV**, the zippering processes eliminate two vertices from the system (marked by the yellow stars).

3.1.3 Electron microscopy

To asses the axonal structure of the zippers, we performed SEM analyses (section 2.3) of our cultures (large scale in fig. 3.5a, magnification 350 ×). One of the relevant questions is what shape the cross-section of an axon assumes in situation of opposing bulk and boundary forces. If adhesive forces between the axon membrane and the culture substrate are stronger than the restoring forces of axonal cohesion and cellular contractility (see Dupré equation, or refer to section 1.5), the axon becomes laterally deformed and flattened[1]. On contrary, if the cellular contractility and membrane surface tension significantly outcompete the interface affinity, the axon maintains rather cylindrical shape, largely uniform in width (along its axis), and forms only limited area of contact with the substrate (detailed in section 3.3.1).

From the SEM data (figs. 3.5b and 3.6), we concluded the axons largely retain their cylindrical shape and do not become significantly flattened by the adhesive interaction with the substrate. Observing the shape of bundles and their mutual interaction, it seems that also axon-axon contact interaction does not extensively deform axon cross-section. We will explore this question in detail in sections 3.3.1 and 3.3.2.

As shown in the axonal network SEM image in fig. 3.5a, the culture is composed of vertex points connected by mostly straight edges. The network shows intricate structure even at the scale below 10 µm; such complicated entanglements and interweaves point to a very dynamic formative conditions. At the scale of order 1 µm, axons form tight bundles (fig. 3.5b) of several axons, ≈1 µm in width, which meet in often complicated junction points (marked by the blue arrow in fig. 3.5b), while side protrusions actively reach out from individual axons and probe the vicinity (marked by red arrows in fig. 3.5b). If observed under optical microscope, these ephemeral protrusions are highly dynamic and may actively interfere with other axons or even apply a pulling force onto their shafts.

Structure of the network

The vertex points (zippers) present in the network can be classified into several types depending on the character of the merger of axons or axon bundles.

simple zipper Axons or bundles meet and adhere without significant intermingling, the filaments form laminar parallel structure (figs. 3.6a and 3.6b), clearly visible segment of adhesion is present. Such zippers are free to increase or decrease the length of adhering segment according to balance of acting forces.

crossing Axons or bundles meet and cross over each other (fig. 3.6c), no segment of parallel adhesion is formed, axons maintain their direction, i.e. opposite angles at the vertex are nearly the same.

entangled zipper Bundles form complex engagement structure, axons from one bundle leave and intermingle with axons of the other bundle (figs. 3.6d and 3.6e); these configurations may extend the zippered segment,

[1] *Lateral* in this context refers to the plane normal to axon axis, i.e. the cross-section. *Flatten* refers to decrease of axon height, the distance between the substrate and axon apex.

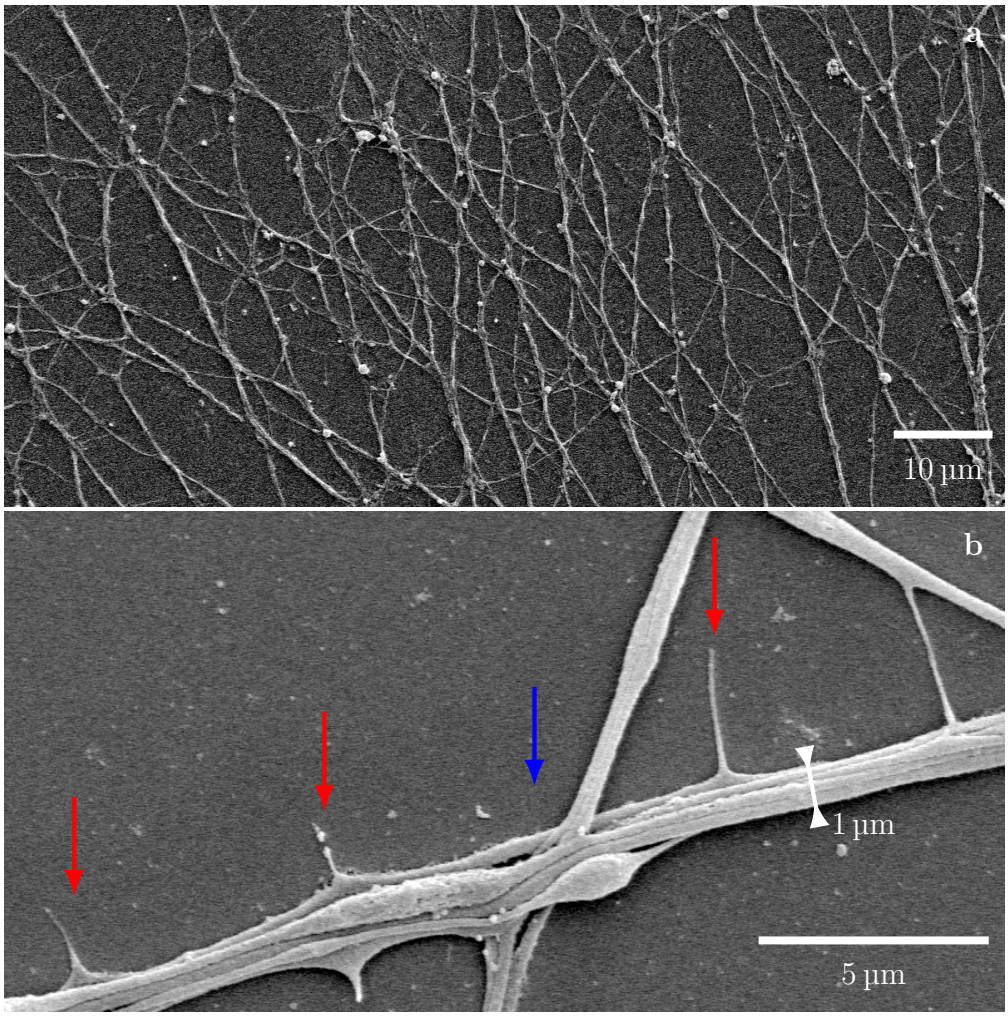

Figure 3.5: Detail of axonal network structure. **a**: low magnification (350 ×) SEM image; **b**: local detail of axon organisation showing a complex junction (blue arrow), transient side processes (red arrows) and bundle width illustration (white line).

but are prohibited from unzippering.

protrusions The side processes extending from the axons are only transient (red arrows in fig. 3.5b), the vertex points they form are not true vertices in the sense of axon-axon interaction, and therefore were excluded from further vertex analyses.

In optical microscopy, it is impossible to distinguish these types of vertices. Crossing can be inferred if no visible segment of adhesion is present and if the angles before and after the interaction (i.e. incidence and separation) are roughly equal. Entangled and simple zippers cannot be discriminated in still optical images, but undergo distinct dynamics in time lapse recordings.

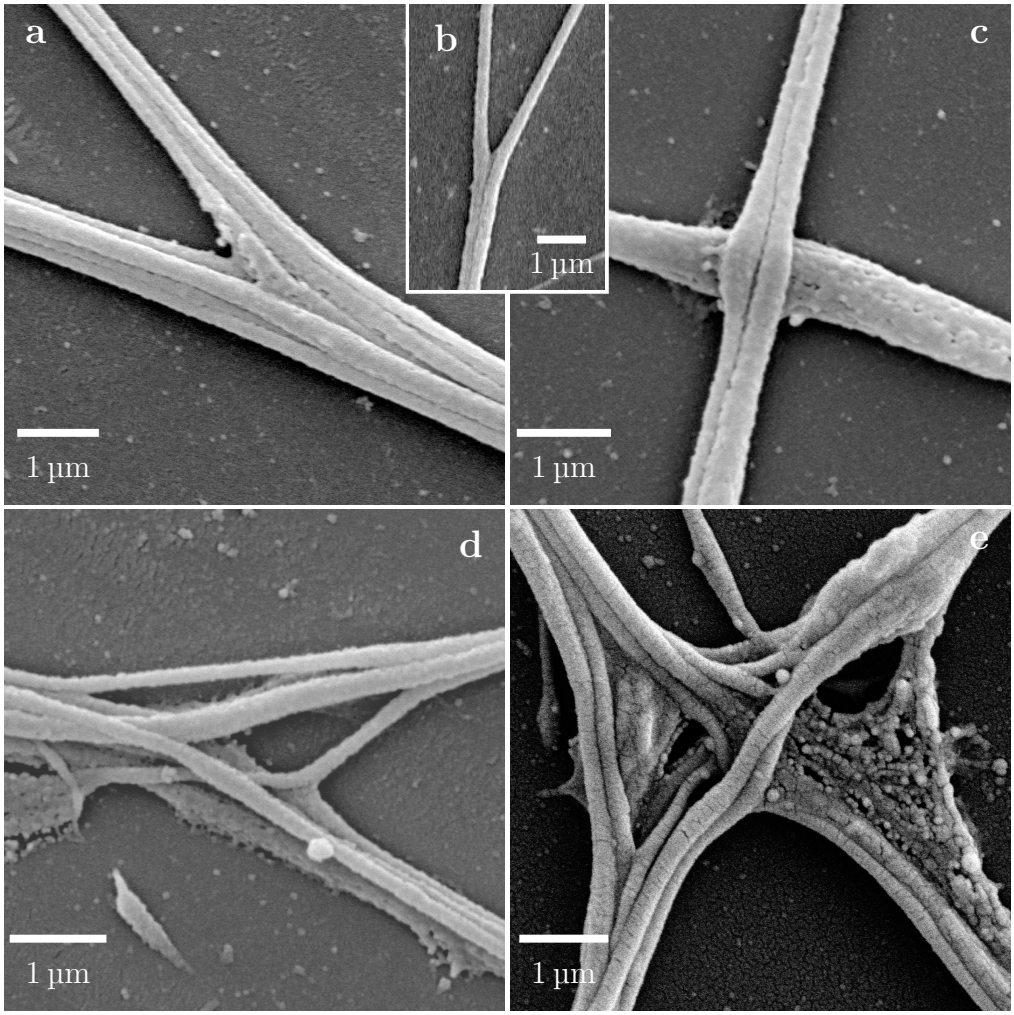

Figure 3.6: Detail of axon morphology and zipper structure. **a**, **b**: laminar vertex structure formed between individual axons (**b**) or small bundles (**a**); **c**: crossing of axon bundles; **d**, **e**: entangled vertices, such configurations are unlikely to unzipper.

To estimate share of each type of vertex in the culture, we classified the vertices in high

magnification (1000 ×) SEM images and calculated statistics (fig. 3.7). Out of the all vertices, our measurements indicate 54 % of simple zippers (134 of 247), 28 % of entangled zippers (69 of 247) and 18 % of crossings (44 of 247). The measurements show, that non-restrained vertices (i.e. capable of dynamics; simple vertices and crossings) form roughly $^3/_4$ majority of network's junction points. Under such conditions, it seems plausible that global dynamics of the network (e.g. coarsening) can arise from a collective effect of individual zipper dynamics.

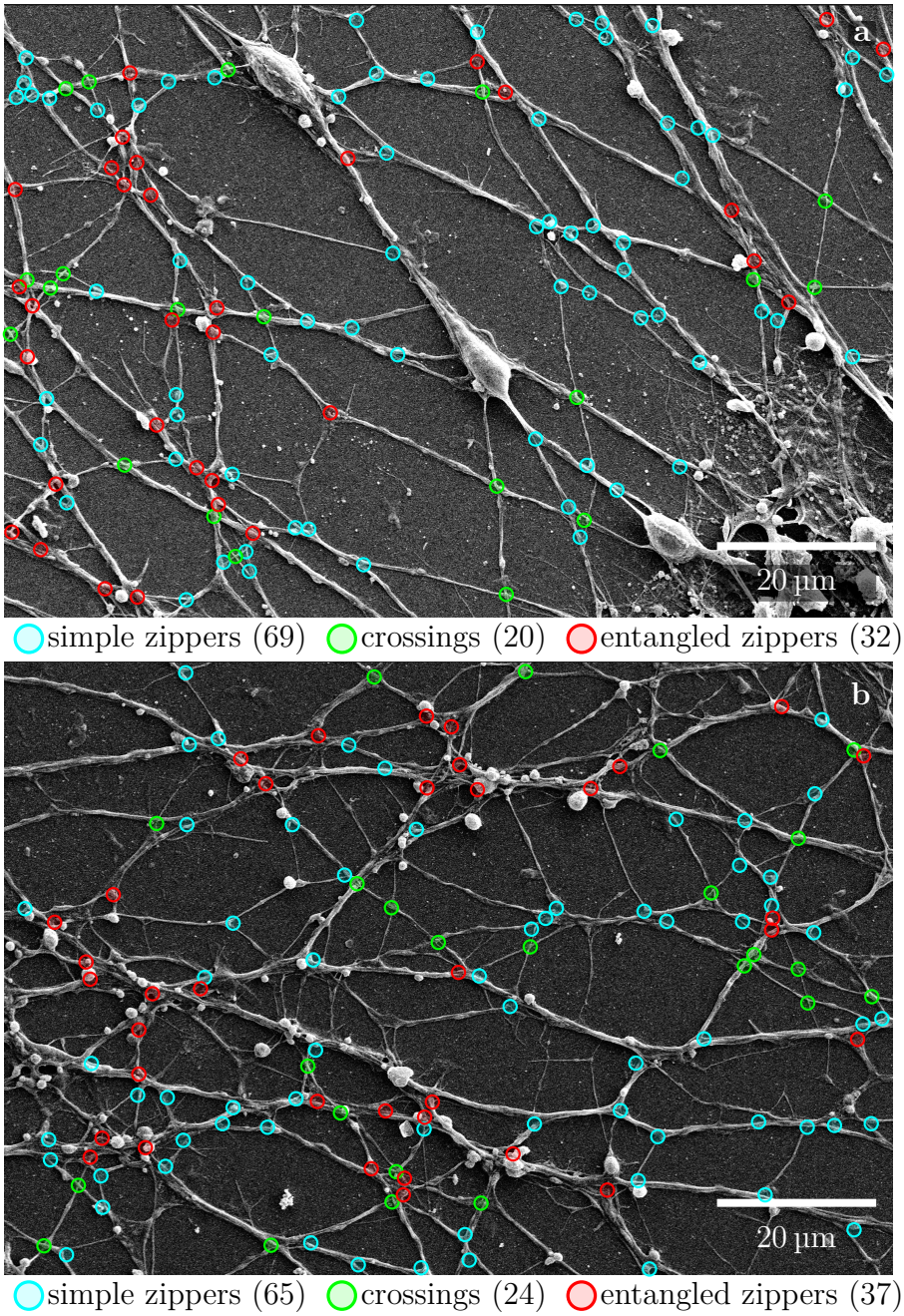

Figure 3.7: Network vertex classification. **a**, **b**: Individual vertices are classified as either simple zippers (blue dots), crossings (green dots) or entangled zippers (red dots); the vertex type counts are indicated under each frame. The two frames cover the same area of the network, and the proportion of zipper types is nearly identical. In some cases, vertices are formed by side protrusions or covered by large lamellipodium, such vertices were excluded from counting.

3.2 Zippers as an adhesion-tension competition

From the zippering processes observed *ex vivo* (section 3.1.2) and detailed static SEM images of zipper vertices (section 3.1.3), it is possible to infer, that the free energy necessary for zipper advance or bound energy restricting zipper retreat originates from adhesive contact between individual shafts. As a zipper advances, mechanical energy is obtained from bonds created at the axon-axon interface, while as a zipper attempts to recede, it has to expend mechanical energy to break established surface bonds. The contact spreading however does not continue infinitely, it is opposed by tensile/elastic forces in the axons. Advancing zipper increases the length of individual axons, which leads to increase in total tensile energy in axons; this energy needs to be obtained from the bonds on newly established interface (introduced in section 1.3.3). Therefore, a zipper can be understood in terms of competition between the energy of adhesion released during contact expansion, and the tensile energy required to extend the axons during the zipper advance.

Hypothesis 1 (Zipper as an adhesion-tension competition)**.** *The geometry of zipper stable equilibrium corresponds to the configuration of local minimum of total mechanical energy of the zipper, composed of tensile energy of the shafts and adhesive energy of mutual contact of these shafts. Such equilibrium remains static, unless it is perturbed; in such case the zipper undergoes a transition, advances or recedes, to attain equilibrium configuration corresponding to the new conditions.*

To qualitatively evaluate the proposal (hypothesis 1), we attempted to alter zipper state from pre-existing stable equilibrium. For this purpose, we used a micropipette mounted on a finely controllable manipulator, and laterally displaced one of the axons forming a zipper by roughly $\sim$5 µm as shown in fig. 3.8. Such limited manipulation does not affect the tensile or adhesion energy, but perturbs the equilibrium geometry (i.e. the angle). According to hypothesis 1, the zipper will undergo a transition to restore its original local equilibrium geometry. We observed such effect in experiment shown in fig. 3.8a: tensile energy in the displaced axon is used to disrupt the bonds along the segment of adhesion, axon shortens, zipper recedes and zipper angle (local equilibrium) is restored to pre-manipulation state. In some cases, as the one illustrated in fig. 3.8b, the experiment however yielded no dynamics, likely due to axon entanglement, as described in figs. 3.6d and 3.6e.

We decided to test the hypothesis 1 also in the inverse sense, changing the biophysical parameters (tension, adhesion) and observing induced changes in equilibrium geometry. Individual uncalibrated experiments as in fig. 3.8 cannot be easily adapted to increase axon tension, without directly affecting zipper geometry. The simplest and robust suitable experiment is to manipulate the tension of the axons using various pharmacological agents or their combinations to effectuate global change on the whole network level. The modification of tensile (or adhesion) energy density should affect the ratio between zippering and unzippering events. Significant modification to this fraction should demonstrate itself in changes to network global descriptors, e.g. total network length or number of vertices, and therefore should be readily observable and relatable to drugs action.

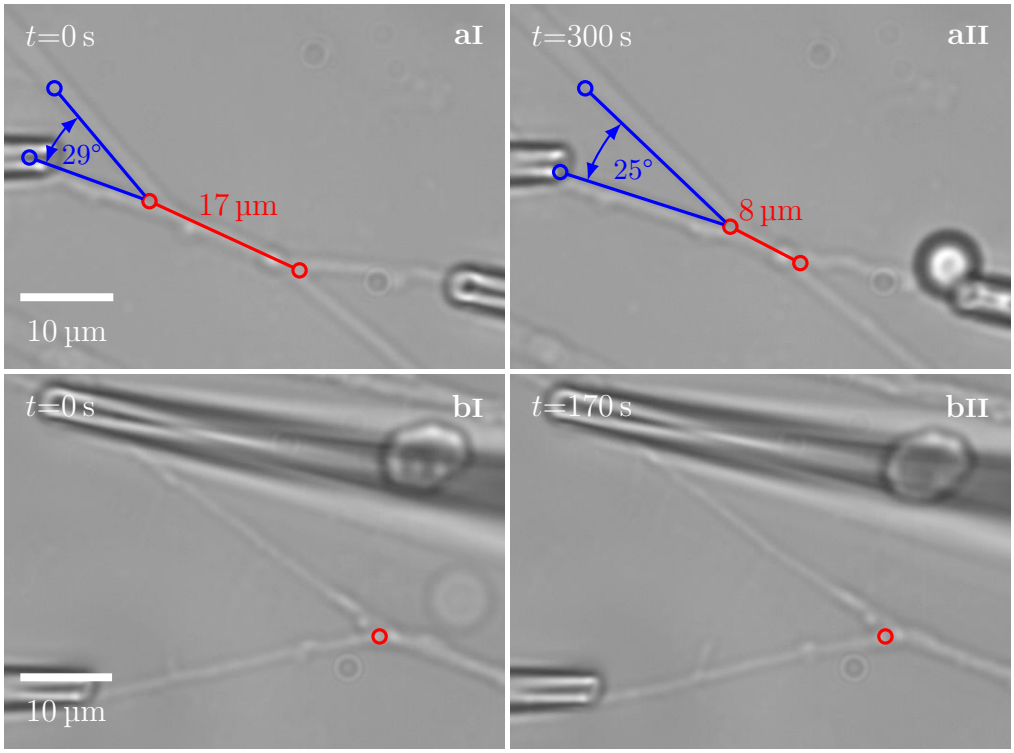

Figure 3.8: **a**: Uncalibrated unzipperng. Pipettes are positioned at the time 0 s, **aI**, and clear unzippering (red line) and decrease in angle (marked in blue) are visible at the time 300 s, **aII**. **b**: Two axons forming a zipper are dragged to the sides by a pair of pipettes, but no change in vertex position is observed within 170 s. The red circle designates the identical frame coordinate in frames **bI** and **bII**.

3.2.1 Pharmacological manipulation of axon tension

As noted in section 3.1.1, for most of the observed cultures, a spontaneous coarsening stage eventually occurs (with an onset delay of up to 2 h). This indicates that in general, zippering events dominate over unzippering events, and drive global fasciculation. In isolated cases, however, a deconstruction of fascicles and increase in network length was observed in limited areas of the network. These cases were often associated with an apparent synchronous contraction of the explant boundary, thus generating a pulling force on the axonal network (see fig. 3.9). The network is static or coarsens slowly before the explant apparent contraction, but a significant increase in network complexity (for particular segments of the network) can be observed after the explant boundary retreats. From the observation, it can be inferred that the mechanical tension in axons can be a driving force in the zippering dynamics and particularly a determining factor between zippering and unzippering. We therefore attempted a controlled pharmacological modification (see section 2.1.3) of the tension in the culture, to seek a support for hypothesis 1.

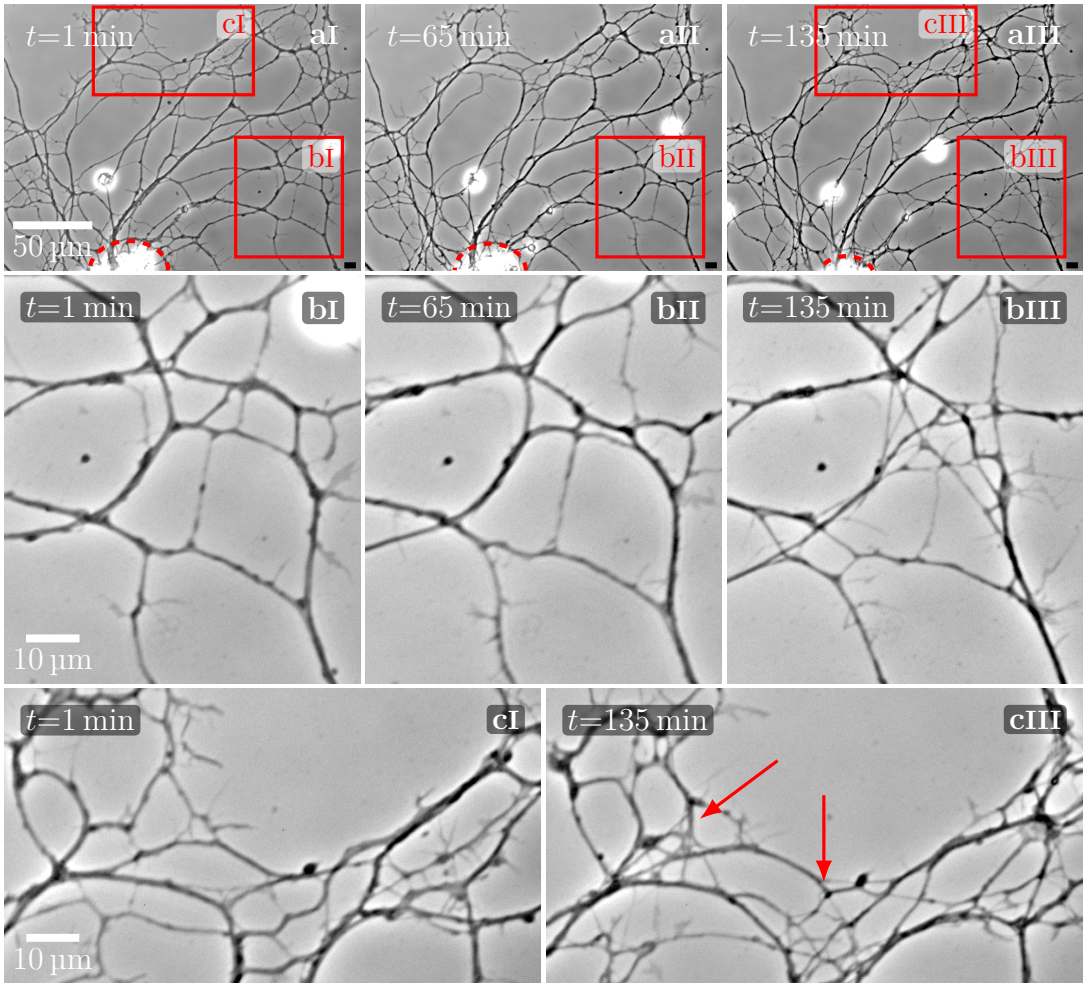

Figure 3.9: **a**: The whole axonal network in the field. Areas of defasciculation (decoarsening) are indicated by red boxes and magnified in the following frames. The explant boundary is indicated by the red dashed line; a visible retreat of the edge occurs between the frames **II** (t=65 min) and **III** (t=135 min). **b**: The subfield of the network is stable between the frames **I** and **II**. After the explant apparent contraction, a visible defasciculation occurs in the subfield **III**. **c**: Less prominent defasciculation can be observed in this subfield; areas of interest are indicate by the red arrows **III**.

Blebbistatin

One possibility to influence the tension is blebbistatin. It is a well known inhibitor of neuronal neuronal Myosin II (NMII) (Kovács et al. 2004), previously shown to decrease cell cortex/membrane tension in a variety of non-neuronal cells (Ayala et al. 2017; Fischer-Friedrich et al. 2014). In our culture system 10 µM blebbistatin dissolved in DMSO did not show any visible signs of change of AS tension, but rather had a stabilising effect on the network, as (i) spontaneous coarsening was inhibited, (ii) activity of filopodia and side-processes was visibly reduced, (iii) the zippers remained mobile. Such effects were not observed in DMSO control experiments. While the treatment with blebbistatin alone did not alter the network behaviour in the desired way, its stabilising effect allowed us to control fluctuations in culture dynamics. Therefore, in drug combination experiment, an effect of another drug could be clearly separated from random network dynamics and coarsening or de-coarsening, if the culture had been pretreated by blebbistatin.

Foetal Bovine Serum

Another possibility to alter the mechanical tension within the axons is to administer GC-stimulating factors (section 1.1.4). Such factors can modify GC motility and advance, and generate traction force, which in turn affects the AS (section 1.4.4). While specific molecular cues to such effect remain unknown, we tested FBS, which contains large variety of growth factors, which could have the desired effect on the GCs motility. Despite the 5 % FBS treatment did not significantly affect the GC activity, it reproducibly induced an apparent explant contraction, similar to the boundary retreat effect we had observed in untreated experiment (fig. 3.9). Such observation can be attributed to a cell-rounding effect of FBS on cultured neurons previously reported in (Jalink and Moolenaar 1992). The explant apparent contraction did initiate de-coarsening and increase in length of some parts of the network as shown in fig. 3.10. The area of the network in the experiment was coarsening before the drug, but within 15 min after the treatment, it exhibited de-coarsening and increase in length (within the area) by roughly 20 %.

Following the observations presented in the section Blebbistatin, we pretreated the culture with blebbistatin and applied the FBS only 1 h later. As shown in the fig. 3.11, a clear effect of an increase in length in some areas is visible. In fig. 3.11a, there was an increase of 15 %, in fig. 3.11b, despite some drift and fluctuation, an increase was ≈50 %. In the videos, we could see an apparent explant contraction (as visible in fig. 3.11a) and emergence of new loops out of junctions (inverse of the process fig. 3.4b). In the designated areas, we can state that the pull lead to prevalence of unzippering over zippering.

Cytochalasin

The FBS-induced pulling allowed us to induce de-coarsening/unzippering through increase in axon tension, so inverse process, coarsening/zippering, should be induced by lowering of the tension. Because we could not decrease the axon tension through NMII

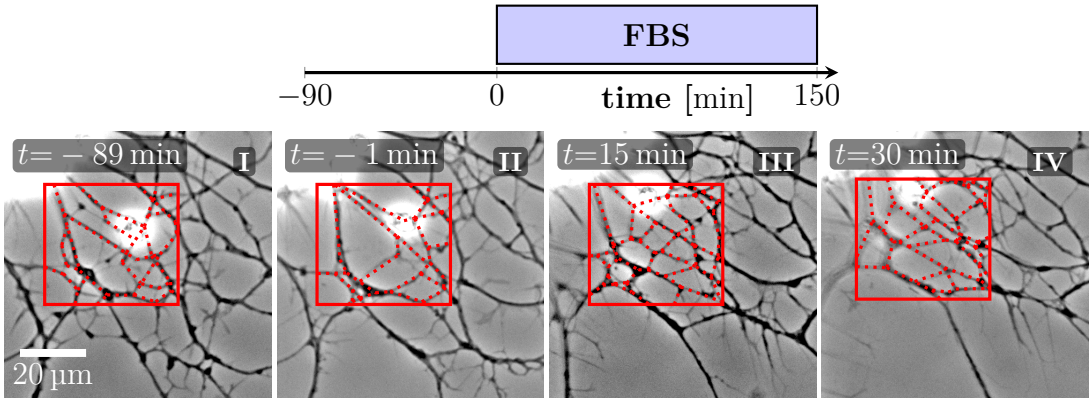

time t	−89 min	−1 min	15 min	30 min
length $\mathcal{L}$	297 µm	283 µm	354 µm	354 µm

Figure 3.10: Illustration of the effect of FBS. The scheme illustrates when the FBS was added to the culture. The subfield of interest of the measured network length is designated by the red box, the tagging marks are shown in red dotted line. Before the drug is added at the time t=0 min, network in the area slightly coarsens, after the FBS administration, area exhibits sustained de-coarsening, which represents an increase in total length of 20 %. The network however collapses short after, possibly due to explant pulling force; retreat of the explant border in the upper left corner can be seen in the images.

inhibition (i.e. blebbistatin), we tried to inhibit actin polymerisation using cytochalasin (reported in (MacLean-Fletcher and Pollard 1980)). In (Dennerll, Joshi, et al. 1988), the drug was shown to lower tension in PC-12 neurites. Observed changes in our system were consistent with the report (ibid.), coarsening dynamics induced by cytochalasin B (dissolved in DMSO) corresponds to the presumed effect of decrease in average axon tension. Total length of initially stable network (fig. 3.12aI-II) decreased after the drug addition (fig. 3.12aIII, and red squares in graph in fig. 3.12cI); the number of vertices in the field also sharply dropped (red squares in fig. 3.12cII). Average area of cordless loops (cycles) in the network increased after the cytochalasin addition (red squares in fig. 3.12cIII). These observations were even more prominent in experiments, where the background fluctuations of the culture were minimised by blebbistatin pretreatment (fig. 3.12b shown as blue half-circles in graphs in fig. 3.12c). Quantification of network features (see section 2.2.4) during the experiment time course shown in fig. 3.12cI-III indicates clear coarsening shortly after the cytochalasin treatment. The effect was not observed in experiments, where only the solvent, DMSO, was added, consistently with observation in (ibid.).

The results of experiments presented in this section support the proposal in the hypothesis 1. Increase in axon tension after explant contraction (fig. 3.9) or induced by FBS (figs. 3.10 and 3.11) shifted the competition in the zipper in favour of tensile forces, more energy was then released by axon shortening, than was expended on breaking of

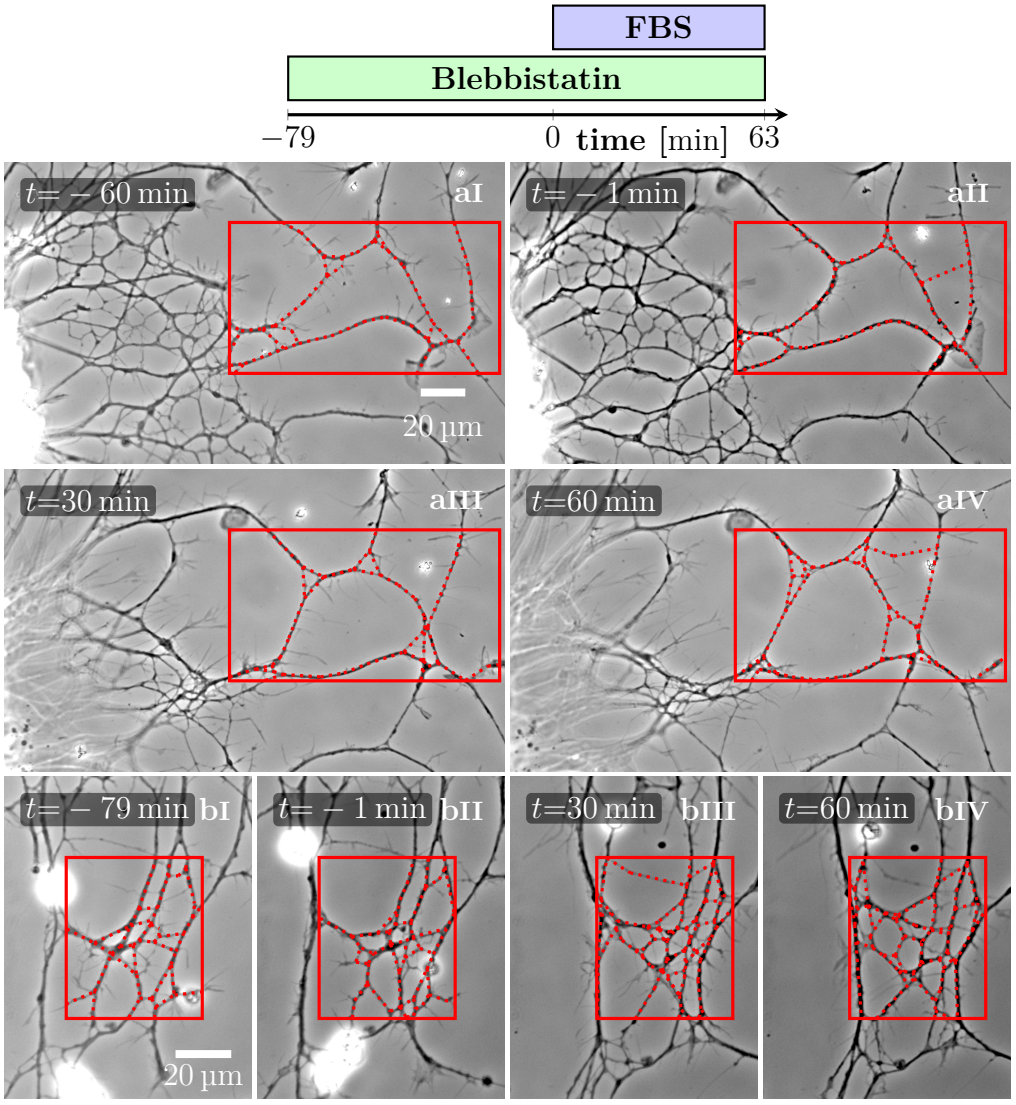

time t	−79 min	−60 min	−1 min	30 min	60 min
length $\mathcal{L}_\mathrm{a}$	N/A	449 µm	448 µm	465 µm	518 µm
length $\mathcal{L}_\mathrm{b}$	339 µm	N/A	354 µm	507 µm	480 µm

Figure 3.11: Defasciculation resulting from FBS-induced explant contraction. The scheme indicates the sequence of the experiment. Culture for pretreated with blebbistatin for stabilisation. **a**: The total length in the designated area was stable before the FBS was added, but increased considerably, due to defasciculation, after the treatment by 15 %. On the left, retreating boundary of the explant is clearly visible between **II** and **III**. Emergence of new loops is apparent in **III** and **IV**. **b**: The minor flow of the network lead to fluctuations in measurement, but initial variability was much lower than the increase after the FBS treatment, an increase of 50 %. The provided length values correspond to the red dotted lines within the red boxes.

the interface bonds, and the vertex zippers visibly retreated, while the network length was measurably increased. On contrary, decrease in axon tension induced by application of cytochalasin B (fig. 3.12) lowered the tensile energy density in the ASs and so the energy of adhesion released by contact expansion during the zipper advance was sufficient to elongate the vertex-forming axons. The drug administration rapidly induced visible coarsening of the network (figs. 3.12a and 3.12b), its total length and number of vertices decreased (fig. 3.12cI,II), while an average area of a closed loop increased (fig. 3.12cIII).

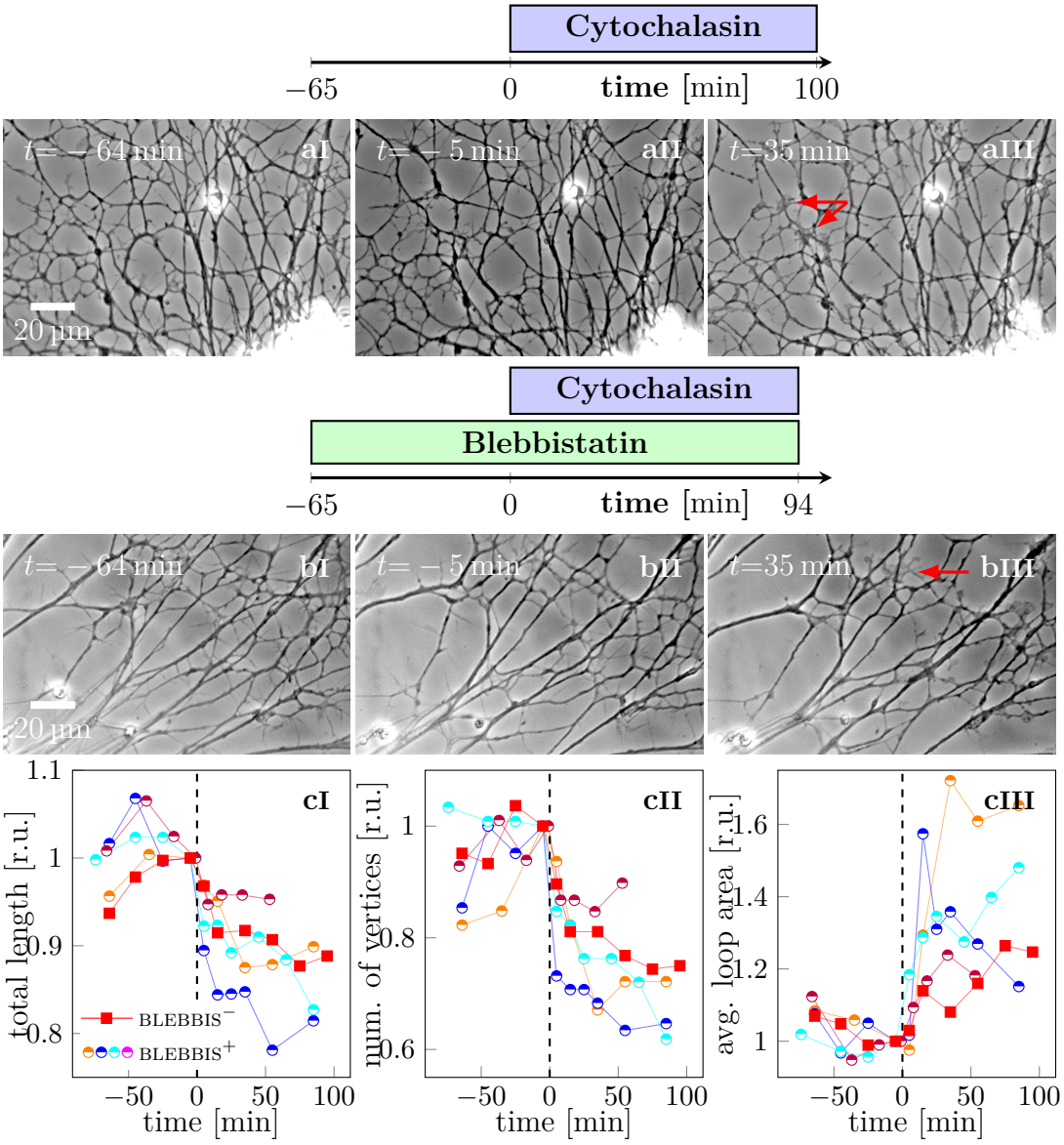

Figure 3.12: Cytochalasin induced fasciculation of axon shafts. The schemes indicate the protocol of drug administration for the experiment shown in the following image strip. **a**: Cytochalasin was applied at t=0 min, culture was not pretreated. Network is largely stable between (−64,−5) min, however visible coarsening occurs during (0,35) min. **b**: Cytochalasin was applied at t=0 min to the culture pretreated (before t= − 65 min) with blebbistatin. The network exhibits only limited change before t=0 min, but coarsens after cytochalasin treatment during the interval (0,35) min. The red arrows in **aIII** and **bIII** indicate a side-effect of cytochalasin, which induces appearance of prominent lamellipodia. **c**: Network statistics (see section 2.2.4) for cytochalasin treatment of the network. Red squares correspond to image strip **a**, blue half-circles to image strip **b**. Other marks are different experiments performed under the same protocol as experiment **b**. The data were aligned so that t=0 min corresponds to the time of cytochalasin addition in each experiment; the data were normalised by the value of the last measurement before the drug addition. Sharp change in the measures shortly after t=0 min, after a stable period preceding the addition (t<0 min), indicates coarsening induced by the cytochalasin.

3.3 Cross-section of axon and bundle of axons

The observations presented in section 3.1 illustrated the phenomenon of axonal network coarsening during experiments *ex vivo*, and pinned down its possible underlying local processes (section 3.2), as a finely balanced interplay between axon mechanical tension and inter-axon adhesion (hypothesis 1). The following sections will provide a detailed systematic analysis of biophysics supporting the interpretation of observations and proposed mechanism of action. We will gradually present the analysis of single axon biophysics, observations and experiments, relevant to the zippering phenomenon.

In this section, we provide analytical arguments regarding the cross-sectional shape of an individual axon or small bundle of axons, and combine them with inferences we can make from the SEM images shown in figs. 3.5 and 3.6. The two will then allow us to make out implications for the zipper dynamics.

3.3.1 Single axon cross-section

The following section illustrates how biophysical properties of axon and substrate determine the axon cross-section. While this explicit calculation provides an insight into axon shape under adhesion, it is not crucial for the understanding of the following sections, and can be skipped.

Energy E of axon cross section, for surface contractility $\tau > 0$ (tensile energy per membrane unit area) and substrate interface energy $\iota > 0$ (work of adhesion per unit area of axon-substrate interface), and cross section constraint constant area S.

$$
\begin{aligned}
{}^1\!/_2\, E &= \underbrace{\tau \int_0^H \sqrt{1 + \left[{}^{ds(p)}\!/_{dp}\right]^2}\, dp}_{\substack{\text{cross-section} \\ \text{free surface energy}}} + \underbrace{s(0)(\tau - \iota)}_{\substack{\text{substrate interface} \\ \text{total energy}}} \\
{}^1\!/_2\, S &= \int_0^H s(p)\, dp,
\end{aligned}
$$

where $s(p)$ determines the shape of the axon cross section (a distance from the axon axis of symmetry, see fig. 3.13a), and $s(0)$ is the semi-width of axon contact with the substrate, H is the height of the axon (i.e. distance of the apex from the substrate) and is determined by the constraining area S through a Lagrange multiplier λ. The first energy term represents contractile energy of the axon free surface, the second term is the total energy of axon-substrate interface. We now solve a variation problem to determine shape function $s(p)$, with the Lagrange multiplier λ, variable end at $p = 0$ and boundary conditions at the $p = H$, at the apex of the axon, where

$$
\begin{aligned}
s(H) &= 0 \\
s'(H) &\to -\infty,
\end{aligned}
$$

see fig. 3.13a.

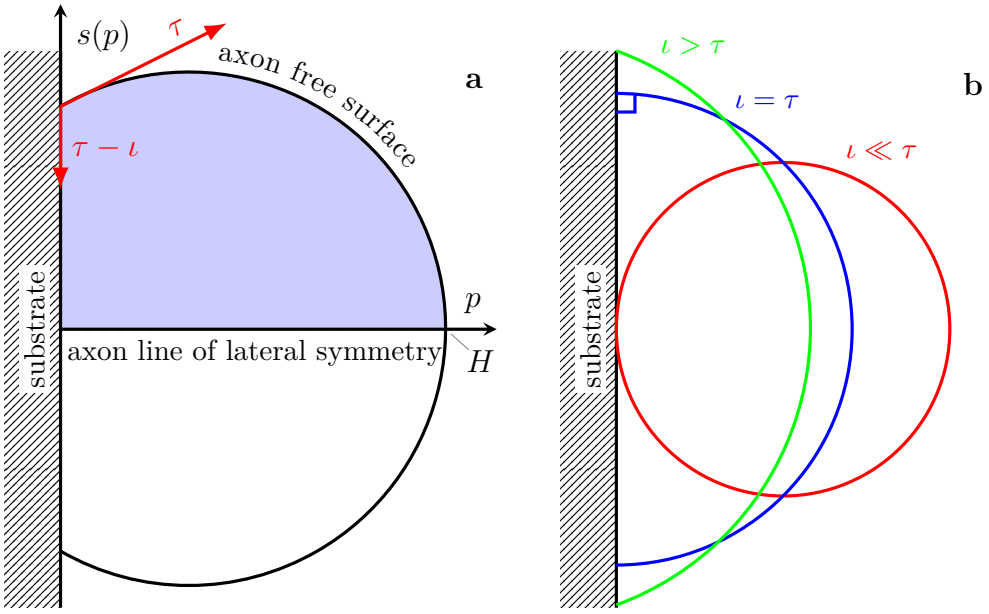

Figure 3.13: Cross-section of axon on a substrate. **a**: Axon is assumed to be laterally symmetric, only upper half (shaded in blue) is variationally optimised in eqs. (3.1) and (3.2). Parameter p describes axon height, $p = H$ denotes axon apex, function $s(p)$ describes axon surface shape in $(0, H)$. The area of axon cross-section is conserved, axon free surface is minimised, while the width of substrate wetting ($2s(0)$) depends on mutual relation of axon-substrate interface energy ι and axon free surface energy τ. Boundary optimisation determines the wetting angle (i.e. $\frac{ds}{dp}|_{p=0}$) relation, the Dupré equation, illustrated by red vectors. **b**: Optimal shapes of axon on substrate for particular values of ι with respect to τ. Optimal shape is always a circular arc, and the area between the curve and the substrate is conserved (i.e. $S = \text{const}$).

Calculating the variation $\delta[E - \lambda S]$ with the variable end at $p = 0$ (i.e. interface term) yields two equations

$$\lambda + \tau \frac{d}{dp}\left(\frac{s'(p)}{\sqrt{1 + [s'(p)]^2}}\right) = 0| \text{ for the free surface } p \in (0, H] \tag{3.1}$$

$$\tau \frac{s'(0)}{\sqrt{1 + [s'(0)]^2}} + (\tau - \iota) = 0| \text{ for the variable end } p = 0. \tag{3.2}$$

The eq. (3.2) describes equilibrium at the point of axon separation from the substrate, it can be readily solved to yield a Dupré equation,

$$\underbrace{\tan(\phi - \pi/2)}_{=\frac{\cos\phi}{\sqrt{1-\cos^2\phi}}} = s'(0) = \frac{\tau - \iota}{2\tau\iota - \iota^2} = \frac{1}{\sqrt{\left(\frac{\tau}{\tau - \iota}\right)^2 - 1}}, \tag{3.3}$$

where ϕ is the wetting angle as defined in section 1.3.3 and fig. 1.9c.

The free axon surface solution yields

$$[s(p)]^2 + \left(p - \frac{\tau - \iota}{\lambda}\right)^2 = \left(\frac{\tau}{\lambda}\right)^2, \tag{3.4}$$

which is an equation of a circular arc, determined by the boundary conditions through λ as stated above. The Lagrange multiplier λ, which scales the arc, and gives an explicit relation between the H and S, is given by the constraint

$$1/2\ S = \frac{\tau}{\lambda}\int_0^H \sqrt{1 - \left(\frac{\lambda}{\tau}p - \frac{\tau - \iota}{\tau}\right)^2}\, dp \;\middle|\; H = \frac{2\tau - \iota}{\lambda},\ \iota \in (0, 2\tau),$$

which can be solved analytically, but the resulting expression is very technical and provides no further insight.

We can investigate two limits of the solution:

1. If adhesion is weak, $\iota/\tau \to 0$, then the centre of the arc moves to $\lim_{\iota/\tau\to 0} \frac{\tau-\iota}{2\tau-\iota}H = \frac{H}{2}$ and the radius becomes $\lim_{\iota/\tau\to 0} \frac{\tau}{2\tau-\iota}H = \frac{H}{2}$, which is a cross section completely detached from the substrate (red in fig. 3.13b).
2. In the other extreme, as $\iota \to 2\tau$, the radius $\lim_{\iota\to 2\tau} \frac{\tau}{2\tau-\iota}H \to \infty$ and the centre moves to $\lim_{\iota\to 2\tau} \frac{\tau-\iota}{2\tau-\iota}H \to -\infty$, which means the cross section melts and completely wets the surface.

The tendency of gradual wetting according to the mutual values of ι and τ is shown in fig. 3.13b. As the ι increases towards 2τ, the axon affinity for the substrate is increasing, at the expense of tensile energy stored in the axon free surface. Because axon interior is (assumed to be) incompressible, the cross-section flattens and stretches.

While the calculation was performed for an axon, the same principles apply to an axon bundle, i.e. there is a surface tissue tension resulting from inter-axonal adhesive contact interactions (see section 1.5) and axonal adhesion to the substrate. On the other hand, such analogy is only valid for a bundle composed of many axons, at the size when individual axons in a bundle act analogically to particles in a liquid droplet. For small bundles (i.e. around 10 axons), the shape and packing of the bundle are determined by rather discrete character of axon-axon and axon-substrate interaction, as discussed in the following section.

3.3.2 Formation and cross-section of a bundle

In the previous section, we derived the optimal transverse shape of a single axon, if it behaves as a continuum ('liquid'). We now apply a similar approach, a competition between energy of cohesion and substrate interface, to examine optimal organisation of a small bundle of discretely interacting axons.

As concluded is the section 3.3.1, an individual axon tends to maintain circular shape unless deformed by increasing adhesive affinity to the substrate. Consulting observations from electron microscopy (EM) (section 3.1.3), it seems that the OSN axons mostly tend to preserve their cylindrical shape, which suggests their contractility is relatively high compared to the axon-axon and axon-substrate adhesions, see section 1.5. From the

AXON CONTACT AREA

fig. 3.6, axons obviously adhere to each other, but they do not 'spread over' each other, i.e. do not envelope the bundle. Because the axon circularity ($\sim {}^{\text{area}}/_{\text{perimenter}}$ ratio, section 2.6.1) is roughly preserved, then the natural tightest packing in a bundle would be hexagonal, and lower limit on axon circumference involved in adhesion would be roughly 15 %. On the other hand, the mutual contact angle of the two axons is certainly $\leq 180°$, which gives an upper limit of ≈ 35 % of circumference. Therefore, we can estimate that roughly (15–35) % of axon circumference participates in contact between two axons.

To simplify the situation, in this section, we will assume OSN axon cross-section is always circular, and ignore possible deformation effects. Under the assumption, the shape of a bundle is dictated by the strength of the discrete adhesive interactions of axons (axon-axon and axon-substrate), and transverse mechanical properties of axon shafts are rather subordinate, see section Differential adhesion hypothesis supporting such approach, and (Manning et al. 2010).

For a discrete system, it is intuitive to understand the optimisation parameters. As argued in section 1.5, the tissue surface tension of a bundle arises from adhesive forces between pairs of individual axons mediated by CAMs—we denote binding energy of one pair per shaft unit length as $A < 0$. Composition and level of expression of these molecules vary not only stochastically between individual axons, but may also depend on particular neuron's gene expression (e.g. OR-type of neuron in the OS). The shafts also interact with their environment, particularly adhere to the substrate—we denote the binding energy per shaft unit length of a single axon in contact with the substrate as $I < 0$. Substrate adhesion is characterised by chemical composition, roughness or geometry.

The axons within bundles continue to axially extend by adding material behind the GC, while the GC generates axial mechanical tension and induces axial axon stretching and flow along the shaft (analysed in (O'Toole, Latham, et al. 2008)). Such dynamic situation, energised also by transient thin side-processes of axons, likely drives reconstruction and rearrangement of the bundles, even is proximal areas[2]. While the axial axon tension does not play a role in the presented scheme, it has an implicit function of facilitating random rearrangement within the fascicle, allowing it to reach minimal energy configuration.

Configurations

We can inspect simple configurations of several axons in small bundles. We assume that (i) either contact decreases energy of the system ($I < 0$ and $A < 0$), (ii) axons prefer to attach to each other over the substrate ($I > A$). For a configuration of two axons, obviously axons will prefer to adhere to each other and the substrate, with the system energy $E = 2I + A < 0$. In case of 3 axons, the third axon will prefer contact with other axons over substrate, and position itself on the top of other axons, see fig. 3.14.

Considering a bundle of four axons, the available configurations are shown in fig. 3.15.

[2] *Proximal* here refers to proximity to the explant. In contrast, *distal* would refer to areas located rather near the GCs.

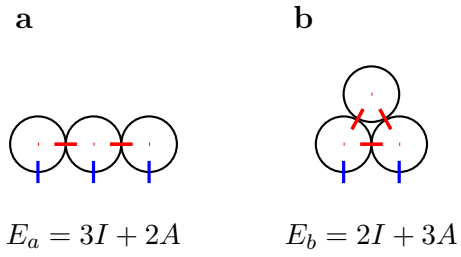

Figure 3.14: Relevant configurations of three axons. The third axon energetically prefers to lose contact with the substrate, and gain adhesion to two other axons, due to assumption $I > A$

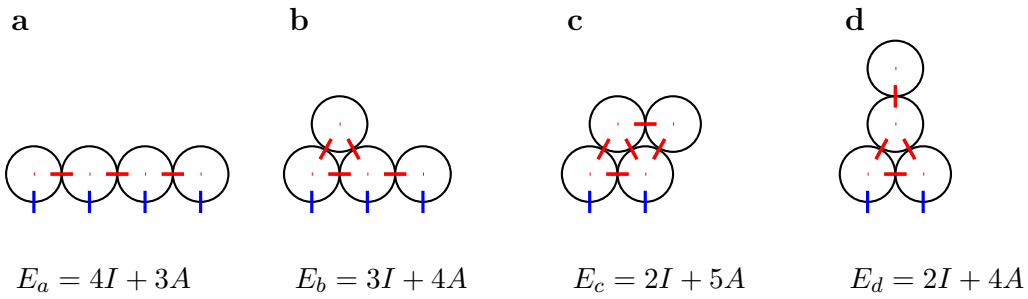

Figure 3.15: Various configurations of four axon bundle. Note the instability $E_d \to E_c < E_d$. In E_a, E_b and E_c, the preferred configuration depends on affinity of A and I; for $A < I$, $E_c < E_b < E_a$, and the bundle tends to minimise its perimeter.

As we can see from the fig. 3.15, axons tend to create compact bundles, while the cross section of the bundle is conserved (high contractility assumption), the bundle minimises its perimeter. Such outcome is consistent with the analogical results of section 3.3.1.

The fig. 3.16 presents configurations for 5 axons, towering configurations were omitted as unstable. The figure illustrates that for small bundles, even if $0 > I \gg A$, the bundle would still orient itself to maximise contact with the substrate, prefer configuration fig. 3.16c over figs. 3.16d to 3.16f. This is a result of discrete character of axon packing, which places more strict constraints on bundle shape, compared to the case discussed in section 3.3.1, where for $\iota/\tau \to 0$ axon detaches from the substrate.

Some of configurations for 6 axons are shown in fig. 3.17. The more compact configurations are preferred, figs. 3.17c to 3.17f, while an energy level can be realised by several configurations (including the minimal level). It is however possible that external (e.g. anisotropic substrate) or internal (e.g. rapid increase in axial tension) influences could further split these energy levels.

This series of simple diagrammatic examples, figs. 3.14 to 3.17, shows us, that for $I > A$ (inferred from the EM images), the small fascicles will tend to minimise their perimeter, but identical configurations of axons will orient themselves to maximise contact with the substrate, and gradually with accretion, energy states of distinct patterns will become closer and therefore transitions relatively more common.

Gradual bundle formation

From the observation of previous section, we may conclude the following:

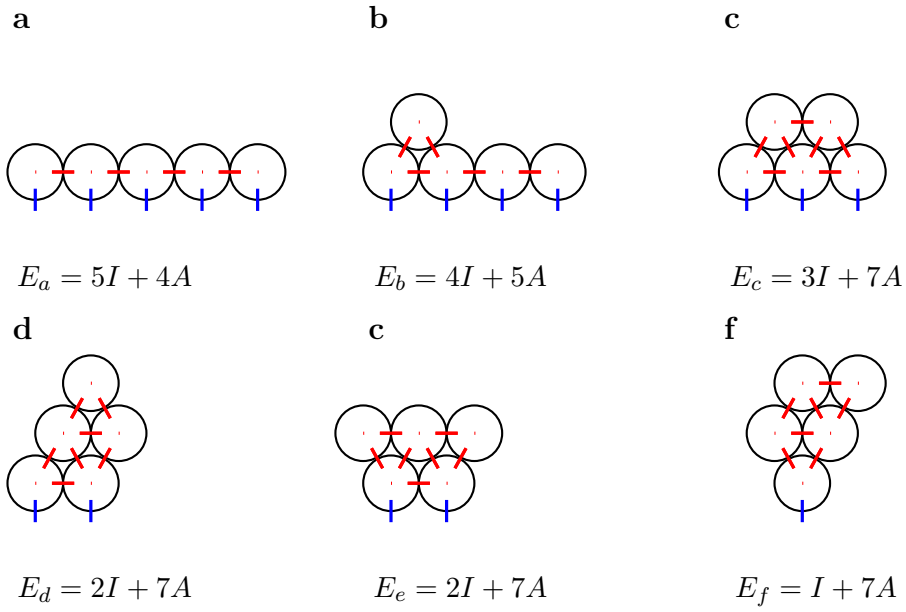

Figure 3.16: Various configurations of five axons. For $A < I$, E_c is minimal configuration. Note, that for identical structures $E_c < E_d = E_e < E_f$, as the bundle not only minimises the perimeter, but maximises attachment to the substrate at the same time.

(i) Under the assumption of low axon compliance, the bundle cross section is conserved for all possible axon arrangements.
(ii) Each axon has limited number of neighbours; they will therefore maximise mutual contact and thus minimise bundle perimeter.
(iii) Even very small substrate adhesion $A \ll I < 0$ influences (small) discrete bundle orientation.
(iv) With growing bundle size, transitions between configurations become relatively easier.

We simulated bundle creation by gradual addition of axons one at a time, and we found that even if each axon sequentially chooses energetically the most optimal site at the time of addition, overall energy of the bundle at the end might not be optimal. Generating random reorganisations of a gradually built bundle (by adding each axon optimally) we were often able to further decrease the total bundle energy. It is therefore likely, that bundles, as they gradually form, do not remain static, but undergo further optimisation. Note also that it is unlikely, the each axon would select the optimal binding site at the time of adhesion.

Some preferred transitions within a bundle are shown in figs. 3.18a to 3.18d. The blue site has higher energy level and prefers a transition to the red site. Note that inverse processes are possible, but would have to be driven by external force (e.g. stemming from axial tension) and their probability decreases with growing energy cost.

We have already noted that two axons prefer to locally adhere if $A < 0$, with marked

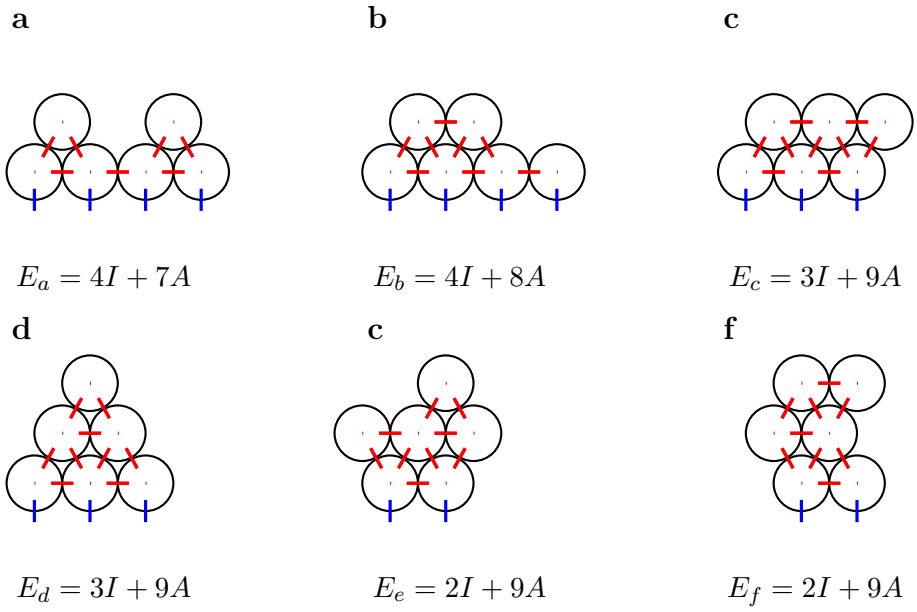

Figure 3.17: Various configurations of six axons in a bundle. For $I > A$, with growing number of axons, relative differences in energy between configurations begin to drop. Notice that the energies $E_c = E_d$ of two distinct, both optimal, configurations.

effects at the contact boundary. Energy gradient arises at the separation point (vertex), a difference of energy before and after the contact boundary is $\Delta E = A$. Such gradient generates force, which drives axial expansion of the contact area, and the process of zippering emerges (section 3.2).

Such process is easily generalised to small fascicles; merger of two small bundles is illustrated in fig. 3.18e. After the initial approach, the final bundle undergoes gradual rearrangement to attain optimal configuration (unlike vertex formed by two axons). The merging and restructuring of the final fascicle as shown in fig. 3.18e decreases the total binding energy by $\Delta E = 4A - I$ (i.e. more than for a single-axon vertex). This difference generates the contact-spreading adhesion force at the vertex, in very much the same way as for the zipper composed of two individual axons. We may assume that such reorganisation process might be hypothetically responsible for entanglement we see in SEM images (figs. 3.6d and 3.6e).

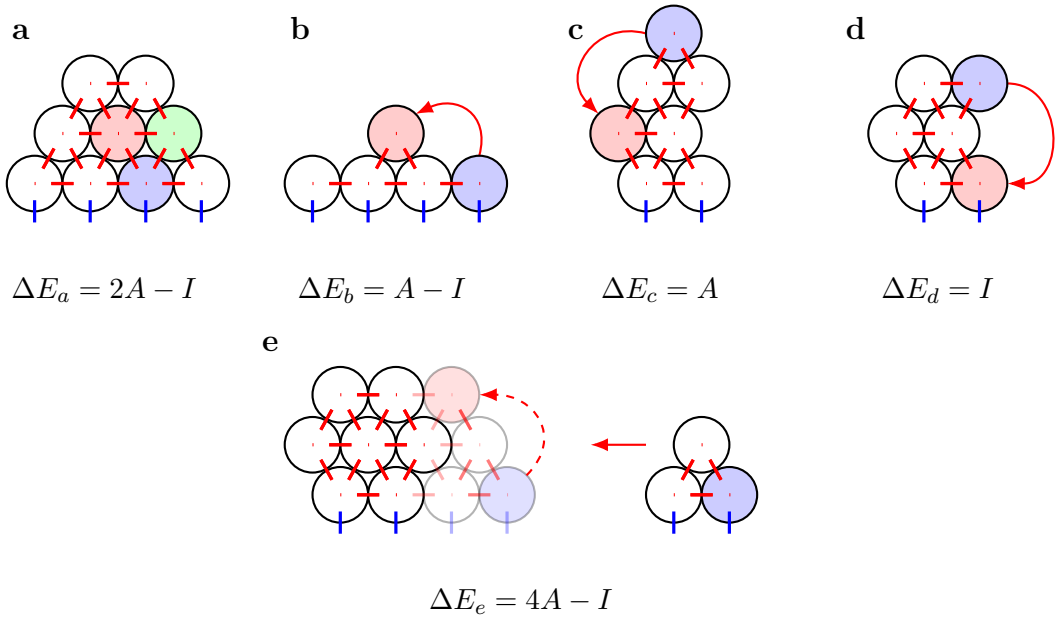

Figure 3.18: Allowed transition in a bundle. **a**: Energy of the red axon is lower ($\Delta E_a < 0$) than energy of the blue axon, which is lower than the green axon. This energy difference generates tissue surface tension—all the sites prefer to exchange place with the red axon, a net centripetal force acts on them. **b**: The blue axon prefers to decrease its energy by changing position to the red site. Axon bundles do not tend to spread into monolayer. **c**: The blue axon decreases its binding energy by transferring to the red site and forming more attachments. Axon bundle tends to minimise its perimeter. **d**: The blue axon will change to the symmetric position with respect to another axons in the bundle, but gains contact with the substrate, further lowering its energy. Bundles therefore form a compact grouping and orient themselves to maximise substrate contact. **e**: Two bundles merge and a subsequent restructuring occurs, blue axon changes position to the red site (dashed line). Note, that newly formed bundle configuration is optimal, it is not towering neither wetting the surface.

3.3.3 Generalisation for large bundles

To generalise the previous observations, we consider the following scaling rules

(i) Cross section area of any bundle scales with number of axons $\sim n$, and is constant for any configuration of n axons.

(ii) Energy of mechanical axial tension per unit length of a bundle of axons $E_T > 0$ is additive, $E_T \sim n > 0$.

(iii) Energy of axon-axon adhesion per unit length of a bundle of axons $E_A < 0$ is proportional to the cross section area, but axons on the perimeter ($\sim \sqrt{n}$) have less binding partners and so higher energy, $E_A \sim An - \frac{A}{2}\sqrt{n} < 0$.

(iv) Energy of axon-substrate adhesion per unit length of a bundle of axons $E_I < 0$ is proportional to bundle perimeter $E_I \sim \sqrt{n} < 0$.

Obviously, when two bundles merge, the tensile energy is simply additive,

$$E_T(n_1) + E_T(n_2) = E_T(n_1 + n_2).$$

Regarding the adhesive energy, where $A < 0$,

$$\begin{aligned}
\Delta E_A &= E_A(n_1 + n_2) - E_A(n_1) - E_A(n_2) \\
&\sim \underbrace{[A(n_1 + n_2) - An_1 - An_2]}_{=0;\text{ full area term}} - \underbrace{[{}^{A}\!/_{2}\sqrt{n_1 + n_2} - {}^{A}\!/_{2}(\sqrt{n_1} + \sqrt{n_2})]}_{\neq 0;\text{ perimeter term}} \\
&\sim -{}^{A}\!/_{2}\left(\sqrt{n_1 + n_2} - (\sqrt{n_1} + \sqrt{n_2})\right) \\
&\sim \begin{cases} -{}^{A}\!/_{2}\left(\sqrt{n_1}(1 + \frac{1}{2}\frac{n_2}{n_1}) - \sqrt{n_1} - \sqrt{n_2}\right) \approx {}^{A}\!/_{2}\sqrt{n_2} < 0 & | \; n_1 \gg n_2 \\ -{}^{A}\!/_{2}\left(\sqrt{2n} - 2\sqrt{n}\right) \approx {}^{A}\!/_{2}(2 - \sqrt{2})n < 0 & | \; n_1 \approx n_2 = n \end{cases}
\end{aligned}$$

The change in energy $\Delta E_A < 0$, so the bundle merger is energetically favourable for $A < 0$. The relative change of energy per axon, where $N = n_1 + n_2$, is then

$$\left|\frac{\Delta E_A}{N}\right| \sim \begin{cases} \frac{\sqrt{n_2}}{n_1} \to 0 & | \; N \approx n_1 \gg n_2 \\ \frac{(2-\sqrt{2})n}{2n} \approx 1 - {}^{1}\!/_{\sqrt{2}} \nrightarrow 0 & | \; n_1 \approx n_2 = n = {}^{N}\!/_{2} \end{cases}$$

which indicates that while two similar bundles would tend to merge and remain largely merged, the addition or removal of a single axon or a small bundle from a larger bundle, is easily possible.

The same scaling rule also holds for the energy of adhesion to the substrate

$$\Delta E_I \sim I\left(\sqrt{n_1 + n_2} - \sqrt{n_1} - \sqrt{n_2}\right) > 0,$$

where $\Delta E_I > 0$ indicates, that as bundles merge, their interaction with the substrate decreases, contribution of substrate-axon energy increases, increasing the total energy of the system.

This section would suggest that axons and bundles would always prefer to merge. This might be true at the level of cross sections (under specific assumptions), however the bundling has impact along the axial dimension of merging bundles (see section 3.2). Extending the contact segment axially stretches the participating axons, which requires an increase in the stored axial tension energy. Also, it generates deformations of bundles, particularly bending. We will assess the effect of bending in the section 3.4.4.

3.4 Mechanical properties of axons in axial direction

The energy of adhesion, which drives spreading of axon-axon interface and thus the zippering, is countered by the tensile (and elastic) energies of axons (section 3.2). Considering axon typical length in culture is $L \approx$(50–100) µm, and its width 200 nm, there is a difference of 3 orders of magnitude. We therefore treat axons (and axon bundles) as 1D objects, and ignore mechanical and elastic effects on their transverse dimensions. The crucial balancing energy to the adhesive energy in axon is therefore axial tensile (and elastic) energy.

3.4.1 Mechanical tension of axon

The pharmacologically induced global changes shown in section 3.2.1 are taking place in region of the culture, where very few GCs are present. This absence lead us to inference, that the global dynamics arises from prevalence of zippering or uzippering processes. To quantitatively understand the underlying mechanism of those processes, we studied individual forces acting at the zipper vertices:

(i) axial mechanical baseline tension within the axon $T_a > 0$ (i.e. tensile energy per unit length of an unstrained axon),

(ii) axon-substrate adhesion $I < 0$ (i.e. interfacial energy of adhesion per unit length of a single axon); this quantity is equivalent to I presented in section 3.3.2,

(iii) axon-axon adhesion $S > 0$ (i.e. work done by adhesion between axons per unit length of a single axon); with correspondence $S = -A$ presented in section 3.3.2,

(iv) bending elastic force in the axon—we commonly observe sharp and persistent turns of axons indicating low bending rigidity, we will therefore consider bending energy negligible as compared to tensile energy, more detailed argument will be presented in section 3.4.4.

We will assume, that these defined single axon quantities (T_a, I, S) can be extrapolated to small bundles of axons, particularly as axons and small bundles cannot be distinguished under optical microscope, and any measurements were therefore most likely performed interchangeably on both. If we assume any scaling of these parameters in the further sections, it will be clearly noted.

T_a represents the tension within a single axon shaft intrinsically generated by the axon, either through the GC activity or active contractility within the shaft (section 1.4.4). For the time scale of zipper processes, it is considered constant and independent on axon strain, relaxation or other manipulations. The baseline tension of an axon T_a could in principle depend on its cross-section area, but we will assume, as in the section 3.3.1, that the axon cross-section area is constant and uniform. If two axons or bundles of tensions T_{a1} and T_{a2} merge/fasciculate, their tensions will add in the newly formed segment, $T_{a12} = T_{a1} + T_{a2}$.

Note that for a single axon or a small bundle of $\lesssim$10 axons, the scaling regime as presented in section 3.3.3 likely does not apply. In small bundles, discrete character of individual axons contravenes the rules valid for large fascicle size. As we have seen in figs. 3.15 to 3.17, discrete character of bundle parts affects the axon packing, substrate contact width and axon-axon adhesion contact (fig. 3.18).

Small bundles tend to maintain extended contact with the substrate (see figs. 3.16 and 3.17), even if substrate affinity is low. It is unlikely, that either of merging small bundles would completely defasciculate before adhering (see fig. 3.18e), particularly for simple zippers (figs. 3.7a and 3.7b). Reorganisation to optimal structure of the newly created merger bundle would occur further from the junction point (vertex). This means, that the substrate interaction energy would simply add at the vertex point, as both bundles would maintain the contact with the substrate for some finite vicinity of the vertex (unlike in the scaling regime for large bundles), i.e. $I_{12} = I_1 + I_2 < 0$. This is the same relation we proposed for the T_a. Under these assumptions, we can therefore

redefine the baseline tension as an effective tension

$$T_0 = T_a + I \mid T_a > 0,\ I < 0. \tag{3.5}$$

It could be the gradual energy-optimising structural changes (e.g. stemming from $I_{12} \neq I_1 + I_2$) in more remote parts of merging segment (as suggested in fig. 3.18e), which generate mechanical energy driving further zippering.

In more general case, considering external mechanical influence, we define actual axial mechanical tension of an axon T,

$$T = T_0 + \mathcal{H}, \tag{3.6}$$

where $\mathcal{H}$ represents all the mechanical influences (e.g Hookean, viscoelasticity, external force), which depend on the geometry of vertex vicinity and may change during the zippering process, i.e. $\mathcal{H} = \mathcal{H}(t)$. Nonetheless, we assume the tension T is homogeneous along the axon across the area of zippering, and any change $\mathcal{H}$ (e.g. Hookean stretch) affects the tension in the area uniformly.

3.4.2 Axon tension measurement

Axon tension T is one of the essential parameters in zippering and zipper vertex stability. The knowledge of the value of tension in OSN axons is therefore crucial for both relatable modelling and estimation of adhesive parameter, which is more difficult to assess experimentally.

Axon tension was measured previously in other systems (Dennerll, Joshi, et al. 1988; Dennerll, Lamoureux, et al. 1989); the neurite rest tension T_0 was shown to be of the order of 1 nN; a wide range of tension values was reported, but most of the values clustered around 0.5 nN for PC-12 neurites. Calibrated MNs or microelectromechanical systems (MEMS) have been successfully employed to measure the tension of axons of DRG or PC-12 neurites, or motor neuron axons of *Drosophila melanogaster* embryo (Rajagopalan et al. 2010). The PC-12 and DRG neurites are widely used in this kind of micromanipulation experiments, because of their robustness and standardised culture conditions. In contrast, the OSNs of OE (our system) are much more demanding to cultivate, their lifespan in culture is limited, and they tend to be rather sensitive to fluctuations in environment. While OSNs' fine structure of 200 nm diameter makes them convenient for detailed studies of intricate dynamics of inter-axonal contact interactions and gradual fasciculation *ex vivo*, one may expect they are much more vulnerable, not only to unsteadiness of cultivation conditions, but also to mechanical disruptions incurred by aforementioned contact measurement techniques. In addition, small size of the manipulated axons makes the techniques prone to contact with the substrate, which invalidates the force reading or severs the AS from the substrate. Therefore, another experimental approach has to be used for these axons.

A suitable technique for tension measurements on the OSN axons is BFP, introduced in section 2.4.1. The technique has been repeatedly tested on biological interfaces, and proved to be gentle and non-invasive to the biological sample (W. Chen, Lou, et al. 2012;

Evans, Ritchie, and Merkel 1995; Heinrich et al. 2005). In the technique, an RBC is firmly aspirated within a micropipette (2 µm aperture in diameter in our experiments) and acts as a force transducer for a SB (3 µm in diameter in our experiments) attached to the RBC's apex. The SB forms a contact with a biotinylated axon (i.e. sample) based on non-covalent bindings of streptavidin-biotin molecules. Through this contact, the force exerted by the probe is mediated onto the sample, and deforms or strains the sample. Accompanying deformation of the transducing RBC then allows precise calculation of the applied force (uncertainty ∼10 pN in our arrangements).

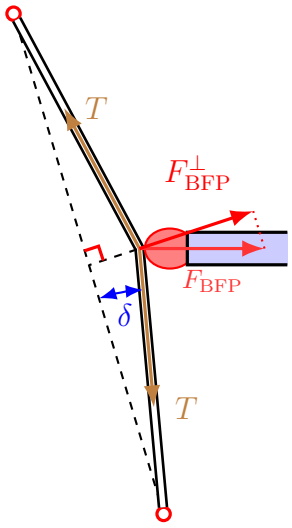

Figure 3.19: Illustration of axon deflection to measure axial tension T. $F^{\perp}_{\mathrm{BFP}}$ is applied force component perpendicular to the undeformed axon, δ is axon deflection. When forces are balanced, the geometry (δ_i) and calibrated force ($F^{\perp}_{\mathrm{BFP},i}$) define a plateau point i as shown in fig. 3.20.

The original idea of manipulation experiment using BFP was to modify tension in an axon near a zipper vertex in equilibrium (defined by vertex zipper angle β_1) by a calibrated known amount $\Delta T_{1\to 2}$. Such change would induce transition to a new equilibrium (β_2; see eqs. (3.9) and (3.27)). Comparison of the two (or more) equilibria in terms of geometry (i.e. angles β_1 and β_2) and change in tension $\Delta T_{1\to 2}$ is sufficient to extract the adhesion parameter S, while analysis of the time course of the transition itself would allow us to estimate parameters of dissipative forces within the system. For several (>2) modified tensions and corresponding equilibria, the S could be extracted from overdetermined system by linear regression. Technical complications however did not allow us to perform such ideal experiment: (i) it was necessary to incubate the SBs with the sample, losing the control of SB positioning in the culture; (ii) the adhesion on RBC-SB or SB-axon interfaces would often fail, limiting the yield of reliable measurements. In such situation, we were able to utilise only the SBs randomly attached to ASs. We therefore chose straight segments of axons decorated with the SBs and performed a series of calibrated consecutive deflections of axons by angle δ_i, i.e. $180° - 2\delta_i$ is the corresponding angle at the deformation kink of deflection step i, see fig. 3.19.

Such procedure (as described in section 2.4.3) does not allow us to measure the S directly for individual zippers, but provides a procedure to estimate tension T ($\approx T_0$) in axons or small bundles (indistinguishable under optical microscope). After each axon deflection i (by angle δ_i), a short period of resting time follows, when the system can equilibrate and a plateau of constant applied force (i.e. constant RBC deformation) is observed. For a plateau i, the normal deforming force applied by the probe $F^{\perp}_{\mathrm{BFP},i}$ on the axon is balanced by the restoring force—transverse component of tension within the shaft T at the apex point, $2T\sin\delta_i$.

For a typical experiment and axon of unstrained length $L{\approx}40$ µm and a maximum

deflection angle $\delta_{\max}\approx 5°$, the extension of the axon is at most

$$\Delta L_{\max} \approx \frac{L}{\cos\delta_{\max}} - L = 0.15\,\mu\text{m},$$

which correspond to a tension increase (for a typical axon stiffness $10\,\frac{\mu\text{dyn}}{\mu\text{m}}=0.1\,\frac{\text{nN}}{\mu\text{m}}$, (Dennerll, Joshi, et al. 1988)) of $\sim$10 pN, or about $\sim$1 % of a typical axon rest tension T_0, and is thus neglected in the analysis.

After several plateaux (see section 2.4.4) are attained—streptavidin-biotin links at the RBC-SB interface tend to fail for angles $\delta\gtrsim 5°$—an average applied force $F^{\perp}_{\text{BFP},i}$ and average deflection angle δ_i are calculated for each plateau i (i.e. averaged over the time interval i). Plateaux of the experiment are then represented by coordinate points $(\sin\delta_i, F^{\perp}_{\text{BFP},i})$, shown as blue points in fig. 3.20, including errorbars representing corresponding quantity's standard deviation during the plateau duration (i.e. $\sigma(\sin\delta_i)$, $\sigma(F^{\perp}_{\text{BFP},i})$). The axon tension T is calculated by linear regression of such coordinate points, as illustrated by red line in fig. 3.20. To circumvent probe calibration difficulties, only measurements with 3 or more plateaux were accepted (see section 2.4.4 for details).

The fig. 3.20 represents 8 robust measurements out of several dozens performed. Corresponding T ($\approx T_0$) obtained by regression are summarised in table 3.1. The number in brackets near the data points is time duration of the corresponding plateau in seconds. Note that in some experiments, plateau durations are shorter ($\sim$1 s; figs. 3.20b to 3.20d), in other experiments, they can last from $\sim$10 s to $\sim$1 min (figs. 3.20e and 3.20g). The same can be said about plateau stability (compare errorbars in fig. 3.20e and fig. 3.20f). The duration of plateaux can be likely attributed to culture viability and probe preparation, as experiments in figs. 3.20b to 3.20d are part of a single experimental session (on distinct explant). Outlying higher value of tension in experiment **h** was likely cause by stretching, and is discussed in section 3.4.3.

For further calculations, we used the values measured on the unstrained axons (i.e. figs. 3.20a to 3.20g) as listed in table 3.1**a**-**g**. Using the mean value of each fit and its standard deviation, we estimated the probability distribution of general axon rest tension T_0 as described in section 2.4.5 and illustrated in fig. 3.21.

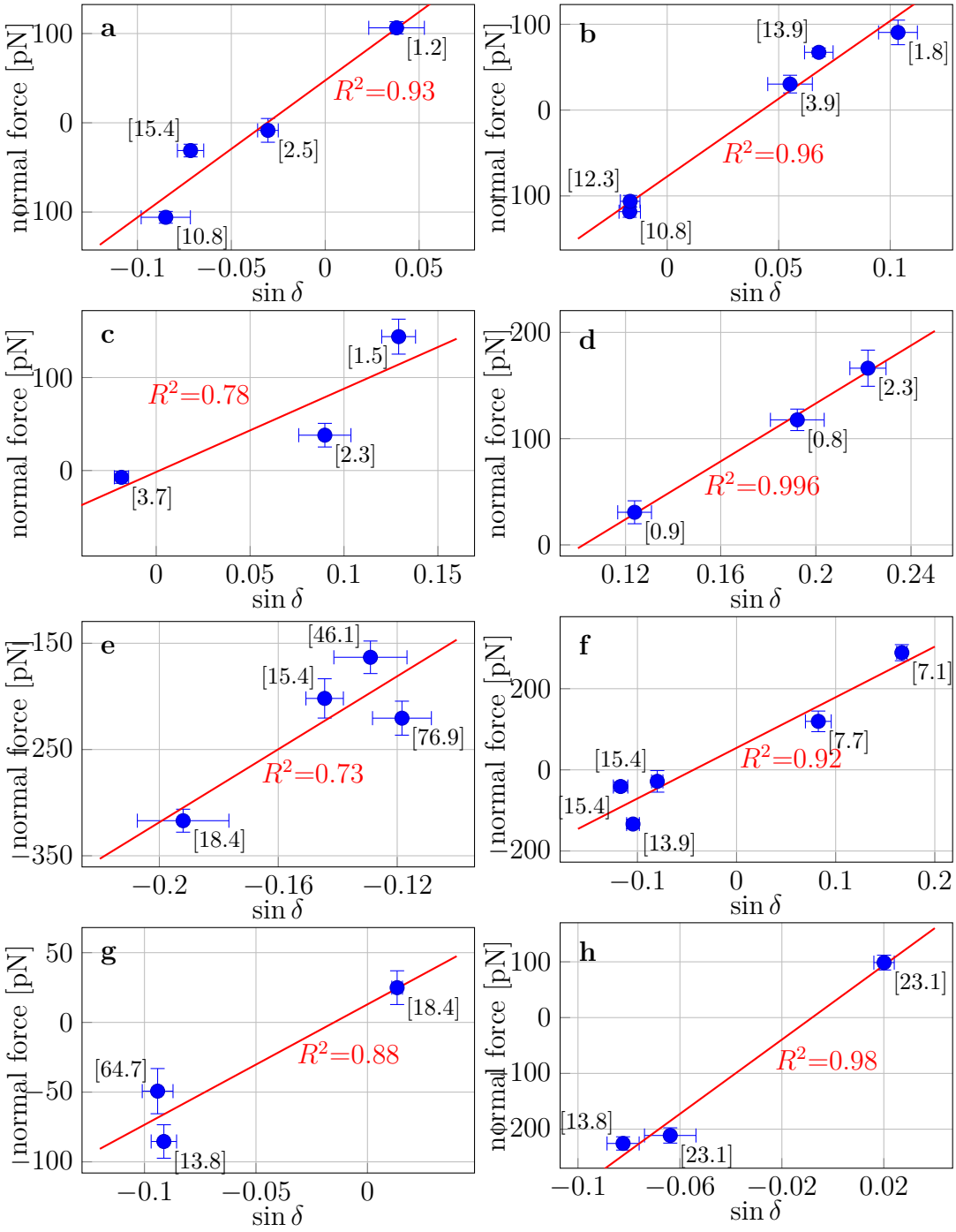

Figure 3.20: A set of selected BFP experiments. Fit results for tensions are summarised in the table 3.1 and individual notable experiments or trends are discussed in the text. The blue dots represent plateaux—normal force applied by the probe is balanced by the restoring tensile force within the deflected axon over a time interval (see fig. 3.19). The error bars correspond to standard deviation of measured quantities during the time of maintained balance (the duration of particular time interval is indicated in seconds in the adjacent brackets). Red lines are linear regression through the data points, with indicated fit goodness R^2.

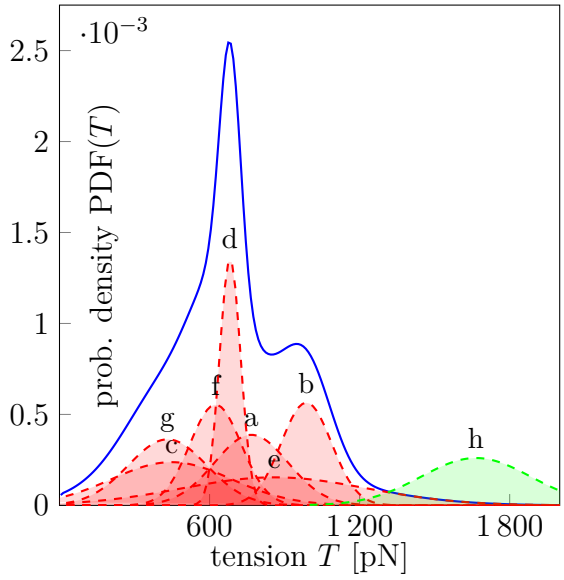

Figure 3.21: Figure illustrates individual measurements of axon tensions in red; the (renormalised) Gaussian blobs are given by mean and deviation parameters as indicated in fig. 3.20 and table 3.1, with corresponding labelling. The distribution of general rest tension of axons in blue, PDF(T), is a direct summation of constitutive Gaussians, with the sharp peak at 679 pN and interquartile range (531–861) pN. The Gaussian representing experiment **h**, indicated in green, is not included in the $\mathrm{PDF}_{\mathrm{exp}}(T)$ calculation, because it was under strain as explained in section 3.4.3; it is clearly an outlier as compared to measurements **a**-**g**.

panel fig. 3.20	tension T [pN]	$\sigma(T)$ [pN]	fit R^2
a	767	147	0.93
b	987	101	0.96
c	448	240	0.78
d	682	42	1.00
e	859	370	0.73
f	624	103	0.92
g	432	157	0.88
h	1665	219	0.98

Table 3.1: Table of measured tension (T), standard deviation of tension ($\sigma(T)$) and fit goodness (R^2), for BFP experiments; details of each experiment can be found in fig. 3.20. This set of measurements inflicted only negligible extension on the axons and therefore $T{\approx}T_0$, except for the measurement **h**.

The PDF(T) in fig. 3.21 in blue has a sharp peak around T=679 pN with mean value at $\bar{T}$=686 pN. The interquartile range is (531–861) pN. Normal distributions based on individual measurements as shown in table 3.1 are plotted (rescaled) in red in the fig. 3.21 and labelled by the corresponding letter from table 3.1; the final PDF(T) is given as their direct sum. Darker red shading denotes range where individual measurements overlap, which is the most prominent around the peak; the high probability around the mode is therefore not only a result of low standard deviation of measurement **d**, but also general clustering of measurements around that value. Measurement **h**, which is not included in the final PDF(T), is shown in green and clearly has a small overlap with the other measurements, it is considered to be an outlier.

3.4.3 Effects of axon stretching

As shown in section 3.4.2, during the BFP measurements, the axon tension changes by $\lesssim$1 %, for typical change in length $L\lesssim$0.2 µm, which has no practical effect on axon tension. During a typical zippering process, when vertex advances by $\Delta y\approx$10 µm and the typical angle is $\beta\approx$50°, the change in length is

$$\Delta L \approx \Delta y\,(1-\cos{}^{\beta}\!/_{2}) = 1\,\mu\mathrm{m},$$

which can already represent $\mathcal{H}\approx$100 pN, or as much as 15 % of axon rest tension T_0. While we will ignore this effect for a simple dynamical model (in section Zipper dynamics model), it will be incorporated in the detailed model (in section Mathematical model of zipper statics and dynamics). We will now discuss two experimental observations of stretching.

Stretching during a BFP measurement

The fig. 3.20g and fig. 3.20h are measurements performed on a single axon, the measurement **h** follows several minutes after **g**. The considerable increase in tension between **g**→**h** (see table 3.1) was likely caused by a visible retreat of explant boundary and stretching of the measured axon by roughly 3 µm, see fig. 3.22. Such stretching is unlikely to occur during spontaneous zipper dynamics in the axonal network, and the measurement **h** was therefore excluded from the calculated distribution of tensions, assuming the typical tensions in axonal network T are close to T_0, possibly within 15 % of T_0, as proposed in first paragraph of section 3.4.3. This measurement (fig. 3.22) however indicates, that the axons exhibit Hookean properties with approximate stiffness at the order $\sim$100 $\frac{\mathrm{pN}}{\mu\mathrm{m}}$, consistent with values in (Dennerll, Joshi, et al. 1988) for PC-12 axons.

FBS-induced stretching

We also observed a considerable stretching during FBS manipulation of culture (see section Pharmacological manipulation of axon tension); emergence of loop and general increase in length in some areas. To quantify actual extend of stretching, we segmented several representative paths within the network, as shown by red, green and blue lines in fig. 3.23; the network corresponds to the experiment presented in fig. 3.11a. The paths are terminated by an explant or an attached debris on the proximal end, and by a plausible GC (indicated by protruding filopodia) on the distal end. As indicated in the fig. 3.23e, the total length of the paths increased by 4 to 10 %, which corresponds to (8–23) µm. At the same time, an apparent straightening occurred, as indicated in fig. 3.23f; the straightness metric is evaluated as a ratio between the direct point-to-point distance between path termini and the total measured length of the path.

Such measurements lead to the following conclusions: (i) the total length of the axon significantly increases within the 15 min period after FBS administration; (ii) the straight segments of the path become more aligned to the general radial direction of the outgrowth, consistently with behaviour of stretched material. The green path does not straighten due to immobile obstacle in the middle of the path. Considering the same

order of magnitude of axon stiffness as previously (i.e. $\sim 0.1\,\frac{\mathrm{nN}}{\mu\mathrm{m}}$), the deformation around $\sim 10\,\mu\mathrm{m}$ should lead to the increase in tension at the order of $\sim 1\,\mathrm{nN}$. Such increase would more than double the presumed average tension of an OSN axon, and therefore induce unzippering and significantly influence the topological organisation of the network.

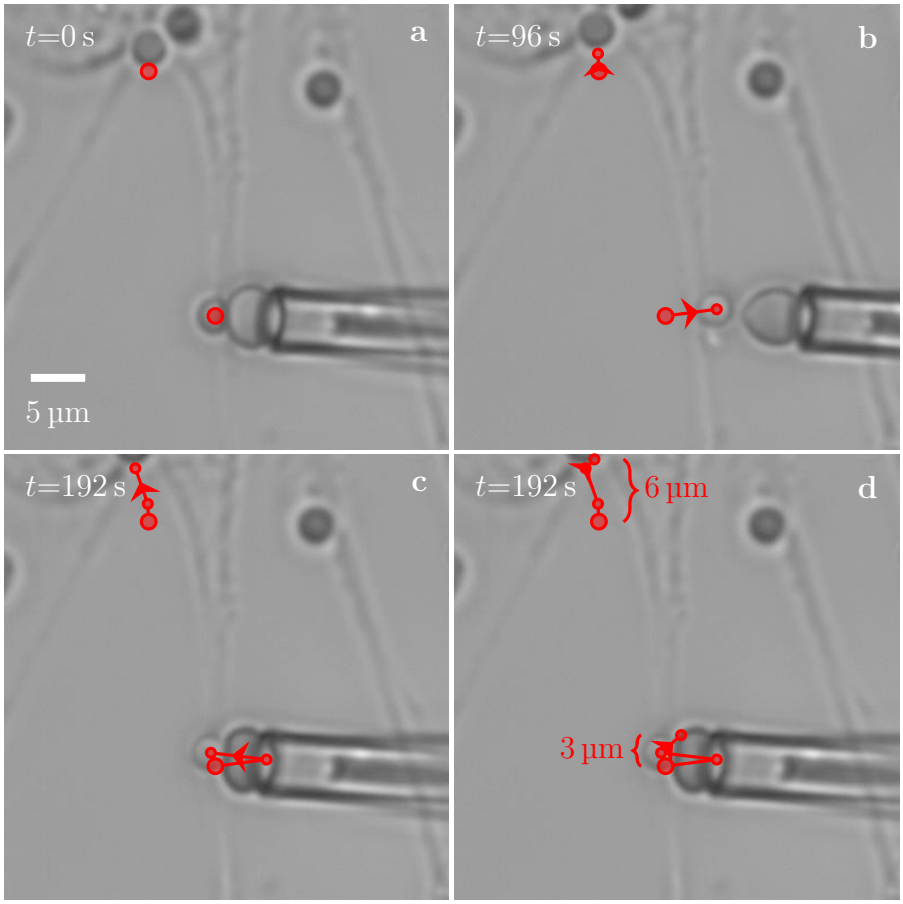

Figure 3.22: Figure illustrates gradual stretching of an axon. Large red rings indicate position of reference marks on the axon at the time t=0 min. Smaller red dots indicate gradual movement of these marks as the experiment progressed, **a** through **d**. The whole culture flowed predominantly proximally (towards the top), the proximal axon section advanced by roughly 6 µm, while the distal section by 3 µm, thus stretching the axon by ≈3 µm. The change in measured tension was ≈1200 pN, thus a stiffness ≈400 $\frac{\mathrm{pN}}{\mu\mathrm{m}}$. The resulting stiffness value however should be only understood as an order of magnitude estimate.

The observations in this section indicate, that while Hookean effects have little significance during spontaneous zippering activity, they might however become important during exceptional cataclysmic events in the axonal network (e.g. collapse, explant contraction) or in case of strong extra-axonal forces (e.g. manipulation experiment, travelling OEC as in fig. 3.2).

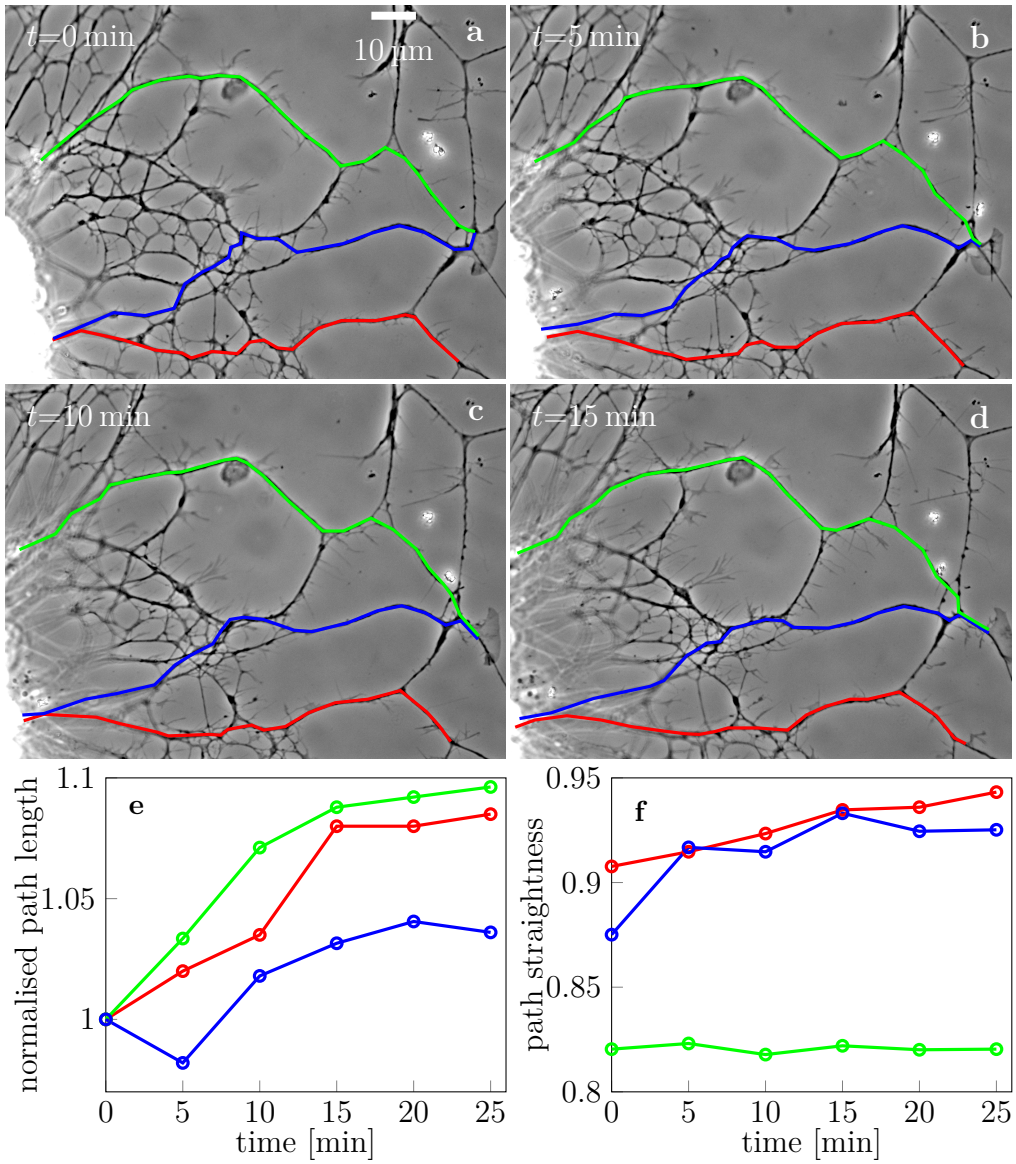

Figure 3.23: **a-d**: Illustrates development of selected paths in the network during 15 min after the addition of the FBS. Retreat of the explant boundary and axon stretching are apparent, as well as gradual smoothing (straightening) of particularly red and blue paths. Note that the two loops forming distal part of the green paths gradually expand with the increasing length of the path. **e**: Increase in total length of each path in time; the colours correspond to the colours used in **a-d**. **f**: Straightening of paths in time evaluated as a ratio between distance of path termini to total path length. Note that the sharp increase in straightness during the first 5 min for the blue path coincides with the temporary decrease in total length.

3.4.4 Bending rigidity

Elastic energy stored in filaments or rods when they bend is conceptually related to the elastic energy of stretching. The amount of this energy depends not only on the material, but mostly on the distribution of deformation within the structure. We will now estimate how bending energy of OSN axons depends on their curvature κ and number of axons in the bundle n. The OSN axons are very thin, with radius of $r_a = 100\,\text{nm}$, which corresponds to cross-section area $S_a \approx 0.03\,\mu\text{m}^2$. Considering density of MTs in axons measured for other systems, (10–200) $\frac{\text{MT}}{\mu\text{m}^2}$ (Peter and Mofrad 2012), OSN axons contain at most 10 MT. The length of individual MT is (50–100) µm in axons, with MT outer radius $r_e = 13\,\text{nm}$ and inner radius $r_i = 8\,\text{nm}$ (Pampaloni et al. 2006).

The observed curvature of axons and bundles at junction points in the culture is about $\kappa \lesssim 1\,\frac{1}{\mu\text{m}}$, i.e. the radius of curvature is of order $R \sim 1\,\mu\text{m}$, while the rest of the axon is mostly straight, $\kappa = 0\,\frac{1}{\mu\text{m}}$. Axon contains the MTs arranged in trains, reinforced and cross-linked by microtubule associated proteins (MAPs) (Peter and Mofrad 2012). The reinforcing MAPs are however unlikely to play a major role within the relatively short region of bending $\sim$1 µm in axonal culture. It was shown in (Pampaloni et al. 2006) that axial stresses (represented by Young modulus E) are 6 orders of magnitude more important for bending than shearing stresses. For a single axon, we therefore estimate its bending rigidity to be a simple sum of bending rigidities of individual MTs $(EJ)_{MT}$, where J is the second moment of MT cross-sectional area S_{MT}.

We apply equations from beam theory to a single axon bending, with rigidity $10 \cdot (EJ)_{MT}$, where $E \approx 1.5\,\text{GPa}$(Peter and Mofrad 2012) and $S_{MT} = \pi(r_e^2 - r_i^2)$, so $J = \pi/2(r_e^4 - r_i^4) \approx 4 \times 10^{-32}\,\text{m}^4$. Combining the two quantities, $(EJ)_{MT} \approx 6 \times 10^{-23}\,\text{N m}^2$. The density of bending energy of idealised beam at position x can be calculated as Roark et al. 2002, p. 127

$$u(x) = \frac{M^2(x)}{2EJ} = \frac{EJ}{2R^2(x)}, \tag{3.7}$$

where $M(x) = \frac{EJ}{R(x)}$ is moment of force. Total bending energy of a beam of length L is given as $U = \int_0^L u(x)dx = \int_0^L \frac{EJ}{2R^2}dx$. Considering the axon has constant curvature near the junction point $R \sim 1\,\mu\text{m}$, and no curvature otherwise ($\kappa = 0$), then the bending energy of OSN axon per unit length at the vicinity of bending point (i.e. vertex) is

$$u = \frac{10 \cdot (EJ)_{MT}}{2R^2} \approx \frac{10 \cdot 6 \times 10^{-23}}{2 \cdot 10^{-12}}[\text{N}] \approx 3 \times 10^{-10}\,\text{N} = 0.3\,\text{nN}$$

which can be compared to adhesive energy $S \approx 0.1\,\text{nN}$[3] and is about order of magnitude lower than tensile energy $T \approx 1\,\text{nN}$ (section 3.4.2). The factor $\sim 1/R^2$ makes the bending energy density u very sensitive to actual curvature of the axon, which is strongly coupled to the zipper angle β. If we consider a constant non-zero axon curvature $1/R = \kappa \neq 0$ only in the vicinity of the perceived vertex up to the distance 1 µm (see fig. 3.24b, typical

[3] Detailed estimate will be provided in section 3.5.3

experimental observation), we can approximate the relation as

$$R \approx \tan\frac{\pi - \beta/2}{2} \cdot 1\,\mu\text{m} = \cot \beta/4[\mu\text{m}].$$

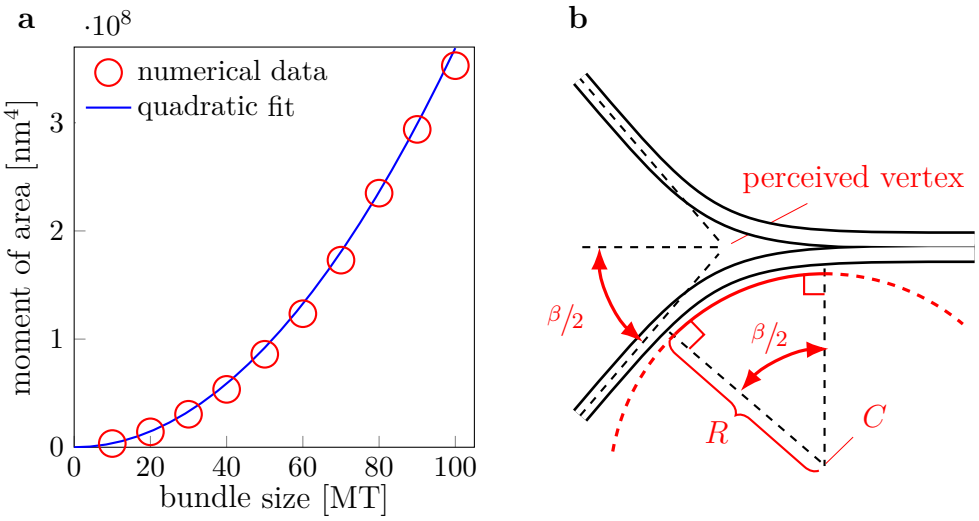

Figure 3.24: **a**: Dependence of J, the second moment of area of a bundle, on the number of MT-like filaments constituting the bundle n. Each filament was generated as a tube with inner and outer radius, energetically minimal cross-section organisation was numerically calculated, and J was calculated using Monte Carlo method (red circles). Numerical data are approximated by a quadratic fit (blue line) $J = 3.7 \cdot 10^4 n^2 - 9.4 \cdot 10^3 n + 1.7 \cdot 10^3$. **b**: Illustration of osculating circle with centre C and radius of curvature R. The point C is estimated as the intersection of (dashed black) lines normal to the axon (with marked right angles) initiated on either side of the perceived vertex at the distance 1 µm. Then, $R = \tan\frac{\pi-\beta/2}{2} \cdot 1\,\mu\text{m} = \cot \beta/4[\mu\text{m}]$ and the length of non-zero curvature ($\kappa \neq 0$) $L_\kappa \approx \beta/2 R$.

For a short zippering process, angle β changes $60° \to 65°$ and adhering segment extends by $\Delta x \approx 3\,\mu\text{m}$. The total bending energy of the axon can be estimated as (see fig. 3.24b)

$$U \approx \underbrace{\beta/2 R}_{\substack{\text{arc}\\ \text{length}}} \underbrace{\frac{(EJ)_{ax}}{2R^2}}_{=u} \approx \frac{\beta (EJ)_{ax}}{4 \cot \beta/4 \cdot 1\,\mu\text{m}}.$$

Calculation gives an estimate of the bending energy as $U(60°) \approx 0.042\,\text{nN}\,\mu\text{m}$ and $U(65°) \approx 0.050\,\text{nN}\,\mu\text{m}$, so the change in bending energy is $\Delta U = 0.008\,\text{nN}\,\mu\text{m}$. For the tensile energy, $\Delta E_T = T(1 - \cos \beta/2)\Delta x = 0.402\,\text{nN}\,\mu\text{m}$ for linear energy density $T = 1\,\text{nN}$. The change in adhesive energy per one axon is $1/2 \Delta E_S = 1/2 S \Delta x = 0.15\,\text{nN}\,\mu\text{m}$ for linear adhesive energy density $S = 0.1\,\text{nN}$. We can see, the change in total energy for a single axon is 1–2 orders of magnitude lower for bending as compared to other

mechanical energies. The simple calculation demonstrates, that the axial density of the bending energy u is comparable to the adhesive energy density; it is however decisive, that the overall change of bending energy ΔU during zippering is orders of magnitude lower than ΔE_T and ΔE_S, and can be therefore neglected for a single-axon zipper.

It is not straightforward to extrapolate changes in bending energy to a bundle of axons[4], because of the term J, which is nonlinear in n and difficult to predict for tubular inner structure of an axon. We numerically tested how the second moment of area J changes, if MTs are gradually added to a bundle (see fig. 3.24a). We simplified the situation and arranged all the MTs into a single fascicle, not compartmentalised into individual axons. These consecutively generated 'superbundles' were arranged into configuration of minimal energy; we calculated J for those configurations and numerically demonstrated, that J scales quadratically with the number of MTs and so with the number of axons, i.e. $J \sim n^2$. As shown in fig. 3.24a, J increases 4-fold from 1 to 10 axons (10 MT each), so it grows very slowly for small bundle sizes, and is unlikely to play any significant role in zippering process for bundles up to 10 axons (cf. fig. 3.6).

Note that while the estimated effect on bending elastic energy is negligible in our context, the bending process can include also irreversible deformation processes. As axons straighten and deform in the vicinity of the vertex in transition, energy can be dissipated by MAP recombination, plastic deformation or breakage of MTs and other processes. We address these effects as part of the zipper transition model in section 3.5.5.

3.4.5 Friction and viscosity of axons

The transition of a zippering process is not determine only by the mutual interplay of adhesion and tension. The rate of transition is mediated by dissipative forces, occurring within the bulk of axon material or on interfaces (see sections 1.3.1 and 1.3.2 and fig. 1.10). We consider only such forms of dissipative processes, which depend only on the longitudinal axon dimension, i.e. we will not explicitly treat processes involving axon cross-section deformation or torque. We also assume, that all the dissipative processes are linear function of material velocity. Particular forms of dissipative forces will be introduced as we gradually expand our model of zippering dynamics.

Slightly different dissipative force we should also consider is medium resistance during axon movement, the Stokes force. For an 'infinite' cylinder, the force per unit length is given by (Landau and Lifshitz 1987)

$$f_S = \frac{4\pi\eta v}{\log\left(3.7\frac{\nu}{Rv}\right)}, \tag{3.8}$$

where we use typical values for radius $R{\approx}100\,\mathrm{nm}$, and branch velocity $v \approx u \sin{}^{\beta}\!/_{2} = 0.009\,\frac{\mu\mathrm{m}}{\mathrm{s}}$, and relevant values of dynamic viscosity of seawater $\eta{=}1.08 \times 10^{-6}\,\frac{\mathrm{nN\,s}}{\mu\mathrm{m}^2}$ and kinematic viscosity of seawater $\nu{=}1.05 \times 10^{6}\,\frac{\mu\mathrm{m}^2}{\mathrm{s}}$. These typical values yield force density $f_S{=}5.5 \times 10^{-9}\,\frac{\mathrm{nN}}{\mu\mathrm{m}}$. For axon length $\lesssim$100 µm, the acting Stokes force would be at

[4] Even the extrapolation of J of MT to a single axon, i.e. $(EJ)_{\mathrm{axon}} \approx 10(EJ)_{MT}$, in the preceding calculation, was a crude approximation.

most F_S=5.5 × 10^{-7} nN. This can be compared to the typical forces in the system, the tensile force ∼1 nN (section 3.4.2), or dissipative forces, which are at the order ∼0.1 nN (estimated in section 3.5.6). Clearly, the Stokes drag is about 10^6 times smaller and therefore negligible.

3.5 Analysis of zippers

In section 3.1.2, we showed examples of observed zippers. Images as those in figs. 3.3 and 3.4 allow us to extract the details of zipper geometry in terms of symmetry or zipper vertex angle, but also record velocity of the zipper during the time lapse. The information about geometry of static equilibrium directly reflects the mutual relationship between the tension and adhesion (hypothesis 1). Therefore, we can use the geometrical observation to draw conclusions about underlying biophysical quantities. As a complement, we have a good knowledge of the distribution of tensions PDF(T) in OSN axons, through the BFP measurements (section 3.4.2 and fig. 3.21). Therefore, we can mathematically relate the zipper geometry and biophysical parameters, and use the relation to determine the parameter of axon-axon adhesion S.

3.5.1 Zipper static equilibrium

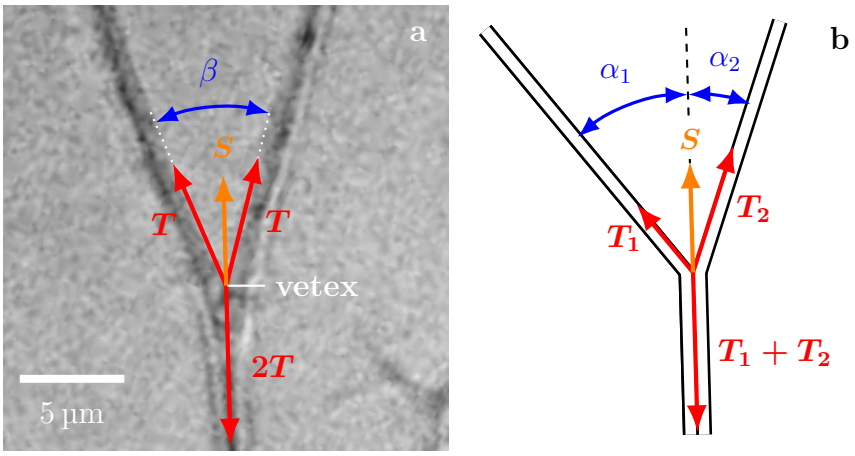

Figure 3.25: Illustration of static vertex equilibrium. **a**: Force vectors laid over an example image of a symmetric zipper. The zipper angle β is marked in blue. The arrows denote vectors of tension T and axon-axon adhesive force S. **b**: Illustration of an asymmetric zipper, markings denote the same forces as in **a**, the tensions are not equal ($T_1 \neq T_2$). The zipper angle $\beta = \alpha_1 + \alpha_2$. Note: the vectors are illustrative, not to scale.

To quantify the conditions for zipper stability, we analyse the force balance in a zipper of two axons. Tensile forces within the two axons and the adhesion force originating at their interface act at the zipper vertex. The zipper will be in static equilibrium, if effective tensile forces T (section 3.4.1) balance the adhesive force S. In a simple case of

symmetric zipper, see fig. 3.25a, where the axons meet under the zipper angle β, and the axial tensions in the left (T_1) and right (T_2) axon are equal, $T = T_1 = T_2$, the symmetry guarantees lateral (i.e. perpendicular to the *zipper axis*) static equilibrium. The axial (i.e. parallel to the *zipper axis*, i.e. to the adhered segment) equilibrium condition of symmetric zipper requires, that the sum of projections of tension in separate axons to the zipper axis $2T\cos\beta/2$ and the adhesive force S, acting to extend the adhered segment, must equal the opposing tension in the adhered segment $2T$,

$$\begin{aligned} 2T &= 2T\cos\frac{\beta}{2} + S \\ S &= 2T\left(1 - \cos\frac{\beta}{2}\right). \end{aligned} \tag{3.9}$$

If T changes between times t_1 and $t_2 > t_1$, and the condition eq. (3.9) is no longer satisfied with initial angle β_1, the zipper may advance ($T(t_2) < T(t_1)$) or recede ($T(t_2) > T(t_1)$). The initiated dynamics will continue until a new equilibrium configuration with another equilibrium angle β_2 is reached. Such changes of tension can be caused by GC activity or internal changes in the axons, which change T_0, or by structural changes of the network, which influence $\mathcal{H}$. It is also possible, that the geometry of the system is modified by the action of external force, which moves the whole axon and changes the equilibrium angle β_i, but T remains unchanged. Under such conditions, the zipper undergoes a transition and reassumes the original static angle β_i.

The balance of forces at a three-way junction of neurites was considered in (Anava et al. 2009; Bray 1979; Condron and Zinn 1997; Shefi, Harel, et al. 2004); the geometric rules for tension distribution at the vertices allowed to sequentially ascribe relative tensions to parts of a branched neurite or network. If the junction point is not otherwise immobilised, the tension force vectors must add to zero in the vertex (without axon-axon adhesion in case of branching). The conceptual difference between the branching points and the zippers is the material flow. Considering a vertex compartmentalises each axon into two segments, then (i) if the stability of a branching point is perturbed, it quickly assumes a new geometry without material transfer between constitutive segments; in contrast (ii) the zipper dynamics transfers the material between the compartments, and the redistribution occurs on longer time scale than the quick adaptation of branching geometry of item (i). We will revisit the considerations of material flow in section Zipper dynamics model.

In our experimental observations, most of the zippers were close to symmetric and the eq. (3.9) should be a good approximation of their equilibrium condition. For asymmetric zippers (fig. 3.25b), a system of more general equations describing static equilibrium can be derived from minimal energy concept (see section 3.6.1).

The configuration of axons in the vertex is determined locally and does not explicitly depend on the external fixations of the boundary of the subsystem. This fact is important for experimental measurement: measuring the angles of static configurations in the network provides us the key information to determine the biophysical parameters (see also eq. (3.27)), regardless of the network actual spatial scale and axon lengths.

3.5.2 Zipper geometry

The presented static vertex model (section 3.5.1) proposes a relationship between the biophysical characteristics of the system and its directly visible geometry, eq. (3.9). The observed typical geometry in axonal network thus reflects the typical biophysical parameters in the axons and typical size of a bundle (cf. system of two-dimensional foams, sections 1.7 and 3.10). Therefore, measuring the experimental distribution of zipper angles $\mathrm{PDF}_{\mathrm{exp}}(\beta)$ can provide us with valuable information elucidating the character of distribution of biophysical parameters.

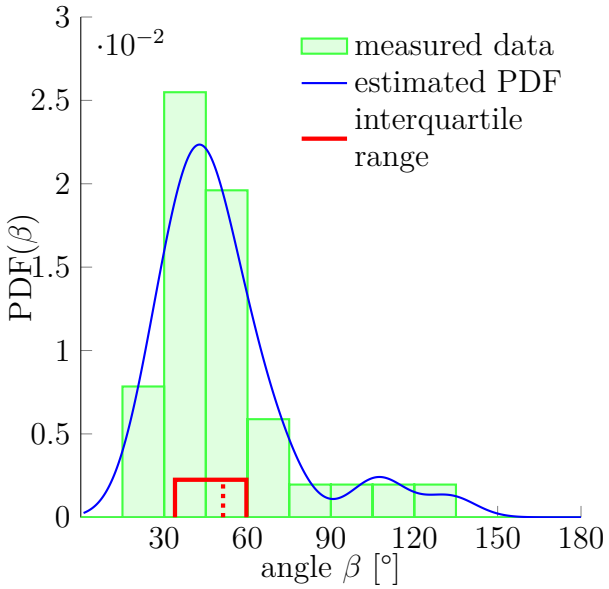

Figure 3.26: Distribution of initial and final equilibrium angles of measured zippers (17 zippers, 34 measurements) originating from 4 distinct cultures (each obtained from a different mother animal), transformed into a probability distribution using convolution with Normal kernel section 2.2.2. The red dashed line marks the average angle value (51.2°) and the solid red box delimits the interquartile range 34°–60°. The values correspond to the full zipper angle β, measured zippers were close to symmetric. The distribution includes only those zippers, which were stable at least 5 min before and after the dynamics.

Characterisation of biophysics involved in zippers through the observed angles β in the culture could be misleading. As described and shown in section 3.1.3 and fig. 3.6, some of the vertices might be entangled and therefore immobile. The entanglement is not visible in the optical microscopy recordings and the apparent equilibrium zipper angles might not be always determined by eq. (3.9), but distorted by the internal knot-like structure (figs. 3.6d and 3.6e). While the simple mobile zippers obeying eq. (3.9) are predominant (see fig. 3.7), the entangled zippers can still account for ≈25 % of the observations. For this reasons, we decided not to measure angles in static images, but only angles of those zippers, for which the zippering dynamics was observed in the *ex vivo* experiments, see section 3.1.1 and figs. 3.3 and 3.4.

We selected 17 zippers in developing culture in time lapse recordings. Each selected zipper was required to undergo a transition between two equilibrium states, and each of the equilibrium states lasted for at least 5 min before and after zippering. For each of such processes, we measured the two equilibrium zipper angles β, preceding and succeeding the dynamics. To simplify the subsequent analysis of the data, we selected the zippers which were symmetric and so described by eq. (3.9), this also allowed us to measure only one well

define total zipper angle per equilibrium β (i.e. not two partial angles α_1, α_2 of asymmetric zippers, cf. fig. 3.25a and fig. 3.25b). We selected zippers formed by individual axons or small bundles, to avoid potential bending effects.

From the 17 selected zippers, we obtained 34 equilibrium angle measurements. We used these results to estimate the angle distribution of equilibrium zipper angles as described in section 2.2.2. The distribution exhibited a sharp peak around 42°, with mean at 51.2° and interquartile range 34°–60°, see fig. 3.26. In combination with tension T estimate, these numbers can be used to estimate the adhesive force between the axons, S.

3.5.3 Estimate of adhesion parameter

The eq. (3.9) relates the biophysical parameters to the geometry. Geometry of simple configurations (i.e. approximately symmetric zippers, section 3.5.2) was quantified by measuring the zipper angle β. Using the eq. (3.9) and mean zipper angle (section 3.5.2), we can estimate that the ratio of tensile and adhesive forces as

$$T/S = 2\,(1 - \cos \bar{\beta}/2) \approx 0.2 |\ \bar{\beta} = 51.2°.$$

If we use the results of measurements of axon axial tension T by BFP technique, $T{\approx}700\,\mathrm{pN}$, we can crudely estimate the adhesion parameter as $S{\approx}140\,\mathrm{pN}$. In the following paragraphs, we will refine this estimate using more sophisticated methods.

Having measured the two distributions, $\mathrm{PDF}_{\mathrm{exp}}(T)$ and $\mathrm{PDF}_{\mathrm{exp}}(\beta)$, we used two methods to estimate the value of axon-axon adhesion force S. In the first method, we assumed that the two distributions are related through the eq. (3.9), which depends on an exact value of parameter S (i.e. S is not treated as a probability distribution). Using the distribution transformation method, as described in section 2.6.2, we obtained a distribution of angles $q(\beta)$, which would correspond to the measured distribution $\mathrm{PDF}_{\mathrm{exp}}(T)$ according to eq. (2.6).

We then numerically found the value of adhesion $S^\star$, for which is realised the maximal correlation between the random variables distributed according to the experimentally measured probability distributions—angle β_{exp} of $\mathrm{PDF}_{\mathrm{exp}}(\beta)$ (see section 3.5.2 and fig. 3.26) and angle $\beta(T;S)$ distributed according to transformed function $q(\beta)$ based on $\mathrm{PDF}_{\mathrm{exp}}(T)$ (see section 2.6.2 and fig. 3.20)—i.e.

$$S^\star = \arg\max_S \mathrm{corr}(\beta_{\mathrm{exp}}, \beta(T;S)). \tag{3.10}$$

We were able to obtain maximal correlation coefficient $\rho^\star = \mathrm{corr}(\beta_{\mathrm{exp}}, \beta(T, S^\star)) = 0.813$ for the adhesion parameter value $S^\star{=}88\,\mathrm{pN}$. The measured experimental distribution and the optimal transformed prediction distribution are shown in fig. 3.27a. This method, however, provides no information about the variance of the result. To illustrate approach to this result, we show values of the correlation coefficient $\rho(\beta_{\mathrm{exp}}, \beta(T;S))$ as a function of adhesion parameter S in fig. 3.27b, where a clear smooth maximum is visible.

The other method we used to estimate the S assumed no explicit relation between the $\mathrm{PDF}_{\mathrm{exp}}(T)$, denoted $p(T)$, and $\mathrm{PDF}_{\mathrm{exp}}(\beta)$, denoted $z(\beta)$, which allowed us to estimate an

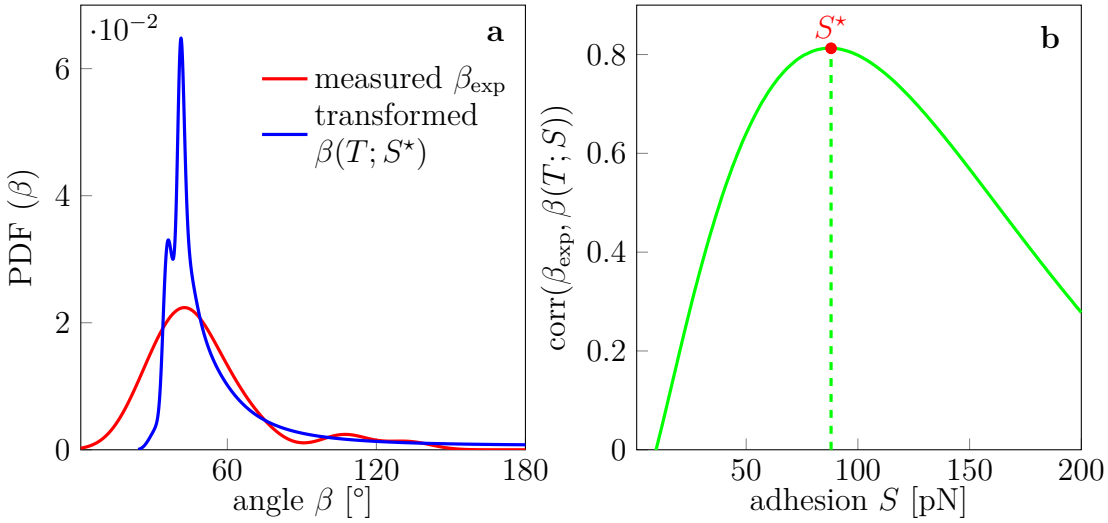

Figure 3.27: **a**: Measured distribution of static zipper angles $\mathrm{PDF}_{\mathrm{exp}}(\beta)$ (in red) and a distribution of angles $\mathrm{PDF}(\beta(T;S^\star))$ (in blue) obtained by applying eq. (2.6) on the experimental distribution of tensions $\mathrm{PDF}_{\mathrm{exp}}(T)$; parameter $S^\star$ was adjusted to maximise correlation between the two distributions. **b**: Dependence of coefficient of correlation between experimental and transformed distribution of static zipper angles $\rho = \mathrm{corr}(\beta_{\mathrm{exp}}, \beta(T,S))$ on a given value of adhesion parameter S. Maximal value $\rho^\star = 0.813$ is indicated by the red dot, and is realised for $S = S^\star$=88 pN.

upper bound on the spread of S values. We constructed the joint probability distribution as a product of the two distributions (shown in fig. 3.28a)

$$j(T,\beta) = p(T)z(\beta), \tag{3.11}$$

treating the distributions as independent. We then used this distribution $j(T,\beta)$ to estimate the $\mathrm{PDF}(S)$, denoted $r(S)$, where $S = S(T,\beta)$ given by eq. (3.9), as

$$r(S) = \iint\limits_{\{T,\beta\}} j(T,\beta)\delta(S - 2T(1-\cos\beta))dTd\beta \tag{3.12}$$

integrating over the full domain of experimental ranges T and β. Such procedure needs to be done numerically, values of S, T and β are discretised into equidistant bins (of width ΔS, ΔT and $\Delta\beta$ respectively). All possible discrete combinations (within measured intervals) of T and β are screened. For each discrete pair (T_k, β_l), a bin of adhesion parameter S_m is determined and incremented by the corresponding probability, i.e.

$$r(S_m)\Delta S = \sum_{\{k,l\}} j(T_k,\beta_l)\Delta T\Delta\beta;\ k,l : 2T_k(1-\beta_l) \in (S_m, S_m + \Delta S). \tag{3.13}$$

The distribution $\mathrm{PDF}(S)$ constructed in this manner is shown in fig. 3.28b. Ideally, the distribution estimate should be rather well centred and symmetric: its variance (width)

is a result of variability of adhesion area and expression levels of CAMs, so a Normal-like shape would be expected.

The reason for visibly non-Gaussian (skewed) shape in fig. 3.28b is, that in reality, PDF(T) and PDF(β) are not independent as we assumed. This method therefore overestimates biophysically unlikely combinations of T and β and so produces excessive extremal values in the PDF(S) estimate. For this reason, the resulting probability distribution does not tend to zero for small values, $\lim_{S\to 0} r(S) \neq 0$, and it forms a long asymmetric tail into the large values. The median value is 102 pN, while the upper bound on interquartile range S=(52–186) pN, consistent with the value 88 pN obtained by the first approach.

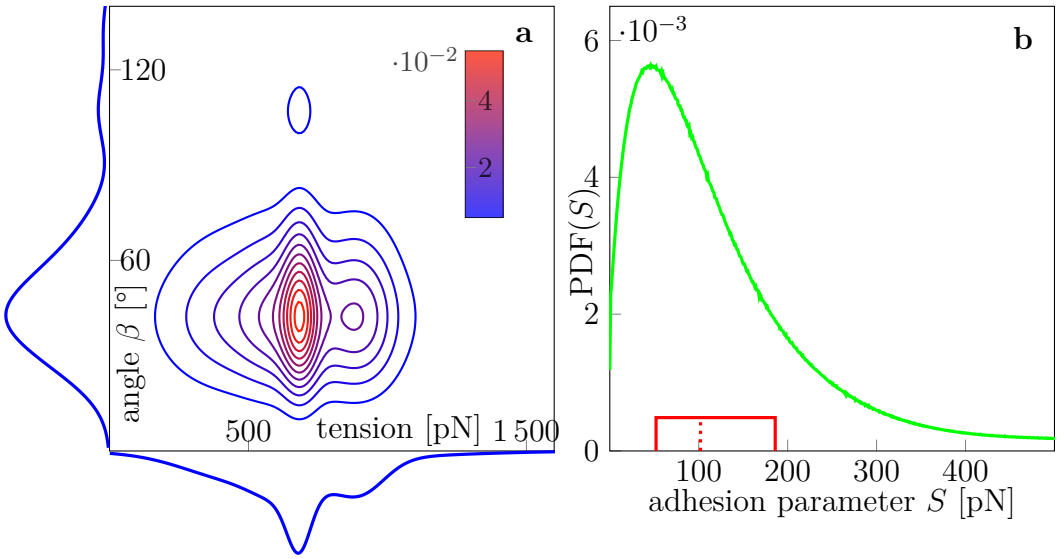

Figure 3.28: **a**: Joint distribution $j(T, \beta)$ obtained as a direct product of marginal distributions $\mathrm{PDF}_{\mathrm{exp}}(T)$ and $\mathrm{PDF}_{\mathrm{exp}}(\beta)$ indicated on the axes. **b**: Estimated distribution of adhesion parameter PDF(S) in green. The red box indicates interquartile range (52–186) pN, while the dotted red line indicates the median 102 pN. Due to the assumption of independence of $\mathrm{PDF}_{\mathrm{exp}}(T)$ and $\mathrm{PDF}_{\mathrm{exp}}(\beta)$, the resulting PDF$(S)$ is considerably asymmetric, and does not tend to zero for $S \to 0$. Ideally, the distribution should be close to Normal distribution.

3.5.4 Zipper dynamics

We observed numerous spontaneous zippering processes in the axonal network (e.g. figs. 3.3 and 3.4). We tracked the course of such dynamics for 17 selected zippers composed of individual axons or small fascicles and nearly symmetric configuration (for simplicity). For each of those, an equilibrated stage took place before and after the transition (lasting for at least 5 min). Some of the zippering time courses are shown in fig. 3.29.

The typical velocities of these observed zippers were in the range (0.3–2.0) $\frac{\mu m}{min}$. The figs. 3.29a and 3.29b show time course of zipper distance $d(t)$ from the final equilibrium coordinate $d(t) = |(x(t), y(t)) - (x'_0, y'_0)|$. Zippers in fig. 3.29a are advancing (i.e. extending adhered segment), fig. 3.29b are receding. In fig. 3.29c, character of the convergence is shown in detail; some of the zippers approach the final equilibrium linearly in time (A6, R3), some are progressing exponentially (A5, R4). The equations of the corresponding fits are shown in eq. (3.14).

$$\begin{aligned} d_{A6}(t) &= -0.45(t + 7.59) \\ d_{R3}(t) &= -1.11(t + 6.94) \\ d_{R4}(t) &= 14.95 \exp\{-0.20(t + 19.14)\} \\ d_{A5}(t) &= 10.42 \exp\{-0.22(t + 19.12)\} \end{aligned} \tag{3.14}$$

In our observations, zippers with linear convergence were more common ($\sim$ 2/3 of cases). They usually start abruptly, advance at constant velocity and stop suddenly. We discuss these exponential/constant velocity characteristic further in sections 3.7.3 and 3.7.4.

The fig. 3.29d shows angles of selected zippers. In these examples, angles of advancing zippers (A1, A4, A6) increase and angles of receding zippers (R4, R5) recede, as predicted by eq. (3.9). Such observations are however not universal—in some other cases (e.g. zipper configuration is more interconnected with the rest of the network) fluctuations within the network easily interfere with the development and the angle trend is influenced by noise.

The average measured zipper velocity was (0.89 ± 0.50) $\frac{\mu m}{min}$, in between the stability periods before and after actual dynamics. Average distance of transition in the measured zippers was (10.46 ± 3.85) µm. In fig. 3.30, typical convergence examples are shown in semi-log plots, to illustrate that some zippers tend to converge more exponentially in time ($d(t) \sim e^{-t}$, fig. 3.30a) and some linearly ($d(t) \sim -t$, fig. 3.30b).

We sought to view the processes in light of the hypothesis 1. The zipper equilibrium is determined by the potential energy E of zipper configuration. For the model introduced in section 3.5.1, the potential energy at a coordinate (x, y) depends on geometrical factors (i.e. axon length, points of axon fixation, etc.; denoted $g(\{\vec{r}_i\})$, where $\vec{r}_i$ are coordinate parameters) and biophysical factors (i.e. T_1, T_2 and S), and can be written as

$$E(x, y) = E(x, y; T_1, T_2, S, g(\{\vec{r}_i\})),$$

and therefore, the potential can change, if parameters change (detailed in section 3.7.1).

The zipper equilibrium (within the model framework for reasonable parameters) is always stable (detailed in section 3.6.1), its robustness towards perturbations however depends on the potential E depth and its spatial steepness ∇E around the equilibrium coordinate (x_0, y_0). The biological systems on this scale are strongly overdamped (section 1.3.2), and inertial force is negligible. Any change of equilibrium geometry, i.e. $(x_0, y_0) \to (x'_0, y'_0)$ is therefore a result of change of potential $E \to E'$.

Considering the complexity and interconnectedness of a typical axonal network, it is very plausible that axial tension of zipper-forming axons T_1 and T_2, or geometrical

factors $g(\vec{r}_i)$ (e.g. points where axons are immobilised) might fluctuate in time. Such perturbation redraws the energy landscape $E(x, y)$, and the vertex equilibrium location shifts to other coordinate (x'_0, y'_0). The steepness and depth of the potential characterise the volatility to these fluctuations. We tested trajectories resulting from particular types of perturbation in section 3.7.3.

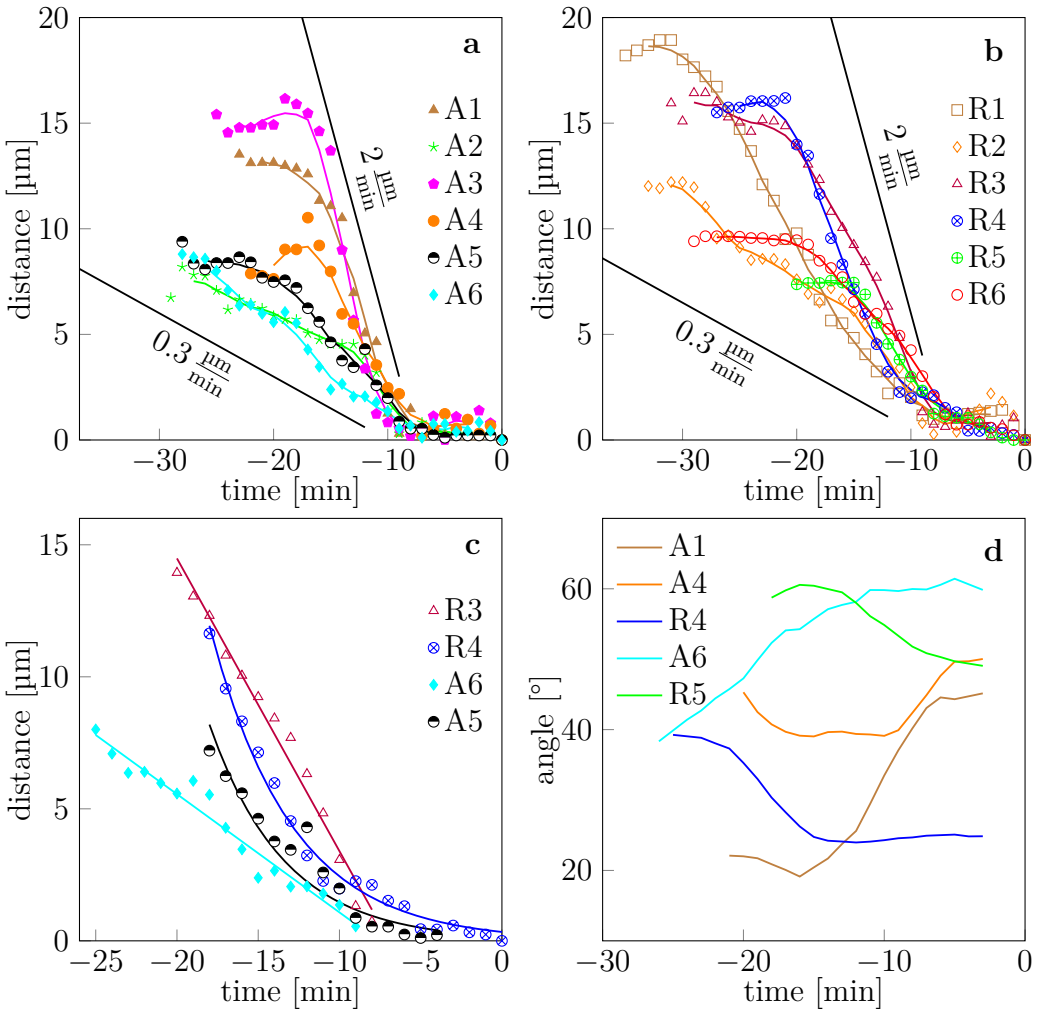

Figure 3.29: Examples of zipper dynamics time courses. The data represented by marker points were measured in each frame, at framerate 1 $\frac{\text{frm}}{\text{min}}$. The are interpolated by a 5 frm sliding average, drawn as a line of corresponding colour. **a**: Time-courses of distance of advancing zippers from final equilibrium at t=0 min with 5 min stable regions before and after the dynamics. **b**: Time-courses of distance of receding zippers from final equilibrium reached at t=0 min. Zippers of both **a** and **b** have typical the velocities in interval (0.3–2.0) $\frac{\mu\text{m}}{\text{min}}$, as indicated by enclosing lines. **c**: Data from graphs **a** and **b** fitted either be a line or an exponential. Zippers can generally follow either of the two. Fit equations provided in eq. (3.14). **d**: Angles of selected zipper, smoothed by a 5 frm sliding average. The angle of advancing zippers increases and angle of receding zippers decreases from one equilibrium to another, consistent with eq. (3.9).

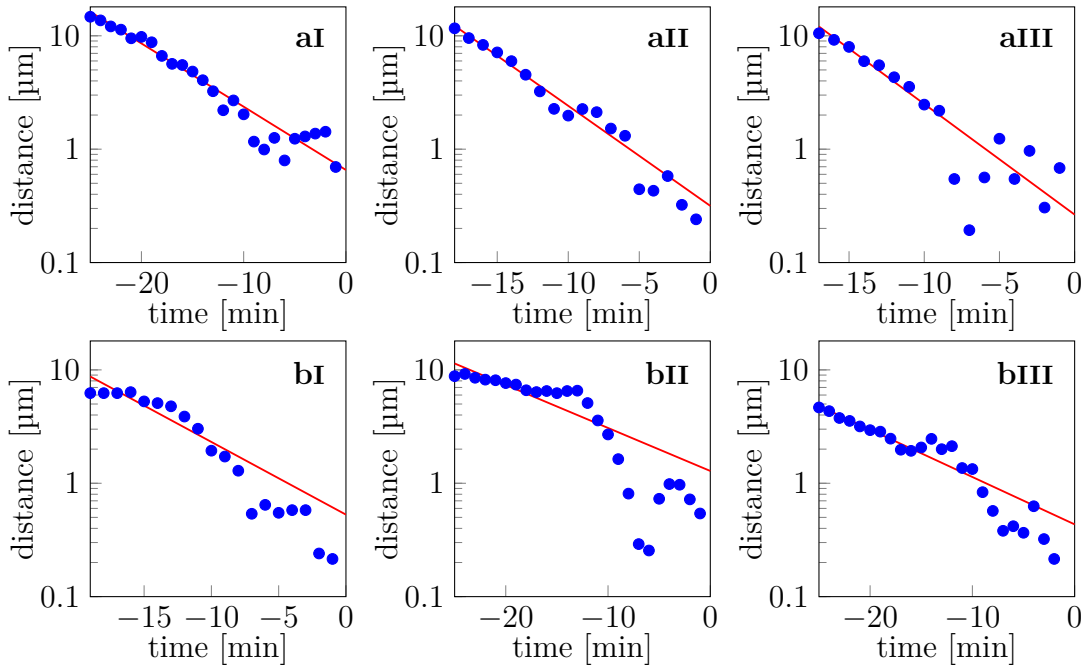

Figure 3.30: Semi-log graphs of zipper convergence. The blue dots represent the measured data, the red line is an exponential fit. **a**: Top graphs are examples of zippers consistent with exponential approach to the final equilibrium. Despite the noise of the data increases in the last 10 min, the data are still close to the trendline. **b**: Bottom graphs represent linearly converging zippers. In the last 10 min, they visibly depart from the exponential fit, and converge faster, consistently with a linear approach. All zippers travel a typical distance ≈10 µm during ≈20 min. Obviously, there is no clear distinction threshold between the exponentially and linearly converging zippers, e.g. compare **aIII** and **bIII**.

3.5.5 Zipper dynamics model

In the hypothesis 1 and in the zipper static equilibrium model presented in section 3.5.1, we introduced the concept of zippers in terms of concurring influences of axon-axon adhesion S and effective axial tensions T. In order to assess if such understanding is consistent with the observed dynamics of zippers presented in sections 3.5.2 and 3.5.4, we developed a biophysical dynamical model for simple zipper system. Within the framework of this model, we derived an effective equation of motion for the zipper vertex. The model does not explicitly treat active biological processes of the axons (i.e. axon guidance, active AS contractility), but may consider them implicitly, in a form of initial conditions, boundary conditions, or time-dependent parameters (cf. section 3.6). Rigorous mathematical foundations and derivation of the model are presented later in sections 3.6 and 3.6.2, at this point, we present the underlying ideas and less technical results.

At a given time t, assume we have a planar zipper configuration as shown in fig. 3.31. Two axons, axon *1* on the left and axon *2* on the right, are fixed in boundary points A, B, and C. The axons meet at the mobile vertex point $V(x, y)$, and adhere to each other along the segment VC, while they remain separated along segments VA and VB. The fixation points may correspond to strong substrate attachments, immobile entanglements to other areas of the network, soma or the GC. When the condition of vertex equilibrium given by eq. (3.9) is not met, the imbalance of concurrent forces generates a net force at the vertex point $\vec{F}_v(x, y)$, and the transition begins at vertex velocity $\vec{u}$, as described in section 3.5.4. The tensile energy is released from the system due to change in geometry (i.e. axon shortening) and is dissipated by friction and material viscosity (section 3.4.5) as the system undergoes the transition.

The dissipative forces depend on the system geometry and linearly on the velocity of the transition. Since the geometry of our system is quite simple, some of the dissipative forces can be expressed as collinear with the conservative forces. Such simplicity allows us to straightforwardly modify the eq. (3.9), and gain insight into the zipper dynamics. It effectively allows us to formulate a simplified equation of motion for the system, however at cost of ignoring particular types of dissipative forces, which cannot be treated so simplistically (see section 3.6.2 for details).

One of the dissipative forces, which can be directly included, is axon *elongational* viscous dissipation (see fig. 3.31). It arises from irreversible internal changes within the axon as it stretches or shortens, which is necessarily happening during the zipper dynamics. Within the linear viscoelasticity regime, the local viscous stress generated by this dissipation is proportional to the local strain rate $\dot{\epsilon}$. Since the section of the axons involved in the dynamics is rather small, compared to the full axon length, we assume that the strain between the fixation points remains uniform—the axon deformation transfers along the axon faster than the zippering dynamics occurs. The strain rate can then be expressed for any point of the axon in the vertex vicinity as $\dot{\epsilon} = \dot{L}/L$, where L is the total length of segments of an axon involved in the zippering process, e.g. for axon *1*, $L_1 = |VA| + |VC|$ (see fig. 3.31). Because the axial strain rate depends on the

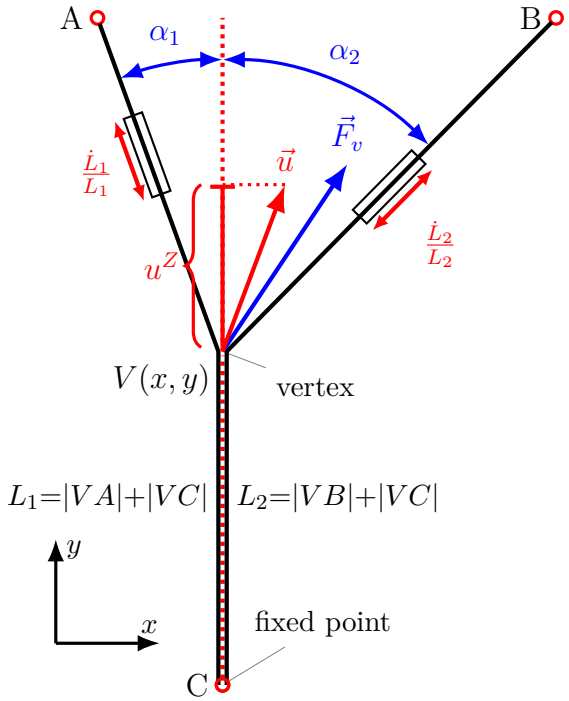

Figure 3.31: Illustration of a dynamical model of zipper transition. The configurations is fixed at points A, B and C, composed of two axons, *1* on the left, *2* on the right, which form a vertex $V(x, y)$ at the particular coordinate. Net conservative force acting acting on the vertex $\vec{F}_v$ arises from imbalance of tensile (T_1, T_2) and adhesive (S) forces at the vertex V. Actual velocity $\vec{u}$ of the moving vertex is generally not collinear with $\vec{F}_v$; u^Z represents vertex velocity component in the zipper axis direction. L_1 and L_2 are total length of the axons *1* and *2* respectively. The strain rate of the axons, $\dot{\epsilon} = \dot{L}/L$, is indicated by a black rectangle for each axon.

axon length, the elongational dissipative force has the same geometrical dependence as the (axial) tensile force T, and can be therefore understood as effectively countering the work done by the tensile forces (or adding to the work external forces must do) , i.e.

$$\tau = T + \eta^{\Updownarrow}\frac{\dot{L}}{L}, \tag{3.15}$$

where T is the axon axial tension and $\eta^{\Updownarrow}$ is coefficient of proportionality for elongation viscosity force. Note the plus sign: (i) if the axon is stretched by external force, $\dot{L} > 0$, then $\tau > T$, the friction dissipates external forces and compounds the elastic tensile resistance to stretching, (ii) if T shortens the axon, $\dot{L} < 0$, then $\tau < T$, and the friction force dissipates the work done by internal tensile forces T.

Another possible source of energy dissipation are axon geometry changes in the immediate vicinity of the vertex in transition; these changes largely depend on extension or reduction of adhered segment length. As the vertex advances or recedes, new regions of the axons deform and bend, while others straighten. We have shown in section 3.4.4 that elastic conservative energies of bending processes during zippering are negligible, it is however possible that the energies driving dynamics are viscoelastically dissipated[5] during internal structural changes accompanying the bending. Another contribution can be the changes in the length of axon-axon adhesion segment VC; if the binding/unbinding is too rapid, non-equilibrium effects take place at the axon-axon interface and result in

[5]Note the bending effects treated in section 3.4.4 considered conservative elastic energy to be stored in the material curvature. Dissipative losses treated here are irreversible.

dissipation. These effects demonstrate themselves as a vertex-localised friction force, which acts anti-parallely to the zipper axis ($\widehat{VC}$) component of vertex velocity $\vec{u}^Z$ (so called *zippering velocity*),

$$\vec{u}^Z = \left[\vec{u}\cdot\left(-\widehat{VC}\right)\right]\left(-\widehat{VC}\right),$$

see fig. 3.31. In geometrical terms, the vertex-localised dissipation force is collinear with the adhesion force $-S\,\widehat{VC}$, and can be understood as effectively decreasing the adhesion force S. We denote such decreased adhesive interaction as χ, given by

$$\chi = S - \eta^Z \vec{u}\cdot\left(-\widehat{VC}\right) = S - \eta^Z u^Z, \tag{3.16}$$

where η^Z is corresponding proportionality vertex-localised friction constant, and $u^Z = \vec{u}\cdot\left(-\widehat{VC}\right)$. This dissipative effect always acts in the direction opposite to the vertex movement.

We can now generalise eq. (3.9) by adding the dynamical dissipative corrections ($\propto \vec{u}$) to T and S terms according to eqs. (3.15) and (3.16). For simplicity, we will again work with a symmetric zipper, where the symmetry is preserved during the dynamics. Initial conditions reduce to $T_1 = T_2 = T$, $\alpha_1 = \alpha_2 = \beta/2$ and $L_1 = L_2 = L$. To further simplify the formalism, we align the axis of zipper symmetry, i.e. the zipper axis $\widehat{VC}$, along y-axis, so that

$$|\vec{u}^Z| \equiv u^Z = \dot{y}$$
$$\dot{L} = (1-\cos\beta/2)\,\dot{y},$$

where segment VC extends in increasing y direction.

After replacing $T \to \tau$ and $S \to \chi$, the eq. (3.9) expresses the total force balance in a moving vertex $V(x,y)$. The equation can be rearranged to find an expression for the zippering velocity $\dot{y}$, the equation of motion of a symmetric zipper,

$$\begin{aligned}
\chi &= 2\tau(1-\cos\beta/2)\\
S - \eta^Z u^Z &= 2\left[T + \eta^{\Updownarrow}\frac{\dot{L}}{L}\right](1-\cos\beta/2)\\
S - \eta^Z \dot{y} &= 2T(1-\cos\beta/2) + 2\eta^{\Updownarrow}\frac{(1-\cos\beta/2)^2\dot{y}}{L}\\
\dot{y}\left[2\eta^{\Updownarrow}\frac{(1-\cos\beta/2)^2}{L} + \eta^Z\right] &= S - 2T(1-\cos\beta/2)\\
u^Z \equiv \dot{y} &= \frac{S - 2T(1-\cos\beta/2)}{2\eta^{\Updownarrow}\frac{(1-\cos\beta/2)^2}{L} + \eta^Z}.
\end{aligned} \tag{3.17}$$

Note that both L and $(1-\cos\beta/2)$ on the right hand side are non-linear functions of vertex coordinate y, and directly depend on the boundary conditions, the fixed points A, B and C. The equation cannot be solved in closed analytical form, however a zipper trajectory $y(t)$ can be obtained through numerical integration. For angle in range of symmetric geometries observed in the *ex vivo* experiments, the numerical integration of eq. (3.17) is stable. If the friction contributions should be roughly comparable, for a typical angle $\beta\approx 52°$ and axon length $L\approx 100\,\mu\text{m}$, then $\eta^{\Updownarrow} \approx 5000\,\mu\text{m}\cdot\eta^Z$ (note this ratio strongly depends on L and β). Figure fig. 3.32 shows the integrated vertex trajectories.

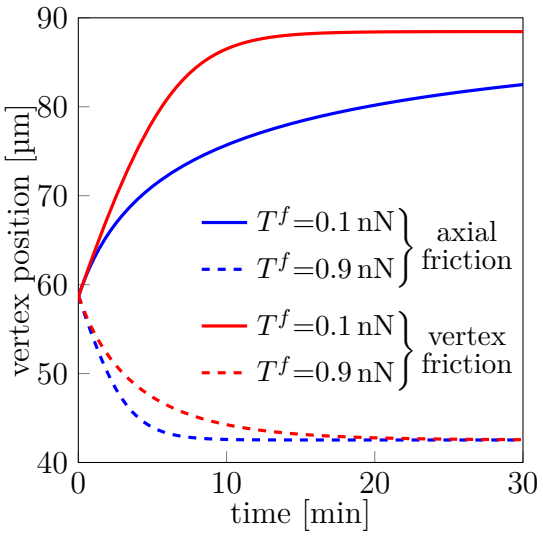

Figure 3.32: Symmetric zippering vertex trajectories calculated by numerical integration of eq. (3.17) for initial configuration T=0.5 nN, S=0.1 nN, normal distance of fixation points from zipper axis p=20 µm and initial (reference) zipper length $y|_{t=0}$=59 µm. T^f is tension of final equilibrium. One type of friction is used at the time, with roughly equal initial effective friction force. Trajectories diverge in time, as axial dissipation depends on geometry, while vertex dissipation does not.

The trajectories start from a symmetric equilibrium point for T=0.5 nN and S=0.1 nN, with perpendicular distance of fixation points A and B from the zipper axis p=20 µm; the initial vertex angle β=52°. The tension is decreased (solid line) or increased (dashed line) by 0.4 nN, one of the two proposed dissipation forces is employed, vertex friction with coefficient η^Z=1 $\frac{\text{nN s}}{\text{µm}}$ (red) or elongational friction with $\eta^{\Updownarrow}$=5000 nN s (blue). With these values of friction proportionality coefficients, the initial friction force is roughly equal at the beginning of integration. As the vertex advances, and the geometry of the system changes, the coefficient of elongational friction proportionality to $\vec{u}$ changes, as it depends on both β and L. Consequently, the trajectory is different from the trajectory of geometry independent zipper friction force. Advancing zipper stops at the angle β_A=120°, receding at the angle β_R=38°. Note the values in this example are not necessarily realistic (e.g. L), but help to illustrate the differences.

This basic model qualitatively agrees with the observations (fig. 3.29). Particular parameter settings allow us to replicate the characteristic convergence shown in fig. 3.29c. To expand the model also into quantitative domain, we have already estimated typical biophysical parameters for tension (section 3.4.2) and adhesion (section 3.5.3), i.e. conservative forces, and typical zipper angle (section 3.5.2), i.e. initial and boundary conditions. Combining the estimates with eq. (3.17) allows us to test the consistency and predictions of this model against dynamics observed in manipulation experiments, and estimate the dissipative terms $\eta^{\Updownarrow}$ and η^Z.

3.5.6 Estimation of dynamical model parameters

As noted in the section 3.4.2, the dynamics of zipper transition would have been ideally tested by local calibrated micro-manipulation of axon tension T. Such experiment was not possible for the reasons discussed in the section Axon tension measurement, we therefore performed uncalibrated manipulations using a micropipette. We selected rather isolated zippers to minimise interference of the surrounding network, and displaced the

AS of one of the zipper-forming axons. Such change in geometry increased the zipper angle β and initiated a zippering towards the new equilibrium configuration, see fig. 3.8a. In some cases, however, the zipper configuration did not change, see fig. 3.8b; this is likely due to entangled zipper structure as described in figs. 3.6d and 3.6e.

In a more complex example, we were able to perform an uncalibrated zipper manipulation, which (i) initiated unzippering and decrease of the zipper angle; (ii) after the pipette was removed, the zipper advanced back towards pre-manipulation equilibrium and angle increased. We tracked the position of the zipper and the zipper angle through the dynamics as shown in fig. 3.33a. The red track indicates the positions of the tracked vertex point in fig. 3.33aII-VI. Interestingly, the zipper undergoes fast lateral equilibration during lateral pull or release (a transient dynamics; see fig. 3.33aII and V), while the zippering dynamics (along the zipper axis) occurs on a longer time scale. The initial fast lateral dynamics is independent on vertex-localised dissipation, because the change in zippered length is negligible as compared to the change in length of both axons. This implies that the elongational dissipation permits much faster dynamics, and that the vertex-localised dissipation plays a decisive role during the slow dynamics of zipper advance, that is $|\eta^Z u^Z| \gg |\eta^{\Updownarrow}\dot{\epsilon}|$ during zippering.

Measured kinetics of this zipper (fig. 3.33) can be understood in terms of eq. (3.17). We will neglect the fast transient dynamics related to manipulation (or release of the pipette), and exclude such data from analysis (marked by pale blue dashed line in fig. 3.33b). Keeping only the data of slower symmetric dynamics, marked by solid blue line, and assuming that:

- zipper is close to symmetric, its geometry is well described by the factor $(1 - \cos {}^{\beta}/_{2})$ (abscissa in fig. 3.33b);
- vertex velocity corresponds to zippering velocity (i.e. $\vec{u} = \vec{u}^Z$), and can be identified with $\dot{y} \equiv u^Z$ in eq. (3.17) (ordinate in fig. 3.33b).

Both quantities ($\dot{y}$ and β) were measured in the video at 1 s interval, and smoothed using a Gaussian kernel of 10 s half-width. The red dashed line represents the best linear fit of the zippering/unzippering data. As pointed out previously, since $|\eta^Z u^Z| \gg |\eta^{\Updownarrow}\dot{\epsilon}|$, we can reduce the eq. (3.17) to

$$\dot{y} = \frac{S - 2T\,(1 - \cos {}^{\beta}/_{2})}{\eta^Z},$$

and relate it to the quantitative results of linear regression of the data.

Under the assumptions, the slope of regression equals ${}^{-2T}/_{\eta^z} = -4.1692\,\frac{\mu\mathrm{m}}{\mathrm{s}}$ and the intercept ${}^{S}/_{\eta^z} = 0.0825\,\frac{\mu\mathrm{m}}{\mathrm{s}}$. This directly allows us to estimate ratio of tension and adhesion ${}^{S}/_{T} = 0.04$; a typical value obtained from the static measurements and estimates is ${}^{S}/_{T} = \frac{88\,\mathrm{pN}}{686\,\mathrm{pN}} = 0.13$, which represents an order of magnitude match. Apparently lower ratio for manipulation experiment can be attributed to two sources, (i) axon tension scales linearly in bundles of all sizes, $T \sim n$ (section 3.3.3); the measurement was performed on axon bundles near the explant boundary, while static configurations were likely single axons; (ii) adhesion parameter remains roughly constant $S \sim$ const. for small bundles, or scales as $S \sim \sqrt{n}$ at worst (see sections 3.3.2 and 3.3.3). These distinct bundle scaling rules shift the ${}^{S}/_{T}$ ratio towards lower values, consistently with the

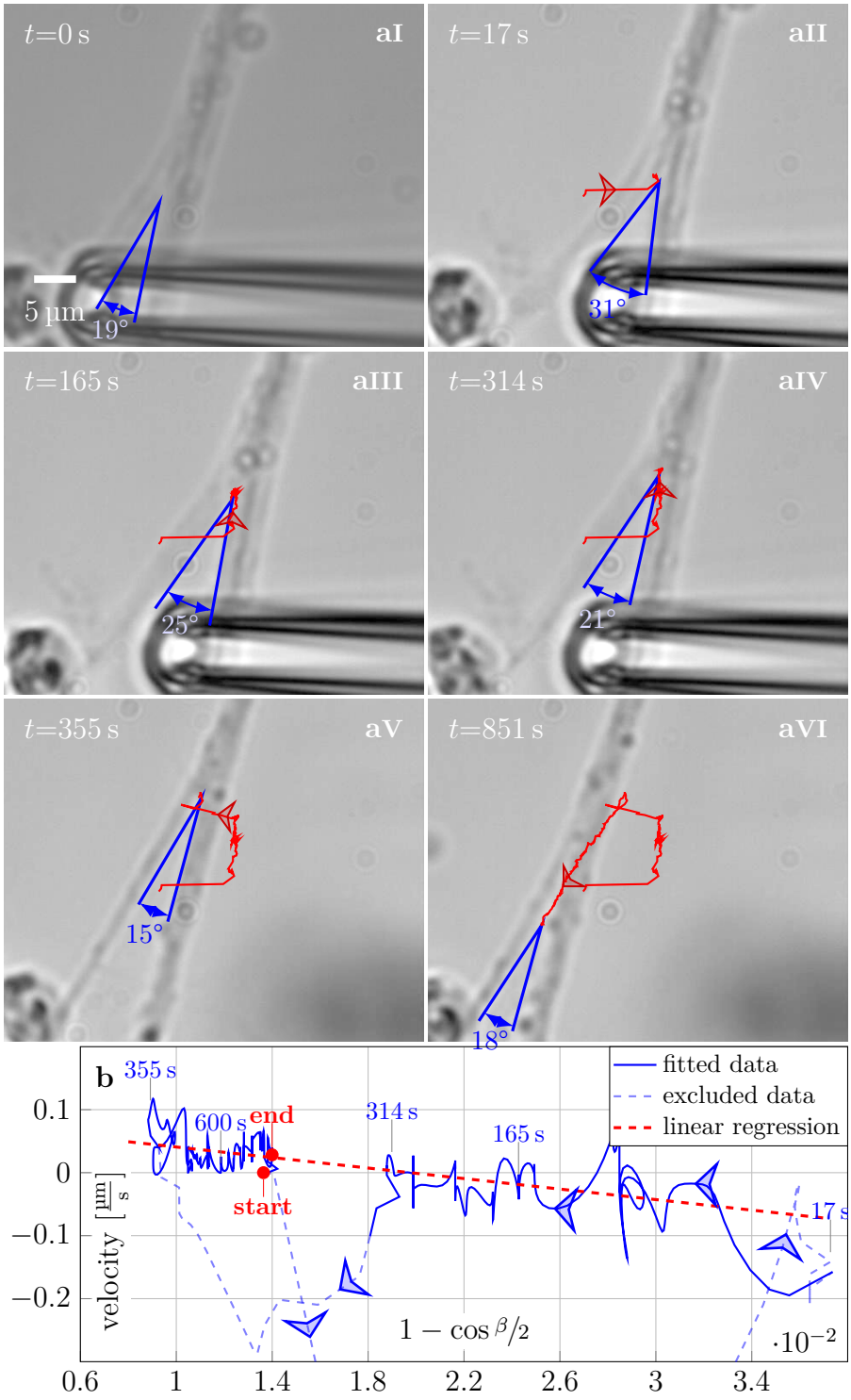

Figure 3.33: **a**: **I** initial zipper configuration is pulled **II** and held fixed **III-IV**. After the release **V**, it zippers back towards the initial equilibrium **VI**. Stretched angle 31° gradually decreases during unzippering to 15°, less than initial equilibrium angle 19°, and is restored during re-zippering. The red path indicates the path of the vertex point. **b**: Plot of measured geometry and velocity at each second of the experiment, with some timestamps indicated. Initial ('start') and final ('end') equilibria are indicated, having very similar geometry. The data of zippering/unzippering process were fitted by linear regression (red dashed line). The data of transient zipper dynamics were excluded from the fit.

observed difference. For a tension of $T{\approx}2\,\mathrm{nN}$, the predicted value of vertex-localised friction coefficient would be $\eta^Z{\sim}1\,\frac{\mathrm{nN\,s}}{\mu\mathrm{m}}$.

This is consistent with a result we would obtain for typical observed dynamics of zippers in culture (section 3.5.4), $v{\approx}1\,\frac{\mu\mathrm{m}}{\mathrm{min}}{\approx}0.02\,\frac{\mu\mathrm{m}}{\mathrm{s}}$, $\beta{\approx}50°$, $S{\approx}0.1\,\mathrm{nN}$, $T_{ini}{\approx}0.5\,\mathrm{nN}$, assuming tension increases to final values of $T_{fin}{\approx}1\,\mathrm{nN}$, so we obtain

$$\eta^Z = \frac{S - 2T\,(1-\cos\beta/2)}{v} \approx \frac{0.1 - 2\,(1-\cos\beta/2)}{-0.02} \approx 5\,\frac{\mathrm{nN\,s}}{\mu\mathrm{m}}.$$

3.5.7 Viscous processes in a single axon

Previous section discussed biophysical parameters and dissipation estimates in case of induced and spontaneous zippering. The zippering process is however more complex than typical dissipative processes associated with viscoelastic relaxation of a single axon. If an axon shaft is put under stress (e.g. external force is applied), viscous processes lead to material creep in the direction of applied force and relaxation of the material stress, as described in section 1.4.3. We assume the time scale of relaxation of *strain/stress gradient* in a single axon is much shorter than the viscoelastic stress relaxation[6], i.e. uniform stress in the axon is quickly restored, followed by a period of uniform stress relaxation (illustrated in fig. 1.8). The uniform stress relaxation effects observed during BFP experiments allow us to estimate viscoelastic dissipation parameters of a single (non-zippering) axon.

Deflection of an axon during a BFP experiment is typically followed by a gradual relaxation of the system. The force transduced by the probe decreases by roughly 10 %, or, ∼10 pN during 1 s after pipette fixation. The geometry of the deflected axon changes only very little during the experiment, $\delta{\lesssim}5°$, therefore geometric proportionality factors relating dissipation to apex relaxation velocity v remain roughly constant. We can therefore estimate an effective friction force as $f_\eta \sim \eta v \sim \eta\dot{h}$, where $h(t)$ is perpendicular deflection of the axon apex. We formulate a simple model for such estimation, $\kappa \approx 0.5\,\frac{\mathrm{nN}}{\mu\mathrm{m}}$ is typical BFP stiffness and $L \approx 20\,\mu\mathrm{m}$ is typical axial length of axon deformation. After the manipulation and fixation of the probe at the time $t{=}0$, where deflection $h(t{=}0){\equiv}h_0$, the axon relaxes and extends in the direction of incurred force $F_0 = F_{\mathrm{BFP}}(t{=}0)$, the deflection increases $h(t{>}0){>}h_0$, and extension of the BFP correspondingly decreases reading lower exerted force $F_{\mathrm{BFP}}(t{>}0) < F_0$. This process can be described as follows,

$$\begin{aligned} F_{\mathrm{BFP}}(t) = F_0 - \kappa(h(t)-h_0) &= \eta\dot{h}(t) + T\frac{h(t)}{L} \\ v = \dot{h}(t) &= -\left[\frac{T+\kappa L}{\eta L}\right] h(t) + \left(\frac{F_0+\kappa h_0}{\eta}\right) \\ h(t) &= h_\infty + (h_0 - h_\infty)e^{-t/\tau}, \end{aligned}$$

where $h_0 < h(t) \le h_\infty = \frac{\kappa h_0 L + F_{\max} L}{T+\kappa L}$ is asymptotic deflection, and relaxation time $\tau = \frac{\eta L}{T+\kappa L}$. Fitting the BFP data with such function yields relaxation times in a range

[6] And therefore also shorter than the time scale of zippering dynamics; which makes the two processes independent under our model. The effects of stress gradient relaxation of axon shaft are discussed in detail in O'Toole, Lamoureux, et al. 2008.

$\tau \approx (0.5\text{–}1)\,\mathrm{s}$, on clearly shorter timescale than zippering experiments. Combined with typical values, effective friction is at the order

$$\eta \approx \tau \frac{T + \kappa L}{L} \approx 0.5\,\frac{\mathrm{nN\,s}}{\mu\mathrm{m}}.$$

If we consider a typical velocity of zippering, $1\,\frac{\mu\mathrm{m}}{\mathrm{min}}$, and corresponding typical transverse axon velocity $0.4\,\frac{\mu\mathrm{m}}{\mathrm{min}}$, then the vertex localised dissipation $1\,\frac{\mu\mathrm{m}}{\mathrm{min}} \cdot 5\,\frac{\mathrm{nN\,s}}{\mu\mathrm{m}} \approx 0.1\,\mathrm{nN}$ is about order of magnitude higher than corresponding viscoelastic dissipative process in the two vertex-forming axons $2 \cdot 0.4\,\frac{\mu\mathrm{m}}{\mathrm{min}} \cdot 0.5\,\frac{\mathrm{nN\,s}}{\mu\mathrm{m}} \approx 0.01\,\mathrm{nN}$, suggesting that vertex-localised friction dominates in zippering processes, as we have previously proposed.

Note that there are many possibilities how to model the relaxation process during the BFP experiments. It turns out that more intricate models yield less sensible and more noise-sensitive results, mostly because the relaxation data quality is not optimal.

3.5.8 Energy dissipation

Of the previously estimated range of circumference of contact between axon shafts, we will assume the middle value, 25 %, of axon surface to be involved. The axon linear adhesion energy density is $S = 100\,\mathrm{pN} = 10^{-7}\,\frac{\mathrm{nJ}}{\mu\mathrm{m}}$, and for the expected perimeter length involved, $0.16\,\mu\mathrm{m}$, the adhesion energy per unit membrane area would be $\gamma = 6 \times 10^{-7}\,\frac{\mathrm{nJ}}{\mu\mathrm{m}^2}$. This is at comparable level with E-cadherin mediated cell-cell adhesion, which we estimated from the separation force measurements of (Chu, Thomas, et al. 2004). The separation ('pull-off') force F_p measurement for cell of radius R_c can be converted to (single) surface energy density using JKR relation (Chu, Dufour, et al. 2005; K. L. Johnson et al. 1971; Spolenak et al. 2005) as $\gamma = \frac{F_p}{3\pi R_c} = (2 \times 10^{-7}\text{–}4 \times 10^{-6})\,\frac{\mathrm{nJ}}{\mu\mathrm{m}^2}$.

The estimate of γ in the previous paragraph was based on static measurements. If we consider independent dynamic estimate, based on section 3.5.6, the friction dominated by $\eta^Z \approx 5\,\frac{\mathrm{nN\,s}}{\mu\mathrm{m}}$, and typical zippering velocity $u^Z \approx 1\,\frac{\mu\mathrm{m}}{\mathrm{min}}$, the energy dissipation rate is of order $R \sim \eta^Z (u^Z)^2 \sim 10^{-7}\,\frac{\mathrm{nJ}}{\mathrm{min}}$. This is consistent with order of dissipation expected in a perturbed zipper, for $S = 10^{-7}\,\frac{\mathrm{nJ}}{\mu\mathrm{m}}$, $\beta = 52°$ and perturbed (increased) tension $T = 10^{-6}\,\frac{\mathrm{nJ}}{\mu\mathrm{m}} = 1\,\mathrm{nN}$,

$$\Delta E = |S - 2T(1 - \cos \beta/2)| \approx 10^{-7}\,\frac{\mathrm{nJ}}{\mu\mathrm{m}}$$

which corresponds to dissipation rate $R \approx 10^{-7}\,\frac{\mathrm{nJ}}{\mathrm{min}}$ for the typical velocity $u^Z \approx 1\,\frac{\mu\mathrm{m}}{\mathrm{min}}$. Which shows that the friction dissipation estimate from dynamical experiment can be reconciled with the typical dissipation estimate from static measurements and SEM observations (section 3.1.3).

3.6 Mathematical model of zipper statics and dynamics

The matters discussed in sections 3.5.1 and 3.5.5 will be generalised and formalised in sections 3.6.1 and 3.6.2. The model will be then inspected both analytically and numerically in section 3.7. This model describes local and isolated system, i.e. not interfering with the rest of the network besides boundary conditions, and therefore applies only to a subset of processes happening in the axonal network as a whole.

We will first introduce notation used in the following sections. In general formulation, we initially consider N axons described by a set of J straight segments. Those axons adhere along I segments, which are a subset of those J segments ($I \leq J$), and so several axons may share a specific segment—i.e. if two axons adhere along one segment, the segment is not counted twice. The system geometry is defined in the following terms:

- l_j represents the length of a straight oriented segment $\vec{l_j}$ forming an axon, index $j \in (1, \ldots, J)$,
- l_i is length of a segment of axon-axon adherence, where index $i \in \{j_1, \ldots, j_I\} = \mathcal{I}$ belongs to a subset $\mathcal{I}$ of segment indices j, which participate in adhesion,
- individual axons are numbered by index $n \in (1, \ldots, N)$,
- $a_n = \{1, \ldots, p\}$ is a set of indices numbering the p segments forming the axon n.

Then, the total length L_n of axon n is given by

$$L_n = \sum_{k \in a_n} |\vec{l_k}| \equiv \sum_{k \in a_n} l_k.$$

Initial (i.e. $t = 0$) unstrained (or reference) axon total length

$$L_{n0} = \sum_{k \in a_n} l_{0k} = \sum_{k \in a_n} l_k(t{=}0)$$

is given as a sum of initial segment lengths $l_{k0} = l_k(t{=}0)$. Extension/compression of axon n at the time t is given by

$$\Delta L_n(t) = L_n(t) - L_{n0} = \sum_{k \in a_n} l_k(t) - l_{0k}.$$

Note that we assume, that the elements of a set a_n are conserved during the dynamics (i.e. the segments forming an axon do not vanish or appear).

Using this geometry notation, the mechanical potential energy E (cf. section 3.5.4, comprises the following contributions:

- energy of effective rest tension of axon n ($T_0 \sum_{j \in a_n} l_j \equiv T_0 L_n$; scales with axon length L_n); T_0 combines axon rest mechanical tension with the axon-substrate adhesion, $T_0 = T_a + I$, see section 3.5.1;
- energy of adhesion of axon n ($\frac{1}{2} S \sum_{j \in a_n} l_j \delta_j(\mathcal{I})$[7], scales with the length of adhered segments);

[7] $\delta_j(\mathcal{I}) = \begin{cases} 0, & j \notin \mathcal{I} \\ 1, & j \in \mathcal{I} \end{cases}$

- energy stemming from stretching of the axon n (Hookean term, $k/2(\Delta L_n)^2$, scales with square of change of axon n length), k is axon stiffness[8].

Overall, the mechanical energy has the form

$$E(l_{\{j\}}(t)) = \sum_{n=1}^{N} \Bigg[\underbrace{T_{0n} \sum_{j \in a_n} l_j(t)}_{\substack{\text{effective tension} \\ \text{energy}}} + \underbrace{\frac{k}{2} \left(\sum_{j \in a_n} (l_j(t) - l_{0j}) \right)^2}_{\text{Hookean energy}} - \underbrace{\frac{S}{2} \sum_{j \in a_n} l_j(t) \delta_j(\mathcal{I})}_{\substack{\text{adhesion} \\ \text{energy}}} \Bigg] \tag{3.18}$$

Which is a general formulation of energy functional of a system of axons.

To simplify the analysis to our object of interest, a zipper, we will significantly reduce this general formulation. We will consider two axons constituting a zipper ($N = 2$), denoted axon *1* and axon *2*, each of which is formed by two straight segments $|a_1| = |a_2| = 2, J = 3$, adhering along one segment $I = 1$ forming one interface. This simplification corresponds to the geometry shown in fig. 3.34, and has only two degrees of freedom: the position of the mobile vertex $V(x, y)$, the three termini, labelled A, B and C, of constitutive axons are fixed and immobile. The equation can be written in a simple form (for a given T_1, T_2 and S), considering index convention as in fig. 3.31 $a_1 = \{A, C\}$, $a_2 = \{B, C\}$, $i = \{C\}$,

$$E(l_A(x,y), l_B(x,y), l_C(x,y)) = T_1(l_A + l_C) + T_2(l_B + l_C) + \frac{k}{2}\left[(\Delta L_1)^2 + (\Delta L_2)^2\right] - S l_C. \tag{3.19}$$

Before we introduce specific model formulation, we introduce a helpful identity, the following property of the first derivatives of tensile terms (with respect to a vertex coordinate (x, y)):

$$\begin{aligned}
&\nabla_{(x,y)} \left[T_{0n} \sum_{j \in a_n} l_j(x,y) + \frac{k}{2} \left(\sum_{j \in a_n} l_j(x,y) - l_{0j} \right)^2 \right] = \\
&= T_{0n} \nabla_{(x,y)} \left(\sum_{j \in a_n} l_j(x,y) \right) + k \left(\sum_{j \in a_n} l_j(x,y) - l_{0j} \right) \nabla_{(x,y)} \left(\sum_{j \in a_n} l_j(x,y) - l_{0j0} \right) \\
&= \left[T_{0n} + k \left(\Delta L_n(x,y) \right) \right] \nabla_{(x,y)} \left(\sum_{j \in a_n} l_j(x,y) \right) \\
&= T_n(x,y) \, \nabla_{(x,y)} L_n(x,y).
\end{aligned} \tag{3.20}$$

We will take advantage of this identity in the following chapters.

3.6.1 General zipper equilibrium equation

In this section, we will lay formal foundations to model presented in section 3.5.1, and generalise the formalism to asymmetric zippers. The system is in an equilibrium, if its

[8] Note this considers axon to behave as a single spring, not as a series of springs. See section 1.3.1 and fig. 1.8.

energy E has a local extremum with coordinate (x_0, y_0); the condition is

$$\nabla E(x,y)|_{(x_0,y_0)} = 0.$$

We insert the energy in the form given by eq. (3.19), take advantage of the identity eq. (3.20) and formulate this condition it in Cartesian coordinates,

$$\begin{aligned}\nabla E(x,y) =&(T_1 + T_2 - S)\nabla\left(\sqrt{(y_C - y)^2 + (x_C - x)^2}\right) + \\ &+ T_1\nabla\left(\sqrt{(y - y_A)^2 + (x - x_A)^2}\right) + T_2\nabla\left(\sqrt{(y - y_B)^2 + (x_B - x)^2}\right)\end{aligned} \tag{3.21}$$

where $T_1 = T_{01} + k\Delta L_1$ and $T_2 = T_{02} + k\Delta L_2$ are tensile forces (or tension energy per unit length) in the left axon *1* and right axon *2*, S is magnitude of adhesive force (or adhesive energy per unit adhered length); there are 3 fixation points (i) $r_A \equiv (x_A, y_A)$ on the left, (ii) $r_B \equiv (x_B, y_B)$ on the right, (iii) $r_C \equiv (x_C, y_C)$ on the top, and (iv) $V(x,y)$ are coordinates of the vertex. The configuration is illustrated in the fig. 3.34a.

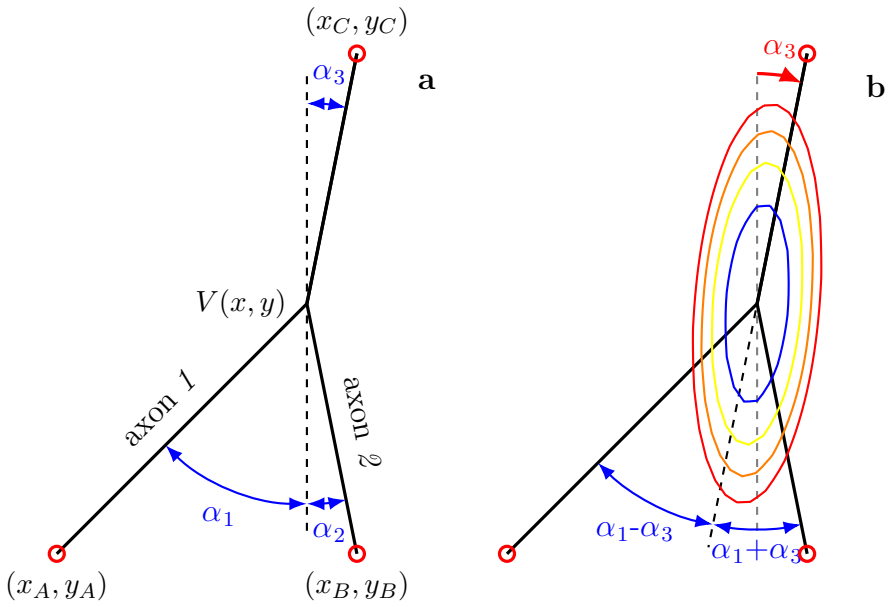

Figure 3.34: **a**: Illustration of general two-axon vertex in Cartesian coordinates. Red circles illustrate fixation points of the axons. **b**: Illustration of rotation of the reference frame (eq. (3.24)) simplifying the formulas if expressed in terms of angles. The contours illustrate energy levels around equilibrium as given by Hessian (eq. (3.28)), increasing value colourcode from blue to red.

We search for conditions for the static vertex configuration $V(x,y) = (x_0, y_0)$, where

the energy function $E(x, y)$ has minimum. Partial derivatives give us:

$$\begin{aligned}\frac{\partial E}{\partial y} &= -(T_1 + T_2 - S)\frac{y_C - y}{\sqrt{(y_C - y)^2 + (x_C - x)^2}} + \\ &+ T_1\frac{y - y_A}{\sqrt{(y - y_A)^2 + (x - x_A)^2}} + T_2\frac{y - y_B}{\sqrt{(y - y_B)^2 + (x_B - x)^2}} \\ &= -(T_1 + T_2 - S)\cos\alpha_3 + T_1\cos\alpha_1 + T_2\cos\alpha_2 \qquad (3.22)\\ \frac{\partial E}{\partial x} &= -(T_1 + T_2 - S)\frac{x_C - x}{\sqrt{(y_C - y)^2 + (x_C - x)^2}} + \\ &+ T_1\frac{x - x_A}{\sqrt{(y - y_A)^2 + (x - x_A)^2}} - T_2\frac{x_B - x}{\sqrt{(y - y_B)^2 + (x_B - x)^2}} \\ &= -(T_1 + T_2 - S)\sin\alpha_3 + T_1\sin\alpha_1 - T_2\sin\alpha_2 \qquad (3.23)\end{aligned}$$

Note, that the whole calculation was simplified by using the eq. (3.20) identity and that T_1 and T_2 are functions of coordinates (x, y) through the Hookean effect.

To show the local extremum is a minimum, we need to calculate second derivatives. At this point, we will neglect the Hookean terms, i.e. $T \approx T_0$. While the Hookean energy term does not change the character of extremum (e.g. from minimum to maximum), it has an influence on the energy landscape in the vicinity of the extremum. From biological point of view, it is likely that the axons forming equilibrated static zippers in the culture are not under a considerable strain (i.e. $T_0 \gg k\Delta L$). The second derivatives have the following form:

$$\begin{aligned}\frac{\partial^2 E}{\partial y^2} &= (T_1 + T_2 - S)\frac{\sin^2\alpha_3}{l_C} + T_1\frac{\sin^2\alpha_1}{l_A} + T_2\frac{\sin^2\alpha_2}{l_B} \\ \frac{\partial^2 E}{\partial x^2} &= (T_1 + T_2 - S)\frac{\cos^2\alpha_3}{l_C} + T_1\frac{\cos^2\alpha_1}{l_A} + T_2\frac{\cos^2\alpha_2}{l_B} \\ \frac{\partial^2 E}{\partial x\partial y} &= -(T_1 + T_2 - S)\frac{\cos\alpha_3\sin\alpha_3}{l_C} - T_1\frac{\cos\alpha_1\sin\alpha_1}{l_A} + T_2\frac{\cos\alpha_2\sin\alpha_2}{l_B}.\end{aligned}$$

We used shortcuts $l_A = \sqrt{(y - y_A)^2 + (x - x_A)^2}$, $l_B = \sqrt{(y - y_B)^2 + (x_B - x)^2}$ and $l_C = \sqrt{(y_C - y)^2 + (x_C - x)^2}$, which are lengths of individual axon segments. An extreme is a local minimum, if eigenvalues of the Hessian matrix are positive. Before we examine the Hessian, we introduce a simplifying coordinate transform.

If we rotate the coordinate frame around the vertex $V(x, y)$ as illustrated by red arrow in fig. 3.34b, to align the new y'-direction to the zipper axis $\widehat{VC}$, we obtain the original points in terms of new (dashed) coordinates:

$$\begin{aligned}V(x, y) &= (x', y') \\ (x_C, y_C) &= (x', y' + l_C) \\ (x_A, y_A) &= (x' - l_A\sin(\alpha_1 - \alpha_3), y' - l_A\cos(\alpha_1 - \alpha_3)) \\ (x_B, y_B) &= (x' + l_B\sin(\alpha_2 + \alpha_3), y' - l_B\cos(\alpha_2 + \alpha_3))\end{aligned} \qquad (3.24)$$

The lengths l_A, l_B, l_C are obviously invariant under the rotation transformation.

Combining the transformation eq. (3.24) with eqs. (3.22) and (3.23), and letting the derivatives equal zero, the equilibrium conditions can be written in dashed coordinates as

$$\frac{\partial E'}{\partial y'} = -(T_1 + T_2 - S) + T_1 \cos(\alpha_1 - \alpha_3) + T_2 \cos(\alpha_2 + \alpha_3) = 0 \tag{3.25}$$

$$\frac{\partial E'}{\partial x'} = T_1 \sin(\alpha_1 - \alpha_3) - T_2 \sin(\alpha_2 + \alpha_3) = 0, \tag{3.26}$$

which can be rewritten into a system of equations similar to eq. (3.9), defining the relation between the S and the T_1, T_2. For simplicity, we will rename the angles in eqs. (3.25) and (3.26), to describe them in terms of angles, which can be directly measured in the system, i.e. $\alpha_1 - \alpha_3 \to \alpha_1$ and $\alpha_2 + \alpha_3 \to \alpha_2$, we will always assume this relabelling in dashed coordinates. The equations relating the geometry and biophysical parameters then have form

$$\begin{aligned} \frac{S}{T_2} &= \left[\frac{\sin\alpha_2}{\sin\alpha_1}(1-\cos\alpha_1) + (1-\cos\alpha_2)\right] \\ \frac{S}{T_1} &= \left[\frac{\sin\alpha_1}{\sin\alpha_2}(1-\cos\alpha_2) + (1-\cos\alpha_1)\right]. \end{aligned} \tag{3.27}$$

We can calculate the vertex equilibrium coordinates (x'_0, y'_0), for which eqs. (3.25) and (3.26) are satisfied, $\frac{\partial E'}{\partial y'}|_{(x'_0,y'_0)}=0$, $\frac{\partial E'}{\partial x'}|_{(x'_0,y'_0)}=0$; the equilibrium can be in principle stable (minimum) or unstable (maximum). This point is determined by the biophysical parameters of the system and the fixation points, which together define the energy landscape through eq. (3.21).

Note that eqs. (3.25) and (3.26) neither eqs. (3.22) and (3.23) explicitly provide the equilibrium coordinates, but only the local equilibrium geometry (i.e. the vertex angles α_1, α_2) consistent with the given S and T_1, T_2. The coordinates (x'_0, y'_0) can be of course obtained using α_1, α_2 and the system overall geometry $g(\{\vec{r}_i\})$, but the equilibrium itself is determined locally, satisfying the relation between zipper angles and biophysical parameters (eq. (3.27)), and is therefore independent on length scale of the system (e.g. if segment lengths l_j were all reduced by half, the α_1, α_2 would not change).

As noted earlier, the vicinity of an extremum given by eqs. (3.22) and (3.23) or eqs. (3.25) and (3.26) can be examined by studying matrix of second derivatives at the equilibrium coordinate, i.e. the Hessian. If the eigenvalues of the Hessian are both positive, then the extremum is minimum, i.e. a stable static equilibrium. Defining a shortcut $T_3 \equiv T_1 + T_2 - S$, the Hessian in Cartesian coordinates has a form

$$H(x_0, y_0) = \begin{bmatrix} T_3\frac{\cos^2\alpha_3}{l_C} + T_1\frac{\cos^2\alpha_1}{l_A} + T_2\frac{\cos^2\alpha_2}{l_B} & -T_3\frac{\cos\alpha_3\sin\alpha_3}{l_C} - T_1\frac{\cos\alpha_1\sin\alpha_1}{l_A} + T_2\frac{\cos\alpha_2\sin\alpha_2}{l_B} \\ -T_3\frac{\cos\alpha_3\sin\alpha_3}{l_C} - T_1\frac{\cos\alpha_1\sin\alpha_1}{l_A} + T_2\frac{\cos\alpha_2\sin\alpha_2}{l_B} & T_3\frac{\sin^2\alpha_3}{l_C} + T_1\frac{\sin^2\alpha_1}{l_A} + T_2\frac{\sin^2\alpha_2}{l_B} \end{bmatrix}$$

After the rotation of coordinate frame using the transformation eq. (3.24), it simplifies to

$$H'(x'_0, y'_0) = \begin{bmatrix} \frac{T_3}{l_C} + T_1\frac{\cos^2\alpha_1}{l_A} + T_2\frac{\cos^2\alpha_2}{l_B} & -T_1\frac{\cos\alpha_1\sin\alpha_1}{l_A} + T_2\frac{\cos\alpha_2\sin\alpha_2}{l_B} \\ -T_1\frac{\cos\alpha_1\sin\alpha_1}{l_A} + T_2\frac{\cos\alpha_2\sin\alpha_2}{l_B} & T_1\frac{\sin^2\alpha_1}{l_A} + T_2\frac{\sin^2\alpha_2}{l_B} \end{bmatrix} \tag{3.28}$$

The Hessian is plotted in fig. 3.34b as a series of equipotential contours of energy locally approximated by the quadric $(\delta x' \ \delta y')\, H' \begin{pmatrix} \delta x' \\ \delta y' \end{pmatrix}$, where $\delta x'$, $\delta y'$ is distance from the equilibrium along the rotated coordinate lines. The levels increase with distance from equilibrium. Notice that non-zero non-diagonal terms of H' misalign the quadric axis from the axial and transverse axis of the zipper geometry.

There is an alternative to finding eigenvalues of Hessian, which is very tedious. The point (x'_0, y'_0) is a local energy minimum, if two conditions are met:

(i) $\frac{\partial^2 E'}{\partial x'^2} > 0$, or equivalently $\frac{\partial^2 E'}{\partial y'^2} > 0$, and

(ii) $\det H(x_0, y_0) = \det H'(x'_0, y'_0) > 0$.

The first condition can be easily met in dashed coordinates.

$$\frac{\partial^2 E'}{\partial y'^2} = T_1 \frac{\sin^2 \alpha_1}{l_A} + T_2 \frac{\sin^2 \alpha_2}{l_B} \geq 0. \tag{3.29}$$

The terms on the right are always non-negative. Furthermore, if $\alpha_1 = \alpha_2 = 0$, then the point belongs to the interior of the adhered segment (i.e. not a vertex), which means that left hand side of eq. (3.29) is strictly positive for a zipper vertex.

The second condition, $\det H'(x'_0, y'_0) > 0$, we straightforwardly calculate the determinant:

$$\begin{aligned}
&\det H'(x'_0, y'_0) = \\
&= \left[\frac{T_3}{l_C} + T_1 \frac{\cos^2 \alpha_1}{l_A} + T_2 \frac{\cos^2 \alpha_2}{l_B}\right] \cdot \left[T_1 \frac{\sin^2 \alpha_1}{l_A} + T_2 \frac{\sin^2 \alpha_2}{l_B}\right] - \\
&- \left[T_1 \frac{\cos \alpha_1 \sin \alpha_1}{l_A} - T_2 \frac{\cos \alpha_2 \sin \alpha_2}{l_B}\right]^2 \\
&= \frac{T_3}{l_3} \left[T_1 \frac{\sin^2 \alpha_1}{l_A} + T_2 \frac{\sin^2 \alpha_2}{l_B}\right] + \\
&+ \cancel{\left[T_1^2 \frac{\sin^2 \alpha_1 \cos^2 \alpha_1}{l_A^2}\right.} + T_1 T_2 \frac{\cos^2 \alpha_1 \sin^2 \alpha_2 + \cos^2 \alpha_2 \sin^2 \alpha_1}{l_A l_B} + \cancel{\left.T_2^2 \frac{\sin^2 \alpha_2 \cos^2 \alpha_2}{l_B^2}\right]} - \\
&- \cancel{T_1^2 \frac{\sin^2 \alpha_1 \cos^2 \alpha_1}{l_A^2}} - \cancel{T_2^2 \frac{\sin^2 \alpha_2 \cos^2 \alpha_2}{l_B^2}} + 2 T_1 T_2 \frac{\cos \alpha_1 \sin \alpha_1 \cos \alpha_2 \sin \alpha_2}{l_A l_B} = \\
&= \frac{T_3}{l_C} \left[T_1 \frac{\sin^2 \alpha_1}{l_A} + T_2 \frac{\sin^2 \alpha_2}{l_B}\right] + \frac{T_1 T_2}{l_A l_B} \underbrace{\left[\cos \alpha_1 \sin \alpha_2 + \cos \alpha_2 \sin \alpha_1\right]^2}_{= \sin^2(\alpha_1 + \alpha_2) = \sin^2 \beta} > 0.
\end{aligned}$$

The last inequality places limits on mutual strength of biophysical parameters T_1, T_2 and S to guarantee existence of stable equilibrium under the given geometry. It can be expanded by substituting back for T_3 to obtain

$$S < (T_1 + T_2) + \frac{T_1 T_2 l_C \sin^2 \beta}{T_1 l_B \sin^2 \alpha_1 + T_2 l_A \sin^2 \alpha_2}. \tag{3.30}$$

And regardless of the complex second term on the right, which is always positive, we see a stricter condition $S < T_1 + T_2$ is easily met in biophysically relevant situations (see figs. 3.21 and 3.26). Based on our estimates, $S \lesssim 0.2T$ for a single axon or a small bundle, and the ratio becomes even lower for larger bundles, see section 3.5.6.

In spite of system seeming complexity, quite a lot can be understood about the static configurations based on the static analysis of the simple model. We have shown that for large range of reasonable values of biophysical parameters, a stable static equilibrium exists for the vertex (eq. (3.30)). We have also shown that the configuration of axons in the vertex is determined locally and does not explicitly depend on the external fixations of the boundary of the subsystem (eq. (3.27)). This fact is important for experimental measurement: measuring the angles of static configurations (α_1, α_2) in the network provides us with key information to determine the biophysical parameters (see eq. (3.27)), regardless of the network typical scale and lengths.

3.6.2 Zipper dynamics model introduction

If initially equilibrated system is perturbed and does not meet the conditions of static state anymore (eq. (3.27) discussed in section 3.6.1), it begins a transition to the new static equilibrium, driven by the mechanical force $\vec{F}_v$. Because the system is strongly over-damped, inertial forces are negligible, the velocity of the vertex $\vec{u}(t)$ is fully determined by the balance between the mechanical force $\vec{F}_v$ and the friction force $\vec{F}_\eta$. Ongoing geometrical change of the system releases free mechanical energy (i.e. tensile energy) at the same rate as the energy is dissipated by the dissipative interaction with the substrate, internal elongational viscosity of the axon, and internal vertex-localised dissipation within the zipper. We assume this dissipative forces (section 3.4.5) are linear functions of vertex velocity $\vec{u}$. The reasoning can be mathematically written as

$$-\nabla E(x,y) = \vec{F}_v(x,y) = \overleftrightarrow{H}(x,y)\vec{u} = -\vec{F}_\eta(x,y), \tag{3.31}$$

where $E(x,y)$ is mechanical conservative energy (i.e. potential, see section 3.5.4 and eq. (3.21)), and $\overleftrightarrow{H}(x,y)$ is a tensor representing combined effect of dissipative forces, which depends on the geometry of zipper configuration (therefore also on vertex position $V(x,y)$), but is itself independent on vertex velocity $\vec{u}$. In case of isotropic, homogeneous friction, i.e. $\overleftrightarrow{H} = c \cdot \overleftrightarrow{1}$, the trajectory of zipper vertex transition would follow the gradient path $-\nabla E(x,y)$.

The position of the vertex $V(x,y)$ uniquely determines the mechanical potential energy $E(x,y)$ of the system under the given boundary conditions (fixations) $g(\{\vec{r}_i\})$. In general case, the energy $E(x,y)$ is given by eq. (3.18), and its gradient at the vertex coordinate $V(x,y)$ determines the vector of conservative force. Note, that all the segment lengths l_j in eq. (3.18) which do not directly form the vertex $V(x,y)$, i.e. $l_j : V(x,y) \notin l_j$, will

vanish under the gradient operator (except in Hookean terms). Therefore,

$$\begin{aligned}\vec{F}_v(x,y) = -\nabla E(x,y) &= -S\vec{t_i} + \sum_{n=1}^{2}\left[(T_{0n} + k\Delta L_n)\sum_{j\in a_n}\vec{t_j}\right] \\ &= -S\vec{t_i} + \sum_{n=1}^{2}\left[T_n\sum_{j\in a_n}\vec{t_j}\right], i \in \mathcal{I}\cap a_1 \cap a_2\end{aligned} \tag{3.32}$$

where we used identity eq. (3.20). The two non-vanishing zipper-forming axons were labelled *1* and *2*, their interface was labelled i. We define tangent unit vectors pointing outwards from the vertex towards the segment fixation points, $\vec{t_j} = \frac{\vec{l_j}}{l_j}$, e.g. $\vec{t}_A = \frac{\vec{l}_A}{l_A} \equiv \widehat{VA}$, also notice $-\nabla l_j = \vec{t_j}$.

The friction term consists of contributions from individual involved axons $\overleftrightarrow{f}_n$ ($n = \{1,2\}$ in this case), composed of J segments in total,

$$\overleftrightarrow{H}(\vec{l}_1,\ldots,\vec{l}_J) = \sum_{n=1}^{2}\overleftrightarrow{f}_n(\vec{l}_{\{j\}},\vec{l}_i);\ j\in a_n, i\in\mathcal{I}\cap a_1\cap a_2. \tag{3.33}$$

Note explicit dependence on the interface segment l_i, as it has an exceptional role in dissipative processes (see also section 3.5.5).

For a particular functional implementation of friction tensor $\overleftrightarrow{H}$, the following simplifying assumptions were made:

Assumption 1. *Axons are modelled as one dimensional viscoelastic filaments on a plane (two dimensional of zero curvature everywhere) with negligible bending energy; i.e. cross section of the axon and internal structure are largely uniform.*

Assumption 2. *Axon segments ($\vec{l_j}$) remain straight between the vertex and fixation points; i.e. straightening dynamics is much faster than the zippering dynamics.*

Assumption 3. *Longitudinal strain is assumed to be uniform along each axon; i.e. the dynamics of internal material redistribution along the axon is much faster than the zippering dynamics.*

Assumption 4. *The dissipative forces are linear functions of local velocities and are mutually independent.*

The friction tensor depends on the involved mechanisms of energy dissipation, some of which were discussed in section 3.5.5. We will consider the 3 following forms of dissipation:

vertex-localised caused by the structural changes in axons in the vicinity of vertex, as the zippering changes local curvature of the filaments (introduced in section 3.5.5);

elongational caused by viscoelastic dissipation within the AS, as it is stretched or compressed (introduced in section 3.5.5);

substrate friction caused by interactions between the AS and the substrate, can be caused by mutual roughness, or by a molecule-mediated adhesion.

In case of the substrate friction, it cannot be formally incorporated into the zipper static equilibrium equation eq. (3.9) as we did for the other two types of friction in section 3.5.5, because its dependence on geometry is non-trivial (i.e. it is not simply collinear with a segment); the rate of substrate dissipation has to be integrated along the axons.

3.6.3 Euler-Lagrange formalism with Rayleigh dissipation function

Dynamics of dissipative systems can be studied using the standard Euler-Lagrange formalism, in which generalised (non-conservative) forces Q_i are represented by Rayleigh dissipation function D. The formalism potential (U) of our system corresponds to the elastic forces stored in the axon geometry, i.e. $U(x, y) \equiv E(x, y)$, as given by eq. (3.19). Since the system is over-damped, the kinetic energy E_K is negligible. The Lagrangian $L = E_K - U$ is therefore give by

$$L = -E = -T_1(l_1 + l_3) - T_2(l_1 + l_3) - \frac{k}{2}\left[(\Delta L_1)^2 + (\Delta L_2)^2\right] + Sl_3 \tag{3.34}$$

with geometry as defined in the fig. 3.34. The equation of motion for the zipper vertex $V(x, y)$ is given by the set of Euler-Lagrange equations

$$\frac{\partial L}{\partial q_i} - \underbrace{\frac{d}{dt}\frac{\partial L}{\partial \dot{q}_i}}_{\frac{\partial L(q_i)}{\partial \dot{q}_i}=0} = Q_i, \tag{3.35}$$

where q_i are spatial coordinates of the vertex and $\dot{q}_i$ are the corresponding velocities. The non-conservative generalised forces Q_i can be defined in terms of the Rayleigh dissipation function. Since the Lagrangian $L = L(q_i)$ is independent on velocities $\dot{q}_i$, the second term on the left-hand side of eq. (3.35) vanishes, as indicated.

The assumption 4 allows us to use the formalism of Rayleigh dissipation function D to express Q_i. The function is defined as

$$D = \sum_{i,j} \frac{1}{2} K_{ij} \dot{q}_i \dot{q}_j \tag{3.36}$$

and the generalised (friction) forces are related to it through velocity gradient,

$$Q_i = -\nabla_{\dot{q}_i} D = -\frac{\partial D}{\partial \dot{q}_i}. \tag{3.37}$$

K_{ij} is a symmetric positive-definite matrix of generalised friction coefficients, which are independent on velocity, but may depend on coordinates, $K_{ij} = K_{ij}(q_k)$. Under these considerations, the eq. (3.35) can be expressed in Cartesian coordinates (see also

eqs. (3.21) to (3.23))

$$\begin{aligned}
\frac{\partial L}{\partial q_i} = -\frac{\partial E}{\partial q_i} &= -(T_1 + T_2 - S)\nabla l_3 - T_1 \nabla l_1 - T_2 \nabla l_2 && = -\nabla_{\dot{q}_i} D \\
-\frac{\partial E}{\partial x} &= (T_1 + T_2 - S)\frac{x_C - x}{l_C} + T_1 \frac{x_A - x}{l_A} + T_2 \frac{x_B - x}{l_B} && = -K_{11}\dot{x} - K_{12}\dot{y} \qquad (3.38) \\
-\frac{\partial E}{\partial y} &= (T_1 + T_2 - S)\frac{y_C - y}{l_C} + T_1 \frac{y_A - y}{l_A} + T_2 \frac{y_B - y}{l_B} && = -K_{21}\dot{x} - K_{22}\dot{y} \qquad (3.39)
\end{aligned}$$

The eqs. (3.38) and (3.39) can be solved, if explicit form of $K_{ij}(x, y)$ is obtained from D, which can be constructed following consideration of particular representations of friction forces F_i^η and calculating their energy dissipation rates R_i^η. The Rayleigh function is then given as a total energy dissipation rate $D = \sum_i R_i^\eta$.

As mentioned in section 3.6.2, we consider three distinct types of friction forces. The elongational ($\eta^{\Updownarrow}$) and vertex-localised (η^Z) were already discussed in section 3.5.5. The third considered friction type originates from the interaction between the axons and the substrate, and depends on the shaft orientation. It follows from the assumptions 2 and 4, that the friction force of an infinitesimal element of AS can be decomposed into two orthonormal directions, along the axon axis $f^\parallel$, and perpendicular to the axis, $f^\perp$.

The **substrate friction** has non-zero components in both of these directions. The assumptions 1 and 2 limit the **elongational dissipation** to axial component, normal component vanishes. The same applies to the **zipper dissipation**, which is further limited to the zippering axis segment (VC in the used geometry). While the friction with the substrate might, or might not, be isotropic, in general case, four independent coefficients of friction proportionality would exist for each infinitesimal element dl, two for normal and axial components of substrate friction $\eta^\perp$ and $\eta^\parallel$, and two axial components of internal friction $\eta^{\Updownarrow}$ and zipper friction η^Z. The assumption 4 allows us to separate the mechanisms, while each is a linear function of vertex velocity $\vec{u}$, and its coefficient of proportionality may depend on current geometry of the system l_A, l_B, l_C.

Substrate friction

This type of friction arises due to the motion of the axons with respect to the substrate and depends on the entire geometry of the zipper configuration. We will consider structure as shown in fig. 3.35a, a vertex forming a zipper attached to 3 fixed points A, B and C. An infinitesimal element dl (one-dimensional by assumption 1) is moved to a new location due to small vertex transition $\delta\vec{x}$. Axial axon mass rearrangement occurs at the same time—axon stretches or shortens. The element dl therefore travels with velocity $\vec{v}$ along a trajectory, which, for small $\delta\vec{x}$, can be decomposed into perpendicular sliding velocity $\vec{v}^\perp$ (see fig. 3.35b) and repositioning along the axon with velocity $\vec{v}^\parallel$, while

$$\vec{v} = \vec{v}^\perp + \vec{v}^\parallel.$$

The trajectory of the element dl depends on its position along the axon segment j, i.e. on the distance l from the fixed endpoint, as illustrated in fig. 3.35b. The perpendicular translation/velocity $\vec{v}^{\perp}$ will be maximal at the mobile end of the segment (cf. assumption 2), and linearly decrease towards the fixed point. For the axial velocity $\vec{v}^{\parallel}$, the argument is not exactly the same, as we will explain shortly.

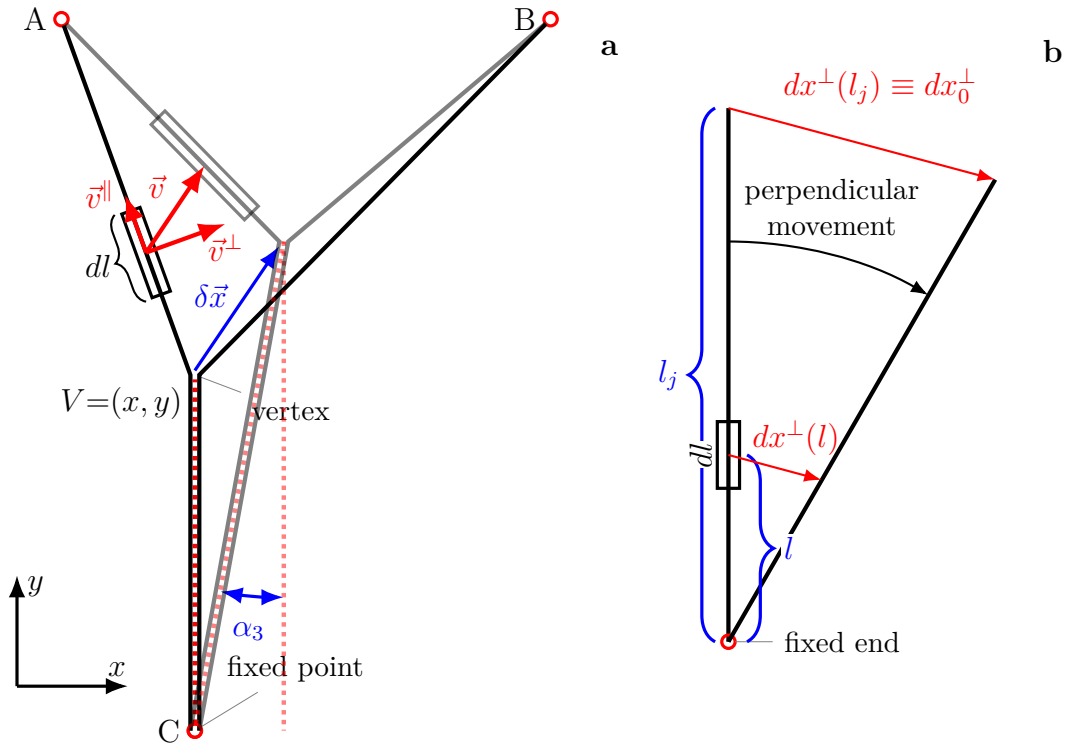

Figure 3.35: **a**: Velocity components of axon element dl, $\vec{v} = \vec{v}^{\parallel} + \vec{v}^{\perp}$, during an infinitesimal transition of vertex $\delta\vec{x}$. Note that because axons are always straight, the velocity $\vec{v}(l)$ depends on the distance l from the fixed end A. The two components of velocity are eigenvectors of two components of substrate friction. **b**: Illustration of perpendicular substrate friction. An element dl undergoes a transition with velocity linearly decreasing from mobile to fixed endpoint.

The substrate friction is anisotropic along the two velocity components, with separate eigenvalues for directions parallel $\eta^{\parallel}$ to the axon segment (axial friction) and perpendicular $\eta^{\perp}$ to the axon segment (transverse friction). The dissipation rate of substrate friction for an element dl at the position l is then given by

$$dR(l) = dR^{\perp}(l) + dR^{\parallel}(l) = \frac{1}{2}\eta^{\parallel}\left(\vec{v}(l)\cdot\vec{t}_j\right)^2 dl + \frac{1}{2}\eta^{\perp}\left(\vec{v}(l)\cdot\vec{n}_j\right)^2 dl, \tag{3.40}$$

where $\vec{t}_j$ and $\vec{n}_j$ denote respectively tangent and normal unit vector to the straight segment j.

To assess the full dissipation rate R_j of an element j, the contributions $dR(l)$ need to be integrated as a function of vertex velocity $\vec{u}$. Such integration is simple for transverse

substrate friction component. Because the element transverse velocity $\vec{v}^{\perp}(l)$ decreases linearly from the vertex to the fixation point, it is given by

$$\vec{v}(l) \cdot \vec{n}_j = \frac{l}{l_j} \vec{u} \cdot \vec{n}_j, \tag{3.41}$$

where l_j is the length of the segment j (see fig. 3.35b). Using eq. (3.41), the transverse dissipation rate integration is

$$R_j^{\perp} = \frac{1}{2} \eta^{\perp} \left(\vec{u} \cdot \vec{n}_j \right)^2 \int_0^{l_j} \left(\frac{l}{l_j} \right)^2 = \frac{1}{6} \eta^{\perp} l_j \left(\vec{u} \cdot \vec{n}_j \right)^2 . \tag{3.42}$$

The transverse dissipation rate of an axon is simply a sum of contributions from individual segments forming the axon (e.g. $R_1^{\perp} = R_A^{\perp} + R_C^{\perp}$ for axon *1*).

We need to be more careful when calculating the axial friction dissipation rate $R^{\parallel}$. While transverse translation of a segment dl can be treated as independent in the two segments constituting an axon (i.e. $\vec{v}_j^{\perp} = \vec{v}_j^{\perp}(l_j)$), this is not the case for axial friction ($\vec{v}_j^{\parallel} = \vec{v}_j^{\parallel}(l_j, l_k)$; $j, k \in a_n$). During the movement of the axon n, the lengths of its segments l_j and l_k ($j, k \in a_n$) generally change, but the assumption 3 of uniform strain implies that a transfer of material has to take place between the segments. In other words, the strain gradient between the axon segments l_j and l_k caused by vertex dynamics is allowed to drive material transfer through the vertex point (at much faster time scale than the vertex dynamics itself)—the axons are 'sliding' along each other, as we have experimentally observed. We therefore consider the extension/compression rate of the whole axon n, $\dot{L}_n$, while each of the segments j undergoes extension/compression at rate $\dot{l}_j$ proportional to its length l_j as a fraction of the total axon n length $L_n = \sum_{j \in a_n} l_j$, i.e.

$$\dot{l}_j = \frac{l_j}{L_n} \dot{L}_n. \tag{3.43}$$

We express the axon total length L_n in our geometry (fig. 3.35a) as a function of vertex coordinate $L_n = L_n(x, y)$. The rate of change in the total length of axon can be then expressed in terms of directional derivative of length at the rate given by the vertex velocity magnitude $|\vec{u}| \equiv u$, i.e. (for axon *1*, WLoG)

$$\begin{aligned} \dot{L}_1 &= |\vec{u}| \nabla_{\vec{e}} L_1 \quad \Big| \quad \vec{e} = \frac{\vec{u}}{u} \\ &= u\vec{e} \cdot \nabla L_1 \\ &= \vec{u} \cdot \nabla L_1 \\ &= -\vec{u} \cdot (\vec{t}_A + \vec{t}_C) \end{aligned} \tag{3.44}$$

where $\vec{e}$ is unit vector in the vertex velocity direction, $\vec{t}_A$ and $\vec{t}_C$ are unit vectors $\widehat{VA}$ and $\widehat{VC}$ respectively. The identity $\nabla L = -(\vec{t}_A + \vec{t}_C)$ follows directly (in Cartesian

coordinates)

$$\begin{aligned}\nabla L_1 = \nabla(l_A + l_C) &= \left(\frac{\partial(l_A + l_C)}{\partial x}, \frac{\partial(l_A + l_C)}{\partial y}\right) = \\ &= \left(\frac{l_{Ax}}{\sqrt{l_{Ax}^2 + l_{Ay}^2}}\frac{\partial l_{Ax}}{\partial x} + \frac{l_{Cx}}{\sqrt{l_{Cx}^2 + l_{Cy}^2}}\frac{\partial l_{Cx}}{\partial x}, \frac{l_{Ay}}{\sqrt{l_{Ax}^2 + l_{Ay}^2}}\frac{\partial l_{Ay}}{\partial y} + \frac{l_{Cy}}{\sqrt{l_{Cx}^2 + l_{Cy}^2}}\frac{\partial l_{Cy}}{\partial y}\right) \\ &\left|\frac{\partial l_{Ax}}{\partial x} = \frac{\partial(x_A - x)}{\partial x} = -1 = \frac{\partial l_{Cx}}{\partial x} = \frac{\partial l_{Ay}}{\partial y} = \frac{\partial l_{Cy}}{\partial y}\right| \\ &= -\left(t_{Ax} + t_{Cx}, t_{Ay} + t_{Cy}\right) = -\left(\vec{t}_A + \vec{t}_C\right),\end{aligned}$$

Or simply, extension ($\nabla l_j > 0$) occurs if vertex coordinate (x, y) moves away from the fixed end (direction $-\vec{t}_j$).

As a sidenote, a simple counterexample against independent treatment for the axial substrate friction can be made. Imagine nearly straight (i.e. $\vec{t}_A \approx -\vec{t}_C$) axon *1* forming a vertex with axon *2* (i.e. case of $T_1 \gg T_2$), then as the vertex advances, the length of axon *1* nearly does not change $\dot{L}_1 = -\vec{u}\cdot(\vec{t}_A + \vec{t}_C) \approx 0$, but if we treated axial substrate friction separately (naively as for the transverse friction), we would obtain considerable dissipation rate contributions $\sim (\vec{u}\cdot\vec{t}_A)^2 + (\vec{u}\cdot\vec{t}_C)^2 \approx 2(\vec{u}\cdot\vec{t}_A)^2$.

The local axial velocity component of element dl at the position l from the fixed point can obtained as $\vec{v}(l)\cdot\vec{t}_j = \frac{l}{l_j}\dot{l}_j$, which can be used with eq. (3.43) to integrate segment's contribution to the axial dissipation rate

$$R_j^{\parallel} = \frac{1}{2}\eta^{\parallel}\left(\frac{\dot{L}_n}{L_n}\right)^2 \int_0^{l_j} l^2 dl = \frac{1}{6}\eta^{\parallel}\frac{l_j^3}{L_n^2}\left(\vec{u}\cdot\nabla L_n\right)^2 \quad \Big| j \in a_n, \tag{3.45}$$

the sum of the contribution from both segments is then the dissipation rate of the whole axon.

Elongational viscosity

The dissipation originating from axial elongation of an axon was already discussed in the section 3.5.5. The elongational friction force is proportional to uniform (see assumption 3) axon strain $\propto \dot{\epsilon} = \frac{\dot{L}}{L}$ (for an axon of length L), which can be expressed as in the previous section,

$$\dot{\epsilon} = \frac{\vec{u}\cdot\nabla L}{L} = -\frac{\vec{u}\cdot\left(\vec{t}_1 + \vec{t}_2\right)}{L}. \tag{3.46}$$

Due to the assumption 3, elongational dissipation rate is uniform along the axon, identical for every element dl at any position l , i.e.

$$dR^{\Updownarrow} = \frac{1}{2}\eta^{\Updownarrow}\dot{\epsilon}^2 dl.$$

The elongational dissipation rate can be trivially integrated for the whole axon length L as

$$R^{\Updownarrow} = \frac{1}{2}\eta^{\Updownarrow}\frac{(\vec{u}\cdot\nabla L)^2}{L}. \tag{3.47}$$

Zippering viscosity

This form of dissipation was also discussed in the section 3.5.5. It is a phenomenological description of processes occurring in the immediate vicinity of the zipper vertex. As opposed to the previous dissipation processes discussed, this process is localised and does not explicitly depend on the system geometry. It depends only on the projection of zipper vertex velocity $\vec{u}$ to the direction of the zipper axis ($\widehat{VC}$), i.e. $u^Z = -\vec{u} \cdot \vec{t}_C$, which is (signed) magnitude of zippering velocity (see fig. 3.31 and section 3.5.5). The dissipation rate is therefore given as

$$R^Z = \frac{1}{2}\eta^Z \left(u^Z\right)^2 = \frac{1}{2}\eta^Z \left(\vec{u} \cdot \vec{t}_C\right)^2 . \tag{3.48}$$

3.6.4 Rayleigh function

The Rayleigh function for one of the axons can be constructed by combining the eqs. (3.42), (3.45), (3.47) and (3.48).

$$\begin{aligned} D = &\frac{1}{6}\eta^{\perp} l_A \left(\vec{u} \cdot \vec{n}_A\right)^2 + \frac{1}{6}\eta^{\perp} l_C \left(\vec{u} \cdot \vec{n}_C\right)^2 + \frac{1}{4}\eta^Z \left(\vec{u} \cdot \vec{t}_C\right)^2 + \\ &+ \frac{1}{6}\eta^{\parallel} \frac{l_A^3 + l_C^3}{L^2} \left(\vec{u} \cdot \left(\vec{t}_A + \vec{t}_C\right)\right)^2 + \frac{1}{2}\eta^{\Updownarrow} \frac{1}{L} \left(\vec{u} \cdot \left(\vec{t}_A + \vec{t}_C\right)\right)^2 , \end{aligned} \tag{3.49}$$

where, for the sake of symmetry of notation for both axons, we assigned $1/2\, R^Z$ to each of the axons.

Each of the terms in eq. (3.49) consists of three characteristic parts, e.g.

$$R_j^{\parallel} = \frac{1}{2} \underbrace{\eta^{\parallel}}_{\substack{\text{friction} \\ \text{coefficient}}} \underbrace{\frac{1}{3} l_j \left(\frac{l_j}{L}\right)^2}_{\substack{\text{geometric} \\ \text{factor}}} \underbrace{\left(\vec{u} \cdot \left(\vec{t}_A + \vec{t}_C\right)\right)^2}_{\substack{\text{velocity} \\ \text{projection}}} .$$

The geometric factor depends on the dimensions of the zipper configuration. The velocity projection characterises the distinct orientational character of the dissipative process, the eigenvector of the particular type of friction.

From the eq. (3.49), we can see, that the dissipative processes have four distinct eigenvectors, i.e. to calculate the total dissipation rate, zipper vertex velocity $\vec{u}$ needs to be projected onto four directions. It is possible to rewrite the Rayleigh function into convenient notation in the form of

$$D = \frac{1}{2} K_{ij} \dot{q}_i \dot{q}_j = (\overleftrightarrow{P}\vec{u})^T \overleftrightarrow{A} \overleftrightarrow{P}\vec{u}, \tag{3.50}$$

where diagonal 4×4 matrix $\overleftrightarrow{A}(x, y)$ contains the friction constants and geometric factors (which depend on current vertex coordinate), and 4×2 matrix $\overleftrightarrow{P}(x, y)$ performs vertex

velocity $\vec{u}$ projections:

$$\overleftrightarrow{A} = \frac{1}{2}\begin{bmatrix} \eta^{\parallel}\frac{1}{3}\left[\frac{l_A^3+l_C^3}{L^2}\right] + \eta^{\Updownarrow}\frac{1}{L} & 0 & 0 & 0 \\ 0 & \frac{1}{3}\eta^{\perp}l_A & 0 & 0 \\ 0 & 0 & \frac{1}{3}\eta^{\perp}l_C & 0 \\ 0 & 0 & 0 & \frac{1}{2}\eta^{Z} \end{bmatrix} \tag{3.51}$$

and

$$P = \begin{bmatrix} \vec{t}_A + \vec{t}_C \\ \vec{n}_A \\ \vec{n}_C \\ \vec{t}_C \end{bmatrix} = \begin{bmatrix} t_{Ax} + t_{C,x} & t_{Ay} + t_{Cy} \\ n_{Ax} & n_{Ay} \\ n_{Cx} & n_{Cy} \\ t_{Cx} & t_{Cy} \end{bmatrix} \tag{3.52}$$

Direct evaluation of eq. (3.50) explicitly reproduces the function D as formulated in eq. (3.49). It is easy to see from eq. (3.50) that 2×2 matrix $\overleftrightarrow{K}$ is obtained in this formalism as $\frac{1}{2}\overleftrightarrow{K} = \overleftrightarrow{P}^T \overleftrightarrow{A} \overleftrightarrow{P}$. Note that so far, we discussed only dissipation of single axons; dissipation rate of the whole zipper configuration is a straightforward sum of matrices for the left and right axon (i.e. axons *1* and *2*).

3.6.5 Equation of motion

Having explicitly formulated the Rayleigh function in composed matrix form for $\overleftrightarrow{K}$, eqs. (3.50) to (3.52) and explicit vector of driving conservative forces $\vec{F}_v$ eqs. (3.38) and (3.39), we can formulate equation of motion for a vertex as

$$\left[\overleftrightarrow{K}_1 + \overleftrightarrow{K}_2\right]\vec{u} \equiv \overleftrightarrow{K}\vec{u} = \vec{F}_v$$

$$\vec{u}(x,y) = \left[\overleftrightarrow{K}(x,y)\right]^{-1}\vec{F}_v(x,y)$$

and in the matrix form

$$\left[\overleftrightarrow{K}(x,y)\right]^{-1}\begin{pmatrix} (T_1+T_2-S)\frac{x_C-x}{l_C} + T_1\frac{x_A-x}{l_A} + T_2\frac{x_B-x}{l_B} \\ (T_1+T_2-S)\frac{y_C-y}{l_C} + T_1\frac{y_A-y}{l_A} + T_2\frac{y_B-y}{l_B} \end{pmatrix} = \begin{pmatrix} \dot{x} \\ \dot{y} \end{pmatrix}. \tag{3.53}$$

Which forms a nonlinear system of two coupled partial differential equations. It is numerically stable for the estimated ranges of biophysical parameters and can be computationally solved, or analytically inspected in particular simplifying limits.

The system given by eq. (3.53) can be solved as long as the rank of matrix $\mathrm{rk}(A) \geq 2$ and therefore matrix $\overleftrightarrow{K}$ is invertible. Matrix $\overleftrightarrow{K}$ is a 2×2 matrix, which transforms (vectors forming) a unit circle onto (vectors forming) an ellipse, with semi-axes generally not aligned to Cartesian axes due to non-zero non-diagonal elements—this explains why $\vec{u} \nparallel \vec{F}_v$. Matrix $\overleftrightarrow{K}$ is a formal representation of the friction tensor $\overleftrightarrow{H}$.

3.7 Analysis of zipper model

Model introduced in the section 3.6 is mathematically complex and depends on several biophysical parameters (T_1, T_2, S,k, η^Z, $\eta^{\Updownarrow}$, $\eta^{\parallel}$, $\eta^{\perp}$) as well as initial conditions (α_1,

α_2) and boundary conditions (fixed points A, B and C, also denoted $g(\{\vec{r}_i\})$). To get a better insight into effects these parameters have on the model, we generated a series of illustrative outputs.

3.7.1 Energy landscape

The static equilibrium configuration (section 3.6.1) but also the driving force $\vec{F}_v$ of zipper vertex dynamics are given by the landscape of mechanical energy $E(x, y)$. We demonstrate in the following fig. 3.36, how the landscape is changed through the adjustment of biophysical parameters. In sections 3.7.1 and 3.7.2, we will refer to direction perpendicular to zipper axis as 'zipper-transverse' and parallel with the zipper axis as 'zipper-axial'.

ZIPPER-TRANSVERSE AND ZIPPER-AXIAL DIRECTION

As shown in fig. 3.36a, the potential forms elongated elliptical contours along the zipper axis (compare to Hessian energy contours of fig. 3.34b). The energy of the configuration increases faster in the zipper-transverse direction, but forms a plateau in a direction parallel to the zipper axis. This corresponds to the observed dynamics, when a perturbed zipper initially equilibrates zipper-transversely, and then follows a slower zippering approach to the final equilibrium (fig. 3.33 and section 3.5.6).

As adhesion parameter value increases (fig. 3.36b), the zippered segment expands. The contours become less elongated, as the adhesion energy begins to dominate the total energy along the zipper axis. If an asymmetry of tensions is added to the system (fig. 3.36c), the landscape shifts transversely and becomes more localised around the axon of higher tension.

If a Hookean term is incorporated, it does not explicitly influence the equilibrium coordinate (see eq. (3.20)), as the static equilibrium coordinate

$$(x_0, y_0) : \ \nabla E|_{(x_0,y_0)} = 0$$

depends explicitly only on the tensions (implicitly modified by Hookean effect), not on the strain. Therefore, the equilibrium coordinate is identical for fig. 3.36a and fig. 3.36d, despite axons in fig. 3.36d have lower basal tension (T_0=0.9 nN in **d**, while $T_0 \equiv T$=1 nN in **a**), but are assumed to be under slight 1 µm-extension with k=0.1 $\frac{\text{nN}}{\text{µm}}$, which makes the final tensions equal in fig. 3.36a and fig. 3.36d.

The Hookean term however influences the energy landscape around the equilibrium point (x_0, y_0). Comparing fig. 3.36d to fig. 3.36a, the landscape becomes more smooth and elliptical; the energy increases more rapidly with the distance from the equilibrium. If we expand the Hookean energy E_H to the second term (for a symmetric zipper in

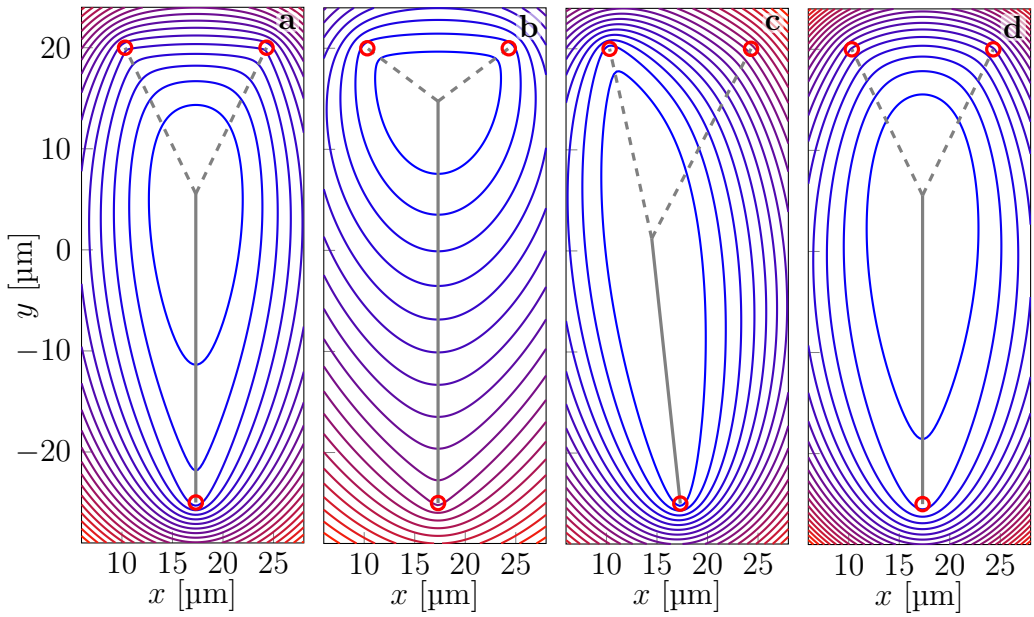

Figure 3.36: All four panes represent energy potential $E(x, y)$ of the system around a static equilibrium configuration. The red circles indicate the same fixation points in all the four panels, the dashed grey lines represent single axons and solid line represents the segment where they adhere. The potential is illustrated in each panel by contours of 20 equidistant energy levels (inter-level interval ΔE is however panel-specific). Tensions T_1 and T_2 correspond to the left and right axons respectively. In panels **a**-**c**, the Hookean stiffness k=0 $\frac{\text{nN}}{\mu\text{m}}$. **a**: Symmetric zipper for parameters T_1=1 nN, T_2=1 nN and adhesion parameter S=0.2 nN. The equipotential contours are rather elongated and centred in the upper part of the field. **b**: Symmetric zipper with high adhesion, T_1=T_2=1 nN and S=0.8 nN. As expected, the configuration is more 'zippered' as compared to the panel **a**. Spatial separation of energy contours along the symmetry axis is dominated by the adhesion. **c**: Asymmetric zipper, T_1=5 nN, T_2=1 nN and S=0.2 nN. The contours are dominated by the geometry of the more tense axon. **d**: Symmetric zipper with non-zero Hookean term k=0.1 $\frac{\text{nN}}{\mu\text{m}}$. The equilibrium is identical to the panel **a**, however the basal tension T_{01}=T_{02}=0.9 nN is increased by $\mathcal{H} = k \cdot \Delta L$=0.1 nN, where ΔL=1 µm is extension of the axons as compared to their rest length. Compared to panel **a**, the energy contours are more smoothed-out and elliptical. The energy grows slowly along the zipper axis, but more rapidly towards the field boundary. Such behaviour is expected, as the tensile energy increment is asymptotically a quadratic function of axon length increment $\sim \Delta L^2$, rather than linear as in the panel **a**.

adapted coordinate system of eq. (3.24), cf. eq. (3.28)),

$$\begin{aligned}
\frac{\partial^2}{\partial x^2} E_H = \frac{\partial^2}{\partial x^2}\frac{1}{2}k\left[L-L_0\right]^2 &= \frac{1}{2}k\frac{\partial}{\partial x}\left[2(L-L_0)\frac{\partial L}{\partial x}\right] \\
&= k\left(\frac{\partial L}{\partial x}\right)^2 + \underbrace{k(L-L_0)\frac{\partial^2 L}{\partial x^2}}_{(I)} \\
k\left(\frac{\partial L_1}{\partial x}\right)^2 = k\left(\frac{\partial l_A}{\partial x} + \underbrace{\frac{\partial l_C}{\partial x}}_{(II)}\right)^2 &\Big| \text{ purely Hookean effect} \\
&= k\sin^2\alpha_1 \geq 0 \\
\delta^2 E(x,y_0) \sim k\sin^2{}^{\beta}\!/_2\,\delta^2 x &\geq 0. \qquad (3.54)
\end{aligned}$$

The term (I) reflects Hookean contribution to tension (i.e. part of $T(x,y)\,L_{,xx}$) at the equilibrium, and does not contribute to the energy landscape difference between the fig. 3.36a and fig. 3.36d. The purely Hookean effect $\sim(L_{,x})^2$ cannot be obtained from non-Hookean tensile energy contributions[9]. Under the adapted coordinates, y-axis is aligned with the zipper axis $\widehat{VC}$ at the equilibrium, so the term (II) does not contribute. The effect of eq. (3.54) increases energy of the configuration regardless of the current state of stretching or shortening of the axon, it contributes to the increased ellipticity of the contour shape.

Similarly,

$$\begin{aligned}
k\left(\frac{\partial L_1}{\partial y}\right)^2 &= k\left(1-\cos{}^{\beta}\!/_2\right)^2 \geq 0 \\
\delta^2 E(x_0,y) \sim k\left(1-\cos{}^{\beta}\!/_2\right)^2\ \delta^2 y &\geq 0 \qquad (3.55)
\end{aligned}$$

Equations (3.54) and (3.55) show, that purely Hookean effects increase the energy in the vicinity of the equilibrium (x_0,y_0). In the adapted coordinates and symmetric system (as presented in fig. 3.36d), the mixed derivatives vanish, $L_{,xy} = L_{,yx} = 0$.

3.7.2 Friction vector fields

As argued in the general model introduction section 3.6.2, the dynamics is given by a combination of two factors, the conservative energy landscape and the vector field of friction. We will illustrate a velocity vector field of a vertex response to a particular form of acting force field. For the purpose, we define 'mobility' tensor, which is an inverse of friction tensor $\overleftrightarrow{H}^{-1}$ and determines velocity of the vertex for a given acting force $\vec{F}_v$ at the given coordinate (x,y).

First, we will illustrate a mobility tensor for several specific implementations of friction tensor (i.e. for various dominating forms of friction, see fig. 3.37). We show, what vertex velocity vector field is generated by these realisations of mobility vector, if a constant

[9] We use comma notation, $L_{,x} \equiv \frac{\partial L}{\partial x}$, $L_{,xx} = \frac{\partial^2 L}{\partial x^2}$, etc.

force vector field acts on the vertex, i.e. a homogeneous field composed of $\binom{1}{0}$ or $\binom{0}{1}$ force vectors at every coordinate (x, y). Note, that we are using the same symmetric configuration of fixation points as we did in the section 3.7.1, with the y-axis aligned along the zipper axis ($\widehat{VC}$). In such way, we can illustrate, how acting zipper-transverse or zipper-axial force $\vec{F}_v$ at various possible positions (x, y) of the vertex $V(x, y)$ translates into vertex velocity $\vec{u}(x, y)$.

The four pairs of panels indicate how the particular vector field is transformed, i.e. how the acting force is transformed into (non-collinear) velocity. The colour code indicates the strength of effective friction at the given location. In the fig. 3.37a, only vertex-localised friction η^Z was used (with minimal substrate friction for numerical stability). We can see, that the friction does not affect the zipper-transverse $\binom{1}{0}$ field, except for boundary effects at the bottom. On the other hand, the zipper-axial field $\binom{0}{1}$ is funnelled towards the zipper axis, where a strong dissipation leads to slow advance. The friction therefore creates a bias in vertex movement in zipper-transverse direction, towards the zipper axis.

In the fig. 3.37b, only elongational friction $\eta^{\Updownarrow}$ was used (with minimal substrate friction for numerical stability). We can see that zipper-transverse field in fig. 3.37bI is redirected, and particular areas arise, where the dissipation hinders movement near the zipper axis. On the other hand, zipper-axial field (fig. 3.37bII) is very little affected by this type of friction. Therefore, a vertex under general force would preferably advance in zipper-axial direction.

While the substrate friction ($\eta^{\perp}$, $\eta^{\parallel}$) presented in the fig. 3.37c forms some interesting domains of intensity of dissipation (particularly fig. 3.37cI), it has nearly no effect on the acting vector field direction, and is, for the most of the area, nearly collinear. Note however, that the axial component of the substrate friction is much lower in dissipation. As in the previous cases (figs. 3.37a and 3.37b), the final vertex velocity $\vec{u}$ is a combination of effects in fig. 3.37cI and II, and the substrate friction (for the given parameters) therefore results in a preference of zipper-axial vertex movement.

The last set of panels, fig. 3.37d, is a combination of all the previous frictions, figs. 3.37a to 3.37c. We can see, that under this particular parameter settings for various friction types, the velocity is going to be generally slightly aligned with the zipper-axial direction, i.e. with higher dissipation for the zipper-transverse $\binom{1}{0}$ motion. This may be offset by a typically prominent zipper-transverse gradient component of conservative forces. Note, however, that if the vertex-localised dissipation is dominant, $R^Z \approx R$, the two phased dynamics, (i) fast transition towards the zipper axis, and (ii) slow approach towards the new equilibrium,is guaranteed by the friction term.

In the fig. 3.37, we could see that the action of dissipative forces is two-fold, it funnels the movement into directions of lower resistance (i.e. $\vec{u} \nparallel \nabla E$) possibly without much energy loss (i.e. case of significant non-diagonal terms), or it dissipates the driving energy, and movement might be collinear but very slow (i.e. diagonal terms dominate).

We can also investigate the friction vector fields on the basis of eigenvalues and eigenvectors. As shown in the fig. 3.38, the mobility tensor (i.e. the same function as shown in fig. 3.37), can be illustrated as an ellipse of tips of velocity vectors, having semi-axes and tilt. The ellipse is the image of a unitary circle of input force vectors. The images of

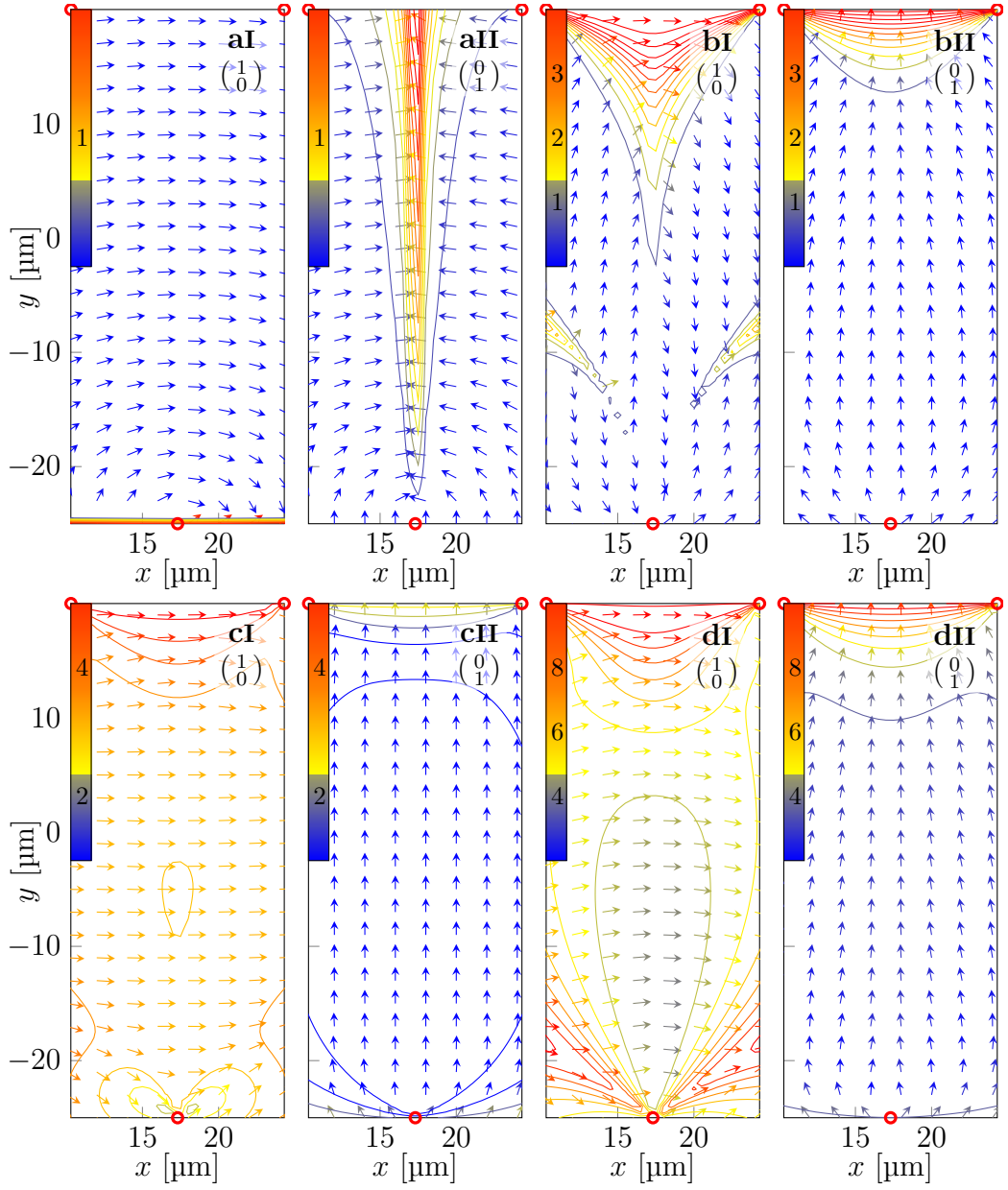

Figure 3.37: The vector fields illustrate the velocities $\vec{u}$ as images of force acting along basis vectors, i.e. $\vec{u} = \overleftrightarrow{H}^{-1}\vec{F}_v$, where force acting at the vertex $\vec{F}_v$ is $\binom{1}{0}$ or $\binom{0}{1}$ as indicated. $\overleftrightarrow{H}^{-1}$ is the inverse of friction tensor, so called 'mobility' tensor. The colour code (calibrated by colourbar at each frame) illustrates effective dissipation at each coordinate $\eta^{\text{eff}}(x, y)$, i.e. $\eta^{\text{eff}}|\vec{u}| = |\vec{F}_v| = 1$. The red circles illustrate axon fixation points; the configuration corresponds to fig. 3.36. **a**: Friction field for dominating vertex friction, η^Z=5 $\frac{\text{nN s}}{\mu\text{m}}$; friction has little effect for zipper-transverse force $\binom{1}{0}$, but strongly redirects and dissipates zipper-axial force $\binom{0}{1}$. **b**: Dominating elongational friction $\eta^{\Updownarrow}$=300 nN s, has a complementary effect to **a**, it redirects and dissipates zipper-transverse force, but zipper-axial force generates collinear movement with little dissipation. **c**: Dominating substrate fiction, $\eta^{\perp}$=200 $\frac{\text{nN s}}{\mu\text{m}^2}$, $\eta^{\parallel}$=200 $\frac{\text{nN s}}{\mu\text{m}^2}$. This type of friction well preserves collinearity of the force and vertex velocity (i.e. $\vec{F}_v \parallel \vec{u}$), while the dissipation for zipper-axial $\binom{0}{1}$ movement is considerably lower. **d**: Combination of **a**-**c**, complete velocity field of a zipper configuration. It shows, that for the given selection of parameters, the dissipation is lower in zipper-axial $\binom{0}{1}$ direction, while the directions of $\vec{u}$ and $\vec{F}_v$ are not significantly misaligned.

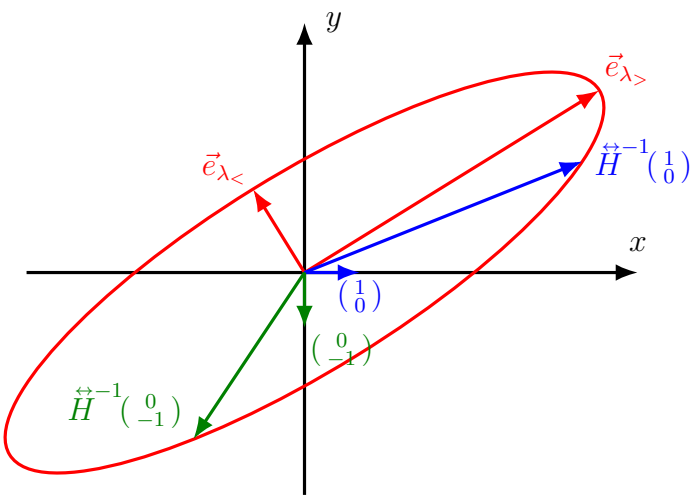

Figure 3.38: Illustration of a tensor (mobility tensor $\overleftrightarrow{H}^{-1}$). The ellipse is an image of a unitary circle $\mathcal{C} = \mathcal{C}(0,0,1)$, i.e. $\overleftrightarrow{H}^{-1}\mathcal{C}$. The eigenvectors illustrate the direction of easiest movement ($\vec{e}_{\lambda_>}$) and the most resisted movement ($\vec{e}_{\lambda_<}$). The blue and green vectors illustrate the Cartesian basis vectors and their images. Note, that the tensor tries to align the input vectors towards the $\vec{e}_{\lambda_>}$, as apparent in fig. 3.37.

basis vectors, $\overleftrightarrow{H}^{-1}\binom{1}{0}$ and $\overleftrightarrow{H}^{-1}\binom{0}{-1}$ correspond to the vectors of the fields in fig. 3.37. Obviously, particular zipper geometry at each point (x, y) of the area determines the particular form of the tensor $\left[\overleftrightarrow{H}(x,y)\right]^{-1}$ and the ellipse-representation varies as much as do the images of the vectors.

The eigenvalues and their corresponding eigenvectors are illustrated in the fig. 3.39. The panels represent the same dominant friction types with the same parameters as in fig. 3.37, to allow easy comparison. This gives an idea of the highest and lowest 'mobility' and movement direction for the particular friction mechanism. The panels labelled **I** correspond to the smaller eigenvalue $\lambda_<$, i.e. higher friction and lower velocity, and panels **II** to greater eigenvalue $\lambda_>$.

The results shown in fig. 3.39 are consistent with the observations in fig. 3.37. The complementary effect of fig. 3.39a (vertex-localised friction) and fig. 3.39b (elongational friction) can be clearly seen, with the zipper-axial direction of maximal dissipation for **a** and zipper-transverse for **b**. The ratio of eigenvalues in **a** and **b**,

$$\frac{\lambda_>}{\lambda_<} \sim 100,$$

which is highly anisotropic friction. Note that the corresponding eigenvectors are always orthogonal (fig. 3.39), i.e. $\vec{e}_{\lambda_<} \perp \vec{e}_{\lambda_>}$, although, their alignment to a particular Cartesian direction ($\binom{1}{0}$ or $\binom{0}{1}$) may change with the vertex position $V(x, y)$, particularly near system boundaries.

The fig. 3.39c (substrate friction) shows a clear separation of directions, consistently with fig. 3.37c, the friction is maximal in zipper-transverse direction; zipper-axial mobility is about 10-fold higher. This has a geometrical explanation:

(i) if vertex moves along $\binom{1}{0}$, it moves all the filaments to the side by δx and generates

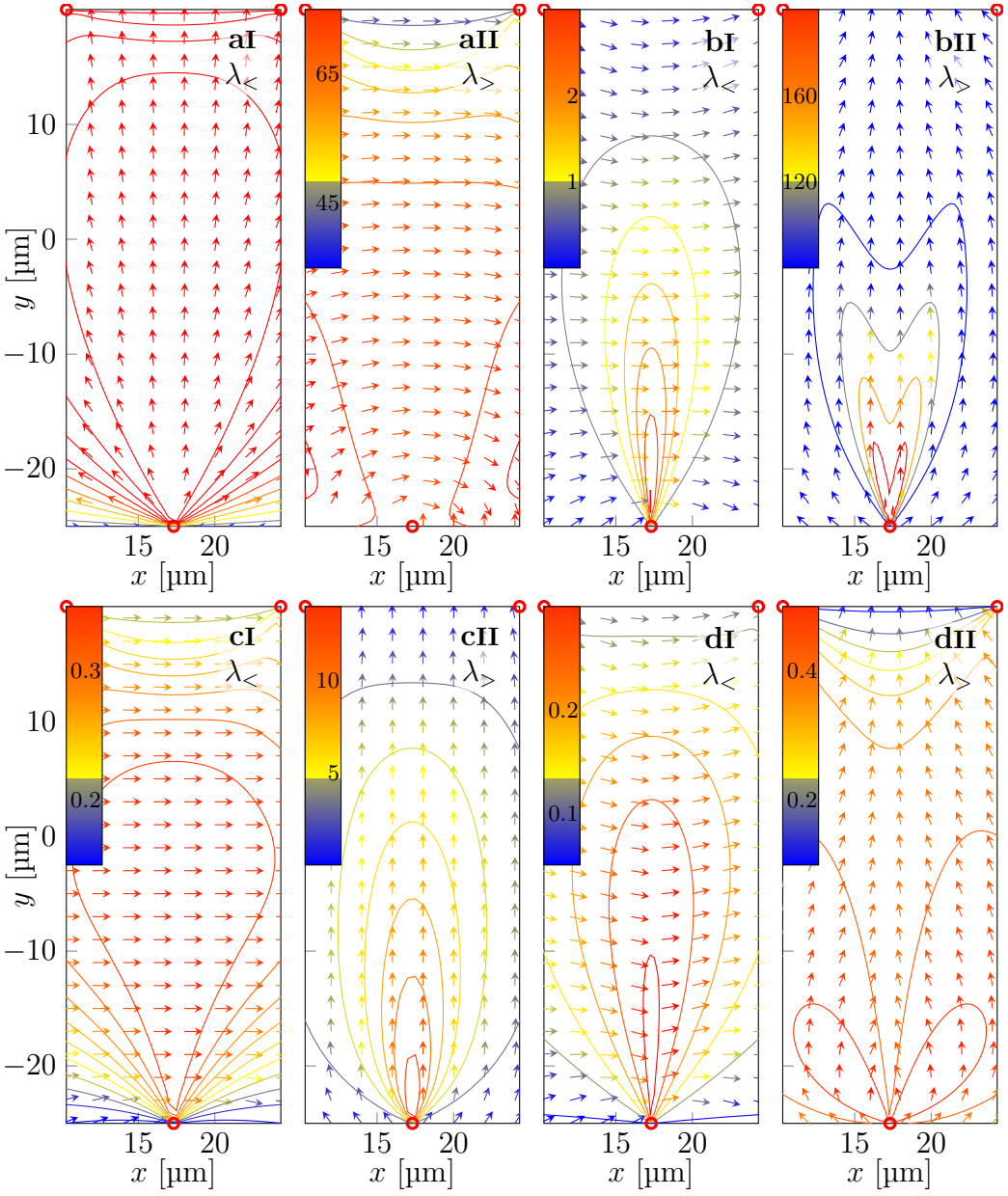

Figure 3.39: The panels illustrate the same area and geometry, the same dominant frictions with the same parameters as fig. 3.37; vector fields show mobility tensor $\overleftrightarrow{H}^{-1}$ eigenvectors corresponding to the larger ($\lambda_>$) and smaller ($\lambda_<$) eigenvalue. **a**: Dominating zipper vertex friction. $\lambda_<$≈0.4 $\frac{\mu m}{nN\,s}$ nearly homogeneous in **aI**, zipper-transverse direction friction is minimal. **b**: Dominating elongational friction offers little resistance along the zipper axis **II**, but roughly 100 × greater friction for the zipper-transverse direction **I**. Interestingly, there is a central region of lower resistance for both eigenvalues. **c**: Dominating substrate friction. Similarly to the elongational friction, the dissipation is about 10 × greater in the zipper-transverse direction, with similar central region of higher mobility. **d**: The combination of friction mechanisms **a-c** shows that combined effect of all mechanisms could act in complementing way and generate roughly homogeneous and isotropic friction. Note the consistency with the figs. 3.37a to 3.37d.

a transverse substrate friction proportional to the the system length along the y-axis

$$\Delta E \sim \eta^{\perp}(L_1 + L_2)|_y \, u \, \delta x.$$

(ii) if vertex moves along $\binom{0}{1}$ by δy, it generates transverse substrate friction in the axon segments l_A and l_B, proportional to the system width in x-axis

$$\Delta E \sim \eta^{\perp}(l_A + l_B)|_x \, u \, \delta y.$$

And for the studied geometry, $45\,\mu\text{m} = (L_1 + L_2)|_y > (l_A + l_B)|_x = 14\,\mu\text{m}$. At the same time, $\beta/2 = 26°$, and therefore the axial substrate friction eigenvector is mostly in the zipper-transverse direction, $(\vec{t}_A + \vec{t}_C) \sim \binom{0.4}{0.1}$. The effects of both substrate friction types combined consistently imply about 10-fold higher friction for $\binom{1}{0}$ direction.

The last pair of panels, fig. 3.39d illustrates the friction tensor field for all the types of friction combined. We can see the complementarity of vertex-localised friction dissipating mainly in $\binom{0}{1}$ direction and other types of friction acting along $\binom{1}{0}$; the effects combine to create roughly homogeneous and isotropic mobility vector field. While this illustrates such 'isotropisation' is possible, it certainly depends on the proportionality coefficients of individual dissipation mechanisms.

3.7.3 Trajectories

To illustrate, how the energy landscape (section 3.7.1) and the friction (or mobility) tensor field (section 3.7.2) interact to produce trajectories of the system, we present a set of possible vertex transition trajectories, see fig. 3.40.

These trajectories document, what we observed in section 3.7.2, that the substrate and elongational dissipation mechanisms tend to hinder zipper-transverse movement but are permissible in zipper-axial direction. Conversely, zipper vertex dissipation has the opposite effect, it drives the vertex towards the zipper axis and then strongly dissipates the mechanical energy as the vertex approaches the new equilibrium.

The described characteristics were observed for two limit cases:

(i) Rapid (sudden) perturbation (figs. 3.40a and 3.40b) of vertex equilibrium; the change generates large gradient of mechanical energy (∇E, with uneven zipper-axial and zipper-transverse components) because the vertex $V(x, y)$ it is far from the minimum (x_0, y_0) of the new energy landscape (see fig. 3.36 and section 3.7.1). The distinct features of observed trajectories are clearly visible for particular dissipation mechanism.

(ii) Slowly unfolding gradual perturbation (figs. 3.40c and 3.40d); vertex closely follows the slowly changing equilibrium coordinate $(x(t), y(t))$ and remains near the energy landscape minimum (x_0, y_0), where energy gradient is small and its components of similar magnitude. Observed trajectories are similar to each other, the typical characteristics are diminished.

We can consider another special trajectory, which follows the energy gradient $-\nabla E$ (see section 3.7.1 and fig. 3.36); such path is realised under isotropic and uniform friction

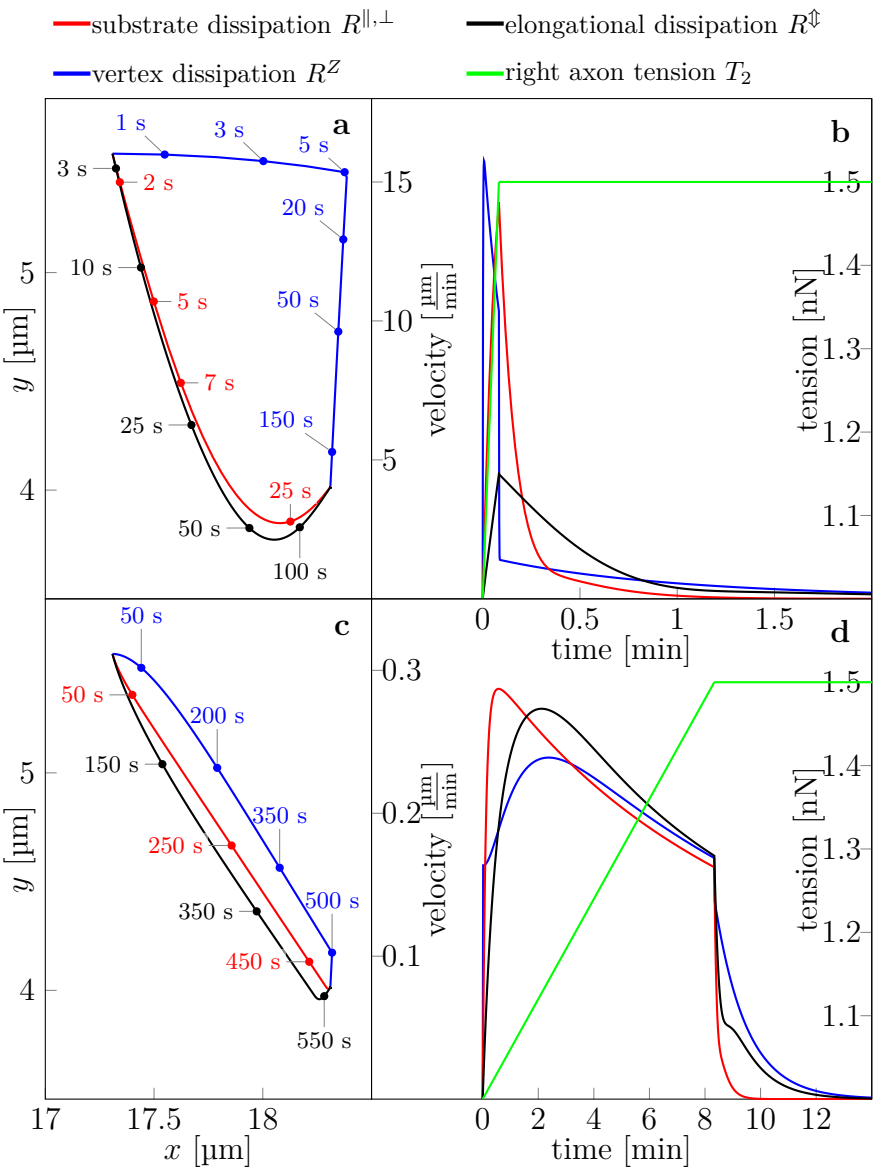

Figure 3.40: Illustration of zipper vertex trajectory and velocity during dynamics. Colour code denotes a dominant form of dissipation for the particular trajectory or the velocity profile, as indicated in the legend. Time-stamps along trajectories in **a** and **c** denote time of the vertex coordinate. **a**: Vertex transition trajectories after sudden change in tension in the right axon T_2, as indicated by green line in panel **b**, from T_2=1 nN to T_2=1.5 nN. The tension in the left axon remains unchanged at T_1=1 nN. While trajectories where substrate friction (red, $\eta^{\perp}=\eta^{\parallel}=100\,\mathrm{Pa\,s}=\frac{\mathrm{pN\,s}}{\mu\mathrm{m}}$) and the elongational friction (black, $\eta^{\Updownarrow}=5000\,\mathrm{nN\,s}$) are dominant are remarkably similar, the dominating zipper vertex friction (blue, $\eta^{Z}=3\,\frac{\mathrm{nN\,s}}{\mu\mathrm{m}}$) trajectory is very divergent. The zipper vertex friction trajectory exhibits characteristic swift transition towards the zipper axis and much slower zipper-axial convergence. **b**: Time-course of zipper vertex velocities and right axon tension (T_2) corresponding to trajectories in panel **a**. **c**: Characteristic trajectories for a specific dominant dissipation (same parameters as in panel **a**), for gradual change in tension (see green line in **d**). For the slowly developing perturbation, all three trajectories are very similar. **d**: Time-course of vertex velocities corresponding to trajectories in **a**. In case of slow perturbation, the zipper velocity has a sudden onset to a plateau of nearly constant advance, and sudden stop after the tension stops increasing.

$\overleftrightarrow{H} = c \cdot \overleftrightarrow{1}$. We showed in fig. 3.39d that such situation can be also created by a combination of conveniently scaled dissipation mechanisms. The gradient trajectory initially approaches the zipper axis and then advances to the new equilibrium very slowly, in a similar manner to the trajectory under dominant vertex-localised dissipation. Therefore, when such gradient approach is combined with anisotropic substrate or elongational dissipation, the two tendencies oppose each other, and the convergence trajectory is not as strongly two-phased, as in the case of vertex-localised friction, see figs. 3.40a and 3.40c.

Comparing the model trajectories with the experimental observations of zippers, we can observe:

(i) two-phased dynamics observed in culture and manipulation experiments (section 3.5.6), when vertex moves swiftly towards the axis and then slowly along the axis, is guaranteed by the model, only if the vertex-localised dissipation is dominant;
(ii) constant velocity of zippering with a sudden halt observed in culture (fig. 3.29) is predicted by the model in cases when equilibrium perturbation unfolds gradually over time.

The item (i) is supported by the manipulation experiment we have presented in detail in fig. 3.33. Note, that such two-phased dynamics is particularly visible for the velocity (blue line) in fig. 3.40b. In the case of item (ii), the model-predicted zipper vertex quasi constant velocities $\approx 0.5\,\frac{\mu m}{min}$ are at the order of magnitude agreement with the actually observed velocities of zippers (see fig. 3.29).

3.7.4 Analytical limits

To conclude presentation of our model, we will examine analytical approximation eq. (3.53) in two limits. We will assume a symmetric configuration, where $T_1 = T_2 = T$ and zipper axis is aligned along the Cartesian y axis, so that $\alpha_1 = \alpha_2 = \beta/2$. Then the equation eq. (3.53) becomes

$$\left[\overleftrightarrow{K}(x,y)\right]^{-1} \begin{pmatrix} 0 \\ S - 2T\,(1 - \cos\beta/2) \end{pmatrix} = \begin{pmatrix} \dot{x} \\ \dot{y} \end{pmatrix}.$$

We further simplify the equation by ignoring the substrate friction, as we did initially in section 3.5.5, removing the two corresponding rows from $\overleftrightarrow{A}$ and $\overleftrightarrow{P}$ matrices, and denoting

the reduced 2×2 matrices as $\overleftrightarrow{A}'$ and $\overleftrightarrow{P}'$. Then, $\overleftrightarrow{K}$ becomes

$$\begin{aligned}
{}^1\!/_2\overleftrightarrow{K}_1 &= \overleftrightarrow{P}'^T \overleftrightarrow{A}' \overleftrightarrow{P}' \\
&= \begin{bmatrix} t_{Ax}+0 & t_{Ay}-1 \\ 0 & -1 \end{bmatrix}^T \begin{bmatrix} \frac{\eta^{\Updownarrow}}{2L_1} & 0 \\ 0 & \frac{\eta^Z}{4} \end{bmatrix} \begin{bmatrix} t_{Ax}+0 & t_{Ay}-1 \\ 0 & -1 \end{bmatrix} \\
&= \begin{bmatrix} \sin\beta/2 & \cos\beta/2-1 \\ 0 & -1 \end{bmatrix}^T \begin{bmatrix} \frac{\eta^{\Updownarrow}}{2L_1} & 0 \\ 0 & \frac{\eta^Z}{4} \end{bmatrix} \begin{bmatrix} \sin\beta/2 & \cos\beta/2-1 \\ 0 & -1 \end{bmatrix} \\
&= \begin{bmatrix} \sin\beta/2 & 0 \\ \cos\beta/2-1 & -1 \end{bmatrix} \begin{bmatrix} \frac{\eta^{\Updownarrow}}{2L_1}\sin\beta/2 & \frac{\eta^{\Updownarrow}}{2L_1}(\cos\beta/2-1) \\ 0 & -\frac{\eta^Z}{4} \end{bmatrix} \\
&= \begin{bmatrix} \frac{\eta^{\Updownarrow}}{2L_1}\sin^2\beta/2 & \frac{\eta^{\Updownarrow}}{2L_1}\sin\beta/2\,(\cos\beta/2-1) \\ \frac{\eta^{\Updownarrow}}{2L_1}\sin\beta/2\,(\cos\beta/2-1) & \frac{\eta^{\Updownarrow}}{2L_1}(\cos\beta/2-1)^2+\frac{\eta^Z}{4} \end{bmatrix}
\end{aligned}$$

while for the $\overleftrightarrow{K}_2$, the $\overleftrightarrow{P}'$ would have opposite x-projection (i.e. term $t_{Ax} \to t_{Bx} = -\sin\beta/2$, while $t_{Ay} = t_{By}$), and therefore, for $\overleftrightarrow{K} = \overleftrightarrow{K}_1 + \overleftrightarrow{K}_2$, the non-diagonal terms will cancel out (consistently with symmetry expectations), and

$$\overleftrightarrow{K} = \begin{bmatrix} 2\frac{\eta^{\Updownarrow}}{L}\sin^2\beta/2 & 0 \\ 0 & 2\frac{\eta^{\Updownarrow}}{L}(\cos\beta/2-1)^2+\eta^Z \end{bmatrix}, \tag{3.56}$$

which is trivially inverted and yields the simplified equation of motion

$$\dot{y} = \frac{S - 2T\,(1-\cos\beta/2)}{2\frac{\eta^{\Updownarrow}}{L}(\cos\beta/2-1)^2+\eta^Z}, \tag{3.57}$$

which exactly corresponds to the intuitively derived equation eq. (3.17), and provides a consistency check.

We can inspect the eq. (3.57) in two limits, for small and large zipper angle β. To streamline the manipulations, we will rewrite the equation into more convenient notation according to fig. 3.41. We place the origin of the coordinate system between the unzippered fixed axon termini A and B. We denote transverse distance of points A and B from the zipper axis as $p = |x_A| = |x_B|$, the vertex coordinate becomes $V(0, y)$, where y grows as vertex recedes (unzippers); the height of the system is given by $y_{\max} = |y_C - y_A|$. The change of coordinate system switches the sign in eq. (3.57). We introduce a shortcut $\eta \equiv 2\eta^{\Updownarrow}\frac{(\cos\beta/2-1)^2}{L} + \eta^Z$, and eliminate the cosine as $\cos\beta/2 = \frac{y}{\sqrt{y^2+p^2}}$. The equation eq. (3.57) is rewritten to

$$\dot{y} = \frac{2T-S}{\eta} - \frac{2T}{\eta}\underbrace{\frac{y}{\sqrt{y^2+p^2}}}_{\cos\beta/2}, \tag{3.58}$$

removing explicit dependence on variable β and allowing expansion in $\frac{y}{p} \ll 1$ or $\frac{p}{y} \ll 1$.

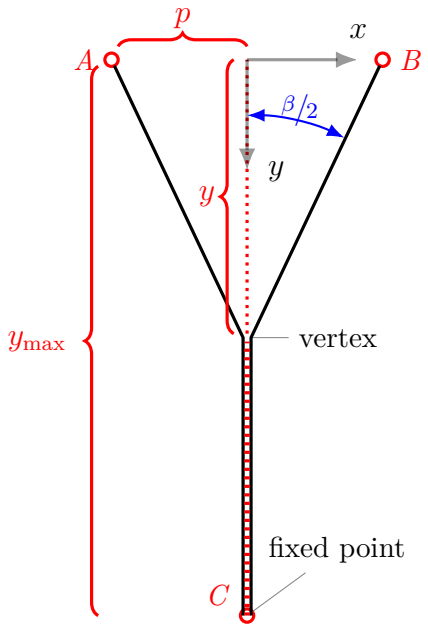

Figure 3.41: The figure illustrates new convenient notation used for calculation of eq. (3.58) limits. Red circles indicate immobile fixation points. Dotted red line is conserved zipper axis. The coordinate origin $(0, 0)$ is placed between the points A and B.

The first of the two limit cases is a large zipper angle, which applies to situations of high S/T ratio:

$$y \ll p : \cos \beta/2 \approx \frac{y}{p};\; L = y_{\max} - y + p\sqrt{1 + \left(\frac{y}{p}\right)^2} \approx y_{\max} + p$$
$$\eta \approx 2\eta^{\Updownarrow}\frac{(y-p)^2}{p^2\,(y_{\max}+p)} + \eta^Z \approx 2\frac{\eta^{\Updownarrow}}{y_{\max}+p} + \eta^Z = \text{const}$$

and we can obtain the analytical result

$$\begin{aligned}
\dot{y} &= \frac{2T-S}{\eta} - \frac{2T}{\eta}\frac{y}{p} \\
\frac{\dot{y}}{1 - \frac{2T}{2T-S}\frac{y}{p}} &= \frac{2T-S}{\eta} && \left| \int dt \right. \\
\log\left(1 - \frac{2T}{2T-S}\frac{y}{p}\right) + C &= -\frac{2T}{\eta p}t && |y(t{=}0) \equiv y_{\text{ini}} \\
1 - \frac{2T}{2T-S}\frac{y}{p} &= \left(1 - \frac{2T}{2T-S}\frac{y_{\text{ini}}}{p}\right) e^{-\frac{2T}{\eta p}t} && \left| \frac{p\,(2T-S)}{2T} \equiv y_\infty \right. \\
y &= y_\infty - (y_\infty - y_{\text{ini}})e^{-\frac{2T}{\eta p}t}. && (3.59)
\end{aligned}$$

The eq. (3.59) describes the exponential convergence of a zipper vertex to the final equilibrium y_∞ from initial position y_{ini} at $t = 0$; exponentially converging zippers were described in the section 3.5.4. Assuming adhesion S is rather unvarying, large angle situations indicate low tension T in the axons (cf. fig. 3.36b). The character of the convergence is independent on S (the y_∞ is determined by S), but has a typical

timescale given by $\tau = \frac{\eta p}{2T}$. If output of eq. (3.59) is compared to the numerical full solution of eq. (3.58), it provides a good approximation for unzippering, but performs rather poorly for zippering (due to $\tau \sim T^{-1}$ factor).

The other analytical limit is for very small angles, typically when S/T ratio is low, suggesting axons under high tension.

$$
\begin{aligned}
y \gg p : \cos\beta/2 &= \frac{1}{\sqrt{1+\left(\frac{p}{y}\right)^2}} \approx 1 - \frac{1}{2}\left(\frac{p}{y}\right)^2 \\
L &= y_{\max} - y + y\sqrt{1+\left(\frac{p}{y}\right)^2} \approx y_{\max} + \frac{1}{2}\frac{p^2}{y} \\
\eta &\approx \frac{1}{2}\eta^{\Updownarrow}\frac{(p/y)^4}{y_{\max} + \frac{1}{2}\frac{p^2}{y}} + \eta^Z \approx \eta^Z = \text{const},
\end{aligned}
$$

inserting these expansions into the eq. (3.58), and using some further simplification later, we obtain

$$
\begin{aligned}
\dot{y} &= -\frac{S}{\eta} + \frac{T}{\eta}\left(\frac{p}{y}\right)^2 \\
\frac{\dot{y}}{1-\frac{T}{S}\left(\frac{p}{y}\right)^2} &= -\frac{S}{\eta} \qquad \Big| \int dt \\
y - \sqrt{\frac{Tp^2}{S}}\tanh^{-1}\left[\frac{y}{p}\sqrt{\frac{S}{T}}\right] + C &= -\frac{S}{\eta}t \\
\left| \tanh^{-1} a - \tanh^{-1} b \equiv \tanh^{-1}\frac{a-b}{1-ab} \right| & \\
y - y_{\text{ini}} - \sqrt{\frac{Tp^2}{S}}\tanh^{-1}\left[\frac{(y-y_{\text{ini}})\sqrt{\frac{S}{Tp^2}}}{1 - y y_{\text{ini}}\frac{S}{Tp^2}}\right] &= -\frac{S}{\eta}t \\
\left| -\tanh^{-1} a = \frac{1}{2}\log\left[\frac{1-a}{1+a}\right] \approx \frac{1}{2}\log(1-2a) \approx -a \right| & \\
-\frac{(y-y_{\text{ini}})\sqrt{\frac{S}{Tp^2}}}{1 - y y_{\text{ini}}\frac{S}{Tp^2}} &= -\sqrt{\frac{S}{Tp^2}}\left(y - y_{\text{ini}} + \frac{S}{\eta}t\right) \\
\frac{y - y_{\text{ini}}}{\frac{T}{S}\frac{p^2}{y y_{\text{ini}}} - 1} &= \frac{S}{\eta}t \qquad (3.60) \\
y &\approx y_{\text{ini}} + \frac{S}{\eta}\left[\frac{T}{S}\left(\frac{p}{y_{\text{ini}}}\right)^2 - 1\right]t.
\end{aligned}
$$

Despite the last calculation took several simplification, the eq. (3.60) should still remain valid near the initial point y_{ini}, the vertex zippering velocity is roughly constant. Our numerical test showed, that agreement with the eq. (3.58) is higher for higher tension T.

This demonstration of linear convergence/constant velocity solution is consistent with the observation of linearly converging zippers in section 3.5.4.

In the small angle limit calculation, the linearisation of logarithm can be avoided and a very complex but exact (to the second order in p/y) expression for vertex trajectory can be obtained. If this expression is properly rescaled (asymptotic correction is necessary), it provides an excellent agreement even for dynamics at intermediate zipper angles (i.e. when $y/p \sim 1$).

3.8 Network

As illustrated in previous sections, the zippering processes incur changes of (i) local geometry, the axon segment length and the zipper vertex angle (section 3.1.2 and figs. 3.3 and 3.4), driven by simple zippering, and (ii) topology, the number of vertices or closed loops (section 3.1.1 and figs. 3.1 and 3.4b), in more complex dynamics. While these processes occur and modify the network locally, their combined effect likely influences the statistics of the network as a whole. In this section, we will inspect the connection between the dynamics of the network and the dynamics of zippers as described by our model. Considering complexity of the network, the argument will be limited to the time course of first and second moments of network statistic.

3.8.1 Network statistics

We measured development of network basic statistics in time. We selected a subsection of a field devoid of material flow or collapse, and time interval, during which culture showed no signs of retraction, in the range (178–295) min. We then sampled the video at 6 to 10 time points, and segmented the network in the range. We then constructed a graph structure (see sections 2.2.4 and 3.8.3) and evaluated time course of the statistics in the area, namely (i) the total length of the network ($\mathcal{L}$), (ii) number of vertices (excluding crossings, $\mathcal{V}$), (iii) mean and median zipper vertex angle ($\bar{\beta}$ and β_M), and (iv) the number of cordless loops (or shortest cycles, $\mathcal{C}$). Results from four such measurements are shown in the fig. 3.42.

Each of the columns, figs. 3.42a to 3.42d, represents a single culture experiment. Note that in all of the experiments, to some extend, the complexity (i.e. the total length $\mathcal{L}$ and the number of vertices $\mathcal{V}$) of the network initially increases; the culture still grows and develops. After some time, the culture begins the coarsening stage, the listed descriptors (rows of fig. 3.42) decrease. These statistics refer to the stable central part of the network, and are not a result of a collapse, draft or retraction. A notable exception to coarsening is fig. 3.42c, which only de-coarsens (becomes more complex) during the observed time period; this experiment was observed only for 150 min, which might be not long enough for some cultures to enter the coarsening stage (cf. fig. 3.42b starts to coarsen only after t=150 min).

Note that the descriptors $\mathcal{L}$, $\mathcal{V}$, $\bar{\beta}$ (β_M) and $\mathcal{C}$ are correlated. During the recorded time interval, we see almost no axon retraction or death and very limited presence of GCs, in the observed area. This absence of material flow, axon removal or active

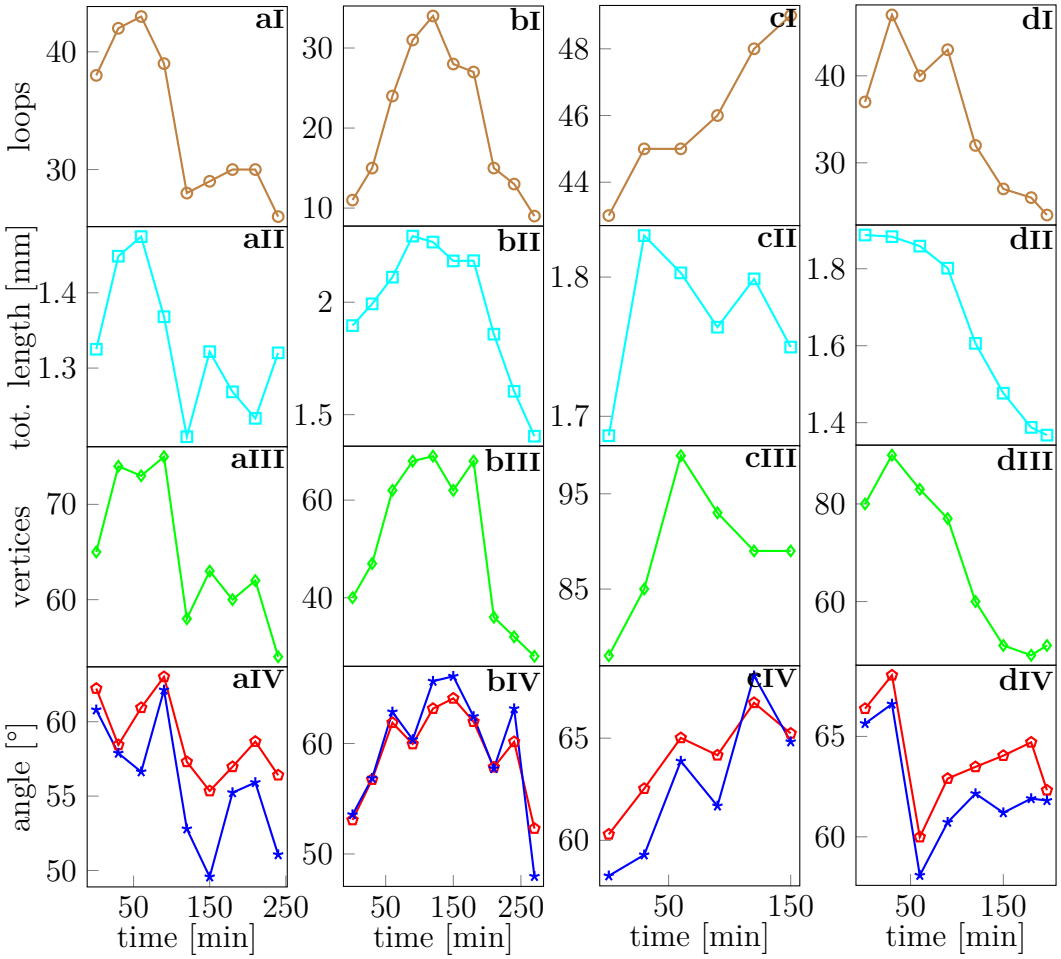

Figure 3.42: Columns **a-d** represent four videomicroscopy time lapse experiments on cultures developing without a pharmacological treatment. A period of initially increasing network complexity is followed by a coarsening stage (except for the experiment **c**). The row **I** shows the number of cordless loops (shortest cycles) $\mathcal{C}$ in the studied network; this number is a good indicator of network complexity (increases with complexity). The row **II** shows total length $\mathcal{L}$ of the network segments within the studied network area. The row **III** is the total count of network vertices $\mathcal{V}$. Rows **II** and **III** include also edges and vertices not constituting a closed loop. The row **IV** shows time course of mean (red pentagons) and median (blue stars) network zipper angle. Rows **I** to **III** are strongly correlated; the row **IV** shows moderate correlation to others. The population angle is fluctuating due to network interactions, and is technically more difficult to measure.

growth suggests that coarsening of the network is a result of in-place restructuring of the network material within a stable boundary. We infer such changes result from zippering-driven fasciculation of individual axons into bundles, which can induce geometrical and topological network remodelling.

As proposed in section 3.3.2, increase in mean number of axons n in fascicle is proportional to the increase in fascicle mean tension, i.e. $\bar{T} \propto n$. Such sustained increase in mean tension $\bar{T}$ (due to coarsening) in the network should influence the local geometrical descriptors of closed loops constituting the graph. The zipper angles at the vertices should decrease with coarsening of the network (and vice versa), which is largely observed in panels IV of fig. 3.42. The increasing tension should also straighten the network radially (i.e. increase anisotropy) and elongate the closed loops (i.e. decrease circularity, see section 2.6.1). The observed local changes are shown in fig. 3.43.

The columns represent the same experiment as in fig. 3.42. Comparing fig. 3.42 with fig. 3.43, we can see that circularity of loops increases with de-coarsening of the network, which is particularly visible in fig. 3.43bI and fig. 3.43cI, and conversely decreases as network coarsens fig. 3.43aI and fig. 3.43dI. Anisotropy generally follows the opposite dependence (fig. 3.43II); coarsening network tends to align the axons radially, as we have anticipated.

Consistently with natural expectations, as the network coarsens, the area of cordless loops (shortest cycles) in the graph tend to increase (row III in figs. 3.43a, 3.43b and 3.43d), and decrease if the culture de-coarsens (fig. 3.43cIII). A remarkable thing about this data is mean/median number of vertices per loop at roughly 4 to 4.5, as shown in fig. 3.43IV. This ratio is well preserved across all the experiments we have analysed, including the pharmacologically treated ones. Interestingly, the mean always stays higher than the median in the observations, and they tend to co-vary, which suggests that the distribution has a stable shape and only shifts during the time course.

Angle distribution

We have already noted in this section that mean/median zipper angle in a network tends to decrease with coarsening and vice versa. The coarsening and de-coarsening processes influence not only the statistical properties of the zipper angle, but also the overall count of the zippers. The whole histogram therefore undergoes a change. The effect of coarsening and de-coarsening is shown in fig. 3.44.

The fig. 3.44 shows, that the mean zipper angle $\bar{\beta}$ increases with de-coarsening (60° to 65°, fig. 3.44a) and decreases with network coarsening (66° to 62° fig. 3.44b). It also shows, that nearly all angles are in the range 20°–120°, with the mean value around 60°–65°. Slightly higher mean zipper angle, than measured for mobile zippers in culture (51.2°, see section 3.5.2) is expected, because present evaluation does not exclude immobile (entangled) zippers, which cannot recede (unzipper), and therefore tend to increase the zipper angle mean.

In the section Local-global dynamics relationship, we will analyse the relationship between the zipper angle and the coarsening more thoroughly, within the framework of our model.

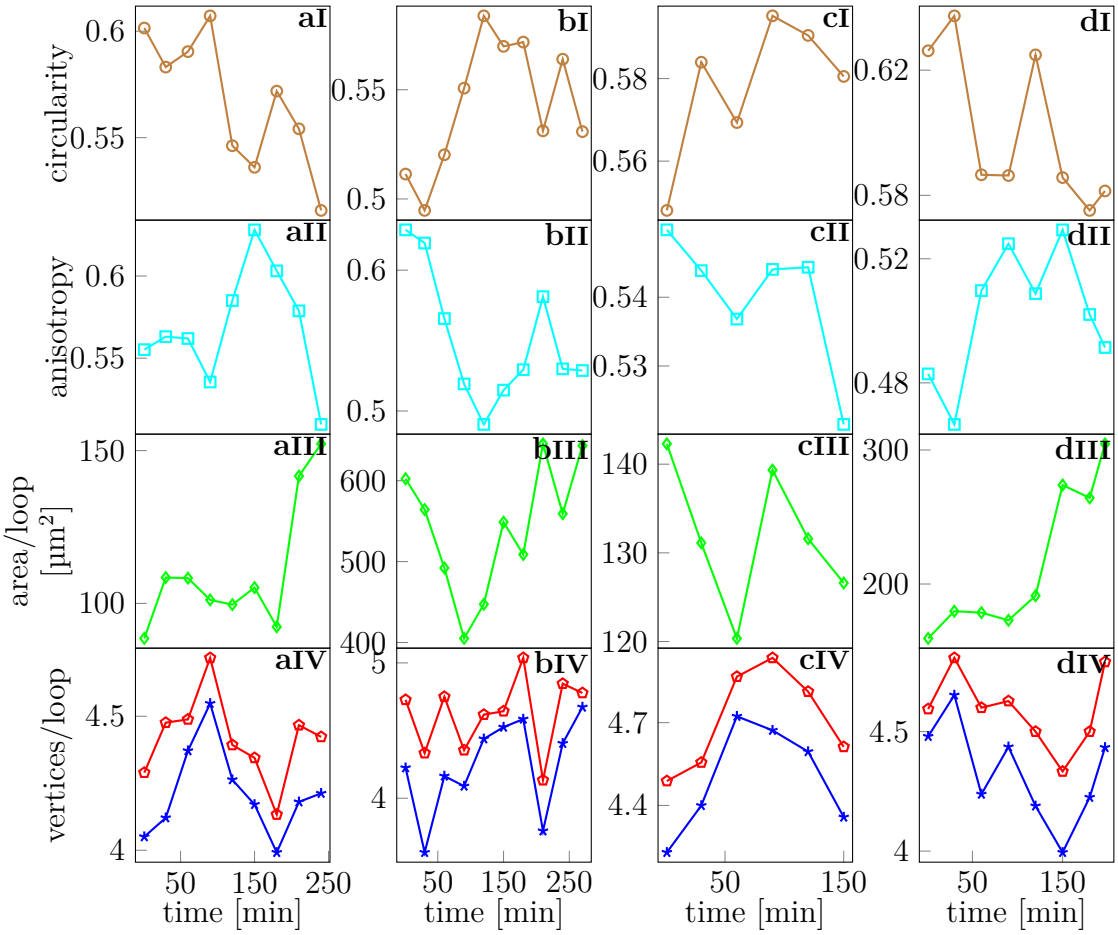

Figure 3.43: Columns **a-d** represent four videomicroscopy time lapse experiments on cultures developing without a pharmacological treatment, the same as presented in the fig. 3.42. The row **I** illustrates the circularity of the closed loops forming the network (see section 2.6.1). As the network de-coarsens, the loops become more circular, while gradual coarsening leads to their elongation. Row **II** shows anisotropy of network segments; the network becomes more aligned/anisotropic, as the coarsening progresses. The row **III** shows average area per loop. This indicator may fluctuate, when topological changes disrupt, merge or remove a large loop; or when a loop crosses the field boundary and is excluded by detection algorithm. The last row **IV** shows mean (red pentagons) and median (blue stars) number of vertices per loop. The values are remarkably similar across experiments, around 4 to 4.5, also note their similar time courses.

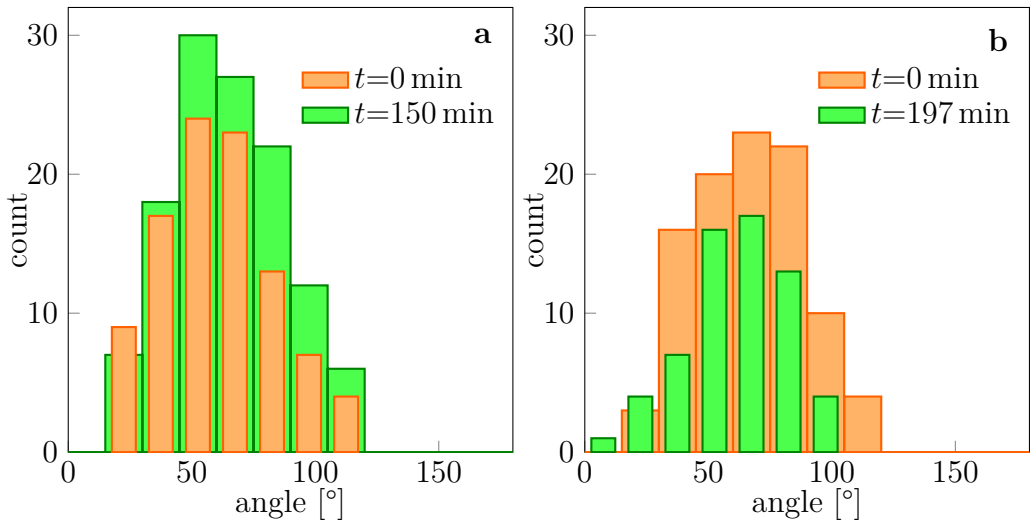

Figure 3.44: Zipper angles histograms at the beginning (orange bars) and the end (green bars) of the experiment recording. Panel **a** corresponds to the experiment **c** in figs. 3.42c and 3.43c. The network de-coarsens during this experiment, the number of vertices increases and so does the total count of the histogram. The mean zipper angle of the distribution increases from 60° to 65°. The panel **b** corresponds to the experiment **d** in figs. 3.42d and 3.43d. The network coarsens during the experiment, the number of vertices decreases (the histogram total count drops), and the mean zipper angle decreases from 66° to 62°.

3.8.2 Correlations

The relations between global network statistics (e.g. total length, number of loops) and shape descriptors (e.g. anisotropy, circularity) can be conveniently studied in correlation matrices. We present such matrices for the four experiments presented in figs. 3.42 and 3.43 in fig. 3.45.

The coefficients in the matrices are consistent with the our earlier observations. The aggregate statistics of the whole observed network, total length, number of loops and vertices, and the inverse of the average loop area $1/\langle a \rangle$, are very strongly correlated (with the exception of de-coarsening short-time experiment labelled **c**, see figs. 3.42c, 3.43c and 3.45c), with the correlation coefficients near 0.8–0.9. Mean angle $\bar{\beta}$ is also correlated to these statistics, but to a lesser extend, around 0.7. The shape descriptors, the isotropy[10] and circularity, are also mildly correlated to the rest of the indicators, with correlation coefficients around 0.5–0.9.

The observations show that the descriptors of the network are significantly correlated, particularly interesting is the connection between the global geometry statistics ($\mathcal{L}$) and topology ($\mathcal{C}$, $\mathcal{V}$), and the mean local geometry (β) and isotropy. While it is true that all the correlations are not equally strong for all the experiments, the described general trend suggests, that there might be a feedback of global structural changes (e.g. fasciculation) driving local geometry-dependent dynamics (e.g. zippering) which in turn induces further changes of structure and topology.

[10] We defined the 'isotropy' as 1 − anisotropy to keep all the correlation coefficients positive.

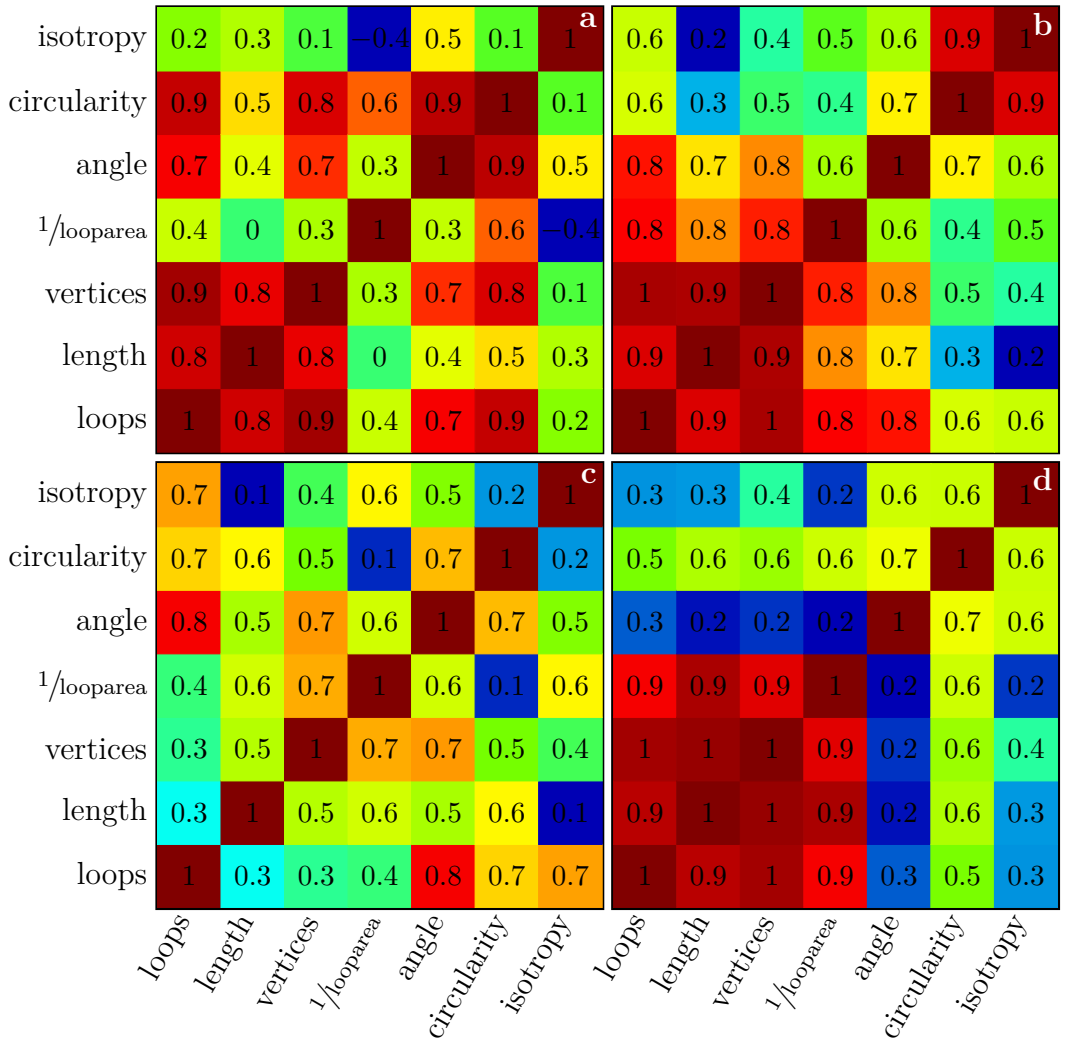

Figure 3.45: Correlation matrices for the experiments presented in figs. 3.42 and 3.43, the labels correspond. Despite some limited differences, common trends can be observed. The global descriptors and the inverse of looparea $\langle a \rangle$ are strongly correlated with each other, with $\rho \approx 0.8$–0.9 (with notable exception of experiment **c**). Particularly interesting is also a good correlation between the mean angle and the number of loops and vertices around $\rho \approx 0.7$. The remaining shape descriptors, circularity and isotropy are still mildly correlated, with coefficient $\rho \approx 0.5$–0.9. The longer lasting experiments (**a**, **b** and **d**), which include at least partially both coarsening and de-coarsening stages, exhibit more robust correlation patters, particularly for global statistics (i.e. total length, number of loops and vertices).

3.8.3 Cordless loop detection algorithm

Before we delve into the foreshadowed relations between network topology and local mechanisms underlying structural changes, we will quickly introduce the algorithm we developed to detect cordless loops within the graph data structure of the axonal network.

Construction of the graph data structure was described in section 2.2.4. Each graph vertex is defined by its coordinates and contains a list of other vertices to which it is connected by edges. Graph vertex is a general junction point, and does not distinguish between zipper vertices or crossings. Isolated vertices of degree zero are immediately discarded. The coordinate system is defined in such way that the data vertex coordinates are always positive, $x \geq 0$, $y \geq 0$.

Before the actual loop detection takes place, several pre-processing steps are taken:

(1) All the loose ends (i.e. vertices of degree 1) and their associated edges are progressively pruned (dashed red lines in fig. 3.46b).

(2) Graph vertices of connectivity degree 2 are kept as points of curvature, but are not counted towards vertices in further network structure analyses (e.g. they are excluded from the total count of vertices within the field, and from calculation of number of vertices per loop).

(3) Outer boundary of each contiguous set of loops is detected by searching the closest edge to the coordinate origin $(0, 0)$ (see dashed blue line fig. 3.46b). Starting from the endpoint of the edge, and successive edges are iteratively added to the boundary set (indicated by the blue arrow in fig. 3.46b), until the boundary path is closed. Depending on the precise choice of coordinate system (see fig. 3.46b), either only leftmost or only rightmost turns are taken at all junction points (i.e. decision points), when circumventing the contiguous set of loops.

(4) If some of the graph vertices remain outside the detected closed boundary, the process is repeated with such outstanding vertex subset, until all vertices (of degree $\geq$2) are part (i.e. border or interior) of a contiguous set of loops.

The detection of cordless loops (shortest cycles) within the initially detected border of contiguous graph is technically similar to the outer border detection. The edges located in the interior are iteratively inspected. For each edge, an adjacent edge is selected in such way, that the path elongation represents a leftmost turn (turning left at the **B**-endpoint of the edge marked in blue, forming loop *1*, in fig. 3.46b); the procedure is repeated for the next edge, and the path is extended by next consecutive leftmost turn (sense is indicated by the circle *1* with arrows). The path is eventually closed at the non-starting end of the initial segment. The same procedure is then repeated for the same edge, but taking rightmost turns (cycle indicated by *2* in fig. 3.46b). Two loops are detected for each internal edge. Duplicate loops are discarded.

The presented method of loop detection utilises the information about vertex Cartesian coordinates, which allow to choose proper consecutive edge (left-most or right-most) at turning points. This makes the method feasible, contrary to generic graph methods,

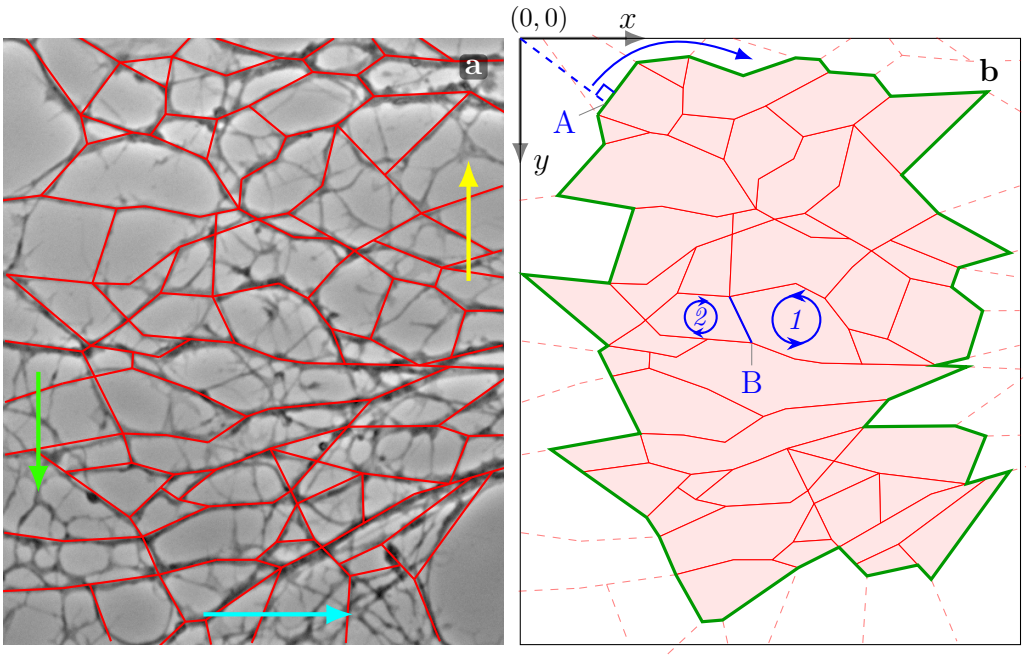

Figure 3.46: Algorithm illustration. **a**: Initial segmented frame; manually-segmented selection was refined (e.g. gaps removal) by a relaxation procedure and graph data structure was extracted. Some network parts (no red lines) were excluded as non-axonal, which can be often distinguished by comparing several consecutive frames in the video. For example, the cyan arrow indicates a structure interfering with a GC, the yellow arrow indicates flattened axon, which underwent a rare removal (death), the green arrow indicates side-processes. **b**: Edges not forming closed loops (dashed) are removed. A segment closest to the origin $(0, 0)$, marked by **A**, is detected. The segment endpoint with larger x-coordinate is selected as initial point of the border path (drawn in green). The border path is constructed by sequentially adding the leftmost-turning consecutive segments, until the path is closed on return to the segment **A**. Similar method is used for the cordless loop detection. For each edge within the boundary (e.g. blue edge near the mark **B**), starting from its endpoint with larger x-coordinate (marked by **B**), leftmost turns are consecutively taken, until the path is closed (illustrated by the blue circle *1*,arrows indicate direction). The procedure is then repeated for the same edge with the sequence of rightmost turns (loop circle *2*). Two loops are detected for each edge, duplicate loops are discarded.

where vertices are abstract, and no explicit spatial ordering exists. The general vertex methods was not computationally viable (on office computer) for networks of more than ∼30 vertices. The areas of networks we studied contain typically 60–100 vertices.

Once the loops are detected, represented by an ordered set of vertices or edges, the shape descriptors can be easily calculated: (i) loop area (standard algorithm for a polygon); (ii) perimeter and circularity; (iii) eccentricity (requires ellipse fitting, section 2.6.1); (iv) vertex per loop count. The details are described in section 2.6.1. The last non-trivial descriptor is anisotropy (and corresponding director), which is however based on all the segmented edges, not restricted to the loops.

Extracting these parameters/descriptors of the network for several consecutive timepoints allows us to gain insight into their mutual relationship, as demonstrated in the sections 3.8.1 and 3.8.2. This method allows us to perform quantitative and systematic analysis across multiple experiments and obtain insight which would be impossible to gain by simple watching of the recorded material, or simple intensity-based analyses. Despite the results of this analysis between individual experiments might slightly diverge, the trends obtained by the analysis seem robust.

3.9 Local-global dynamics relationship

In the following sections, we will try to reconcile our zipper model (sections 3.5.1 and 3.5.5) with the network data (section 3.8.1) and propose explanation, how the tension-adhesion interplay (see hypothesis 1) brings about the global dynamics of developing axonal network. We will try to elucidate tends and make predictions mostly at the level on network statistics averages.

3.9.1 Topological changes and the loop stability

The observed axonal networks start to gradually decrease their total length (e.g. fig. 3.1 and fig. 3.42II). This suggests, that in our experimental setting, where network is not influenced by direct (contact) GC activity or axon retraction, local interactions reducing total length are prevalent, or in other words, the zippering is more prominent than unzippering. Consistently with such inference, we also observe the decrease in number of vertices (figs. 3.1, 3.42 and 3.45), which naturally occurs during zippering, if an advancing zipper vertex encounters and merges with another vertex.

Such merger processes occur in the developing network, as shown in fig. 3.4b (while their inverse can occur after perturbation, figs. 3.9 and 3.11a). A triangular loop gradually contracts and the three vertices converge into a single-vertex configuration, see fig. 3.47.

During such processes, the loop typically retains its inner zipper angles and contracts in size, preserving its shape. Such dynamics can be a result of uniform decrease in tension in the involved axons. In such case, the equilibrium inner angles become larger than the current zipper angles (stemming from eq. (3.9)), and the vertices of the loop start to advance (as illustrated in fig. 3.47a). Under these circumstances, inner angles cannot be rearranged to restore equilibrium, simply because the sum of inner angles is constant,

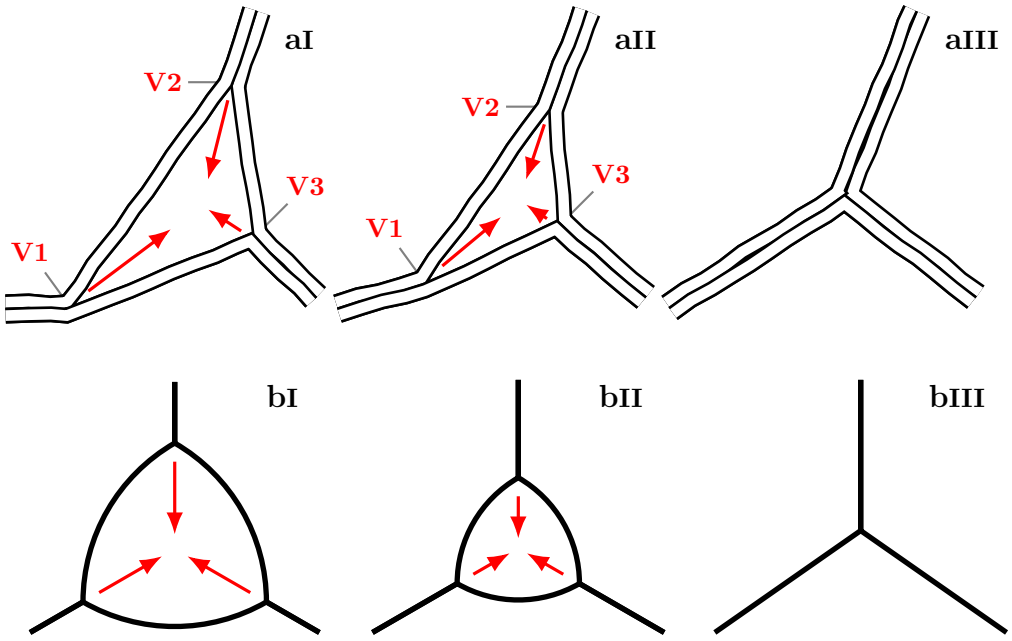

Figure 3.47: **a**: Gradual collapse of a triangular axon loop **I**, by simultaneous advance of the three loop-forming vertices **II** towards a single-vertex quasi-stable configuration **III**. Two vertices are removed from the system in the process, and the total length of the configuration is reduced. Axons preserve their identity in **III**. **b**: Topologically analogical process of loop removal in 2D foams. A triangular foam loop has curved walls to satisfy 120° angle condition at the vertices, **I**. Gas diffuses outwards from the bubble driving the collapse **II**, until the loop is completely removed **III**. The walls (films) completely merge and lose their initial identity (process is irreversible).

and all zipper angles have an incentive to increase. In addition, the velocity of advance is proportional to the deviation of current zipper angle β from the new equilibrium angle β_0, i.e. $|\vec{v}| \propto |\cos\beta_0/2 - \cos\beta/2|$. If the zippers advanced asynchronously, the departure from initial inner angle distribution would hinder the 'faster' zippers (whose angles grew larger ahead of others) and stimulate the 'slower' zippers (whose angles were compressed). This mechanism preserves the angle distribution in the loop largely stable during the collapse.

The zipper dynamics during loop collapse is different from the simple zipper dynamics described in section 3.5.5 and analysed in section 3.6.3. There, the zipper endpoints A, B and C are fixed (see fig. 3.31) and the zipper angle β gradually approaches the angle of equilibrium geometry β_0, which is not feasible during the loop collapse.

Axon loop collapse is also fundamentally different from similar collapse occurring in 2D foams (fig. 3.47b). The foam loop contracts into a single vertex in an irreversible manner, the foam walls irreversibly merge. The axons on contrary preserve their identity and reversal of the process is possible if axon tension is restored, as observed in the loop emergence/expansions process in fig. 3.11a.

Observed zippering dynamics, the dynamics resulting from manipulations, and model predictions, indicate that the transition initiated by sudden perturbation happens at the scale of 1 to 10 min. In contrast, the coarsening of the network has only gradual onset and develops over hours.

The values in fig. 3.42 indicate total length change around $\Delta\mathcal{L}$=100 µm, for roughly $\mathcal{V}$=75 vertices over 30 min. The upper bound on the number of active zippers[11] in the network can be obtained assuming that n zippers are active during a 10 min interval. They advance or recede with equal probability $P = 1/2$, at the typical average velocity $v \approx 1\ \frac{\mu m}{min}$, i.e. the network length changes as a random walk in n. Then, for an interval Δt=10 min, the change of network total length is $\Delta\mathcal{L} \approx \sqrt{n} v \Delta t \approx 30\,\mu m$ and so, even for unbiased system, for the typical observed rate of change in network total length $\Delta\mathcal{L} \approx 3\ \frac{\mu m}{min}$, 9 active zippers are sufficient, which amounts to roughly 15 % of vertices $\mathcal{V}$. Truly unbiased system would exhibit fluctuation of $\mathcal{L}$, while our observations show rather steady trends and low volatility. We therefore assume the fraction of active zippers is $\leq$15 %, and the system dynamics is mildly driven, without strong abrupt perturbations.

The observed separation of time scales (i.e. zippering and coarsening) rather suggests that the network is in the quasi-equilibrium state corresponding to the distribution of axon tension. Most of the vertices are either static, or fluctuate around their equilibrium position, while the proportion of zippers in transition (advancing or receding) is small. We will further assume, that the majority of the zippers have their zipper angle close to the equilibrium value given by the eq. (3.9).

3.9.2 Locally driven fasciculation

Throughout the observed network coarsening, manifested by decrease in total network length $\mathcal{L}$, implies that larger fascicles are gradually formed. While it is not possible to determine the number of axons forming particular bundle under the limitations of DIC microscope, the bundle structure (size) directly determines the bundle tension T (section 3.3.3), and is therefore reflected in the observed equilibrium zipper angle β, as indicated by eq. (3.9). We used the method presented in section 2.2.4, and semi-manually extracted the distribution of zipper vertex angles in the observed network at several time-points; distribution example is shown in fig. 3.44.

The typical shape of the extracted distribution was localised within the range 20°–120°, with mean around 55°–65°, see figs. 3.42 and 3.44. The mean angle $\bar{\beta}$ typically exhibited mild correlation with the total network length $\mathcal{L}$, as shown in fig. 3.45; coefficient of this correlation was usually around $\rho(\bar{\beta}, \mathcal{L}) \approx 0.5$. $\bar{\beta}$ is even more strongly correlated to other global network statistics like (i) number of loops $\rho(\bar{\beta}, \mathcal{C}) \approx 0.7$, and (ii) number of vertices $\rho(\bar{\beta}, \mathcal{V}) \approx 0.7$, see fig. 3.45. In the experiments entering a coarsening stage, the $\bar{\beta}$ tends to gradually decrease with the shortening of network total length $\mathcal{L}$ (fig. 3.42), in some cases by more than 10°, or roughly 15 %.

To quantify the relation between the decreasing $\mathcal{L}$, growing mean fascicle size n (through coarsening) and decreasing mean zipper vertex angle $\bar{\beta}$, we use the transfor-

[11] A symmetric zipper at the typical zipper angle β=52°, changes in length (overall shortening) for a zipper advance δx approximately as $-2\delta x \cos(26°) + \delta x \approx -\delta x$.

mation eq. (2.6), which is a population generalisation of eq. (3.9). The eq. (2.6) allows us to transform the distribution of tensions $p(T)$ into a model-predicted distribution of zipper angles $q(\beta)$ in axonal network equilibrated according to eq. (3.9). This requires to make preliminary assumptions on T and S, particularly their scaling rules as axons bundle.

Assumption 1. *The distribution of tension in individual axons in culture matches the estimated tension distribution from the BFP experiments $PDF_{exp}(T)$ (section 3.4.2 and figs. 3.20 and 3.21).*

Assumption 2. *The distribution of tension in zipper-forming axons is not altered by the bundling process. The distribution of tension of a bundle of axons (e.g. axons* 1 *and* 2*, $PDF(T_{1+2})$) can be treated as a distribution of sum of independent random variables ($PDF(T_1 + T_2)$). Therefore, the mean of fascicle tension distribution scales as $\bar{T} \sim n$ and its standard deviation as $\sigma(T) \sim \sqrt{n}$ (section 3.3.2).*

Assumption 3. *The adhesion parameter S between two filaments scales with their contact area and therefore the filament surface. The adhesion between fascicles of n axons would scale as $S \sim \sqrt{n}$ (section 3.3.2).*

To make a quantitative assessment of the change of $q(\beta)$ with increase of mean fascicle size n, we supplement assumptions 1 to 3 with two simplifications:

(i) the experimental tension distribution for mean bundle size n, $\mathrm{PDF}(T;n)$, was replaced by a lognormal distribution

$$\begin{aligned}\mathrm{PDF}(T,n) &\approx \underbrace{\mathrm{PDF}(\bar{T}_{\mathrm{BFP}},\sigma_{\mathrm{BFP}}) \star \ldots \star \mathrm{PDF}(\bar{T}_{\mathrm{BFP}},\sigma_{\mathrm{BFP}})}_{n\text{-fold convolution}} \approx \\ &\approx \mathrm{PDF}_{\log}(n\bar{T}_{\mathrm{BFP}}, \sqrt{n}\sigma_{\mathrm{BFP}}) \approx \mathrm{PDF}_{\log}(\bar{T}, \sigma(T)),\end{aligned}$$

so that the tension distribution $p(T;n) \equiv \mathrm{PDF}_{\log}(n\bar{T}_{\mathrm{BFP}}, \sqrt{n}\sigma_{\mathrm{BFP}})$[12], with experimental mean $\bar{T}_{\mathrm{BFP}}$=0.69 nN and standard deviation σ_{BFP}=0.25 nN; and

(ii) the possible variance of S was ignored, and only a single value (rescaled with mean bundle size n) was used.

Combining the assumptions 1 to 3 and items (i) and (ii) with eq. (2.6), the predicted distribution of zipper angles $q(\beta) \equiv \mathrm{PDF}(\beta;n)$ is given by the value of n, which scales the implicit biophysical parameters ($\bar{T} = n\bar{T}_{\mathrm{BFP}}$, $\sigma(T) = \sqrt{n} \cdot \sigma_{\mathrm{BFP}}$ and $S = \sqrt{n} \cdot 0.17\,\mathrm{nN}$), as explained in section 2.6.2.

The results of the quantitative analysis are shown in fig. 3.48. The distribution of angles of the example from fig. 3.1 (but not presented in section 3.8.1) is shown in fig. 3.48a. Consistently with fig. 3.44b, the angle distribution of a culture in coarsening stage moves towards lower values. As shown in fig. 3.48b, the trendline estimates decrease in median angle β_M during coarsening by 7.7°, with correlation coefficient $\rho(\beta_M, \mathcal{L}) = 0.6$. The change is consistent with typical angle change shown in figs. 3.42 and 3.44.

[12] We numerically verified, that the lognormal approximation of tension distribution for fascicles $n \geq 2$ closely corresponds to the tension distribution obtained by n-fold convolution of $\mathrm{PDF}_{\exp}(T_{\mathrm{BFP}})$.

Using eq. (2.6) method with $\mathrm{PDF}_{\log}(\bar{T}_{\mathrm{BFP}}, \sigma_{\mathrm{BFP}})$, and initial adhesion coefficient 0.17 nN, to match initial experimental β_M=59.3°, we constructed initial distribution of angles, the orange line in fig. 3.48c. Initially, the mean number of axons in a bundle is set to $n = 1$, even though the choice is arbitrary, because the scaling of biophysical parameters depends on the scaling of n, not its actual value.

During the experiment, measured total length drops from $\mathcal{L}|_{0\,\mathrm{min}}$=758 µm to $\mathcal{L}|_{178\,\mathrm{min}}$=495 µm, reduced by factor of $^2/_3$. We assume the axons are conserved, i.e. they are not removed, but fasciculate with other bundles, and so

$$\mathcal{L}_1 n_1 = \mathcal{L}_2 n_2. \tag{3.61}$$

Therefore, the mean number of axons in the presented experiments increases by factor $n = {}^3/_2$ and so $\bar{T} = {}^3/_2\bar{T}_{\mathrm{BFP}}$, $\sigma(T) = \sqrt{{}^3/_2}\,\sigma_{\mathrm{BFP}}$ and $S = \sqrt{{}^3/_2} \cdot 0.17\,\mathrm{nN}$. Combining the scaled values with the eq. (2.6), we obtained the green line in fig. 3.48c. The median value of the constructed distribution, β_M=52.9° is 6.4° lower that the for the initial distribution, which is in a good agreement with the trendline-predicted decrease of 7.7° (see fig. 3.48b).

We applied the same analysis to the (coarsening stage of) experiment presented in fig. 3.48b, where a trendline indicated angle decrease of 11.9° and increase in n by a factor of 1.6. Adapting initial tension to 0.66 nN to meet the initial median angle β_M, with S=0.17 nN, the procedure predicted an angle change of 9.1°, which supports consistency of the method with experimental data.

To illustrate the effect of increasing tension, presumably driven by coarsening, we constructed predicted distributions of angles $\mathrm{PDF}(\beta; n)$ in fig. 3.48d. The orange line represents $\mathrm{PDF}(\beta; 1)$, the parameters are those obtained from BFP experiments, with S=0.17 nN. The median angle is 59.3°. As the mean number of axons in bundle doubles, $n = 2$, the angle distribution $\mathrm{PDF}(\beta; 2)$ corresponds to the blue line (scaled values of biophysical parameters shown in the legend) and β_M=49.0°, the distribution becomes leaner. If the mean bundle size triples, $n = 3$, the distribution $\mathrm{PDF}(\beta; 3)$, drawn in red, becomes even more narrow, and β_M=44.0°. Note however, that all the distributions are negligible below β=30°, consistently with the experimental observations shown in figs. 3.44 and 3.48a. Therefore, as coarsening progresses and the tension in the bundles gradually increases, the distribution of angles in the network tends to move towards smaller angles and its variance decreases. At the same time, the distribution appears to remain very low below the $\beta \leq 30°$ threshold.

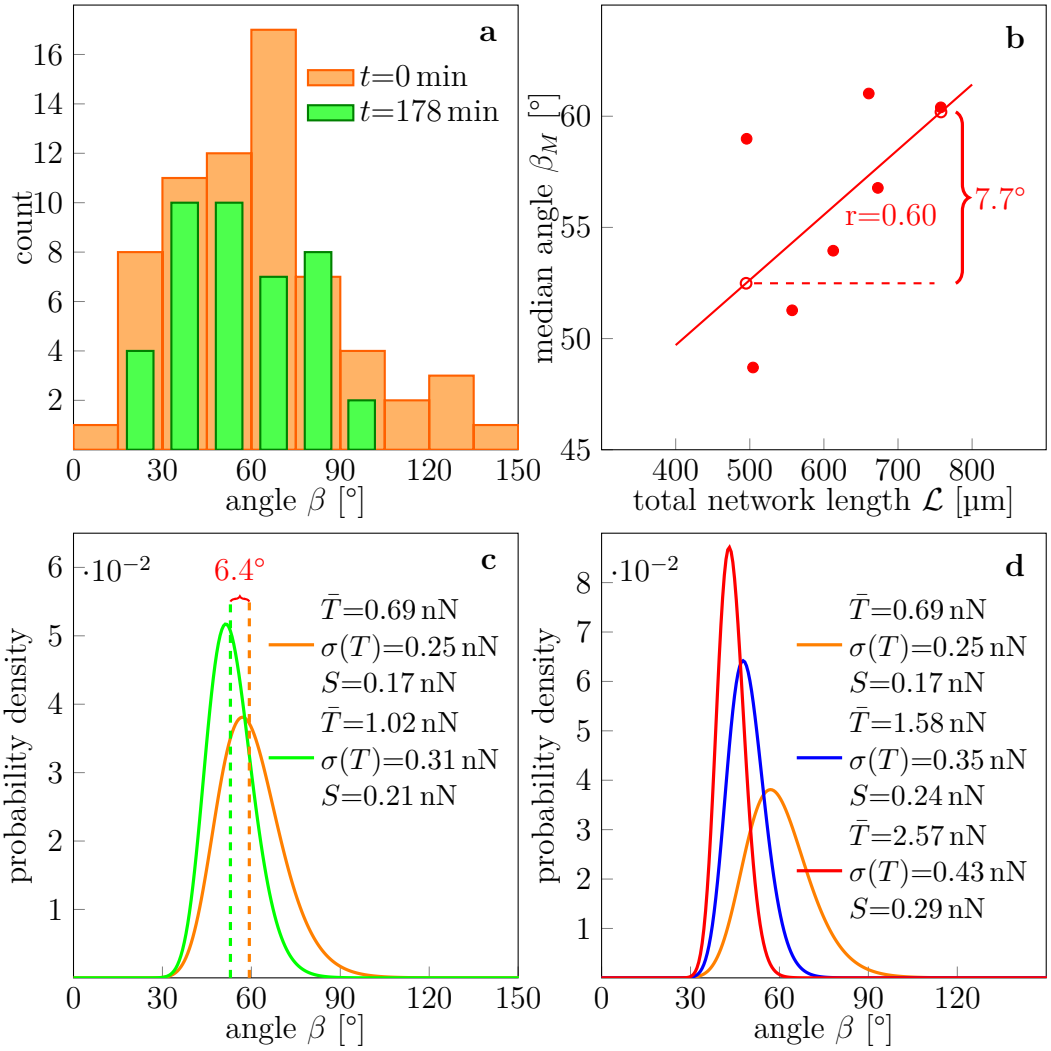

Figure 3.48: Quantitative analysis of relation between PDF(β) and PDF(T) of population of axons in a network, under the assumption that coarsening leads to increase in mean bundle size n and scaling of tension T. **a**: Change of histogram of zipper angles in a coarsening network. The number of vertices is reduced and the distribution shifts towards smaller angle values. **b**: Correlation between the network total length $\mathcal{L}$ and median angle β_M, $\rho(\mathcal{L}, \beta_M)$=0.6, the measured data points are drawn as red dots, the correlation trendline is drawn in red. The change in angle during the coarsening given by the trendline, 7.7°, is indicated. **c**: Comparison of distributions of tension PDF$(\beta; n)$ predicted using eq. (2.6) with PDF$_{\log}(n\bar{T}_{\mathrm{BFP}}, \sqrt{n}\sigma_{\mathrm{BFP}})$ and S=0.17 nN. The orange line corresponds to PDF$(\beta; 1)$, i.e. $n = 1$, the green line to PDF$(\beta; 1.5)$, i.e. $n = 3/2$. The trend and position of model-predicted distributions can be directly compared to the corresponding histograms (identified by the same colour code) in **a**. **d**: Change of predicted PDF$(\beta; n)$ for growing mean bundle size $n = 1, 2, 3$, corresponding to orange, blue and red line respectively. The distribution becomes more narrow and shifts towards smaller values, while it does not visibly extend beyond the 30° mark.

3.9.3 Structure of sensory neurite plexus in *Xenopus* embryo

The dynamical *ex vivo* observation of axonal network presented in the section 3.9.2 bear many similarities to *in vivo* observations of Roberts and Taylor in (Roberts and J. S. H. Taylor 1982), who studied the formation of the sensory neurite plexus on the basal lamina of trunk skin in *Xenopus* embryos. Using SEM at magnifications 1000–2500 ×, they recorded neurite network on the trunk and the inside skin surface, and quantified the angles under which the neurites fasciculated or crossed, so-called 'incidence angles', β_{inc}.

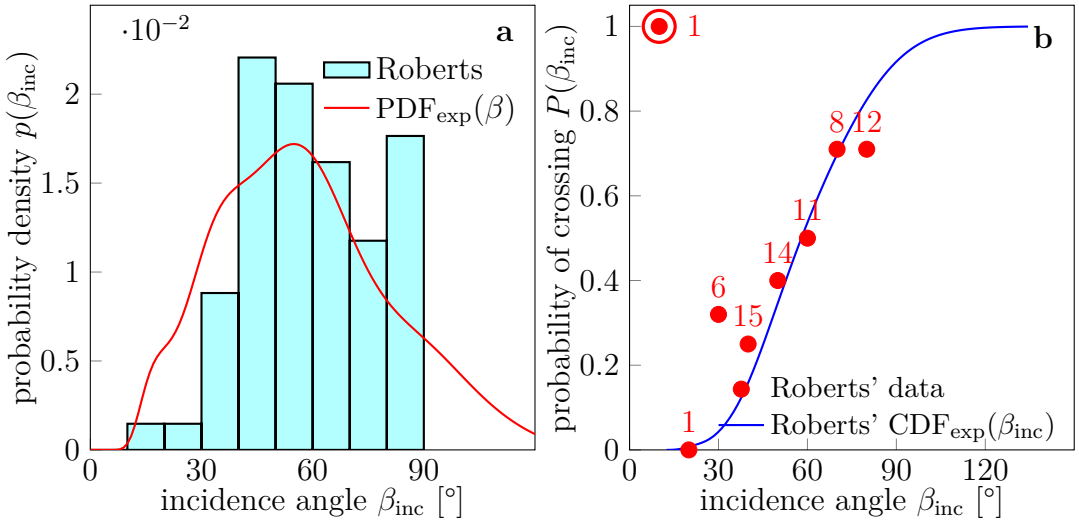

Figure 3.49: Original data of (Roberts and J. S. H. Taylor 1982) and their comparison with predictions of our model. **a**: The (renormalised) histogram illustrates probability density $p(\beta_{\text{inc}})$ of incidence angles β_{inc} to belong to particular 10° range. It is compared to the $\text{PDF}_{\text{exp}}(\beta)$ (red line) we obtained from our experiment (figs. 3.1 and 3.48a). **b**: Red dots illustrate observed probability of neurite crossing for the given 10° angle bin $P(\beta_{\text{inc}})$, reported in (Roberts and J. S. H. Taylor 1982). The numbers near the dots indicate the number of observed events in the particular bin. A sole outlier in the first bin is marked by the red ring. The data are compared to the $\text{CDF}_{\text{exp}}(\beta_{\text{inc}})$ of angle distribution observed by Roberts and Taylor (i.e. the histogram in **a**).

The data obtained in (ibid.) are shown in form of a (renormalised) histogram in fig. 3.49a, and compared to a typical distribution of zipper angles we observe in our network $\text{PDF}_{\text{exp}}(\beta)$, shown in red. The two cases have many similarities: (i) they reach maxima around 50°–60°; (ii) angles below 30° are under-represented (see also figs. 3.44 and 3.48). Which is in contrast with the expectation, that the distribution of angles in an isotropically growing (non-interacting) network would be uniform; the distribution would be even expected to over-represent lower angles, if it grows in a preferred direction.

Roberts and Taylor therefore proposed a mechanism of neurite shaft adjustment after

initial encounter (section 1.1.6), which is driven by the contact adhesive interaction, analogous to the zippering processes directly observed in our experiments. Such local adjustment would tend to remove small angles as well as the large angles (in specific situations) as illustrated in fig. 3.50.

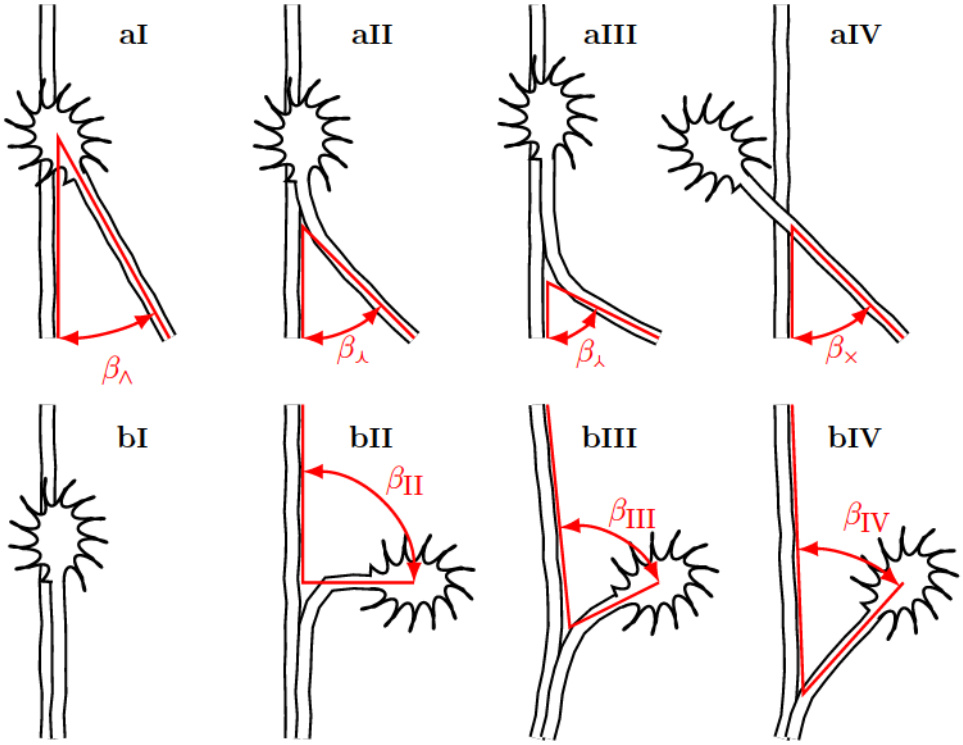

Figure 3.50: **a**: Encounter of a GC and AS. Growing GC stochastically approaches an AS of another axon **I**, and starts to follow it **II**, if their mutual affinity overcomes GC-substrate affinity. Once initial adhesive contact is established, is tends to spread, driven by the adhesion of shafts, and the segment of mutual contact expands **III**, which increases the incidence angle, $\beta_\wedge < \beta_\lambda$. If the mutual affinity of the neurites falls short of the substrate affinity, the axons cross, **IV**. **b**: An axon leaves a fascicle **I**, **II** and creates a separation angle at the vertex β_{II}. An imbalance at the vertex leads to initial vertex transition (without zippering) **III** and decrease of angle $\beta_{III} < \beta_{II}$. In the next stage, the shafts gradually reduce the length of mutual contact, until the separation angle $\beta_{IV} < \beta_{III}$ corresponds to the static equilibrium angle of the two axons.

In the situation when axons grow in a preferred direction[13] (particularly during developmental stage), a GC of one axon commonly encounters AS of another axon (fig. 3.50aI) under small angle $\beta_\wedge$. If GC affinity to the AS is sufficient (stronger than to the substrate), it starts to follow the AS (fig. 3.50aII) and forms a short initial segment of adhesion. This segment then expands under the effect of contact adhesive forces, and

[13]This is the case for observations in (Roberts and J. S. H. Taylor 1982) as well as in our experiemnts.

the incidence angle increases, $\beta_{\wedge}<\beta_{\curlywedge}$, as shown in fig. 3.50aIII, until it reaches the equilibrium zipper angle. If the GC-AS affinity is lower than GC's affinity to the substrate, the axons will cross (fig. 3.50aIV) and no segment of adhesion is formed. As Roberts and Taylor remarked, the GC preference for fasciculation depends on the surface available on the AS at the time of encounter, and is therefore higher for small angles; such zippering preference for small angles further drives small angle removal.

In the opposite process, a GC may leave a fascicle (fig. 3.50bI-II) under angle β_{II}. The traction force generated by the GC then increases tension in the AS and creates a force imbalance at the vertex point (point of separation). Such imbalance leads to lateral adjustment of the vertex position (fig. 3.50bIII), which decreases the angle at the vertex $\beta_{\mathrm{III}}<\beta_{\mathrm{II}}$. A slower adjustment then follows and the adhered segment length is reduced, to restore the force balance (fig. 3.50bIV), decreasing the angle towards the equilibrium angle, $\beta_{\mathrm{IV}}<\beta_{\mathrm{III}}$. This process thus drives removal of large angles.

Such mechanism is consistent with our observations of zippering dynamics and with our biophysical model of basic zipper (sections 3.5.1 and 3.5.5). Note, that it is usually not possible to distinguish incidence and separation angles, which however does not affect the implications for our model, because both processes (figs. 3.50a and 3.50b) are governed by the same biophysical mechanism. The proposal of (Roberts and J. S. H. Taylor 1982) also suggests that zippering should be more prominent in the network, which contains extremal angle values ($\leq 30°$, distant from typical equilibrium). Those values are however under-represented in our data (figs. 3.44 and 3.48), which supports our inference that most of the zippers are close to local static equilibrium during the development of the network.

The study of the SEM data in (ibid.) also evaluated probability of crossing of two neurites as a function of their incidence angle, $P(\beta_{\mathrm{inc}})$. The measured relationship data are shown as the red dots in fig. 3.49b, the probability of crossing was evaluated on 10° bin basis. It is evident that the probability increases with the angle, as the authors argued (i.e. smaller incidence angles imply higher inter-neurite affinity).

We sought to quantitatively explain the dependence $P(\beta_{\mathrm{inc}})$ within our zippering framework (section 3.5.1). We start with two arguments:

(1) Our model predicts, that two axons will not fasciculate (zipper) if their incidence angle exceeds their equilibrium angle, i.e. $\beta_{\mathrm{inc}}>\beta_{\mathrm{eq}}$. This is obvious, as zippering an only increase vertex angle towards equilibrium; at the same time, exceeding the equilibrium angle generates an unzippering net force. In such situation, only stable configuration is crossing (fig. 3.50aIV).

(2) As we have argued earlier, the majority of network zippers is in the state of equilibrium, or very close to it. Therefore, distribution of incidence angles in a network $\mathrm{PDF}_{\mathrm{exp}}(\beta_{\mathrm{inc}})$ largely corresponds to the ideal distribution of equilibrium angles $\mathrm{PDF}(\beta_{\mathrm{eq}})$. Therefore, on a population level (complementary to item (1)), any given pair of axons will cross with the probability that their equilibrium angle β_{eq} is smaller than their incidence angle $\Pi(\beta_{\mathrm{inc}} < \beta_{\mathrm{eq}})$, with β_{eq} given by the $\mathrm{PDF}(\beta_{\mathrm{eq}})\approx\mathrm{PDF}_{\mathrm{exp}}(\beta_{\mathrm{inc}})$.

Therefore, the probability of crossing $P(\beta_{\mathrm{inc}})$ is equivalent to the probability $\Pi(\beta_{\mathrm{inc}} < \beta_{\mathrm{eq}})$, which is given by the cumulative distribution function $\mathrm{CDF}(\beta_{\mathrm{eq}}=\beta_{\mathrm{inc}})\approx\mathrm{CDF}_{\mathrm{exp}}(\beta_{\mathrm{inc}})$

of $\mathrm{PDF}_{\mathrm{exp}}(\beta_{\mathrm{inc}})$ for the given value of incidence angle. This $\mathrm{CDF}_{\mathrm{exp}}(\beta_{\mathrm{inc}})$ was calculated using the data of (Roberts and J. S. H. Taylor 1982) ($\mathrm{PDF}_{\mathrm{exp}}(\beta_{\mathrm{inc}})$, histogram in fig. 3.49a) and is shown in fig. 3.49b as the blue curve. We can see a good agreement between the experimental observation of probability of crossing (red dots) and our model estimate, i.e. $P(\beta_{\mathrm{inc}}) \approx \mathrm{CDF}_{\mathrm{exp}}(\beta_{\mathrm{inc}})$. This illustrates, that our framework is not limited to dynamics of culture, but can be also successfully applied to a developing axonal networks *in vivo*.

3.10 Two-dimensional foams

Topologically, the structure of the axon network observed in our experiments is similar to the structure of a 2D liquid foams with low liquid fraction (introduced in section 1.7). The structures are compared in fig. 3.51. A typical experimental realisation of 2D liquid foam is depicted in fig. 3.51a, obtained by constraining a foam between two closely position glass plates. It can be compared to the structure of axonal network (figs. 3.46a and 3.51b), where axons were highlighted by the red line (other filaments were excluded as non-axonal side processes). The structures are geometrically different (i.e. angles, loop shapes), but share some topological properties, which can be more easily identified in figs. 3.51c and 3.51d.

In figs. 3.51c and 3.51d, the two structures are represented as graphs composed of edges and vertices. In foams, each stable vertex is formed by exactly 3 edges (i.e. vertex of degree 3); these edges are formed by films of equal surface tension, therefore, they must converge at angles 120° to satisfy force balance (see Plateau laws in section 1.7.1). In axons, most of the vertices are also formed by 3 edges—as a structure of two axons forming a zipper. The tension in individual axons is generally not equal, and the tension in the zippered segment is a sum of individual tensions reduced by the adhesive interaction (eq. (3.9)). The angles at the zipper vertex are therefore generally unequal.

In addition, vertices in the axonal network are not restricted to the degree 3. Metastable configurations (lasting for tens of minutes) are sometimes formed and observed:

(1) crossings (fig. 3.50aIV) are vertices of degree 4 and turn into a pair of degree 3 vertices, if tension decreases;
(2) vertices of higher degree (≥ 3) are formed when several zippers stop at the same point, the edges eventually fasciculate as tension decreases;
(3) self-loops can be formed when an axon leaves a bundle and rejoins it later, supported by locally increased substrate adhesion; they tend to collapse when tension increases.

The network graph shown in figs. 3.51c and 3.51d consist only of closed loops (cycles), boundary of the set of cycles is drawn in green. In the axonal network, the loops are formed by axons or axon bundles, and are topological equivalent of the foam bubbles.

In sections 1.7.2 and 1.7.3 and figs. 1.18b and 1.19, we explained that, on average, foam bubbles of less than 6 sides curve under excessive inner pressure, contract and vanish through outwards air diffusion; in the topological process *T2* (see also fig. 3.47b). Axons also form curved edges, but such curvature is supported by local substrate ad-

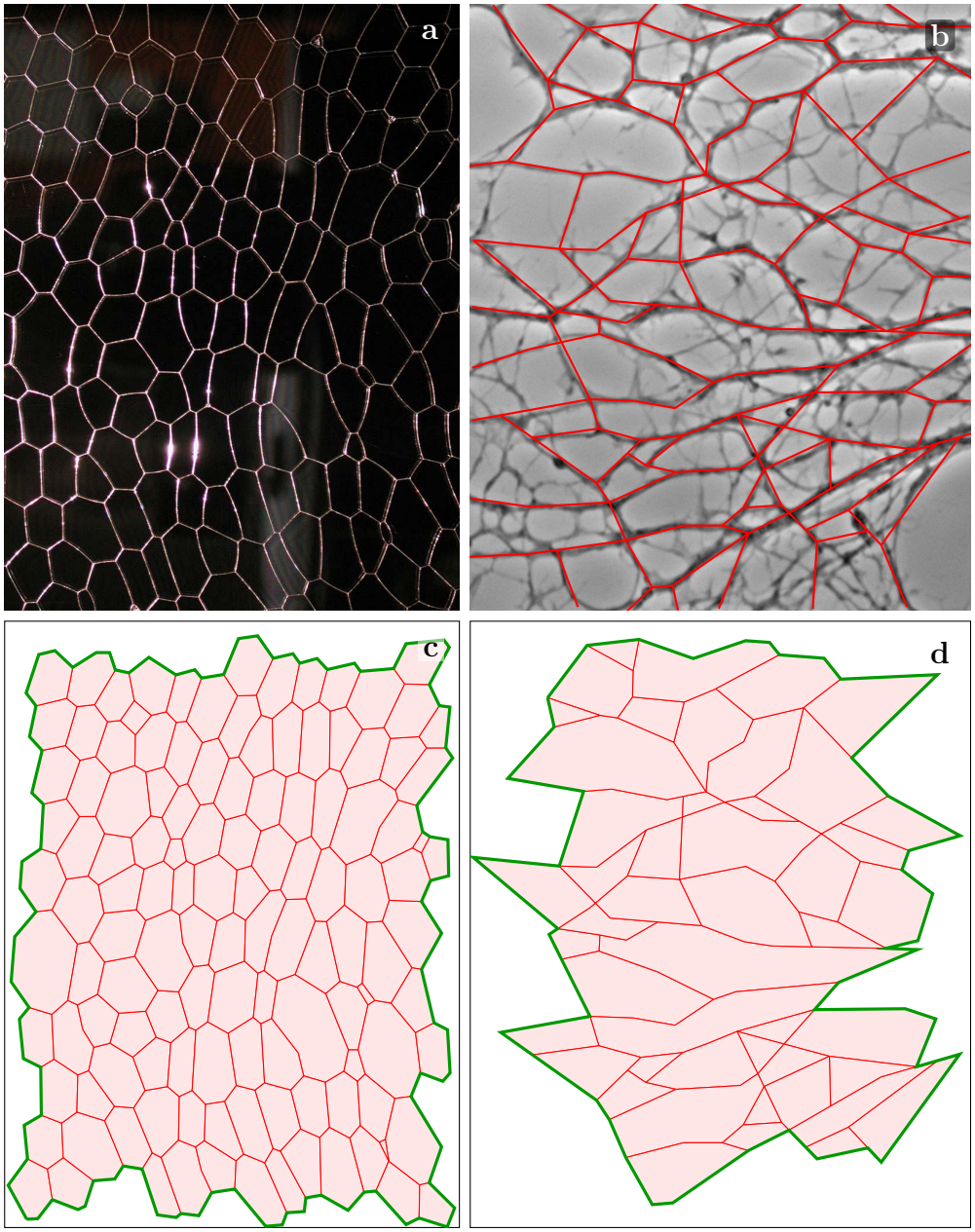

Figure 3.51: Illustration of topological similarity between foams (froths) and the axonal network. **a**: A two-dimensional soap foam obtained by enclosing a foam between two glass plates of small separation. Courtesy (Keller 2002). **b**: A typical axonal network, axons are highlighted by red line, other filaments were excluded as non-axonal processes. **c**: Graph representation of the foam of panel **a**. Only contiguous set of closed loops was kept, remaining edges were pruned. **d**: Graph representation of axonal network of panel **c**; also consists only of closed loops.

hesion (cf. item (3)), rather than internal air pressure. The coarsening of the axonal network is therefore not driven by pressure differences, however the observed shrinking and disappearance of triangular loops (fig. 3.47a) is a topological analogue of the *T2* process (cf. fig. 3.47b).

Another topological process, *T1*, makes a conformational change in the foam (section 1.7.2 and figs. 1.18a and 3.52a), where two neighbouring bubbles ($\mathcal{A}$, $\mathcal{B}$ in fig. 3.52aI) are pushed apart and separated by other bubbles forming a new wall ($\mathcal{C}$, $\mathcal{D}$ in fig. 3.52bII). Notice that *T1* process does not change the network length neither the number of vertices, once the equilibrium is restored.

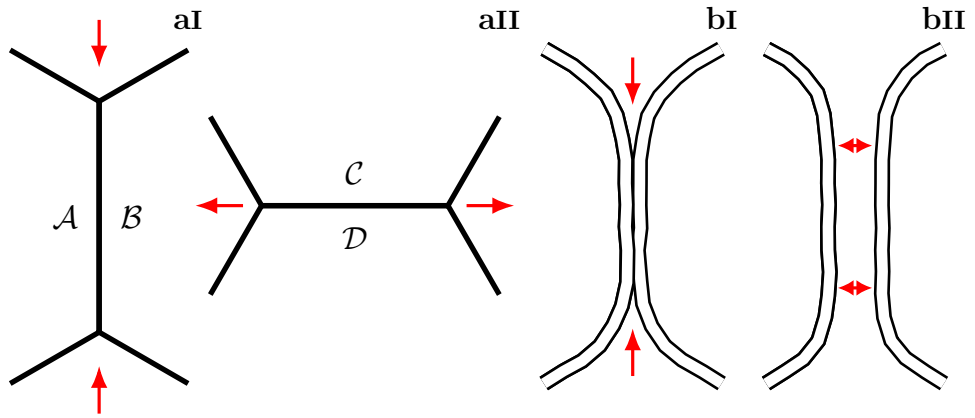

Figure 3.52: **a**: Illustration of *T1* process in foams. The bubbles $\mathcal{A}$ and $\mathcal{B}$ are pushed apart **I**, and a new wall is formed in place **II** between other two bubbles $\mathcal{C}$ and $\mathcal{D}$. **b**: Attempted *T1* process for zippered axons. The separation commences **I**, but as the zippered segment diminishes, a new wall cannot be established, and a wall rupture occurs **II**.

As illustrated in fig. 3.52b, the formation of a new wall in not possible in *T1* analogue in axonal network. After the adhered segment is reduced to zero, the axons separate, such process is occasionally observed in experiments. Therefore, a *T1* analogue does not exist in axonal network; it is effectively replaced by another topological process (also known in foams), a wall rupture. The process as described in fig. 3.52b leads to increase in network length (adhered segment separates to two) and removal of two vertices (unlike true *T1* process); this implies the process is not frequent in a coarsening axonal network, as the total length and the number of vertices are strongly correlated (see fig. 3.45).

Combination of the processes *T1* and *T2* drives indefinite coarsening of a foam, with similar effects obtained in axonal network through *T2* analogue combined with the wall rupture process. It seems obvious that axon networks also posses some of the properties of more complex wet foams. If fraction of liquid is slightly increased to create a dry (but not ideal) foam, the equilibrium Plateau laws (section 1.7.2) remain valid, allowing to treat dry foams as ideal foams. However adding more liquid makes Plateau laws less respected, allowing for instance formation of stable vertex of degree four. This

may suggest that also the axonal network may exhibit increased topological stability as compared to idealised two-dimensional foam.

The independence on supportive pressure (and volatility caused by its diffusion) gives loops of axonal network more robust stability. While the coefficient of variation of average loop area $\langle a \rangle$ of the typical foam shown in figs. 3.51a and 3.51c is $\frac{\sigma(a)}{\langle a \rangle} \approx 0.4$, the same statistical descriptor is typically $\frac{\sigma(a)}{\langle a \rangle} \gtrsim 1$ in axonal network. This shows (consistently with impression given by fig. 3.51d) that axonal network dynamics can support much wider variability of loop sizes.

In a series of observations, we noticed the following differences in network descriptors (foam data were extracted from fig. 3.51c):

(1) As expected for a liquid foam, the average angle was 120°, while in the axonal network, the typical zipper angle is 55°–65°. Of course, non-zipper angles at the vertices can be much higher than 60°.

(2) The anisotropy of the liquid foam was lower, at 0.45, than typical anisotropy in axonal network, 0.55–0.6. This can be explained by the fact that the axons grow radially from the explant, and therefore tend to be locally more aligned along the radial direction (as confirmed by director). The foam edges were aligned normally to the presumed direction of gravity.

(3) The alignment and smaller (zipper) angles at the vertices tend to flatten the loops in axonal network (recall Roberts observation that smaller angles promote fasciculation), their typical circularity is around 0.55 as compared to rather circular loops in the foam at 0.8.

(4) The average number of vertices in a loop in the foam was nearly 6, which is the stable bubble configuration. In the axonal network, the average number of vertices in a loop was, surprisingly consistently across experiments, very close to 4.5.

All these observations suggest that, compared to liquid foams, the loops of axonal network are more elongated, aligned and have smaller inner angles—stability condition of 120° vertex angle is loosely replaced by zipper equilibrium angle $\beta_{\mathrm{eq}} \approx 60°$, even though not all loop inner angles are the zipper angles. The axons are not under internal gas pressure, and therefore are less constrained and can form turning edges even without an intermediate vertex. Therefore, the small angles at the zipper vertices are compensated by vertex-less turns of elongated edges, which allows those loops to be closed and stable with fewer vertices, than would be necessary for a stable foam bubble.

The predominant degree of vertex in axonal networks is still three. If we consider that Euler's theorem and so eq. (1.20) is approximately valid, then the lower number of edges per loop consequently means more loops will be formed for the same amount of edges. For the same amount of edges/vertices, the axonal network will be fragmented into more loops than an ideal foam would be.

The expansion or contraction of loops in axonal network (fig. 3.47a) can result from the zipper angles at the loop vertices being smaller or larger than the equilibrium zipper

angles respectively (see section 3.9.1). Such behaviour was repeatedly demonstrated in the experiments, where the equilibrium angle was modified by (i) generated pull (figs. 3.9 to 3.11), or (ii) lowering of tension (fig. 3.12). The presumed equilibrium zipper angle is around 50°–60°, the triangular loops (with average inner angle 60°) are therefore close to equilibrium, and would contract or expand only very slowly, unless an adjustment of tension changes equilibrium angle. On contrary, rectangular (and >4-gonal) loops would have larger average inner angles, and would be therefore unstable towards expansion.

Such predictions are expected to be true for simple vertices of individual axons at the early stage of coarsening. The progressing fasciculation can lead to creation of entangled zippers or other more complex structures, which can hinder otherwise unopposed coarsening. Our preliminary data analysis suggests, that during coarsening stage, the average loop area is roughly linearly proportional to elapsed time, i.e. $\langle a \rangle \propto t$; the same scaling is predicted for liquid foams with small liquid fraction. We however acknowledge that the observed range of time scale is too short to make conclusions about the coarsening power law. Nevertheless, these observations show, that despite distinct realisations, the zippering axon network presents a remarkable example of an *ex vivo* system exhibiting topological and dynamical analogies to froths.

Chapter 4

Discussion

4.1 Axon-axon interactions in explant culture

4.1.1 The new role of contact interaction of axon shafts

Axon fasciculation during development was previously studied on the basis of GC-mediated interaction. The GCs may adhere to the neighbouring axons and drive fasciculation and formation of larger bundles of axons, or they may separate from such bundles and drive defasciculation. Both processes are based on the GC motility and mostly controlled by external cues (e.g. chemotaxis or mechanotaxis). In this work, we gathered evidence, that an additional mechanism is involved, which may play an important role in regulating axon fasciculation. This novel mechanism does not involve GCs, but is specific to ASs, it arises from local contacts of ASs and drives zippering or unzippering of individual axons or small bundles of axons. Such mechanisms allowed axons of our culture system to reorganise and substantially change the structure of the outgrown network, without participation of GCs, over the time scale of 10 h. It also enables the axonal network to flexibly respond to mechanical or biochemical perturbations (e.g. remote GC activity, external force, effects of GCMs), and gradually propagate changes resulting from such perturbations (e.g. AS deformation, stretching, increase in tension) in one area of the network across a broader region (figs. 3.9 and 3.10). The described processes were not studied in detail in previous works. To our knowledge, axon zippering was only inferred from SEM imagery to occur *in vivo* by (Roberts and J. S. H. Taylor 1982), and observed for axons in culture in (Barry et al. 2010; Voyiadjis et al. 2011) as part of general fasciculation process. In this work, we characterised axon zippering and unzippering, described and modelled its dynamics, and discussed its significance for network dynamics. We will discuss its possible biological significance later in this section.

4.2 Zippering processes

4.2.1 Adhesion and tension in equlibrated vertices

We combined experimental observations with biophysical modelling and showed that the zippering processes are a result of competition between adhesive contact interaction of axon shafts and axial mechanical tension within individual axons. The adhesive force

acts to expand the mutual contact of the axons, while the tensile force tends to minimise the axon total length, countering the adhesion, and promoting unzippering. Competition of the two forces can reach static equilibrium for two axons, their relative strength then determines the separation angle at the zipper vertex, as formulated in hypothesis 1. In this hypothesis, we neglected effects of elastic bending, as justified in fig. 3.24. To estimate the involved forces, we used BFP technique to measure the mechanical tension of the OSN axons grown *ex vivo*, with results around 700 pN, in the interquartile range (531–861) pN. Such results were comparable with results reported in previous literature for PC-12 neurites grown in culture (Dennerll, Joshi, et al. 1988).

We then combined this measurement with measurements of typical static zipper vertex angles, and using multiple methods estimated the adhesion force at the level around 100 pN. Which is, to our knowledge, first such estimate for any system. This value can be combined with information about apparent axon shape at mutual contact obtained from SEM imagery (fig. 3.6) to estimate adhesion energy density per membrane unit area. Such estimates were at the order of magnitude agreement with the measurement performed for E-cadherin mediated cell-cell adhesion in (Chu, Thomas, et al. 2004), around $10^{-6}\,\frac{\mathrm{nJ}}{\mu\mathrm{m}^2}$.

While the technique used to measure the axon tension, BFP, is well established (introduced in (Evans, Ritchie, and Merkel 1995)) and accurate (measurement imprecision estimated in the Methodology, see also (Simson et al. 1998)), the procedure of sample preparation (i.e. biotinylation) might influence the axon mechanical properties. It would be beneficial to perform the measurements using another method to verify the results. Choice of such method is however difficult, as the other bead-based methods (e.g. optical or magnetic tweezers) would also require biotinylation, and one may expect that the direct manipulation methods (e.g. AFM, MN) would probably (i) damage the very thin OSN axons, or (ii) interact with the substrate. We attempted to perform manipulations using optical tweezers (Pacoret et al. 2009), however the setup was not capable of exerting a sufficient force to displace the axon. In other cases, the trapped bead would tend to move over the axon and escape from the trap.

4.2.2 Vertex transition and dissipative forces

The zipper model of hypothesis 1 could be directly verified, if one could apply a calibrated force nearby a zipper vertex and observe unzippering. Unfortunately, we were not able to control the bead distribution in the BFP experiments, and of the several attempts we made nearby a vertex, none yielded reliable results. To circumvent this difficulty, we performed the series of pharmacological treatments to modify the axon biophysical properties in the network globally and observe the induced geometrical changes; the results were consistent with the model on qualitative level, as discussed in section 4.4.2.

While the calibrated manipulation was not feasible, we were able to reproducibly induce unzippering by an uncalibrated axon manipulation using micropipette. After the pipette was removed from the system, the zipper resumed to its original equilibrium geometry. Analysing data from such processes in the framework of our model allowed us to make an independent dynamical estimate of tension and adhesion between the axons.

These results were consistent with the estimates obtained from static vertex equilibria. From these uncalibrated experiments, we were also able to estimate vertex-localised friction coefficient at the level $\sim 1 \frac{\mathrm{nN\,s}}{\mu\mathrm{m}}$. This can be compared with the effective viscoelastic friction coefficient, $\sim 0.1 \frac{\mathrm{nN\,s}}{\mu\mathrm{m}}$, estimated for axon relaxation during a small deflection (i.e. deflection $\ll$ axon length), which does not involve zippering. Such order of magnitude disproportion of friction coefficients implies similar disproportion of corresponding friction forces during typical zippering, and indicates, that the vertex-localised dissipation dominates in the zippering dynamics over other types of dissipation.

The latest observation was supported by the vertex trajectory predictions of our model. To imitate the characteristic vertex transition as observed in the uncalibrated manipulation, the vertex-localised dissipation has to be the dominant dissipative mechanism of the model. Such trajectory cannot be obtained by any combination of other types of dissipative forces. Based on these experiments, we were able to predict energy dissipation rate within the advancing zipper, $\sim 10^{-7} \frac{\mathrm{nJ}}{\mathrm{min}}$, which is consistent with predictions based on the typical values measured in static situations and the observed velocities.

4.2.3 Differential adhesion

In previous works on axon fasciculation, the process was often introduced in terms of differential adhesion, that is, a GC would experience stronger adhesion to another axon than to the environment (Acheson et al. 1991; Roberts and J. S. H. Taylor 1982); it could also exhibit variable affinity to many types of axons, based on their surface CAMs composition or level of expression (cf. sections 1.2 and 1.5). While we observe axon preference to grow on other axons in our system (fig. 3.6), for the zippering process, this assumption is not necessary. Individual axons or small bundles can undergo zippering and decrease the system energy without losing contact with the substrate (which would lead to energy increase). We did not include any of the axon rearrangement processes (i.e. within the bundle, or losing substrate contact) in our model.

4.3 Modelling of axon interactions

The biophysical model we developed to describe the local contact interactions represents the first systematic characterisation of statics (sections 3.5.1 and 3.6.1) and dynamics (sections 3.5.5 and 3.6.5) of individual axon zippers. While both aspects (i.e. static and dynamic) of the model are based on the mechanical energy of the system (i.e. tensile and adhesion energy), the static model is constrained to a vicinity of a single point of the energy landscape, the minimum, and its structure is therefore very simple. On contrary, the dynamical model is not restricted to the static equilibrium; it allows us to understand the effects of time scale of perturbations of conservative forces, and provides insight into the complex interplay of dissipative forces (section 3.7.2) and distinct characteristics of vertex trajectories (section 3.7.3).

4.3.1 Relevance of biophysical model predictions

We extensively explored the mathematical structure of the model (section 3.7) and showed, that the vertex trajectory is determined in a complex way (section 3.7.3). While any change of adhesion or tension defines new energy potential and the location of the new unique equilibrium, the vertex transition trajectory is far from determined by the energy landscape alone.

(1) The transition depends on the time scale of perturbation. If perturbation is very rapid, the energy landscape changes 'instantly', and the vertex undergoes a transition according to predetermined energy gradient, often following curved trajectory. In such case, the velocity profile tends to be exponential, initially fast, and slowly decaying near the final equilibrium. Conversely, if the perturbation unfolds 'very slowly', the vertex is nearly equilibrated at each position; the gradual change of the energy landscape leads to rather constant velocity of transition, and the trajectory is a straight path between initial and final point.

(2) The transition characteristic is determined by the prominence of particular dissipative processes involved. Dominant vertex-localised dissipation reproduces the trajectories observed in the uncalibrated experiments. On the other hand, straight trajectories of constant velocity often observed in culture result from dominant elongational and substrate frictions.

The strong dependence of dynamics on the form dissipation has a potential significance. Spatial variability of the substrate friction might promote or discourage zippering in particular areas, while temporal changes in axon internal structure during maturation can lead to changes in elongational dissipation and help to preserve already established network topology.

4.3.2 Model simplifications

We made a series of general biophysical assumptions about the axons in the model, which are justified only to a certain degree. While axon are apparently reasonably approximated by piece-wise straight and one-dimensional segments, it is not as clear, if their strain and tension are uniform and equilibrate on a time scale faster than the zippering time scale. Besides these simplifications, we have neglected processes, which may play an important role, notably

side processes The lateral dynamical protrusions extended from axons/bundles and visibly influence the network. They can reach to other axons and even pull them with apparently large force (the axons become visibly deformed) and so facilitate a contact between two separate filaments.

GC activity GCs are distant from the modelled network zone, however they generate the traction force, which may influence the axon tension.

bending force We have shown in section 3.4.4, that the bending force for small bundles is likely negligible, however if the axons bundle into large fascicles (>10), the importance of bending grows super-linearly.

Another important simplification is geometrical. The zipper model is two-dimensional, planar, and the axons only touch each other, they do not cross over, the loss of axon-substrate contact is therefore not explicitly considered. Such effects become crucial, if we wish to model the transition between crossing and zippering, or if we ask questions about larger bundle formation, where some of the axons certainly lose contact with the substrate. However, for the dynamics of individual axons or small bundles, as we have shown in section 3.3.2, these effects can be neglected.

4.3.3 Comparison to previous models

The proposed biophysical model of zippering can be incorporated into earlier mathematical models of axon guidance and bundling. Such studies previously focused on the GC dynamics, and modelled GC guidance by diffusible GCMs (G. J. Goodhill and Urbach 1999), the influence of tension forces and anchor points/focal adhesions on GC trajectory (G.-H. Li et al. 1995; H. Nguyen et al. 2016), as well as contact interactions of GCs with other axons (Chaudhuri, Borowski, and Zapotocky 2011; Hentschel and A. v. Ooyen 1999). The dynamics of ASs, however, was not included in the previous models. Such mechanism is not explicitly considered even in highly generalised models of axon guidance (Hentschel and A. v. Ooyen 1999; Krottje and A. v. Ooyen 2006) or general path formation formulation of (Helbing, Keltsch, et al. 1997; Helbing, Schweitzer, et al. 1997).

One of the explanations why such feature was not implemented into other models, is a serious complexity of mathematical formulation in larger system. The model we present is isolated and simplified (e.g. straight axons, effective tension), while in general the physics of filaments is mathematically demanding; even more so in case of physics of filament interaction, particularly if they become very thin (i.e. width $\ll$ length) and cross over each other (i.e. three-dimensional situation). We address some of these issues in the section 4.7.2.

4.3.4 Numerical simulation

An advantage of our model is simplicity of its numerical implementation. The zipper configuration geometry is defined by a single variable, the vertex coordinate, and its time derivative is given by the equation of motion, section 3.6.5. Since the friction tensor $\overleftrightarrow{H}$ is invertible (for biophysically reasonable range of parameters and geometry), the matrix formulation of eq. (3.53) can be easily solved at each time step, and the trajectory integrated using Euler method. The coefficients of the matrix are straightforwardly calculated from the current geometry, the energy gradient is given analytically by eqs. (3.22) and (3.23).

This computational simplicity allows us to easily explore the large parameter space (i.e. T_1, T_2, S, k, $g(\{\vec{r}_i\})$, η^Z, $\eta^\perp$, $\eta^\parallel$, $\eta^{\Updownarrow}$). While some trajectory aspects can arise from multiple parameter combinations, some of the experimentally observed trajectories could be replicated using only very specific set of parameter values. This shows that even a simple and adaptable model can help us determine some of natural limits of the studied system. The model can be easily extended to include application of external

force, to model some of our manipulation experiments. It can be also implemented as part of larger network of several vertices, to observe how the perturbation is propagated.

4.4 Network structural changes

4.4.1 Coarsening

The culture system we observed in *ex vivo* experiments gradually coarsened in time and initial small bundles and axons formed larger fascicles. The coarsening progressed at the 10 h time scale, which is clearly much longer, that the 10 min time scale of a zipper transition. The coarsening is therefore unlikely a result of gradual relaxation of axon configurations with static tensions. One possibility would be, that the prolonged coarsening stems from gradual decrease of the average axon tension as the culture matures; such process would allow the unaffected axon-axon adhesion to overcome tension in the initially equilibrated vertices, and zippering would become preferred in the network. The proposal can be supported by the observed sequence of culture maturation stages,

(i) early axon elongation followed by
(ii) stalled growth intermediate stage (during which recordings take place), and
(iii) final phase of retraction and collapse of the culture.

It has been reported by (Dennerll, Lamoureux, et al. 1989) that the axonal elongation occurs only in axons with tension above a particular threshold (estimated as 1 nN for PC-12 axons), which points to the possibility, that the stalled stage (i.e. item (ii)) is a result of the axon tension decline. This is further supported by observed GC detachments from substrate later during the intermediate stage; decoupling of adhesion complexes disrupts generation of the traction force at the GC (Lamoureux, Buxbaum, et al. 1989), which forms a large portion of the overall axon tensile force (O'Toole, Lamoureux, et al. 2015).

4.4.2 Pharmacological manipulation of OSN culture

To directly test if a decrease in average axon tension leads to coarsening, we used cytochalasin, a drug that was previously shown to significantly decrease the tension in PC-12 neurites (Dennerll, Joshi, et al. 1988). Within 30 min of cytochalasin application, we observed an increased rate of coarsening in initially stabilised network (fig. 3.12), without visible slackening of axons. The effect of cytochalasin likely affected all the directions in the evolving network equally, because we did not observe significant change to the structure of the network. Although we were not able to measure the axon tension in cytochalasin-treated culture, the visible tautness of axons suggests that the drug effect on the axon tension was not devastating. We did observe local morphological changes (the GC acquiring a stub-like shape with suppressed filopodia, and a reduction in number of axonal side processes) consistent with previous studies (Dennerll, Joshi, et al. 1988; Letourneau et al. 1987), in which cytochalasin-induced reduction of axon tension was assessed.

As a second strategy aiming to perturb axon tension, we used blebbistatin, an inhibitor of NMII, previously shown to decrease cell cortex/membrane tension in non-neuronal

cells (Ayala et al. 2017; Fischer-Friedrich et al. 2014) and to decrease tension generated in smooth muscle (Ratz and Speich 2010). In growth cones of isolated DRG neurons, Sayyad et al. (Sayyad et al. 2015) showed that blebbistatin increased the force exerted by lamellipodia, but surprisingly reduced the force exerted by filopodia. Other studies found that the blebbistatin-dependent NMII inhibition may have opposite effects on axon extension, depending on the substrate, for example in (Hur et al. 2011; Ketschek et al. 2007). These studies suggest that while blebbistatin decreases cell cortex contractility, its effect on axon shaft tension may depend on additional factors. In our model system, we did not observe an obvious effect of blebbistatin on axon tension or on axon extension. Further analyses would be required to explain why blebbistatin has a stabilising effect on OSN axons grown in our experimental conditions.

Lastly, in a complementary tension perturbation, we tried to increase the axon tension by stimulating GC activity and motility. While specific biological agents are unknown for the OSN explant culture, we tested FBS, which contains a variety of growth factors and bioactive molecules. The FBS did not significantly stimulate the GC activity, but it clearly induced an apparent contraction of the explant boundary generating a pulling force on the outgrowing axons. The apparent contraction can be likely attributed to rounding of individual cells constituting the explant; the individual cell-rounding effect of FBS was reported in (Jalink and Moolenaar 1992), and was likely due to lysophosphatic acid (LPA) known to induce both cell rounding and neurite retraction (Jalink, Eichholtz, et al. 1993).

The increase in axon tension resulting from the explant contraction can be quantitatively estimated from the extension and the expected axon stiffness. Axons of our system have mechanical properties (basal tension and length) comparable to measurements on PC-12 and DRG neurites of Dennerll in (Dennerll, Joshi, et al. 1988; Dennerll, Lamoureux, et al. 1989); in these works, Dennerll estimated the stiffness of axons to be of order $100\,\frac{\mathrm{pN}}{\mu\mathrm{m}}$. We obtained similar estimates of stiffness from detailed analysis of the BFP experiments:

(1) estimate from the relaxation data after probe is fixed (fitting more complex model than used in section 3.5.7),
(2) estimate based on two tension measurements, between which the axon was significantly stretched (see fig. 3.22).

All the methods yielded results of the same order of magnitude. The stiffness of such magnitude should lead to increase in axon tension $\gtrsim 1\,\mathrm{nN}$ for the measured extension of $\sim 15\,\mu\mathrm{m}$ in the FBS experiments. Such increase is significant in OSN axon, as it more than doubles the typical axon tension. Within 20 min after FBS application, the culture underwent significant de-coarsening in parts of the network, including inverse of *T2* process (emergence of a loop), see figs. 3.10 and 3.11.

4.4.3 Regulation of fasciculation

The pharmacological manipulation experiments showed that the extent of axon fasciculation can be regulated by modification of axon tension. Lowering axon tension leads to axon-axon contact length expansion, prevalent zippering and promotes coarsening,

conversely increase in axon tension drives axon shortening, prevalent unzippering and de-coarsening. The tension change magnitude estimate also indicates that such changes are functionally viable *in vivo*. The effects are clearly visible in time course of network statistics; non-treated network evolves smoothly and monotonously during each of two stages (initial monotonous network growth/increase in complexity, followed by monotonous coarsening), no rapid changes are visible (see figs. 3.42 and 3.43), while the tension manipulation induces observable and rapid changes to otherwise monotonous statistical descriptors (see fig. 3.12 and caption of fig. 3.11).

4.4.4 Network-zipper relation

As the axon network coarsens, the zippers become predominantly formed by axon fascicles, rather than by individual axons. The tension of a fascicle grows with the number of constituting axons, which changes the distribution of tension within the filaments of the network. At the same time, the adhesion between the filaments increases with the growing surface of the bundles. Therefore, the bundling has direct implications for the geometry of the zippers we observe in the network. We used our model to predict the dependence of the zipper vertex angles in the network on the mean bundle size, which can be inferred from the observable change of network total length. These predictions were in agreement with the evolution of the observed median zipper angle and the network length, not only qualitatively, but also quantitatively. This consistency suggests that the axon zipper framework, based on tensile and adhesion forces, can be directly extended to the fascicle level.

We were also able to indirectly verify model consistency using *in vivo* data of Roberts and Taylor (Roberts and J. S. H. Taylor 1982). They recorded a histogram of incidence angles between neurites of sensory plexus on the basal lamina of trunk skin in *Xenopus*, while they kept record on whether the incident neurites crossed or formed an extended adhesive contact (i.e. zippered). These two sets of data can be reconciled within the framework of our model, which states, that the neurites will zipper, if their incidence angle is below the equilibrium angle (determined by the tension and adhesion). Assuming the observed distribution of incidence angles $\mathrm{PDF}_{\mathrm{exp}}(\beta)$ is close to the distribution of equilibrium angles $\mathrm{PDF}(\beta)$, the straightforward model prediction says that two neurites will zipper with the probability P_{zip} that their incidence angle β_{inc} is smaller that the probabilistically distributed equilibrium angle β (distributed according to $\mathrm{PDF}_{\mathrm{exp}}(\beta)$), i.e.

$$P_{\mathrm{zip}}(\beta_{\mathrm{inc}}) = \int_{\beta_{\mathrm{inc}}}^{\infty} \mathrm{PDF}_{\mathrm{exp}}(\beta) d\beta.$$

The data well agreed with such model framework prediction.

4.5 Froths-like characteristics of axonal networks

There are many similarities of the axonal network with froths of various kind. The most apparent analogy can be found with topological properties of two-dimensional liquid foams.

4.5.1 Comparison to liquid foams

Axonal network and two-dimensional liquid foam both exhibit characteristic separation of time scales. We can recognise (i) faster local relaxation under quasi-static forces which maintains validity of Plateau laws in foams, and analogical zippering processes in the axonal networks, and (ii) slower global coarsening, which is driven by diffusion according to von Neumann's law, and possibly (supported by section 3.2.1) by gradual tension decline in axon bundles in axonal network. The time scale separation allows us to separate the two dynamics, and model them independently. While the froth coarsening is well described by von Neumann's law, in the axonal network, the coarsening dynamics is under stochastic influence of internal axon processes and cell motility and therefore less deterministic.

The two systems can be compared in terms of basic topological processes. While the *T2* process (loop collapse, see fig. 3.47) is commonly observed in both systems, *T1* process cannot be realised in axonal network (border swap, see fig. 3.52) because the axons preserve their identity during topological changes and cannot merge. For the same reason is process *T2* reversible in axonal networks, the axon identity is conserved, so if tension is sufficiently restored (and so zipper equilibrium angle decreases), the loop would re-emerge (see fig. 3.11). An attempted *T1* process in the axonal network is doomed to result in another topological process, a 'wall rupture', in which the ASs of two axons completely unzipper and detach. On the other hand, new walls can in principle be formed in axonal network, when a side process pulls two separated axons into contact; such processes were however rarely observed.

When compared to liquid foams, axons bear more similarity to wet foams with higher liquid fraction. As the liquid fraction increases, the *Plateau borders* topological rules become less respected, and foam geometry becomes more relaxed, while new instabilities (Weaire, Vaz, et al. 2006) and viscoelastic properties (Lauridsen et al. 2002; Pratt and Dennin 2003) appear. We can naïvely identify some apparent analogies in axonal networks, as summarised in table 4.1.

One of the characteristic features of the wet foams is slower coarsening, $r \sim t^{1/3}$ in contrast to $r \sim t^{1/2}$ in the ideal and dry foams. However, we were not able to test the detailed functional dependence of average loop radius on time, due to noisiness and short time range of our data.

wet foams	**axonal network**
angles not strictly 120°	zipper angles are robust to small perturbations (e.g. when slightly moved by side process)
stable vertices of degree >3	common to observe vertices with degree >3, as advancing zippers can stop at the same place, such vertices are only metastable
unstable towards avalanches initiated by *T1* processes (Weaire, Vaz, et al. 2006)	*T1* process in axonal networks develops into a wall rupture and likely introduces spreading defect to the system
react elastically to external stress, the bubbles shear (Lauridsen et al. 2002; Pratt and Dennin 2003)	axons respond elastically to induced stress, loops exhibit shear deformation, see fig. 3.11
exhibit stick-slip flow under protracted stress (Lauridsen et al. 2002; Pratt and Dennin 2003)	zippers can exhibit stick-slip dynamics under prolonged stress (sometimes observed during OEC activity)

Table 4.1: Speculation on apparent analogy between wet foams and axonal network

4.5.2 Axon-specific effects

The zipper structure implies the vertex geometry does not obey the Plateau laws of ideal foams. The zipper vertices are governed by the eq. (3.9), and their equilibrium angles are typically around 60°. While not all the inner angles of a polygonal loop are the zipper angles, the typical zipper angle size (compare to 120° dictated by Plateau laws) will place constraint on the typical number of vertices per loop of stable network, which we observed to be very robustly ∼4.5, as compared to 6 in dry foams. As the system coarsens and the average bundle size increases, the typical zipper angle decreases and the larger loops (i.e. having more vertices) become even more unstable to *T2* processes. In a puzzling observation, the system visibly coarsens, but the vertex per loop number remains remarkably stable. This might be caused by developed entanglement at the vertex points.

We also observed two interesting effects at the level of the network. The first is a *Poisson's effect*, or 'necking', which develops when the network is under radial stress during explant contraction. The axons straighten and stretch radially while shift and contract laterally to form several 'necks' similar to basins, leaving largely empty space in between them. The effect can be probably ascribed to axons which laterally interconnect the radially oriented bundles, as their tension increases, so does the lateral pull on the nearby fascicles. The second interesting feature was *clustering*. After cytochalasin is added to the culture, prominent lamellipodia form. If the network is dense enough,

these can reach to neighbouring axons and pull them together in a form of cluster. In such way, roughly concentric areas of higher axon density are formed. Both of the processes decrease the network density and induce topological changes. They however disrupt the network structure and increase inhomogeneity and anisotropy. Therefore, when studying the coarsening of axonal network within the zippering framework, these processes have to be carefully considered.

Lastly, there are interesting local topological features not otherwise present in the foams. The axons are not supported by pressure, however their shape is supported by the substrate adhesion or strong friction. This offers more rich geometry, which also reflects the properties of the substrate. The potentially crucial role of substrate interaction was highlighted in section Substrate friction. The axons also influence their local environment by active processes, GC filopodia and side processes are particularly active and allow the axon to interact with the rest of the network at a finite range. This can not only bring axons into contact, but also induce perturbations in the network and initiate zippering.

4.5.3 Comparison to biological froth-like system

Analogies between froths and biological tissues consisting of closely packed cells have been investigated in previous literature, e.g. (Corson et al. 2009; Käfer et al. 2007). Such analogies are complicated by two aspects: (i) the active cortical mechanics of the cells (which make the interfacial tension dependent on the cell configuration (Käfer et al. 2007; Manning et al. 2010)), (ii) and restrictions on the volume of animal cells (which prevent pronounced coarsening). However, in (Corson et al. 2009), a growing plant tissue (meristem of *Arabidopsis thaliana*) was converted into a 'living froth' when oryzalin was used to depolymerise microtubules attached to the cell walls. In the resulting tissue, the topology and geometry of the cell interfaces was consistent with a typical froth, and pronounced coarsening of the structure was observed during the plant growth. The system we investigated—the zippering axon network—presents a remarkable example of an *ex vivo* system exhibiting both topological and dynamical analogies to froths. In our system, the coarsening is not limited by any cell volume restrictions, and can proceed rapidly, on the time scale of hours. However, structural features such as complex loop configurations and entangled zippers can limit the final extent of coarsening.

4.6 Zippering in vivo—functional significance

4.6.1 Inferred zippering in vivo

Current methods are not capable of imaging the zippering dynamics *in vivo* in mice, however inferences have been made about the zippering in other model organisms. In *Xenopus* embryos, the geometry of the sensory neurite plexus on the basal lamina of trunk skin exhibits features likely resulting from axon zippering, as proposed by Roberts and Taylor (Roberts and J. S. H. Taylor 1982), and illustrated in fig. 3.50. This *in vivo* configuration is similar to the *ex vivo* axonal network we studied, it has planar character

and absence of obstacles to zippering. In *C. elegans*, axon fascicles from the left and right ventral nerve cords fuse into a single fascicle if a specific medial interneuron is ablated at a late stage, when the axons have already reached their targets (Aurelio et al. 2002). This 'axon flip-over' phenotype appears very likely to be due to AS zippering, which is supported by abnormal fasciculation profiles observed between shafts which never fasciculate in non-manipulated animals. It was further shown that this phenotype was absent in immobilized animals, indicating that axon zippering was facilitated by mechanical forces exerted during the wriggling locomotion of the worm (ibid.). The inhibition of zippering in wild type animals is due to secretion by the medial interneuron of a 2-immunoglobulin-domain protein, which was proposed to bind and inhibit the activity of homophilic molecules expressed by the left/right contralaterally analogous axons (ibid.). These two examples illustrate the ability of ASs to zipper *in vivo*.

To put into perspective, the developing mammalian nervous system provides a lot of extracellular space (Lehmenkühler et al. 1993), with potential for AS zippering. While the available space decreases in time, the environment is still compatible with zippering, as long as no obstacles are formed—such barriers might be myelination, or cytoplasmic processes of Schwann cells, which appear with nerve maturation. The central nervous system however remains free of such separation, and shaft-shaft contact of unmyelinated axons persists in numerous areas.

4.6.2 Zippering in the olfactory system

Our *ex vivo* experiments with OE explants were motivated by the projection pattern of the mammalian OS, where large heterogeneous (∼1000 types) population of OSN axons from the OE fasciculates into a number of segregated bundles throughout the growth towards the target glomeruli of the OB (section 1.2). These axons are not myelinated and form tight bundles wrapped by the accompanying OECs; processes of the OECs may interdigitate into the bundle, but they do not separate individual axons (Y. Li, Field, et al. 2005). Within each bundle, the axons experience extensive contact interaction with each other, which may lead to bundle reorganisation as proposed in section 3.3.2, while such changes might be propagated along the bundle axis through the zippering. Such situation could be interpreted as a segregation processes described by the DAH generalised to cylindrical geometry (section 1.5), which predicts emergence of separated heterotypical subpopulations.

The DAH interpretation might be difficult to conceive for hundreds of axonal types; the OS sorting is however hierarchical and presorts the population in several steps, particularly along D-V and A-P axes. While the general projection area of a given axon is in primarily believed to be determined by GCM complementary gradients, the binary sorting itself within the ON can be easily driven by differential adhesion. Such mechanism would push apart dorsally and ventrally bound axons, while the anterior-bound population would become engulfed by the posterior-bound axons. The DAH does not require any specific composition of CAMs, the mere differential level of molecule expression was shown to suffice (Ramsey A. Foty and Malcolm S. Steinberg 2005). Considering the sorting process comprises millions of OSN axons with filamentous geometry (as opposed to

particles of general DAH), then a flexible form of contact between axons would be more optimal than binary yes/no contact relation between two DAH particles. The zippering might be able to provide such form of interaction. Imagine the following situation:

(1) Two axons (A and B) maintain contact along some segments of their length,
(2) at the other sections, they locally separate as axon A migrates (consistently with the DAH) to energetically more favourable area of the bundle,
(3) during the rezippering, the axon B has an energetical incentive to follow axon A,
(4) both axons shift to the more favourable location.

This shows that zippering could propagate local structure optimisations along the axon, extending the DAH mechanism to cylindrical geometry. Such process is however only speculative as the dynamics of axon contact interaction *in vivo* is yet to be investigated, particularly in relation to the differential adhesion, and the relation between the CAM, their level of expression and the OR-type of axons.

4.6.3 Regulated axon zippering in vivo

There are several levels at which regulated axonal zippering can have functional consequences *in vivo*. **first**| As the GC navigates towards its target, the ability to zipper can regulate the probability with which it would cross or fasciculate with another axon, as illustrated in section 3.9.3 using data of (Roberts and J. S. H. Taylor 1982). **second**| For outgrown axons with more distant GCs, the extent of fasciculation of their shafts may be regulated through zippering processes. During both the development and maturation of neural networks, ephaptic interactions between axons may be favoured in tightly fasciculated segments, thus influencing the synchrony of transmitted action potentials, or generating ectopic spikes (Bokil et al. 2001). Controlling the degree of fasciculation of axons through a regulation of zippering might possibly modulate such ephaptic interactions. **third**| The structure of developed fascicles might have important consequences for the later developmental stages or maturation of networks. Two opposing tendencies exist, (i) tight pioneer bundles form more robust guidance path for the follower axons, while (ii) the looser bundles may facilitate myelination. It is possible that the system goes from one configuration to another in between stages of development, while regulation of zippering or unzippering may serve to achieve such transition. **fourth**| In pathological contexts of axon regeneration following injury, or of axon demyelination, the unmyelinated axons or axon segments may undergo zippering in tracts. In tightly bundled tracts of partially demyelinated axons, ephaptic interactions are predicted to permit recovery of robust conduction (Reutskiy et al. 2003).

We have identified two principal ways the zippering and unzippering can be regulated *in vivo*. By a **tension control**, either through GC activity (O'Toole, Lamoureux, et al. 2008) or AS contractility (O'Toole, Lamoureux, et al. 2015). Such perturbation triggers zippering or unzippering as illustrated by our model (section 3.7.3) and may reorganise the network on the time scale of $\sim$10 min. On a slower time scale, the zippering processes can be modulated by **adhesion control**, by changes in CAM expression or their post-translational modification; e.g. NCAM involved in axon-axon adhesion are post-translationally regulated by binding of PSA, and so high levels of PSA lead to decline

in inter-axonal adhesion (Hoffman and Edelman 1983; Rutishauser 2008; Rutishauser et al. 1983; Sadoul et al. 1983). In many systems, fasciculation is controlled by GCMs through signalling pathways; it is at the moment unclear, how these signals affect tension or adhesion.

The traction force generated by axon GC (O'Toole, Lamoureux, et al. 2008), depends on the mechanical properties of its environment (reviewed in (Athamneh and Suter 2015)), likely through micro-scale elastic deformation of adhesion complexes between the axon actin network and the substrate (Athamneh, Cartagena-Rivera, et al. 2015; Mejean et al. 2013). In (Franze et al. 2009; Koch et al. 2012), the GC traction force was found to increase linearly with the substrate stiffness (before saturation); a similar relation was found in non-neuronal cells (Ghibaudo et al. 2008; Yip et al. 2013) (reviewed in (Kerstein et al. 2015)). In (Koch et al. 2012), a DRG neuron GC traction stress gradually doubled with increasing substrate stiffness, saturating at substrate stiffness $\sim$1000 Pa, with net traction force $\sim$1.2 nN. Spatial changes in substrate stiffness may therefore regulate the distal axon shaft tension (through GC activity) and hence the extent of zippering, potentially triggering fasciculation/defasciculation of a population of axons during development, when their GCs arrive to a specific target area. In our experiments with FBS-induced explant pull, we observed marked defasciculation following an estimated tension increase of $\sim$1 nN, comparable to GC generated values reported by (ibid.). This magnitude agreement suggests that significant changes in fasciculation may result from GC transitions between tissues with distinct elastic properties. Similarly, the general increase in stiffness of brain tissue during development (Franze 2013) may gradually increase the GC traction force and as a consequence facilitate unzippering and defasciculation as the growing tracts differentiate. In comparison, the substrate stiffness in our *ex vivo* experiments is more homogeneous and static, simplifying the zippering-driven dynamics.

As we have shown, the zippering of axon shafts can induce the formation of axon fascicles without participation of GCs *ex vivo*, while it has also been inferred *in vivo* (Aurelio et al. 2002; Roberts and J. S. H. Taylor 1982). Complementarily, the GCs are able to modify their traction force, which in part determines the axon tension; such ability can serve as a control mechanism to promote or inhibit zippering and in effect influence fasciculation/defasciculation and thus the formation of neural circuits.

4.7 Perspectives

4.7.1 Type-specific interactions of OSN axons

We performed a series of experiments on OSN culture, observing the development of OSN axons network over the time course of $\sim$10 h. In most of the experiments, the network exhibited clear gradual coarsening in absence of GCs, implying the novel fasciculation process. Under the differential interference contrast (DIC) microscope, it was not possible to quantify fascicle accretion; OSN axons are of small diameter (200 nm), and the DIC imagery does not allow to distinguish individual axons from small bundles, or the number of axons in a bundle in general. At the same time, the population

of OSNs comprises ∼1000 types of neurons, which differ by expressed OR, single OR is expressed in each neuron. Therefore, it might be possible to take advantage of such neuronal identity, and use OR-specific labelling, where particular OR-type neuron would express green fluorescent protein (GFP) (M. Q. Nguyen et al. 2007). This would allow us to distinguish particular axons and study their type-specific interactions.

4.7.2 Model extension

We will discuss two general directions in which the model should be extended to be more realistic, namely more detailed modelling of its continuum viscoelastic properties, and explicit modelling of adhesive contact interactions.

The **continuum properties** of axons in our context can be modelled as one-dimensional filaments with reasonable accuracy, while we assume axons are torsion-free. We may model stiffness and bending within the framework of the molecular dynamics (Alder and Wainwright 1959; Haile 1992; Rapaport 2004) as *beads and springs* model. In such formulation, the axon mass is discretised into a set of beads, the material stresses (both stretching and bending) are modelled as springs connecting individual beads. Compared to our initial model, such formulation allows to explicitly describe bending of axon and relaxation of curvature, as well as axial strain/stress gradient. The model introduces a time scale of axon viscoelastic response to external forces, without any *a priori* assumptions about strain distribution. At the same time, each bead is under the influence of substrate friction, linearly proportional to its velocity, i.e. the friction is strictly local, removing rather complex assumption-based formulation of friction tensor for the whole zipper configuration. It is straightforward to incorporate local stress-strain rate ($\tau \sim \dot{\epsilon}$) relation or more complex friction dependence, based on the bead immediate vicinity, i.e. relation with other surrounding beads.

The major difficulty of such model, however, is modelling of the **adhesive contact interaction**. Any bead-centric pair-wise form of potential (e.g. Lennard-Jones potential (Jones 1924)) leads to formation of close pairs of beads and stick-slip effects in the dynamics, caused by the discrete nature of the model. Attempting to use other models of interaction, it becomes difficult to satisfy conservation laws. In addition, the contact between the axon surfaces is attractive only in a relatively narrow distance range of roughly (20–50) nm (for NCAMs and cadherins), where the CAM domains overlap. Any closer approach leads to steric repulsion. Under this approach, overlaps of adhesive/repulsive domains are calculated, final magnitude of interaction, as a combination of attractive and repulsive, is calculated for the given segment, and distributed among the beads on the axons in such way, which respects the conservation laws (i.e. momentum and moment of force). The method is computationally inefficient and breaks down when axons cross.

A possible solution to the interaction modelling seems to be **JKR adhesive contact model** (Barthel 2008; K. L. Johnson et al. 1971), which describes adhesive contact of bodies, their steric repulsion as well as adhesion-induced surface deformation (i.e. an 'adhesive neck'). The model can be straightforwardly adapted to a contact of two finite cylinders in 3D (Jin et al. 2014); it provides a simple formula to calculate mutual force,

depending on cylinder curvature radius and mutual distance of centrelines. Therefore, if we consider each segment connecting two beads a cylinder around the centreline, we only need to calculate geometric distance between the centrelines and the corresponding contact areas of the cylinders (as given by JKR model). For two axons adhering while keeping the contact with the substrate, the two segments will be parallel and calculation trivial, but when the axons cross over one another, the 3D formulation provides simple yet non-trivial expressions to calculate the forces involved.

4.7.3 Automatic image segmentation can improve the analysis

Analysis of the network coarsening and topology section 3.8.1 is complicated by tedious manual segmentation. While DIC microscopy, which amounts for the majority of our recordings, enhances contrast in unstained samples, it is not suitable for automated image analysis detecting linear objects (i.e. ridge detection algorithm). The ridge detection algorithms generally trace the locally maximal pixels, however the DIC image frequently causes a bundle to change its contrast along its length, switching between dark and bright. This makes robust detection non viable. The situation can be improved by using phase-contrast microscopy, where the filaments preserve their contrast polarity. In such case, the ridges can be detected using scale-space technique pioneered by Tony Lindeberg (Lindeberg 1994, 1998, 2007).

The scale-space technique is suitable for the analysis of the network of variable fascicle width. It transforms a video frame into a series of images on different spatial scales, and detects ridge pixels on each scale by calculating invariants, which are functions of higher order derivatives of the image intensity. Such approach allows robust detection of ridges at the most optimal spatial scale; each ridge/filament is in the end represented by a set of coordinates, which define the backbone of the ridge. Such data structure can be easily used to calculate many descriptors, like degree of vertices, total length, curvature, loop area etc. While the manual segmentation yields a set of straight piece-wise segments, this methods provides detailed geometry of the filaments. It is of course simple to transform curved lines into straight segments between vertices, if necessary.

Chapter 5

Conclusions

In section Goals and hypothesis, we proposed, that if we could reduce the intrinsic *in vivo* complexity of neural development, axon targeting and fasciculation, into a simpler *ex vivo* system, it would be possible to characterise the interactions between shafts of axons, and assess their impact on the development of the system as a whole. In this work, we were able to successfully achieve such reduction for sensory neurons of olfactory system, by culturing explants of olfactory epithelium from embryonic mouse on planar permissive substrate *ex vivo*. The axons outgrowing from the explant developed into a dynamically interacting network, which slowly evolved in time and remained viable for days (section 3.1.1). We performed time lapse recordings of the outgrown network in an intermediate stage. During this stage, the growth cones are positioned on a remote periphery of the network and do not directly influence the observed central field; no material flow, axon retraction or removal, or apparent change to mechanical properties of axons are visible.

Under such desirable conditions of system evolving on slow time scale, we observed and characterised dynamical interactions between axon shafts occurring locally on much shorter time scale than the system evolution. In those interactions, partially adhering axons or small bundles expand (spread onto each other) or shrink (peel off each other) their mutual contact area, we called these processes *zippering* and *unzippering* respectively (section 3.1.2). The isolation of the observed region and minimal directed cell motility indicate that these processes are a natural property of the shafts of olfactory sensory neurons. We assessed the involved forces and proposed a hypothesis that zippering/unzippering results from local competition of axon mechanical tension and axon-axon adhesive interaction (section 3.2). If the two forces are balanced, two axons form static configuration with well-defined separation angle, otherwise they undergo dynamical transition.

We verified the zippering hypothesis by pharmacologically altering the axon tension on network level (section 3.2.1), or mechanically modifying axon geometry nearby a separation point (vertex; see fig. 3.8). Both types of experiments yielded results qualitatively consistent with our proposed hypothesis 1. To analyse zippers quantitatively, we formulated the hypothesis as a biophysical model of axon zippering. We used calibrated probe to measure axon tension (section 3.4.2), and several independent methods to estimate axon adhesion parameter, which was the first estimate of axon-axon adhesion force magnitude (section 3.5.3). We combined these parameters with the biophysical model, and performed a detailed analysis of the dynamics (sections 3.5.5 and 3.6.2),. Through this

detailed study of possible zippering transitions, we assessed the dissipative processes involved in zippering and axon shaft dynamics in general, and inferred their mutual significance in particular contexts. The transition velocity (observed), and biophysical parameters, measured (tension), model-deduced (adhesion), and inferred (dissipation), were consistent with measurements of analogical or related quantities in other systems. In line with our stated goals, the zippering was described and studied by the local biophysical model incorporating quantified biophysical parameters.

To relate the local model to the whole network, we generalised model prediction to population level (section 3.9). We then quantitatively analysed statistics and local geometry of the axonal network in time, and found it qualitatively consistent with our model predictions. To obtain purely quantitative assessment, we applied our model to observed axonal network coarsening and predicted, how such increase in mean fascicle size would affect network zippering angles; our prediction was in a good agreement with the change measured in the experiment *ex vivo*. This agreement provided a piece of evidence that the global network dynamics might be driven by the local zippering processes. In an apparent analogy to the dynamics and time scale separation of well-studied two-dimensional foams; we explored this analogy further, and described more notable similarities between the two, as well as important distinctions (section 3.10). We were able to connect the local and global features of the axonal network through our model, while shown, that such form of collective dynamics is not at all unique, but analogical to other studied system, with particular and well-understandable differences.

Finally, we contemplated the role of zippering *in vivo*. While it is not directly possible to extrapolate our results to any *in vivo* system, we were able to perform limited verification on *in vivo* data of *Xenopus* sensory plexus neurites growing on the trunk skin measured by Roberts and Taylor (Roberts and J. S. H. Taylor 1982). These neurites grow on a surface, where they are free to interact, similarly to our *ex vivo* setting. In images from scanning electron microscope, the neurites exhibit geometry, which is presumably a result of zippering. The authors collected two sets of data, but did not propose a mechanism to reconcile them. We were able to apply predictions of our model, and convincingly explain one set of data in the terms of another (section 3.9.3). We were able to use our model framework to quantitatively analyse, what Roberts and Taylor inferred from the observations. Developing organisms could invoke various mechanisms of zippering regulation, for instance (i) axon tension regulation, (ii) regulation of expression of cell adhesion molecules, or (iii) modulation of growth cone traction force. In such way, they may modify the extent of axonal fasciculation, and control the process of nervous system development.

Acronyms

AB	axon bundle.
ACIII	adenylyl cyclase type III.
AFM	atomic force microscope.
AP	action potential.
A-P	anterior-posterior.
apCAM	*Aplysia* cell adhesion molecule.
AS	axon shaft.
ATF5	activating transcription factor 5.
AuC	auditory cortex.
AuS	auditory system.
β2-AR	β2-adrenergic receptor.
BAS	bead adhesion site.
BFP	biomembrane force probe.
BSA	bovine serum albumin.
CAM	cell adhesion molecule.
C-domain	central domain.
CNG	cyclic-nucleotide gated.
CNS	central nervous system.
CNT	carbon nanotube.
DAH	differential adhesion hypothesis.
DIC	differential interference contrast.
DIV	days *in vitro*.
DMSO	dimethyl sulfoxide ($(CH_3)_2SO$).
DRG	dorsal root ganglion.
D-V	dorsal-ventral.
ECM	extra cellular matrix.
EM	electron microscopy.
EX	embryonic day X.
F-actin	fibrilar actin.
FBS	foetal bovine serum.
FSM	fluorescent speckle microscopy.

GC	growth cone.
GCM	guidance cue molecule.
GFP	green fluorescent protein.
GnRH	gonadotropin-releasing hormone.
GPCR	G-protein-coupled receptor.
GUI	graphical user interface.
HC	hair cell.
IC	inferior colliculus.
Ig	immunoglobulin.
LCR	locus control region.
LPA	lysophosphatic acid.
LVT	low velocity transport.
MAP	microtubule associated protein.
MEMS	microelectromechanical systems.
MFP	molecular force probe.
MM	migratory mass.
MN	micro-needle.
MRR	molecular receptive range.
MT	microtubule.
NA	numerical aperture.
NCAM	neural cell adhesion molecule.
NMII	neuronal Myosin II.
OB	olfactory bulb.
OC	olfactory cortex.
OCAM	olfactory cell adhesion molecule.
OE	olfactory epithelium.
OEC	olfactory ensheathing cell.
OMP	olfactory marker protein.
ON	olfactory nerve.
ONF	olfactory nerve fibroblast.
ONL	olfactory nerve layer.
OP	olfactory placode.
OR	odourant receptor.
OS	olfactory system.
OSN	olfactory sensory neuron.
PDF	probability density function.

P-domain	peripheral domain.
PSA	polysialic acid.
RBC	red blood cell.
RBI	restrained bead interaction.
RGC	retinal ganglion cell.
RMP	RBC-mounted pipette.
SB	streptavidin-coated micro-bead.
SC	superior colliculus.
SEM	scanning electron microscopy.
SFA	surface force apparatus.
SFM	scanning force microscope.
SGN	spiral ganglion neuron.
T-domain	transitional domain.
UPR	unfolded protein response.
VS	visual system.
WT	wild type.

Symbolslist

Sign	Description	Unit
A	axon-axon adhesion energy per unit length, $A < 0$	$\mathrm{J/m}$
a	loop (or 2D bubble) area	m^2
$\mathcal{C}$	total number of closed loops (shortest cycles)	
D	Rayleigh function	$\mathrm{J/s}$
E	energy	J
E	Young modulus (*duplicate* in section 1.3.1)	Pa
$\vec{e}$	unit vector	
F, $\vec{F}$	force	N
G	shear modulus	Pa
$\mathcal{H}$	Hookean contribution to axon mechanical tension	N
H	dashpot constant	$\mathrm{N\,s/m}$
H	mean curvature (*duplicate* in section 1.7.1)	$\mathrm{1/m}$
$\overleftrightarrow{H}$	friction tensor	$\mathrm{N\,s/m}$
$\overleftrightarrow{H}^{-1}$	'mobility' tensor, inverse of friction tensor	$\mathrm{m/s\,N}$
I	axon-substrate adhesion energy per unit length	$\mathrm{J/m}$
J	second moment of area	m^4
$\overleftrightarrow{K}$	friction tensor representation in Rayleigh formalism	$\mathrm{N\,s/m}$
k	Hookean stiffness	$\mathrm{N/m}$
L	length	m
l	segment length	m
$\mathcal{L}$	total network length	m
M	moment of force	N m
n	number of axons in a bundle	
$\vec{n}$	normal unit vector	
p, P	pressure	Pa
$\overleftrightarrow{P}$	projection operator	
R	radius	m
R	dissipation rate (*duplicate* in section 3.6.3)	$\mathrm{J/s}$
S	work of axon-axon adhesion per unit length, everywhere, except for section 3.3.1	$\mathrm{J/m}$
S	transverse section area of axon (*duplicate* in section 3.3.1)	m^2

Sign	Description	Unit
T	axon mechanical tension	N
T_0	axon baseline mechanical tension combined with substrate adhesion	N
T_a	axon baseline mechanical tension	N
$\vec{t}$	tangent unit vector	
$\vec{u}$	vertex velocity	m/s
u^Z	vertex zippering velocity magnitude	m/s
$\mathcal{V}$	total number of vertices	
$\vec{v}$	velocity of an element	m/s
W	work of adhesion	J/m^2
β	angle at the zipper vertex	deg
$\bar{\beta}$	mean network zipper angle	deg
β_{inc}	axon incidence angle	deg
β_M	median network zipper angle	deg
ϵ	material strain	
$\eta^{\Updownarrow}$	elongational friction coefficient	$\mathrm{N\,s}$
$\eta^{\perp}$	transverse axon-substrate friction	$\mathrm{N\,s}/\mathrm{m}^2$
$\eta^{\parallel}$	axial axon-substrate friction	$\mathrm{N\,s}/\mathrm{m}^2$
η^Z	vertex-localised friction coefficient	$\mathrm{N\,s}/\mathrm{m}$
γ	energy per unit surface, $\gamma > 0$	J/m^2
ι	axon-substrate energy of adhesion per unit area, $\iota > 0$	$\mathrm{J}^2/\mathrm{m}^2$
κ	diffusion coefficient	m^2/s
κ	curvature (*duplicate* in section 3.4.4)	$1/\mathrm{m}$
σ	surface tension	J/m^2
σ	tissue surface tension (*duplicate* in section 1.5)	J/m^2
τ	axon mechanical tension combined with elongational dissipation force	J/m
χ	adhesion force combined with vertex-localised dissipation	N

Glossary

CDF(X) cumulative distribution function of random variable X.

CDF$_{\text{exp}}$ (X) experiment-based estimate of cumulative distribution function of random variable X.

PDF(X) probability distribution function of random variable X.

PDF$_{\text{exp}}$ (X) experiment-based estimate of probability distribution function of random variable X.

axial substrate friction friction of axon shaft and substrate for axial axon movement; alias *parallel friction*.

chemotaxis movement of an organism in response to a chemical stimulus.

coarsening process of a network or structure becoming more coarse: decreasing total length, increasing size of voids.

de-coarsening inverse process of coarsening.

defasciculation deconstruction of bundles (fascicles) of axons.

elongational friction dissipative process caused by stretching or compressing an axon shaft in axial direction.

entangled zipper zipper with complex structure, which cannot recede.

fasciculation formation of bundles (fascicles) of axons.

growth cone structure at the tip of axon responsible for sensing, navigation and traction force generation.

Maxwell fluid model viscoelastic model, serial organisation of a spring and a dashpot model.

mechanotaxis movement of an organism in response to a mechanical stimulus.

side process a transcendent protrusion extending from the axon shaft that dynamically probes the environment and can exert force on other objects.

simple zipper zipper laminary parallel structure, which can recede and advance.

T1 topological process when two bubbles lose a common wall, and another two bubbles for a new common wall in place.

T2 topological process of a loop contraction/collapse.

tissue surface tension apparent tension at the tissue surface resulting from mutual adhesion of tissue cells.

traction force force generated by growth cone activity.

transverse substrate friction friction of axon shaft and substrate for transverse axon movement; alias *perpendicular friction*.

vertex a point where two adhering axons separate.

vertex-localised friction dissipative process caused by structural and irreversible binding changes at the vertex.

viscoelastic fluid material relaxes to zero stress under constant strain.

viscoelastic solid material relaxes to non-zero stress under constant strain.

Voigt element viscoelastic model, parallel organisation of a spring and a dashpot.

zipper dynamical process of interaction of two adhering axon shafts; the shafts expand or reduce their segment of adhesion.

zipper angle angle at the vertex where two adhering axons separate, i.e. a separation angle.

zipper axis axis in the system defined by the direction of the segment of axon-axon adhesion.

zipper-axial aligned with zipper axis.

zipper-transverse transverse (perpendicular) to zipper axis.

List of publications

Full length papers in peer reviewed journals

Daniel Šmít, Coralie Fouquet, Frederic Pincet, Martin Zapotocky, and Alain Trembleau (2017). 'Axon tension regulates fasciculation/defasciculation through the control of axon shaft zippering'. *eLife*. in press

Daniel Šmít, Coralie Fouquet, Mohamed Doulazmi, Frederic Pincet, Alain Trembleau, and Martin Zapotocky (2017). 'BFPTool: a software tool for analysis of Biomembrane Force Probe experiments'. *BMC Biophysics* 10.1, p. 2. ISSN: 2046-1682. DOI: 10.1186/s13628-016-0033-2.

Published open-source software

Daniel Šmít and Mohamed Doulazmi (2017). *BFPtool — A tool to analyse videos of BFP experiments*. GitHub. URL: https://github.com/smitdaniel/BFPtool (visited on 03/28/2017)

Published abstracts (in journals with impact factor)

Daniel Šmít, Coralie Fouquet, Frederic Pincet, Alain Trembleau, and Martin Zapotocky (2015). 'Axon zippering in neuronal cell culture and its biophysical modeling'. *BMC Neuroscience* 16 (Suppl 1), P298. ISSN: 1471-2202. DOI: 10.1186/1471-2202-16-S1-P298.

Bibliography

Acheson, A., J. L. Sunshine, and U. Rutishauser (1991). 'NCAM polysialic acid can regulate both cell-cell and cell-substrate interactions.' *The Journal of Cell Biology* 114.1, pp. 143–153. ISSN: 0021-9525, 1540-8140. DOI: 10.1083/jcb.114.1.143.

Aeschlimann, Mélanie and Laurent Tettoni (2000). 'Biophysical model of axonal pathfinding'. PhD thesis.

Ahmadzadeh, Hossein, Douglas H. Smith, and Vivek B. Shenoy (2014). 'Viscoelasticity of Tau Proteins Leads to Strain Rate-Dependent Breaking of Microtubules during Axonal Stretch Injury: Predictions from a Mathematical Model'. *Biophysical Journal* 106.5, pp. 1123–1133. ISSN: 0006-3495. DOI: 10.1016/j.bpj.2014.01.024.

Ahmed, Wylie W. and Taher A. Saif (2014). 'Active transport of vesicles in neurons is modulated by mechanical tension'. *Scientific Reports* 4, p. 4481. ISSN: 2045-2322. DOI: 10.1038/srep04481.

Alder, B.J. and T.E. Wainwright (1959). 'Studies in Molecular Dynamics. I. General Method'. *The Journal of Chemical Physics* 31.2, pp. 459–466. ISSN: 0021-9606. DOI: 10.1063/1.1730376.

Almgren, Frederick J. and Jean E. Taylor (1976). 'The Geometry of Soap Films and Soap Bubbles'. *Scientific American* 235, pp. 82–93. ISSN: 0036-8733. DOI: 10.1038/scientificamerican0776-82.

Anava, Sarit et al. (2009). 'The Regulative Role of Neurite Mechanical Tension in Network Development'. *Biophysical Journal* 96.4, pp. 1661–1670. ISSN: 0006-3495. DOI: 10.1016/j.bpj.2008.10.058.

Armstrong, Nicola J., Kevin J. Painter, and Jonathan A. Sherratt (2006). 'A continuum approach to modelling cell–cell adhesion'. *Journal of Theoretical Biology* 243.1, pp. 98–113. ISSN: 00225193. DOI: 10.1016/j.jtbi.2006.05.030.

Athamneh, Ahmad I. M., Alexander X. Cartagena-Rivera, et al. (2015). 'Substrate Deformation Predicts Neuronal Growth Cone Advance'. *Biophysical Journal* 109.7, pp. 1358–1371. ISSN: 0006-3495. DOI: 10.1016/j.bpj.2015.08.013.

Athamneh, Ahmad I. M. and Daniel M. Suter (2015). 'Quantifying mechanical force in axonal growth and guidance'. *Frontiers in Cellular Neuroscience*, p. 359. DOI: 10.3389/fncel.2015.00359.

Atherton, Tim J. and Darren J. Kerbyson (1999). 'Size invariant circle detection'. *Image and Vision computing* 17.11, pp. 795–803.

Aurelio, Oscar, David H. Hall, and Oliver Hobert (2002). 'Immunoglobulin-Domain Proteins Required for Maintenance of Ventral Nerve Cord Organization'. *Science* 295.5555, pp. 686–690. ISSN: 0036-8075, 1095-9203. DOI: 10.1126/science.1066642.

Ayala, Yareni A. et al. (2017). 'Effects of cytoskeletal drugs on actin cortex elasticity'. *Experimental Cell Research* 351.2, pp. 173–181. ISSN: 0014-4827. DOI: 10.1016/j.yexcr.2016.12.016.

Bak, Magdalena and Scott E. Fraser (2003). 'Axon fasciculation and differences in midline kinetics between pioneer and follower axons within commissural fascicles'. *Development* 130.20, pp. 4999–5008. ISSN: 0950-1991, 1477-9129. DOI: 10.1242/dev.00713.

Ballard, D. H. (1981). 'Generalizing the Hough transform to detect arbitrary shapes'. *Pattern Recognition* 13.2, pp. 111–122. ISSN: 0031-3203. DOI: 10.1016/0031-3203(81)90009-1.

Barry, Joshua, Yuanzheng Gu, and Chen Gu (2010). 'Polarized Targeting of L1-CAM Regulates Axonal and Dendritic Bundling in vitro'. *The European journal of neuroscience* 32.10, pp. 1618–1631. ISSN: 0953-816X. DOI: 10.1111/j.1460-9568.2010.07447.x.

Barthel, E. (2008). 'Adhesive elastic contacts: JKR and more'. *Journal of Physics D: Applied Physics* 41.16, p. 163001. ISSN: 0022-3727. DOI: 10.1088/0022-3727/41/16/163001.

Baumgart, Florian (2000). 'Stiffness — an unknown world of mechanical science?' *Injury* 31, pp. 14–84. ISSN: 0020-1383. DOI: 10.1016/S0020-1383(00)80040-6.

Berg, H. C. and E. M. Purcell (1977). 'Physics of chemoreception'. *Biophysical Journal* 20.2, pp. 193–219. ISSN: 0006-3495. DOI: 10.1016/S0006-3495(77)85544-6.

Bergou, Miklós et al. (2008). 'Discrete elastic rods'. In: *ACM transactions on graphics (TOG)*. Vol. 27. ACM, p. 63.

Bernal, Roberto, Pramod A. Pullarkat, and Francisco Melo (2007). 'Mechanical Properties of Axons'. *Physical Review Letters* 99.1, p. 018301. DOI: 10.1103/PhysRevLett.99.018301.

Betz, Timo et al. (2011). 'Growth cones as soft and weak force generators'. *Proceedings of the National Academy of Sciences* 108.33, pp. 13420–13425. ISSN: 0027-8424, 1091-6490. DOI: 10.1073/pnas.1106145108.

Bokil, Hemant et al. (2001). 'Ephaptic interactions in the mammalian olfactory system'. *J Neurosci* 21, pp. 1–5.

Borisyuk, Roman, Tom Cooke, and Alan Roberts (2008). 'Stochasticity and functionality of neural systems: Mathematical modelling of axon growth in the spinal cord of tadpole'. *Biosystems* 93.1, pp. 101–114. ISSN: 03032647. DOI: 10.1016/j.biosystems.2008.03.012.

Borisyuk, Roman et al. (2011). 'Modeling the Connectome of a Simple Spinal Cord'. *Frontiers in Neuroinformatics* 5. ISSN: 1662-5196. DOI: 10.3389/fninf.2011.00020.

– (2014). 'A Developmental Approach to Predicting Neuronal Connectivity from Small Biological Datasets: A Gradient-Based Neuron Growth Model'. *PLOS ONE* 9.2, e89461. ISSN: 1932-6203. DOI: 10.1371/journal.pone.0089461.

Boye, Kristian (2007). 'Development and Application of Biomembrane Force Probe Technique'. PhD thesis. University of Southern Denmark. 183 pp.

Bozza, Thomas et al. (2009). 'Mapping of Class I and Class II Odorant Receptors to Glomerular Domains by Two Distinct Types of Olfactory Sensory Neurons in the Mouse'. *Neuron* 61.2, pp. 220–233. ISSN: 0896-6273. DOI: 10.1016/j.neuron.2008.11.010.

Bray, D. (1979). 'Mechanical tension produced by nerve cells in tissue culture'. *Journal of Cell Science* 37.1, pp. 391–410. ISSN: 0021-9533, 1477-9137.

– (1984). 'Axonal growth in response to experimentally applied mechanical tension'. *Developmental Biology* 102.2, pp. 379–389. ISSN: 0012-1606. DOI: 10.1016/0012-1606(84)90202-1.

Brodland, G. Wayne (2002). 'The Differential Interfacial Tension Hypothesis (DITH): A Comprehensive Theory for the Self-Rearrangement of Embryonic Cells and Tissues'. *Journal of Biomechanical Engineering* 124.2, pp. 188–197. ISSN: 0148-0731. DOI: 10.1115/1.1449491.

Brodland, Wayne G and Helen H Chen (2000). 'The mechanics of cell sorting and envelopment'. *Journal of Biomechanics* 33.7, pp. 845–851. ISSN: 0021-9290. DOI: 10.1016/S0021-9290(00)00011-7.

Brown, Anthony (2000). 'Slow axonal transport: stop and go traffic in the axon'. *Nature Reviews Molecular Cell Biology* 1.2, pp. 153–156. ISSN: 1471-0072. DOI: 10.1038/35040102.

Brown, Anthony, Lei Wang, and Peter Jung (2005). 'Stochastic Simulation of Neurofilament Transport in Axons: The "Stop-and-Go" Hypothesis'. *Molecular Biology of the Cell* 16.9, pp. 4243–4255. ISSN: 1059-1524, 1939-4586. DOI: 10.1091/mbc.E05-02-0141.

Brusés, Juan L and U. Rutishauser (2001). 'Roles, regulation, and mechanism of polysialic acid function during neural development'. *Biochimie* 83.7, pp. 635–643. ISSN: 03009084. DOI: 10.1016/S0300-9084(01)01293-7.

Camalet, Sébastien and Frank Jülicher (2000). 'Generic aspects of axonemal beating'. *New Journal of Physics* 2.1, p. 24.

Chang, Yu-Ju et al. (2013). 'Micropatterned stretching system for the investigation of mechanical tension on neural stem cells behavior'. *Nanomedicine: Nanotechnology, Biology and Medicine* 9.3, pp. 345–355. ISSN: 15499634. DOI: 10.1016/j.nano.2012.07.008.

Chaudhuri, Debasish, Peter Borowski, P. K. Mohanty, et al. (2009). 'Dynamics of path aggregation in the presence of turnover'. *EPL (Europhysics Letters)* 87.2, p. 20003. ISSN: 0295-5075. DOI: 10.1209/0295-5075/87/20003.

Chaudhuri, Debasish, Peter Borowski, and Martin Zapotocky (2011). 'Model of fasciculation and sorting in mixed populations of axons'. *Physical Review E* 84.2, p. 021908. DOI: 10.1103/PhysRevE.84.021908.

Chédotal, Alain and Linda J. Richards (2010). 'Wiring the brain: the biology of neuronal guidance'. *Cold Spring Harbor Perspectives in Biology* 2.6, a001917. ISSN: 1943-0264. DOI: 10.1101/cshperspect.a001917.

Chen, Wei, Evan A. Evans, et al. (2008). 'Monitoring Receptor-Ligand Interactions between Surfaces by Thermal Fluctuations'. *Biophysical Journal* 94.2, pp. 694–701. ISSN: 0006-3495. DOI: 10.1529/biophysj.107.117895.

Chen, Wei, Jizhong Lou, et al. (2012). 'Observing force-regulated conformational changes and ligand dissociation from a single integrin on cells'. *The Journal of Cell Biology* 199.3, pp. 497–512. ISSN: 0021-9525, 1540-8140. DOI: 10.1083/jcb.201201091.

Chen, Yunfeng et al. (2015). 'Fluorescence Biomembrane Force Probe: Concurrent Quantitation of Receptor-ligand Kinetics and Binding-induced Intracellular Signaling on a Single Cell'. *Journal of Visualized Experiments* 102. ISSN: 1940-087X. DOI: 10.3791/52975.

Chernov, Nikolai (2009). *Ellipse Fit (Direct method) - File Exchange - MATLAB Central*. URL: http://www.mathworks.com/matlabcentral/fileexchange/22684-ellipse-fit--direct-method- (visited on 03/30/2017).

Chilton, John K. (2006). 'Molecular mechanisms of axon guidance'. *Developmental Biology* 292.1, pp. 13–24. ISSN: 0012-1606. DOI: 10.1016/j.ydbio.2005.12.048.

Chu, Yeh-Shiu, Sylvie Dufour, et al. (2005). 'Johnson-Kendall-Roberts theory applied to living cells'. *Physical review letters* 94.2, p. 028102.

Chu, Yeh-Shiu, William A. Thomas, et al. (2004). 'Force measurements in E-cadherin–mediated cell doublets reveal rapid adhesion strengthened by actin cytoskeleton remodeling through Rac and Cdc42'. *The Journal of Cell Biology* 167.6, pp. 1183–1194. ISSN: 0021-9525. DOI: 10.1083/jcb.200403043.

Clausen-Schaumann, Hauke et al. (2000). 'Force spectroscopy with single bio-molecules'. *Current Opinion in Chemical Biology* 4.5, pp. 524–530. ISSN: 1367-5931. DOI: 10.1016/S1367-5931(00)00126-5.

Cline, Hollis T (1998). 'Topographic maps: Developing roles of synaptic plasticity'. *Current Biology* 8.23, R836–R839. ISSN: 0960-9822. DOI: 10.1016/S0960-9822(07)00525-8.

Clowney, E. Josephine et al. (2011). 'High-throughput mapping of the promoters of the mouse olfactory receptor genes reveals a new type of mammalian promoter and provides insight into olfactory receptor gene regulation'. *Genome Research* 21.8, pp. 1249–1259. ISSN: 1088-9051, 1549-5469. DOI: 10.1101/gr.120162.110.

Condron, Barry G and Kai Zinn (1997). 'Regulated neurite tension as a mechanism for determination of neuronal arbor geometries in vivo'. *Current Biology* 7.10, pp. 813–816. ISSN: 0960-9822. DOI: 10.1016/S0960-9822(06)00343-5.

Cooke, Julie E., Hilary A. Kemp, and Cecilia B. Moens (2005). 'EphA4 Is Required for Cell Adhesion and Rhombomere-Boundary Formation in the Zebrafish'. *Current Biology* 15.6, pp. 536–542. ISSN: 0960-9822. DOI: 10.1016/j.cub.2005.02.019.

Corson, Francis et al. (2009). 'Turning a plant tissue into a living cell froth through isotropic growth'. *Proceedings of the National Academy of Sciences* 106.21, pp. 8453–8458. ISSN: 0027-8424, 1091-6490. DOI: 10.1073/pnas.0812493106.

Cramer, K.S. and M.L. Gabriele (2014). 'Axon guidance in the auditory system: Multiple functions of Eph receptors'. *Neuroscience* 277, pp. 152–162. ISSN: 03064522. DOI: 10.1016/j.neuroscience.2014.06.068.

Dalton, Ryan P., David B. Lyons, and Stavros Lomvardas (2013). 'Co-Opting the Unfolded Protein Response to Elicit Olfactory Receptor Feedback'. *Cell* 155.2, pp. 321–332. ISSN: 0092-8674. DOI: 10.1016/j.cell.2013.09.033.

De Odrowaz Piramowicz, Marzena et al. (2006). 'Dynamic force measurements of avidin-biotin and streptavdin-biotin interactions using AFM'. *Acta biochimica polonica* 53.1, pp. 93–100. ISSN: 0001-527X.

Dennerll, T. J., H. C. Joshi, et al. (1988). 'Tension and compression in the cytoskeleton of PC-12 neurites. II: Quantitative measurements.' *The Journal of Cell Biology* 107.2, pp. 665–674. ISSN: 0021-9525, 1540-8140. DOI: 10.1083/jcb.107.2.665.

Dennerll, T. J., P. Lamoureux, et al. (1989). 'The cytomechanics of axonal elongation and retraction.' *The Journal of Cell Biology* 109.6, pp. 3073–3083. ISSN: 0021-9525, 1540-8140. DOI: 10.1083/jcb.109.6.3073.

Dent, Erik W., Stephanie L. Gupton, and Frank B. Gertler (2011). 'The Growth Cone Cytoskeleton in Axon Outgrowth and Guidance'. *Cold Spring Harbor Perspectives in Biology* 3.3. ISSN: 1943-0264. DOI: 10.1101/cshperspect.a001800.

Dickson, Barry J. (2002). 'Molecular Mechanisms of Axon Guidance'. *Science* 298.5600, pp. 1959–1964. ISSN: 0036-8075, 1095-9203. DOI: 10.1126/science.1072165.

Duda, Richard O. and Peter E. Hart (1972). 'Use of the Hough Transformation to Detect Lines and Curves in Pictures'. *Commun. ACM* 15.1, pp. 11–15. ISSN: 0001-0782. DOI: 10.1145/361237.361242.

Duguay, Duke, Ramsey A Foty, and Malcolm S Steinberg (2003). 'Cadherin-mediated cell adhesion and tissue segregation: qualitative and quantitative determinants'. *Developmental Biology* 253.2, pp. 309–323. ISSN: 0012-1606. DOI: 10.1016/S0012-1606(02)00016-7.

Ekberg, Jenny A.K. et al. (2012). 'The Migration of Olfactory Ensheathing Cells during Development and Regeneration'. *Neurosignals* 20.3, pp. 147–158. ISSN: 1424-8638, 1424-862X. DOI: 10.1159/000330895.

Engler, Adam J. et al. (2006). 'Matrix Elasticity Directs Stem Cell Lineage Specification'. *Cell* 126.4, pp. 677–689. ISSN: 0092-8674. DOI: 10.1016/j.cell.2006.06.044.

Evans, Evan A. and K. Ritchie (1997). 'Dynamic strength of molecular adhesion bonds'. *Biophysical Journal* 72.4, pp. 1541–1555. ISSN: 0006-3495. DOI: 10.1016/S0006-3495(97)78802-7.

Evans, Evan A., K. Ritchie, and R. Merkel (1995). 'Sensitive force technique to probe molecular adhesion and structural linkages at biological interfaces'. *Biophysical Journal* 68.6, pp. 2580–2587. ISSN: 00063495. DOI: 10.1016/S0006-3495(95)80441-8.

Farbman, Albert I. (1994). 'Developmental biology of olfactory sensory neurons'. *Seminars in Cell Biology* 5.1, pp. 3–10. ISSN: 1043-4682. DOI: 10.1006/scel.1994.1002.

Fischer-Friedrich, Elisabeth et al. (2014). 'Quantification of surface tension and internal pressure generated by single mitotic cells'. *Scientific Reports* 4, p. 6213. ISSN: 2045-2322. DOI: 10.1038/srep06213.

Fitzgibbon, A., M. Pilu, and R. B. Fisher (1999). 'Direct least square fitting of ellipses'. *IEEE Transactions on Pattern Analysis and Machine Intelligence* 21.5, pp. 476–480. ISSN: 0162-8828. DOI: 10.1109/34.765658.

Foty, R. A. et al. (1996). 'Surface tensions of embryonic tissues predict their mutual envelopment behavior'. *Development* 122.5, pp. 1611–1620. ISSN: 0950-1991, 1477-9129.

Foty, Ramsey A., Gabor Forgacs, et al. (1994). 'Liquid properties of embryonic tissues: Measurement of interfacial tensions'. *Physical Review Letters* 72.14, pp. 2298–2301. DOI: 10.1103/PhysRevLett.72.2298.

Foty, Ramsey A. and Malcolm S. Steinberg (2004). 'Cadherin-mediated cell-cell adhesion and tissue segregation in relation to malignancy'. *The International Journal of Developmental Biology* 48.5, pp. 397–409. ISSN: 0214-6282. DOI: 10.1387/ijdb.041810rf.

– (2005). 'The differential adhesion hypothesis: a direct evaluation'. *Developmental Biology* 278.1, pp. 255–263. ISSN: 0012-1606. DOI: 10.1016/j.ydbio.2004.11.012.

Franze, Kristian (2013). 'The mechanical control of nervous system development'. *Development* 140.15, pp. 3069–3077. ISSN: 0950-1991, 1477-9129. DOI: 10.1242/dev.079145.

Franze, Kristian et al. (2009). 'Neurite Branch Retraction Is Caused by a Threshold-Dependent Mechanical Impact'. *Biophysical Journal* 97.7, pp. 1883–1890. ISSN: 00063495. DOI: 10.1016/j.bpj.2009.07.033.

Freund, L.B. (2009). 'The Stiffness of a Biomembrane Force Probe Vesicle'. *Mathematics and Mechanics of Solids* 14.1, pp. 148–160. ISSN: 1081-2865. DOI: 10.1177/1081286508092608.

Gañán-Calvo, A. M. et al. (2004). 'Coarsening of monodisperse wet microfoams'. *Applied Physics Letters* 84.24, pp. 4989–4991. ISSN: 0003-6951, 1077-3118. DOI: 10.1063/1.1762992.

Gauger, Erik (2005). 'Hydrodynamics of nanomachines in biology'. PhD thesis.

Georges, Penelope C. et al. (2006). 'Matrices with Compliance Comparable to that of Brain Tissue Select Neuronal over Glial Growth in Mixed Cortical Cultures'. *Biophysical Journal* 90.8, pp. 3012–3018. ISSN: 0006-3495. DOI: 10.1529/biophysj.105.073114.

Ghibaudo, Marion et al. (2008). 'Traction forces and rigidity sensing regulate cell functions'. 4.9, pp. 1836–1843. ISSN: 1744-6848. DOI: 10.1039/B804103B.

Glazer, Roland (1999). *Biophysics*. 5th ed. Germany: Springer-Verlag. ISBN: 3-540-67088-2.

Glazier, J. A. and D. Weaire (1992). 'The kinetics of cellular patterns'. *Journal of Physics: Condensed Matter* 4.8, p. 1867. ISSN: 0953-8984. DOI: 10.1088/0953-8984/4/8/004.

Glazier, James A. and Francois Graner (1993). 'Simulation of the differential adhesion driven rearrangement of biological cells'. *Physical Review E* 47.3, pp. 2128–2154. DOI: 10.1103/PhysRevE.47.2128.

Glazier, James A. and Joel Stavans (1989). 'Nonideal effects in the two-dimensional soap froth'. *Physical Review A* 40.12, pp. 7398–7401. DOI: 10.1103/PhysRevA.40.7398.

Goodhill, G. J., M. Gu, and J. S. Urbach (2004). 'Predicting Axonal Response to Molecular Gradients with a Computational Model of Filopodial Dynamics'. *Neural Computation* 16.11, pp. 2221–2243. ISSN: 0899-7667. DOI: 10.1162/0899766041941934.

Goodhill, G. J. and J. S. Urbach (1999). 'Theoretical analysis of gradient detection by growth cones'. *Journal of Neurobiology* 41.2, pp. 230–241. ISSN: 0022-3034.

Goodhill, Geoffrey J. and Linda J. Richards (1999). 'Retinotectal maps: molecules, models and misplaced data'. *Trends in Neurosciences* 22.12, pp. 529–534. ISSN: 0166-2236. DOI: 10.1016/S0166-2236(99)01469-1.

Goodhill, Geoffrey J. and Jun Xu (2005). 'The development of retinotectal maps: A review of models based on molecular gradients'. *Network: Computation in Neural Systems* 16.1, pp. 5–34. ISSN: 0954-898X. DOI: 10.1080/09548980500254654.

Gourier, Christine et al. (2008). 'A Nanospring Named Erythrocyte. The Biomembrane Force Probe'. *Cellular and Molecular Bioengineering* 1.4, pp. 263–275. ISSN: 1865-5025, 1865-5033. DOI: 10.1007/s12195-008-0030-x.

Graham, William (2011). *Stars, Bubbles and Beehives – Complexity Joined*. Nature's Web Of Life. URL: http://www.freshvista.com/2011/stars-bubbles-and-beehives-complexity-joined/ (visited on 03/27/2017).

Graner, Francois (1993). 'Can Surface Adhesion Drive Cell-rearrangement? Part I: Biological Cell-sorting'. *Journal of Theoretical Biology* 164.4, pp. 455–476. ISSN: 0022-5193. DOI: 10.1006/jtbi.1993.1167.

Graner, Francois and James A. Glazier (1992). 'Simulation of biological cell sorting using a two-dimensional extended Potts model'. *Physical Review Letters* 69.13, pp. 2013–2016. DOI: 10.1103/PhysRevLett.69.2013.

Graner, Francois and Yasuji Sawada (1993). 'Can Surface Adhesion Drive Cell Rearrangement? Part II: A Geometrical Model'. *Journal of Theoretical Biology* 164.4, pp. 477–506. ISSN: 0022-5193. DOI: 10.1006/jtbi.1993.1168.

Graziadei, P. P. C. and G. A. Monti Graziadei (1979). 'Neurogenesis and neuron regeneration in the olfactory system of mammals. I. Morphological aspects of differentiation and structural organization of the olfactory sensory neurons'. *Journal of Neurocytology* 8.1, pp. 1–18. ISSN: 0300-4864, 1573-7381. DOI: 10.1007/BF01206454.

Grubmüller, H., B. Heymann, and P. Tavan (1996). 'Ligand binding: Molecular mechanics calculation of the streptavidin-biotin rupture force.' *Science* 5251, pp. 997–999. ISSN: 0036-8075. DOI: 10.1126/science.271.5251.997.

Haile, J. M. (1992). *Molecular dynamics simulation*. Vol. 18. Wiley, New York.

Hanein, Y. et al. (2011). 'Neuronal soma migration is determined by neurite tension'. *Neuroscience* 172, pp. 572–579. ISSN: 03064522. DOI: 10.1016/j.neuroscience.2010.10.022.

Harris, Albert K. (1976). 'Is cell sorting caused by differences in the work of intercellular adhesion? A critique of the steinberg hypothesis'. *Journal of Theoretical Biology* 61.2, pp. 267–285. ISSN: 0022-5193. DOI: 10.1016/0022-5193(76)90019-9.

Heinrich, Volkmar, Andrew Leung, and Evan A. Evans (2005). 'Nano- to Microscale Dynamics of P-Selectin Detachment from Leukocyte Interfaces. II. Tether Flow Terminated by P-Selectin Dissociation from PSGL-1'. *Biophysical Journal* 88.3, pp. 2299–2308. ISSN: 0006-3495. DOI: 10.1529/biophysj.104.051706.

Helbing, Dirk, Joachim Keltsch, and Péter Molnár (1997). 'Modelling the evolution of human trail systems'. *Nature* 388.6637, pp. 47–50. ISSN: 0028-0836. DOI: 10.1038/40353.

Helbing, Dirk, Frank Schweitzer, et al. (1997). 'Active walker model for the formation of human and animal trail systems'. *Physical Review E* 56.3, pp. 2527–2539. DOI: 10.1103/PhysRevE.56.2527.

Hentschel, H G and A van Ooyen (1999). 'Models of axon guidance and bundling during development.' *Proceedings of the Royal Society B: Biological Sciences* 266.1434, pp. 2231–2238. ISSN: 0962-8452.

Hoffman, S. and G. M. Edelman (1983). 'Kinetics of homophilic binding by embryonic and adult forms of the neural cell adhesion molecule.' *Proceedings of the National Academy of Sciences of the United States of America* 80.18, p. 5762.

Honig, M. G. et al. (1998). 'In vitro studies of growth cone behavior support a role for fasciculation mediated by cell adhesion molecules in sensory axon guidance during development'. *Developmental Biology* 204.2, pp. 317–326. ISSN: 0012-1606. DOI: 10.1006/dbio.1998.9093.

Howard, Joe and Anthony A. Hyman (2003). 'Dynamics and mechanics of the microtubule plus end'. *Nature* 422.6933, pp. 753–758. ISSN: 0028-0836. DOI: 10.1038/nature01600.

Howard, Jonathon (2001). *Mechanics of Motor Proteins and the Cytoskeleton*. New edition. Sunderland, Mass.: Sinauer Associates. 384 pp. ISBN: 978-0-87893-333-4.

Hur, Eun-Mi et al. (2011). 'Engineering neuronal growth cones to promote axon regeneration over inhibitory molecules'. *Proceedings of the National Academy of Sciences* 108.12, pp. 5057–5062. ISSN: 0027-8424, 1091-6490. DOI: 10.1073/pnas.1011258108.

Husson, Julien, M. Dogterom, and Frederic Pincet (2009). 'Force spectroscopy of a single artificial biomolecule bond: The Kramers' high-barrier limit holds close to the critical force'. *The Journal of Chemical Physics* 130.5, p. 051103. ISSN: 0021-9606, 1089-7690. DOI: 10.1063/1.3077010.

Imai, Takeshi et al. (2009). 'Pre-Target Axon Sorting Establishes the Neural Map Topography'. *Science* 325.5940, pp. 585–590. ISSN: 0036-8075, 1095-9203. DOI: 10.1126/science.1173596.

Isenberg, Cyril (1978). *The Science of Soap Films and Soap Bubbles*. Google-Books-ID: PdsVME_LXTYC. Courier Corporation. 244 pp. ISBN: 978-0-486-26960-3.

Israelachvili, Jacob N. (1985). *Intermolecular and Surface Forces: With Applications to Colloidal and Biological Systems*. Google-Books-ID: rPG2SgAACAAJ. Academic Press. 296 pp. ISBN: 978-0-12-375180-5.

Izrailev, S. et al. (1997). 'Molecular dynamics study of unbinding of the avidin-biotin complex'. *Biophysical Journal* 72.4, pp. 1568–1581. ISSN: 0006-3495. DOI: 10.1016/S0006-3495(97)78804-0.

Jalink, K., T. Eichholtz, et al. (1993). 'Lysophosphatidic acid induces neuronal shape changes via a novel, receptor-mediated signaling pathway: similarity to thrombin action'. *Cell Growth & Differentiation* 4.4, p. 247.

Jalink, K. and W. H. Moolenaar (1992). 'Thrombin receptor activation causes rapid neural cell rounding and neurite retraction independent of classic second messengers.' *The Journal of Cell Biology* 118.2, pp. 411–419. ISSN: 0021-9525, 1540-8140. DOI: 10.1083/jcb.118.2.411.

Janmey, Paul A., Penelope C. Georges, and Søren Hvidt (2007). 'Basic Rheology for Biologists'. In: *Methods in Cell Biology*. Vol. 83. Elsevier, pp. 1–27. ISBN: 978-0-12-370500-6.

Jin, Fan et al. (2014). 'Adhesion between elastic cylinders based on the double-Hertz model'. *International Journal of Solids and Structures* 51.14, pp. 2706–2712. ISSN: 0020-7683. DOI: 10.1016/j.ijsolstr.2014.04.003.

Johnson, C. P. et al. (2004). 'Mechanism of homophilic adhesion by the neural cell adhesion molecule: Use of multiple domains and flexibility'. *Proceedings of the National Academy of Sciences* 101.18, pp. 6963–6968. ISSN: 0027-8424, 1091-6490. DOI: 10.1073/pnas.0307567100.

Johnson, K. L., K. Kendall, and A. D. Roberts (1971). 'Surface Energy and the Contact of Elastic Solids'. *Proceedings of the Royal Society of London A: Mathematical, Physical and Engineering Sciences* 324.1558, pp. 301–313. ISSN: 1364-5021, 1471-2946. DOI: 10.1098/rspa.1971.0141.

Jones, J. E. (1924). 'On the Determination of Molecular Fields. II. From the Equation of State of a Gas'. *Proceedings of the Royal Society of London A: Mathematical, Physical and Engineering Sciences* 106.738, pp. 463–477. ISSN: 1364-5021, 1471-2946. DOI: 10.1098/rspa.1924.0082.

Joshi, H. C. et al. (1985). 'Tension and compression in the cytoskeleton of PC 12 neurites.' *The Journal of Cell Biology* 101.3, pp. 697–705. ISSN: 0021-9525, 1540-8140. DOI: 10.1083/jcb.101.3.697.

Käfer, Jos et al. (2007). 'Cell adhesion and cortex contractility determine cell patterning in the Drosophila retina'. *Proceedings of the National Academy of Sciences* 104.47, pp. 18549–18554. ISSN: 0027-8424, 1091-6490. DOI: 10.1073/pnas.0704235104.

Kalil, Katherine (1996). 'Chapter 3 Growth cone behaviors during axon guidance in the developing cerebral cortex'. In: *Progress in Brain Research*. Ed. by R. Ranney Mize and Reha S. Erzurumlu. Vol. 108. Elsevier, pp. 31–40.

Keller, Klaus-Dieter (2002). *2-dimensional foam (bubbles lie in one layer)*.

Kerstein, Patrick C., Robert H. Nichol IV, and Timothy M. Gomez (2015). 'Mechanochemical regulation of growth cone motility'. *Frontiers in Cellular Neuroscience*, p. 244. DOI: 10.3389/fncel.2015.00244.

Ketschek, Andrea R., Steven L. Jones, and Gianluca Gallo (2007). 'Axon extension in the fast and slow lanes: Substratum-dependent engagement of myosin II functions'. *Developmental Neurobiology* 67.10, pp. 1305–1320. ISSN: 1932-846X. DOI: 10.1002/dneu.20455.

Keyvan-Fouladi, Naghmeh, Geoffrey Raisman, and Ying Li (2003). 'Functional repair of the corticospinal tract by delayed transplantation of olfactory ensheathing cells in adult rats'. *The Journal of neuroscience* 23.28, pp. 9428–9434.

Kobayakawa, Ko et al. (2007). 'Innate versus learned odour processing in the mouse olfactory bulb'. *Nature* 450.7169, pp. 503–508. ISSN: 0028-0836. DOI: 10.1038/nature06281.

Koch, Daniel et al. (2012). 'Strength in the Periphery: Growth Cone Biomechanics and Substrate Rigidity Response in Peripheral and Central Nervous System Neurons'. *Biophysical Journal* 102.3, pp. 452–460. ISSN: 0006-3495. DOI: 10.1016/j.bpj.2011.12.025.

Kolodkin, Alex L. and Marc Tessier-Lavigne (2011). 'Mechanisms and molecules of neuronal wiring: a primer'. *Cold Spring Harbor Perspectives in Biology* 3.6. ISSN: 1943-0264. DOI: 10.1101/cshperspect.a001727.

Kovács, Mihály et al. (2004). 'Mechanism of Blebbistatin Inhibition of Myosin II'. *Journal of Biological Chemistry* 279.34, pp. 35557–35563. ISSN: 0021-9258, 1083-351X. DOI: 10.1074/jbc.M405319200.

Krottje, Johannes K. and Arjen van Ooyen (2006). 'A Mathematical Framework for Modeling Axon Guidance'. *Bulletin of Mathematical Biology* 69.1, pp. 3–31. ISSN: 0092-8240, 1522-9602. DOI: 10.1007/s11538-006-9142-4.

Kulkarni, Rajan P., Magdalena Bak-Maier, and Scott E. Fraser (2007). 'Differences in protein mobility between pioneer versus follower growth cones'. *Proceedings of the National Academy of Sciences* 104.4, pp. 1207–1212. ISSN: 0027-8424, 1091-6490. DOI: 10.1073/pnas.0610142104.

Lagomarsino, M.C., F. Capuani, and C.P. Lowe (2003). 'A simulation study of the dynamics of a driven filament in an Aristotelian fluid'. *Journal of Theoretical Biology* 224.2, pp. 215–224. ISSN: 00225193. DOI: 10.1016/S0022-5193(03)00159-0.

Lamoureux, P., Robert E. Buxbaum, and Steven R. Heidemann (1989). 'Direct evidence that growth cones pull'. *Nature* 340.6229, pp. 159–162. ISSN: 0028-0836. DOI: 10.1038/340159a0.

Lamoureux, P., Steven R. Heidemann, et al. (2010). 'Growth and elongation within and along the axon'. *Developmental Neurobiology* 70.3, pp. 135–149. ISSN: 1932-846X. DOI: 10.1002/dneu.20764.

Landau, L. D. and E.M. Lifshitz (1987). *Fluid Mechanics*. second. Vol. 6. Course of Theoretical Physics. Pergamon Press. ISBN: 0-08-033933-6.

Lauridsen, John, Michael Twardos, and Michael Dennin (2002). 'Shear-Induced Stress Relaxation in a Two-Dimensional Wet Foam'. *Physical Review Letters* 89.9, p. 098303. DOI: 10.1103/PhysRevLett.89.098303.

Lee, Aih Cheun and Daniel M. Suter (2008). 'Quantitative analysis of microtubule dynamics during adhesion-mediated growth cone guidance'. *Developmental Neurobiology* 68.12, pp. 1363–1377. ISSN: 1932-846X. DOI: 10.1002/dneu.20662.

Lehmenkühler, A. et al. (1993). 'Extracellular space parameters in the rat neocortex and subcortical white matter during postnatal development determined by diffusion analysis'. *Neuroscience* 55.2, pp. 339–351. ISSN: 0306-4522. DOI: 10.1016/0306-4522(93)90503-8.

Letourneau, Paul C., Terri A. Shattuck, and Alice H. Ressler (1987). '"Pull" and "push" in neurite elongation: Observations on the effects of different concentrations of cytochalasin B and taxol'. *Cell Motility and the Cytoskeleton* 8.3, pp. 193–209. ISSN: 1097-0169. DOI: 10.1002/cm.970080302.

Lewcock, Joseph W. and Randall R. Reed (2004). 'A feedback mechanism regulates monoallelic odorant receptor expression'. *Proceedings of the National Academy of Sciences of the United States of America* 101.4, pp. 1069–1074. ISSN: 0027-8424, 1091-6490. DOI: 10.1073/pnas.0307986100.

Lewis, A. K. and P. C. Bridgman (1992). 'Nerve growth cone lamellipodia contain two populations of actin filaments that differ in organization and polarity.' *The Journal of Cell Biology* 119.5, pp. 1219–1243. ISSN: 0021-9525, 1540-8140. DOI: 10.1083/jcb.119.5.1219.

Lewis, J. P. (1995). 'Fast normalized cross-correlation'. In: *Vision interface*. Vol. 10, pp. 120–123.

Li, Guo-Hua, Cheng-de Qin, and Li-Wen Wang (1995). 'Computer model of growth cone behavior and neuronal morphogenesis'. *Journal of Theoretical Biology* 174.4, pp. 381–389. ISSN: 0022-5193. DOI: 10.1006/jtbi.1995.0106.

Li, Ying, Patrick Decherchi, and Geoffrey Raisman (2003). 'Transplantation of Olfactory Ensheathing Cells into Spinal Cord Lesions Restores Breathing and Climbing'. *The Journal of Neuroscience* 23.3, pp. 727–731. ISSN: 0270-6474, 1529-2401.

Li, Ying, Pauline M. Field, and Geoffrey Raisman (2005). 'Olfactory ensheathing cells and olfactory nerve fibroblasts maintain continuous open channels for regrowth of olfactory nerve fibres'. *Glia* 52.3, pp. 245–251. ISSN: 1098-1136. DOI: 10.1002/glia.20241.

Li, Yun Rose and Hiroaki Matsunami (2013). 'Unfolding the Mystery of Olfactory Receptor Gene Expression'. *Developmental Cell* 27.2, pp. 128–129. ISSN: 1534-5807. DOI: 10.1016/j.devcel.2013.10.012.

Lin, C. H., E. M. Espreafico, et al. (1996). 'Myosin Drives Retrograde F-Actin Flow in Neuronal Growth Cones'. *Neuron* 16.4, pp. 769–782. ISSN: 0896-6273. DOI: 10.1016/S0896-6273(00)80097-5.

Lin, C. H. and P. Forscher (1993). 'Cytoskeletal remodeling during growth cone-target interactions.' *The Journal of Cell Biology* 121.6, pp. 1369–1383. ISSN: 0021-9525, 1540-8140. DOI: 10.1083/jcb.121.6.1369.

Lin, Chi-Hung and Paul Forscher (1995). 'Growth cone advance is inversely proportional to retrograde F-actin flow'. *Neuron* 14.4, pp. 763–771. ISSN: 0896-6273. DOI: 10.1016/0896-6273(95)90220-1.

Lin, David M et al. (2000). 'Formation of Precise Connections in the Olfactory Bulb Occurs in the Absence of Odorant-Evoked Neuronal Activity'. *Neuron* 26.1, pp. 69–80. ISSN: 0896-6273. DOI: 10.1016/S0896-6273(00)81139-3.

Lindeberg, Tony (1994). 'Scale-space theory: a basic tool for analyzing structures at different scales'. *Journal of Applied Statistics* 21.1, pp. 225–270. ISSN: 0266-4763. DOI: 10.1080/757582976.

– (1998). 'Edge Detection and Ridge Detection with Automatic Scale Selection'. *International Journal of Computer Vision* 30.2, pp. 117–156. ISSN: 0920-5691, 1573-1405. DOI: 10.1023/A:1008097225773.

– (2007). 'Scale-Space'. In: *Wiley Encyclopedia of Computer Science and Engineering*. DOI: 10.1002/9780470050118.ecse John Wiley & Sons, Inc. ISBN: 978-0-470-05011-8.

Liu, Kuo-Kang (2006). 'Deformation behaviour of soft particles: a review'. *Journal of Physics D: Applied Physics* 39.11, R189–R199. ISSN: 0022-3727, 1361-6463. DOI: 10.1088/0022-3727/39/11/R01.

Lo, Chun-Min et al. (2000). 'Cell Movement Is Guided by the Rigidity of the Substrate'. *Biophysical Journal* 79.1, pp. 144–152. ISSN: 0006-3495. DOI: 10.1016/S0006-3495(00)76279-5.

Lodovichi, Claudia and Leonardo Belluscio (2012). 'Odorant Receptors in the Formation of the Olfactory Bulb Circuitry'. *Physiology* 27.4, pp. 200–212. ISSN: 1548-9213, 1548-9221. DOI: 10.1152/physiol.00015.2012.

Lowe, Christopher P (2003). 'Dynamics of filaments: modelling the dynamics of driven microfilaments.' *Philosophical Transactions of the Royal Society B: Biological Sciences* 358.1437, pp. 1543–1550. ISSN: 0962-8436. DOI: 10.1098/rstb.2003.1340.

Lu, Yun-Bi et al. (2006). 'Viscoelastic properties of individual glial cells and neurons in the CNS'. *Proceedings of the National Academy of Sciences* 103.47, pp. 17759–17764. ISSN: 0027-8424, 1091-6490. DOI: 10.1073/pnas.0606150103.

Luo, Liqun and John G. Flanagan (2007). 'Development of Continuous and Discrete Neural Maps'. *Neuron* 56.2, pp. 284–300. ISSN: 0896-6273. DOI: 10.1016/j.neuron.2007.10.014.

Lyons, David B. et al. (2014). 'Heterochromatin-Mediated Gene Silencing Facilitates the Diversification of Olfactory Neurons'. *Cell Reports* 9.3, pp. 884–892. ISSN: 2211-1247. DOI: 10.1016/j.celrep.2014.10.001.

MacLean-Fletcher, Susan and Thomas D. Pollard (1980). 'Mechanism of action of cytochalasin B on actin'. *Cell* 20.2, pp. 329–341. ISSN: 0092-8674. DOI: 10.1016/0092-8674(80)90619-4.

Maître, Jean-Léon and Carl-Philipp Heisenberg (2011). 'The role of adhesion energy in controlling cell–cell contacts'. *Current Opinion in Cell Biology* 23.5, pp. 508–514. ISSN: 0955-0674. DOI: 10.1016/j.ceb.2011.07.004.

Mancini, Marco (2005). 'Structure and evolution of soap-like foams'. PhD thesis. Citeseer.

Manning, M. Lisa et al. (2010). 'Coaction of intercellular adhesion and cortical tension specifies tissue surface tension'. *Proceedings of the National Academy of Sciences* 107.28, pp. 12517–12522. ISSN: 0027-8424, 1091-6490. DOI: 10.1073/pnas.1003743107.

Marchalot, J. et al. (2008). '2D foam coarsening in a microfluidic system'. *EPL (Europhysics Letters)* 83.6, p. 64006. ISSN: 0295-5075, 1286-4854. DOI: 10.1209/0295-5075/83/64006.

Maskery, Susan M., Helen M. Buettner, and Troy Shinbrot (2004). 'Growth Cone Pathfinding: a competition between deterministic and stochastic events'. *BMC Neuroscience* 5, p. 22. ISSN: 1471-2202. DOI: 10.1186/1471-2202-5-22.

Mejean, Cecile O. et al. (2013). 'Elastic Coupling of Nascent apCAM Adhesions to Flowing Actin Networks'. *PLOS ONE* 8.9, e73389. ISSN: 1932-6203. DOI: 10.1371/journal.pone.0073389.

Merkel, R. et al. (1999). 'Energy landscapes of receptor|[ndash]|ligand bonds explored with dynamic force spectroscopy'. *Nature* 397.6714, pp. 50–53. ISSN: 0028-0836. DOI: 10.1038/16219.

Michaelis, Leonor and Maud L. Menten (1913). 'Die kinetik der invertinwirkung'. *Biochem. z* 49.333, p. 352.

Miller, Alexandra M., Lydia R. Maurer, et al. (2010). 'Axon fasciculation in the developing olfactory nerve'. *Neural Development* 5, p. 20. ISSN: 1749-8104. DOI: 10.1186/1749-8104-5-20.

Miller, Alexandra M., Helen B. Treloar, and Charles A. Greer (2010). 'Composition of the migratory mass during development of the olfactory nerve'. *The Journal of Comparative Neurology* 518.24, pp. 4825–4841. ISSN: 1096-9861. DOI: 10.1002/cne.22497.

Miller, Kyle E. and Steven R. Heidemann (2008). 'What is slow axonal transport?' *Experimental Cell Research* 314.10, pp. 1981–1990. ISSN: 00144827. DOI: 10.1016/j.yexcr.2008.03.004.

Missaire, Mégane and Robert Hindges (2015). 'The role of cell adhesion molecules in visual circuit formation: From neurite outgrowth to maps and synaptic specificity: Cell Adhesion Molecules in the Visual System'. *Developmental Neurobiology* 75.6, pp. 569–583. ISSN: 19328451. DOI: 10.1002/dneu.22267.

Mombaerts, Peter (2006). 'Axonal Wiring in the Mouse Olfactory System'. *Annual Review of Cell and Developmental Biology* 22.1, pp. 713–737. DOI: 10.1146/annurev.cellbio.21.012804.093915.

Monahan, Kevin and Stavros Lomvardas (2015). 'Monoallelic Expression of Olfactory Receptors'. *Annual Review of Cell and Developmental Biology* 31.1, pp. 721–740. ISSN: 1081-0706. DOI: 10.1146/annurev-cellbio-100814-125308.

Mori, Kensaku and Hitoshi Sakano (2011). 'How Is the Olfactory Map Formed and Interpreted in the Mammalian Brain?' *Annual Review of Neuroscience* 34.1, pp. 467–499. DOI: 10.1146/annurev-neuro-112210-112917.

Mortimer, Duncan et al. (2009). 'A Bayesian model predicts the response of axons to molecular gradients'. *Proceedings of the National Academy of Sciences* 106.25, pp. 10296–10301. ISSN: 0027-8424, 1091-6490. DOI: 10.1073/pnas.0900715106.

Nakashima, Ai et al. (2013). 'Agonist-Independent GPCR Activity Regulates Anterior-Posterior Targeting of Olfactory Sensory Neurons'. *Cell* 154.6, pp. 1314–1325. ISSN: 0092-8674. DOI: 10.1016/j.cell.2013.08.033.

Nedelec, Stéphane, Caroline Dubacq, and Alain Trembleau (2005). 'Morphological and molecular features of the mammalian olfactory sensory neuron axons: What makes these axons so special?' *Journal of Neurocytology* 34.1, pp. 49–64. ISSN: 0300-4864, 1573-7381. DOI: 10.1007/s11068-005-5047-7.

Nguyen, Huyen et al. (2016). 'A mathematical model explains saturating axon guidance responses to molecular gradients'. *eLife* 5, e12248. ISSN: 2050-084X. DOI: 10.7554/eLife.12248.

Nguyen, Minh Q. et al. (2007). 'Prominent Roles for Odorant Receptor Coding Sequences in Allelic Exclusion'. *Cell* 131.5, pp. 1009–1017. ISSN: 0092-8674, 1097-4172. DOI: 10.1016/j.cell.2007.10.050.

Nguyen-Ba-Charvet, Kim T. et al. (2008). 'Robos and Slits Control the Pathfinding and Targeting of Mouse Olfactory Sensory Axons'. *The Journal of Neuroscience* 28.16, pp. 4244–4249. ISSN: 0270-6474, 1529-2401. DOI: 10.1523/JNEUROSCI.5671-07.2008.

Nishizumi, Hirofumi, Kouhei Kumasaka, et al. (2007). 'Deletion of the core-H region in mice abolishes the expression of three proximal odorant receptor genes in cis'. *Proceedings of the National Academy of Sciences* 104.50, pp. 20067–20072. ISSN: 0027-8424, 1091-6490. DOI: 10.1073/pnas.0706544105.

Nishizumi, Hirofumi and Hitoshi Sakano (2015). 'Developmental regulation of neural map formation in the mouse olfactory system'. *Developmental Neurobiology* 75.6, pp. 594–607. ISSN: 1932-846X. DOI: 10.1002/dneu.22268.

Norotte, C. et al. (2008). 'Experimental evaluation of apparent tissue surface tension based on the exact solution of the Laplace equation'. *EPL (Europhysics Letters)* 81.4, p. 46003. ISSN: 0295-5075. DOI: 10.1209/0295-5075/81/46003.

O'Toole, Matthew, P. Lamoureux, and Kyle E. Miller (2008). 'A Physical Model of Axonal Elongation: Force, Viscosity, and Adhesions Govern the Mode of Outgrowth'. *Biophysical Journal* 94.7, pp. 2610–2620. ISSN: 0006-3495. DOI: 10.1529/biophysj.107.117424.

O'Toole, Matthew, P. Lamoureux, and Kyle E. Miller (2015). 'Measurement of Subcellular Force Generation in Neurons'. *Biophysical Journal* 108.5, pp. 1027–1037. ISSN: 0006-3495. DOI: 10.1016/j.bpj.2015.01.021.

O'Toole, Matthew, Robert Latham, et al. (2008). 'Modeling mitochondrial dynamics during in vivo axonal elongation'. *Journal of Theoretical Biology* 255.4, pp. 369–377. ISSN: 00225193. DOI: 10.1016/j.jtbi.2008.09.009.

O'Toole, Matthew and Kyle E. Miller (2011). 'The Role of Stretching in Slow Axonal Transport'. *Biophysical Journal* 100.2, pp. 351–360. ISSN: 0006-3495. DOI: 10.1016/j.bpj.2010.12.3695.

Pacoret, Cécile et al. (2009). 'Touching the microworld with force-feedback optical tweezers'. *Optics Express* 17.12, pp. 10259–10264. ISSN: 1094-4087. DOI: 10.1364/OE.17.010259.

Pampaloni, Francesco et al. (2006). 'Thermal fluctuations of grafted microtubules provide evidence of a length-dependent persistence length'. *Proceedings of the National Academy of Sciences* 103.27, pp. 10248–10253. ISSN: 0027-8424, 1091-6490. DOI: 10.1073/pnas.0603931103.

Panorchan, Porntula et al. (2006). 'Single-molecule analysis of cadherin-mediated cell-cell adhesion'. *Journal of Cell Science* 119.1, pp. 66–74. ISSN: 0021-9533, 1477-9137. DOI: 10.1242/jcs.02719.

Peter, Stephen J. and Mohammad R. K. Mofrad (2012). 'Computational Modeling of Axonal Microtubule Bundles under Tension'. *Biophysical Journal* 102.4, pp. 749–757. ISSN: 0006-3495. DOI: 10.1016/j.bpj.2011.11.4024.

Pincet, Frederic and Julien Husson (2005). 'The Solution to the Streptavidin-Biotin Paradox: The Influence of History on the Strength of Single Molecular Bonds'. *Biophysical Journal* 89.6, pp. 4374–4381. ISSN: 0006-3495. DOI: 10.1529/biophysj.105.067769.

Pittman, Andrew J., Mei-Yee Law, and Chi-Bin Chien (2008). 'Pathfinding in a large vertebrate axon tract: isotypic interactions guide retinotectal axons at multiple choice points'. *Development* 135.17, pp. 2865–2871. ISSN: 0950-1991, 1477-9129. DOI: 10.1242/dev.025049.

Plateau, Joseph Antoine Ferdinand (1873). *Statique expérimentale et théorique des liquides soumis aux seules forces moléculaires*. Google-Books-ID: Tw9ZAAAAcAAJ. Gauthier-Villars. 512 pp.

Prakasam, A. K., V. Maruthamuthu, and D. E. Leckband (2006). 'Similarities between heterophilic and homophilic cadherin adhesion'. *Proceedings of the National Academy of Sciences* 103.42, pp. 15434–15439. ISSN: 0027-8424, 1091-6490. DOI: 10.1073/pnas.0606701103.

Pratt, Ethan and Michael Dennin (2003). 'Nonlinear stress and fluctuation dynamics of sheared disordered wet foam'. *Physical Review E* 67.5, p. 051402. DOI: 10.1103/PhysRevE.67.051402.

Rajagopalan, Jagannathan, Alireza Tofangchi, and M. Taher A. Saif (2010). 'Drosophila Neurons Actively Regulate Axonal Tension In Vivo'. *Biophysical Journal* 99.10, pp. 3208–3215. ISSN: 0006-3495. DOI: 10.1016/j.bpj.2010.09.029.

Rapaport, D. C. (2004). *The art of molecular dynamics simulation*. 2nd ed. Cambridge, UK ; New York, NY: Cambridge University Press. 549 pp. ISBN: 978-0-521-82568-9.

Raper, Jonathan and Carol Mason (2010). 'Cellular Strategies of Axonal Pathfinding'. *Cold Spring Harbor Perspectives in Biology* 2.9, a001933. ISSN: , 1943-0264. DOI: 10.1101/cshperspect.a001933.

Rasmussen, Søren G. F. et al. (2011). 'Crystal structure of the β2 adrenergic receptor-Gs protein complex'. *Nature* 477.7366, pp. 549–555. ISSN: 0028-0836. DOI: 10.1038/nature10361.

Ratz, Paul H. and John E. Speich (2010). 'Evidence that actomyosin cross bridges contribute to "passive" tension in detrusor smooth muscle'. *American Journal of Physiology - Renal Physiology* 298.6, F1424–F1435. ISSN: 1931-857X, 1522-1466. DOI: 10.1152/ajprenal.00635.2009.

Ressler, Kerry J., Susan L. Sullivan, and Linda B. Buck (1993). 'A zonal organization of odorant receptor gene expression in the olfactory epithelium'. *Cell* 73.3, pp. 597–609. ISSN: 0092-8674. DOI: 10.1016/0092-8674(93)90145-G.

Reutskiy, S., E. Rossoni, and B. Tirozzi (2003). 'Conduction in bundles of demyelinated nerve fibers: computer simulation'. *Biological Cybernetics* 89.6, pp. 439–448. ISSN: 0340-1200, 1432-0770. DOI: 10.1007/s00422-003-0430-x.

Roark, Raymond J., Warren C. Young, and Richard G. Budynas (2002). *Roark's formulas for stress and strain*. 7th ed. New York: McGraw-Hill. 852 pp. ISBN: 978-0-07-072542-3.

Roberts, Alan, Deborah Conte, et al. (2014). 'Can Simple Rules Control Development of a Pioneer Vertebrate Neuronal Network Generating Behavior?' *Journal of Neuroscience* 34.2, pp. 608–621. ISSN: 0270-6474, 1529-2401. DOI: 10.1523/JNEUROSCI.3248-13.2014.

Roberts, Alan and J. S. H. Taylor (1982). 'A scanning electron microscope study of the development of a peripheral sensory neurite network'. *Development* 69.1, pp. 237–250. ISSN: 0950-1991, 1477-9129.

Rodriguez, Ivan (2013). 'Singular Expression of Olfactory Receptor Genes'. *Cell* 155.2, pp. 274–277. ISSN: 0092-8674. DOI: 10.1016/j.cell.2013.09.032.

Rodriguez-Gil, Diego J. et al. (2015). 'Odorant receptors regulate the final glomerular coalescence of olfactory sensory neuron axons'. *Proceedings of the National Academy of Sciences* 112.18, pp. 5821–5826. ISSN: 0027-8424, 1091-6490. DOI: 10.1073/pnas.1417955112.

Round, Jennifer and Elke Stein (2007). 'Netrin signaling leading to directed growth cone steering'. *Current Opinion in Neurobiology* 17.1, pp. 15–21. ISSN: 0959-4388. DOI: 10.1016/j.conb.2007.01.003.

Rutishauser, U. (2008). 'Polysialic acid in the plasticity of the developing and adult vertebrate nervous system'. *Nature Reviews Neuroscience* 9.1, pp. 26–35. ISSN: 1471-003X, 1471-0048. DOI: 10.1038/nrn2285.

Rutishauser, U., M. Grumet, and G. M. Edelman (1983). 'Neural cell adhesion molecule mediates initial interactions between spinal cord neurons and muscle cells in culture'. *The Journal of Cell Biology* 97.1, pp. 145–152. ISSN: 0021-9525.

Sadoul, R. et al. (1983). 'Adult and embryonic mouse neural cell adhesion molecules have different binding properties'. *Nature* 304.5924, pp. 347–349. ISSN: 0028-0836.

Salmon, E. D. and Clare M. Waterman (2011). 'How we discovered fluorescent speckle microscopy'. *Molecular Biology of the Cell* 22.21, pp. 3940–3942. ISSN: 1059-1524. DOI: 10.1091/mbc.E11-07-0646.

Satomi, Ryo, Paul Grassia, and Christophe Oguey (2013). 'Modelling relaxation following T1 transformations of foams incorporating surfactant mass transfer by the Marangoni effect'. *Colloids and Surfaces A: Physicochemical and Engineering Aspects* 438, pp. 77–84.

Sayyad, Wasim A. et al. (2015). 'The role of myosin-II in force generation of DRG filopodia and lamellipodia'. *Scientific Reports* 5, p. 7842. ISSN: 2045-2322. DOI: 10.1038/srep07842.

Schaefer, Andrew W., Nurul Kabir, and Paul Forscher (2002). 'Filopodia and actin arcs guide the assembly and transport of two populations of microtubules with unique dynamic parameters in neuronal growth cones'. *The Journal of Cell Biology* 158.1, pp. 139–152. ISSN: 0021-9525, 1540-8140. DOI: 10.1083/jcb.200203038.

Schaefer, Michele L., Thomas E. Finger, and Diego Restrepo (2001). 'Variability of position of the P2 glomerulus within a map of the mouse olfactory bulb'. *The Journal of Comparative Neurology* 436.3, pp. 351–362. ISSN: 1096-9861. DOI: 10.1002/cne.1072.

Schindelin, Johannes et al. (2012). 'Fiji - an Open Source platform for biological image analysis'. *Nature methods* 9.7. ISSN: 1548-7091. DOI: 10.1038/nmeth.2019.

Schneider, Caroline A., Wayne S. Rasband, and Kevin W. Eliceiri (2012). 'NIH Image to ImageJ: 25 years of image analysis'. *Nature Methods* 9.7, pp. 671–675. ISSN: 1548-7091. DOI: 10.1038/nmeth.2089.

Schoetz, Eva-Maria (2007). 'Dynamics and Mechanics of Zebrafish Embryonic Tissues'. PhD thesis. Dresden, Germany: Technische Universität Dresden. 187 pp.

Schwarting, Gerald A. and Timothy R. Henion (2011). 'Regulation and function of axon guidance and adhesion molecules during olfactory map formation'. *Journal of Cellular Biochemistry* 112.10, pp. 2663–2671. ISSN: 07302312. DOI: 10.1002/jcb.23203.

Serizawa, S. (2003). 'Negative Feedback Regulation Ensures the One Receptor-One Olfactory Neuron Rule in Mouse'. *Science* 302.5653, pp. 2088–2094. ISSN: 0036-8075, 1095-9203. DOI: 10.1126/science.1089122.

Serizawa, Shou et al. (2006). 'A Neuronal Identity Code for the Odorant Receptor-Specific and Activity-Dependent Axon Sorting'. *Cell* 127.5, pp. 1057–1069. ISSN: 0092-8674. DOI: 10.1016/j.cell.2006.10.031.

Shefi, Orit, Eshel Ben-Jacob, and Amir Ayali (2002). 'Growth morphology of two-dimensional insect neural networks'. *Neurocomputing* 44–46, pp. 635–643. ISSN: 0925-2312. DOI: 10.1016/S0925-2312(02)00451-4.

Shefi, Orit, Amir Harel, et al. (2004). 'Biophysical constraints on neuronal branching'. *Neurocomputing*. Computational Neuroscience: Trends in Research 2004 58–60, pp. 487–495. ISSN: 0925-2312. DOI: 10.1016/j.neucom.2004.01.085.

Simpson, Hugh D. and Geoffrey J. Goodhill (2011). 'A simple model can unify a broad range of phenomena in retinotectal map development'. *Biological Cybernetics* 104.1, pp. 9–29. ISSN: 0340-1200, 1432-0770. DOI: 10.1007/s00422-011-0417-y.

Simson, D A et al. (1998). 'Micropipet-based pico force transducer: in depth analysis and experimental verification.' *Biophysical Journal* 74.4, pp. 2080–2088. ISSN: 0006-3495.

Sivasankar, S. et al. (1999). 'Direct molecular force measurements of multiple adhesive interactions between cadherin ectodomains'. *Proceedings of the National Academy of Sciences* 96.21, pp. 11820–11824. ISSN: 0027-8424, 1091-6490. DOI: 10.1073/pnas.96.21.11820.

Šmít, Daniel and Mohamed Doulazmi (2017). *BFPtool — A tool to analyse videos of BFP experiments*. GitHub. URL: https://github.com/smitdaniel/BFPtool (visited on 03/28/2017).

Šmít, Daniel, Coralie Fouquet, Mohamed Doulazmi, et al. (2017). 'BFPTool: a software tool for analysis of Biomembrane Force Probe experiments'. *BMC Biophysics* 10.1, p. 2. ISSN: 2046-1682. DOI: 10.1186/s13628-016-0033-2.

Šmít, Daniel, Coralie Fouquet, Frederic Pincet, Alain Trembleau, et al. (2015). 'Axon zippering in neuronal cell culture and its biophysical modeling'. *BMC Neuroscience* 16 (Suppl 1), P298. ISSN: 1471-2202. DOI: 10.1186/1471-2202-16-S1-P298.

Šmít, Daniel, Coralie Fouquet, Frederic Pincet, Martin Zapotocky, et al. (2017). 'Axon tension regulates fasciculation/defasciculation through the control of axon shaft zippering'. *eLife*. in press.

Soucy, Edward R et al. (2009). 'Precision and diversity in an odor map on the olfactory bulb'. *Nature Neuroscience* 12.2, pp. 210–220. ISSN: 1097-6256. DOI: 10.1038/nn.2262.

Sperry, R. W. (1963). 'Chemoaffinity in the Orderly Growth of Nerve Fiber Patterns and Connections'. *Proceedings of the National Academy of Sciences* 50.4, pp. 703–710. ISSN: 0027-8424, 1091-6490.

Spolenak, Ralph et al. (2005). 'Effects of contact shape on the scaling of biological attachments'. *Proceedings of the Royal Society of London A: Mathematical, Physical and Engineering Sciences* 461.2054, pp. 305–319. ISSN: 1364-5021, 1471-2946. DOI: 10.1098/rspa.2004.1326.

St. John, James A. et al. (2003). 'Sorting and convergence of primary olfactory axons are independent of the olfactory bulb'. *The Journal of Comparative Neurology* 464.2, pp. 131–140. ISSN: 1096-9861. DOI: 10.1002/cne.10777.

Steinberg, Malcolm S. (1970). 'Does differential adhesion govern self-assembly processes in histogenesis? Equilibrium configurations and the emergence of a hierarchy among populations of embryonic cells'. *Journal of Experimental Zoology* 173.4, pp. 395–433. ISSN: 1097-010X. DOI: 10.1002/jez.1401730406.

Steinberg, Malcolm S (2007). 'Differential adhesion in morphogenesis: a modern view'. *Current Opinion in Genetics & Development* 17.4, pp. 281–286. ISSN: 0959-437X. DOI: 10.1016/j.gde.2007.05.002.

Strotmann, Jörg et al. (2000). 'Local Permutations in the Glomerular Array of the Mouse Olfactory Bulb'. *The Journal of Neuroscience* 20.18, pp. 6927–6938. ISSN: 0270-6474, 1529-2401.

Suter, Daniel M. and Kyle E. Miller (2011). 'The Emerging Role of Forces in Axonal Elongation'. *Progress in neurobiology* 94.2, pp. 91–101. ISSN: 0301-0082. DOI: 10.1016/j.pneurobio.2011.04.002.

Tabakow, Pawel et al. (2013). 'Transplantation of Autologous Olfactory Ensheathing Cells in Complete Human Spinal Cord Injury'. *Cell Transplantation* 22.9, pp. 1591–1612. DOI: 10.3727/096368912X663532.

Takeuchi, Haruki et al. (2010). 'Sequential arrival and graded secretion of Sema3F by olfactory neuron axons specify map topography at the bulb'. *Cell* 141.6, pp. 1056–1067. ISSN: 1097-4172. DOI: 10.1016/j.cell.2010.04.041.

Tan, Longzhi, Chenghang Zong, and X. Sunney Xie (2013). 'Rare event of histone demethylation can initiate singular gene expression of olfactory receptors'. *Proceedings of the National Academy of Sciences* 110.52, pp. 21148–21152. ISSN: 0027-8424, 1091-6490. DOI: 10.1073/pnas.1321511111.

Tang, Jicheng, U. Rutishauser, and Lynn Landmesser (1994). 'Polysialic acid regulates growth cone behavior during sorting of motor axons in the plexus region'. *Neuron* 13.2, pp. 405–414. ISSN: 0896-6273. DOI: 10.1016/0896-6273(94)90356-5.

Tasinkevych, Mykola and Denis Andrienko (2010). 'Colloidal particles in liquid crystal films and at interfaces'. *arXiv preprint arXiv:1011.1189*.

Tessier-Lavigne, Marc and C. S. Goodman (1996). 'The molecular biology of axon guidance'. *Science (New York, N.Y.)* 274.5290, pp. 1123–1133. ISSN: 0036-8075.

The Mathworks, Inc. (2015). *Matlab release 2015b*. Version 8.6.0.267246. Nattick, MA, USA.

– (2017a). *Find circles using circular Hough transform - MATLAB imfindcircles*. URL: `https://www.mathworks.com/help/images/ref/imfindcircles.html` (visited on 03/28/2017).

– (2017b). *MATLAB Gateway to LibTIFF library routines - MATLAB*. URL: `https://www.mathworks.com/help/matlab/ref/tiff-class.html` (visited on 03/28/2017).

– (2017c). *Normalized 2-D cross-correlation - MATLAB normxcorr2*. URL: `https://www.mathworks.com/help/images/ref/normxcorr2.html` (visited on 03/28/2017).

– (2017d). *Supported File Formats for Import and Export - MATLAB & Simulink*. URL: `https://www.mathworks.com/help/matlab/import_export/supported-file-formats.html?searchHighlight=supported%20file%20formats%20for%20import%20and%20export&s_tid=doc_srchtitle` (visited on 03/28/2017).

Treloar, Helen B. et al. (2002). 'Specificity of glomerular targeting by olfactory sensory axons'. *The Journal of Neuroscience: The Official Journal of the Society for Neuroscience* 22.7, pp. 2469–2477. ISSN: 1529-2401. DOI: 20026239.

Tsuboi, Akio, Takaaki Miyazaki, et al. (2006). 'Olfactory sensory neurons expressing class I odorant receptors converge their axons on an antero-dorsal domain of the olfactory bulb in the mouse'. *European Journal of Neuroscience* 23.6, pp. 1436–1444. ISSN: 1460-9568. DOI: `10.1111/j.1460-9568.2006.04675.x`.

Tsuboi, Akio, Sei-ichi Yoshihara, et al. (1999). 'Olfactory Neurons Expressing Closely Linked and Homologous Odorant Receptor Genes Tend to Project Their Axons to Neighboring Glomeruli on the Olfactory Bulb'. *The Journal of Neuroscience* 19.19, pp. 8409–8418. ISSN: 0270-6474, 1529-2401.

Van Vactor, David (1998). 'Adhesion and signaling in axonal fasciculation'. *Current Opinion in Neurobiology* 8.1, pp. 80–86. ISSN: 0959-4388. DOI: `10.1016/S0959-4388(98)80011-1`.

Voyiadjis, A. G. et al. (2011). 'Fasciculation and defasciculation of neurite bundles on micropatterned substrates'. *Annals of Biomedical Engineering* 39.1, pp. 559–569. ISSN: 1573-9686. DOI: `10.1007/s10439-010-0168-2`.

Walz, Andreas et al. (2006). 'Disrupted compartmental organization of axons and dendrites within olfactory glomeruli of mice deficient in the olfactory cell adhesion molecule, OCAM'. *Molecular and Cellular Neuroscience* 32.1, pp. 1–14. ISSN: 1044-7431. DOI: `10.1016/j.mcn.2006.01.013`.

Weaire, D., Vincent Langlois, et al. (2007). 'Foam as granular matter'. *Granular and Complex Materials, World Scientific Lecture Notes in Complex Systems* 8, pp. 1–26.

Weaire, D., M. F. Vaz, et al. (2006). 'Instabilities in liquid foams'. *Soft Matter* 3.1, pp. 47–57. ISSN: 1744-6848. DOI: `10.1039/B608466B`.

Webber, Audra and Yael Raz (2006). 'Axon guidance cues in auditory development'. *The Anatomical Record Part A: Discoveries in Molecular, Cellular, and Evolutionary Biology* 288A.4, pp. 390–396. ISSN: 1552-4884, 1552-4892. DOI: `10.1002/ar.a.20299`.

Whitesides, John G. and Anthony-Samuel LaMantia (1996). 'Differential adhesion and the initial assembly of the mammalian olfactory nerve'. *The Journal of Comparative Neurology* 373.2, pp. 240–254. ISSN: 1096-9861. DOI: `10.1002/(SICI)1096-9861(19960916)373:2<240::AID-CNE7>3.0.CO;2-3`.

Wieland, Julie A., Andrew A. Gewirth, and Deborah E. Leckband (2005). 'Single Molecule Adhesion Measurements Reveal Two Homophilic Neural Cell Adhesion Molecule Bonds with Mechanically Distinct Properties'. *Journal of Biological Chemistry* 280.49, pp. 41037–41046. ISSN: 0021-9258, 1083-351X. DOI: `10.1074/jbc.M503975200`.

Wiggins, Chris H. and Raymond E. Goldstein (1998). 'Flexive and Propulsive Dynamics of Elastica at Low Reynolds Number'. *Physical Review Letters* 80.17, pp. 3879–3882. DOI: `10.1103/PhysRevLett.80.3879`.

Wong, Joyce, Ashutosh Chilkoti, and Vincent T. Moy (1999). 'Direct force measurements of the streptavidin–biotin interaction'. *Biomolecular engineering* 16.1, pp. 45–55.

Xu, Jun et al. (2005). 'Adaptation is not required to explain the long-term response of axons to molecular gradients'. *Development* 132.20, pp. 4545–4552. ISSN: 0950-1991, 1477-9129. DOI: `10.1242/dev.02029`.

Yip, Ai Kia et al. (2013). 'Cellular Response to Substrate Rigidity Is Governed by Either Stress or Strain'. *Biophysical Journal* 104.1, pp. 19–29. ISSN: 0006-3495. DOI: `10.1016/j.bpj.2012.11.3805`.

Yuen, HK et al. (1990). 'Comparative study of Hough Transform methods for circle finding'. *Image and Vision Computing* 8.1, pp. 71–77. ISSN: 0262-8856. DOI: 10.1016/0262-8856(90)90059-E.

Zheng, J. et al. (1991). 'Tensile regulation of axonal elongation and initiation'. *The Journal of Neuroscience: The Official Journal of the Society for Neuroscience* 11.4, pp. 1117–1125. ISSN: 0270-6474.

Zou, Dong-Jing, Alexander Chesler, and Stuart Firestein (2009). 'How the olfactory bulb got its glomeruli: a just so story?' *Nature Reviews Neuroscience* 10.8, pp. 611–618. ISSN: 1471-003X. DOI: 10.1038/nrn2666.

Zubler, Frederic et al. (2009). 'A framework for modeling the growth and development of neurons and networks'. *Frontiers in Computational Neuroscience* 3, p. 25. DOI: 10.3389/neuro.10.025.2009.